



# Carbonate-silicate reactions at conditions of the Earth's mantle and the role of carbonates as possible trace-element carriers

Nicole Biedermann, M.Sc. Geowissenschaften

Dissertation

zur Erlangung des akademischen Grades

„doctor rerum naturalium“

(Dr.rer.nat.)

in der Wissenschaftsdisziplin „Mineralogie“

eingereicht an der

Mathematisch-Naturwissenschaftlichen Fakultät  
der Universität Potsdam

Anfertigung der Arbeit:

European XFEL GmbH

Datum der Disputation: 15. Oktober 2020

**Betreuer:**

Prof. Dr. Max Wilke, Universität Potsdam

Dr. Karen Appel, European XFEL

**Gutachter:**

Prof. Dr. Max Wilke, Universität Potsdam

Prof. Dr. Monika Koch-Müller, Technische Universität Berlin

Dr. habil. Catherine McCammon, Universität Bayreuth

## **Eidesstattliche Erklärung**

Hiermit erkläre ich, Nicole Biedermann, geboren am 25. Juli 1990 in Berlin, Deutschland, an Eides statt, dass ich die beigefügte Dissertation selbstständig verfasst und keine anderen als die angegebenen Hilfsmittel genutzt habe. Alle wörtlich oder inhaltlich übernommenen Stellen habe ich als solche gekennzeichnet.

Ich versichere außerdem, dass ich die beigefügte Dissertation nur in diesem und keinem anderen Promotionsverfahren eingereicht habe und dass diesem Promotionsverfahren kein endgültig gescheitertes Promotionsverfahren vorausgegangen ist.

Schenefeld, den 10. Juni 2020

Nicole Biedermann





## Daraus hervorgegangene Publikationen

**Biedermann, N.**, Bykova, E., Morgenroth, W., Efthimiopoulos, I., Mueller, J., Spiekermann, G., Glazyrin, K., Pakhomova, A., Appel, K. and Wilke, M. (2020). Equation of state and high-pressure phase behaviour of SrCO<sub>3</sub>. *Eur. J. Mineral.* **32(6)**:575-586.

Spiekermann, G., Kuppenko, I., Petitgirard, S., Harder, M., Nyrow, A., Weis, C., Albers, C., **Biedermann, N.**, Libon, L., Sahle, C. J., Cerantola, V., Glazyrin K., Konopkova, Z., Morgenroth, W., Sergeev, I., Yavas, H., Dubrovinsky, L., Tolan, M., Sternemann, C., Wilke, M. (2020). A portable on-axis laser-heating system for near-90° X-ray spectroscopy: application to ferropericlase and iron silicide. *J. Synchrotron Rad.* **27(2)**:414-424.



# Acknowledgements

This study was funded by the Deutsche Forschungsgemeinschaft (DFG, under project number AP 262/1-1), the German Research Centre GFZ Potsdam and the European XFEL GmbH in the framework of the research group ‘CarboPaT’ which deals with the structure, properties and reactions of carbonates at high pressure and high temperature. The doctoral thesis was further supported by a PhD scholarship from the Potsdam graduate school (PoGS). I would like to thank these institutions for their financial support and help. Special thanks to all the researchers of ‘CarboPaT’ for their support and sharing their knowledge, data and results in several meetings.

I would like to express my deep gratitude to Prof. Dr. Max Wilke and Dr. Karen Appel for giving me the opportunity to work in the field of HP/HT mineralogy and their outstanding scientific support. I am thankful for their constant encouragement and patience with me, especially when new exciting scientific problems occurred or personal circumstances have changed.

Thanks to all former and present colleagues at the GFZ Potsdam who provided fruitful discussions and help in many situations during my first year as a PhD. Special thanks to Dr. Sergio Speziale, who introduced me to the mineral strontianite and its unknown physical properties as well as constantly giving me encouragement, criticism, inspiration and hope during my time as a PhD. In addition, I would like to thank Prof. Dr. Monika Koch-Mueller, Dr. Bernd Wunder, Dr. Matthias Gottschalk and Dr. Hans Josef Reichmann for their useful comments as well as Hans-Peter Nabein and Reiner Schulz for providing technical support.

I am grateful for the support and inspiration of Dr. Georg Spiekermann by sharing with me his experimental expertise and his enthusiasm on laser-heated DAC experiments. I always enjoyed our lively discussions and the work together as a team. I also want to thank Dr. Christina Günther and Christine Fischer from the institute for geosciences at the University of Potsdam for the preparation and performance of EMPA analyses and Lelia Libon for her scientific input and the time that we spent together.

Many thanks to the staff of beamline ID27 at the ESRF. In particular, I would like to thank Dr. Mohamed Mezouar, Dr. Gaston Garbarino and Dr. Volodymyr Svitlyk for their hospitality and help in supporting this work during my prolonged research stay at the ESRF in summer 2017. I also gratefully acknowledge the staff of beamline P02.2 at PETRA III for their technical support during our beamtimes. Dr. Elena Bykova, Dr. Anna Pakhomova, Dr. Maxim Bykov, Dr. Konstantin Glazyrin and Dr. Hanns-Peter Liermann are thanked for their useful comments and scientific support.

Prof. Dr. Björn Winkler, Dr. Lkhamsuren Bayarjargal and Dr. Chris-Julian Fruhner are thanked for their support and guidance in performing offline heating experiments using the CO<sub>2</sub>-laser system at the central laser facility of ‘CarboPaT’ at the University of Frankfurt. Special thanks also to Dr. Wolfgang Morgenroth for his support, advice and contributions that significantly improved this work in many aspects.

The outcome of my thesis would not have been the same without the excellent work of Dr. Richard Wirth and Anja Schreiber on the TEM at the GFZ Potsdam. Many thanks for the preparation of the TEM foils and for their help during TEM measurements.

Furthermore, I would like to thank everybody from the HED group at European XFEL for their support. Being the first PhD student in the HED team makes me proud but sometimes also made me feel being the "guinea pig" for several administrative and bureaucratic issues. Thanks to my PhD fellows, Markus Schoelmerich, Lennart Wollenweber, Christian Plueckthun and Johannes Kaa for creating such a warm atmosphere, especially in the last two years of my PhD, and for making me laugh a lot!

Finally, I want to thank my family, my friends and my partner Hendrik for their continuous support during all these years. You never stopped believing in me and helped me to keep the balance between work and life!

# Kurzfassung

Karbonate spielen eine entscheidene Rolle in der Chemie und Dynamik unseres Planeten. Sie sind in verschiedensten Lithologien auf der Erde verbreitet und stehen im direkten Zusammenhang mit dem CO<sub>2</sub>-Haushalt unserer Atmosphäre und dem tiefen, erdinneren Kohlenstoff-Kreislauf. Darüber hinaus haben jüngste Studien gezeigt, dass subduzierte Karbonate entlang des geothermischen Gradienten bis hinunter zu unteren Erdmantelbedingungen stabil sind, wobei sich ihre Kristallstruktur und die damit verbundenen Eigenschaften ändern. Ebenso können subduzierte Karbonate mit Mantelsilikaten reagieren und dabei neue Phasen bilden. Diese Reaktionen führen zu einer Umverteilung von Elementen, welche von den subduzierten Karbonaten hinunter in die Tiefen der Erde transportiert werden können. Die Elemente, um die es sich hauptsächlich handelt, sind dabei Calcium (Ca), Magnesium (Mg), Eisen (Fe) und Kohlenstoff in Form von Kohlenstoffdioxid (CO<sub>2</sub>). Aber auch Spurenelemente, wie beispielsweise Strontium (Sr) und Seltene Erdelemente (REE), können über Karbonate in den unteren Erdmantelbereich gelangen. Die Stabilität der Karbonate in Gegenwart von Mantelsilikaten bei relevanten Temperatur- und Druckbedingungen ist jedoch bei Weitem nicht bekannt. Ebenso ist nur sehr wenig über die Verteilungsprozesse von Spurenelementen zwischen Karbonaten und Mantelsilikaten bekannt. Um diese Prozesse zu beleuchten, wurden Reaktionen zwischen Sr- und REE-haltigem CaCO<sub>3</sub> und Mg/Fe-haltigen Silikaten aus dem pseudo-binären System (Mg,Fe)<sub>2</sub>SiO<sub>4</sub>–(Mg,Fe)SiO<sub>3</sub> unter hohem Druck und hoher Temperatur mit  $\mu$ -aufgelöster Röntgenbeugung ( $\mu$ -XRD) und Röntgenfluoreszenz ( $\mu$ -XRF) in einer lasergeheizten Diamantstempelzelle durchgeführt. Dabei wird Röntgenbeugung verwendet, um die strukturellen Änderungen der Phasenreaktionen abzuleiten, während Röntgenfluoreszenz Informationen über die chemischen Änderungen in der Probe liefert. Die Experimente wurden an der Messstation P02.2 bei PETRA III (Hamburg, Deutschland) und während eines längeren Forschungsaufenthalts an der Messstation ID27 an der ESRF (Grenoble, Frankreich) durchgeführt. Zusätzlich zu  $\mu$ -XRD und  $\mu$ -XRF wurden Aufnahmen am geheizten und zurückgewonnenen Probenmaterial mittels Transmissionselektronenmikroskopie (TEM) durchgeführt und lieferten weitere Erkenntnisse zur Reaktionskinetik.

Unsere Untersuchungen zeigen, dass CaCO<sub>3</sub> in Gegenwart von Mantelsilikaten bei über 1700 K instabil ist und eine Reaktion stattfindet, bei der Magnesit und CaSiO<sub>3</sub>-Perowskit gebildet werden. Die Untersuchung der Stabilität von SrCO<sub>3</sub> oder Sr-haltigem CaCO<sub>3</sub> – einem wichtigen Bestandteil in natürlichen Karbonaten – beruht auf der Idee, dass eine Reaktion mit Silikaten ein möglicher Mechanismus für den Ein-

bau von Sr in Mantelphasen sein könnte. Darüber hinaus zeigten jüngste Erkenntnisse zu Mineraleinschlüssen in Diamanten der Übergangszone signifikante Mengen an Sr in den Einschlüssen. In der Tat fanden wir heraus, dass  $\text{SrCO}_3$  mit  $(\text{Mg,Fe})\text{SiO}_3$ -Perowskit unter Bildung von Magnesit reagiert, und es gibt auch Hinweise zur Bildung von  $\text{SrSiO}_3$ -Perowskit, obwohl die Analyse dieser Phase auf einer begrenzten Datenmenge beruht. Ergänzend zu unserer Studie führten wir Pulver-Röntgenbeugung in Kombination mit Einkristall-Röntgenbeugung bei Umgebungstemperatur und bis zu 49 GPa am Endglied Strontianit ( $\text{SrCO}_3$ ) durch. Wir beobachteten eine Umwandlung von  $\text{SrCO}_3$ -I in eine neue Hochdruckphase  $\text{SrCO}_3$ -II bei etwa 26 GPa mit  $Pmmn$ -Kristallstruktur und einem Kompressionsmodul von 103(10) GPa. Solche Informationen sind sehr wichtig, da sie Aufschlüsse sowohl über das Phasenverhalten als auch über die Stabilität von Karbonaten in Gegenwart von Mantelsilikaten geben und helfen, sie vollständig zu verstehen.

Das gleichzeitige Erfassen von  $\mu$ -XRD und  $\mu$ -XRF über den lasergeheizten Bereich liefert räumliche Informationen sowohl über die Phasenreaktionen als auch über die Elementumverteilung zwischen den Phasen während des Reaktionsverlaufes. Ein Vergleich der räumlichen Intensitätsverteilungen von XRF Signalen vor und nach dem Heizen zeigt eine Änderung in der Elementverteilung von Sr und eine Zunahme der Sr-Konzentration um den neugebildeten  $\text{SrSiO}_3$ -Perowskit. Zusätzliche TEM-Aufnahmen am zurückgewonnenen, abgeschreckten Probenmaterial lieferten wichtige Erkenntnisse zur Elementumverteilung sowohl im Probenquerschnitt als auch im Submikrometer-Bereich. Entgegen den Erwartungen eines Einbaus der Seltenen Erdelemente in die neugebildeten Mantelsilikate, haben wir aus kombinierten  $\mu$ -XRD-,  $\mu$ -XRF- und TEM-Messungen festgestellt, dass La und Eu entweder isolierte Oxidphasen ( $\text{Eu}_2\text{O}_3$ ,  $\text{La}_2\text{O}_3$ ) oder Hydroxyl-Bastnäsit ( $\text{La}(\text{CO}_3)(\text{OH})$ ) bilden. Ebenfalls war zu beobachten, dass  $(\text{Mg,Fe})\text{SiO}_3$ -Perowskit sich während der Druckentlastung in Clinoenstatit umgewandelt hat. Die monokline Struktur dieser Phase ermöglicht den Einbau von Ca und, im geringeren Maße, Sr, wie durch zusätzliche EDX-Analysen gezeigt wurde.

Basierend auf den Erkenntnissen aus unseren Experimenten können wir schließen, dass ein Nachweis von Spurenelementen *in-situ* unter hohem Druck und hoher Temperatur eine Herausforderung bleibt. Unsere Ergebnisse deuten jedoch darauf hin, dass Silikate die Spurenelemente, welche von den Karbonaten transportiert werden, aufnehmen können und demzufolge Karbonate einen wesentlichen Einfluss auf den Spurenelementgehalt von Mantelphasen haben.

# Abstract

Carbonates play a key role in the chemistry and dynamics of our planet. They are directly connected to the CO<sub>2</sub> budget of our atmosphere and have a great impact on the deep carbon cycle. Moreover, recent studies have shown that carbonates are stable along the geotherm down to Earth's lower mantle conditions, changing their crystal structure and related properties. Subducted carbonates may also react with silicates to form new phases. These reactions will redistribute elements, such as calcium (Ca), magnesium (Mg), iron (Fe) and carbon in the form of carbon dioxide (CO<sub>2</sub>), but also trace elements, that are carried by the carbonates. The trace elements of most interest are strontium (Sr) and rare earth elements (REE) which have been found to be important constituents in the composition of the primitive lower mantle and in mineral inclusions found in super-deep diamonds. However, the stability of carbonates in presence of mantle silicates at relevant temperatures is far from being well understood. Related to this, very little is known about distribution processes of trace elements between carbonates and mantle silicates. To shed light on these processes, we studied reactions between Sr- and REE-containing CaCO<sub>3</sub> and Mg/Fe-bearing silicates of the pseudo-binary system (Mg,Fe)<sub>2</sub>SiO<sub>4</sub>–(Mg,Fe)SiO<sub>3</sub> at high pressure and high temperature using synchrotron radiation based  $\mu$ -X-ray diffraction ( $\mu$ -XRD) and  $\mu$ -X-ray fluorescence ( $\mu$ -XRF) with  $\mu$ m-resolution in a laser-heated diamond anvil cell. X-ray diffraction is used to derive the structural changes of the phase reactions whereas X-ray fluorescence gives information on the chemical changes in the sample. *In-situ* experiments at high pressure and high temperature were performed at beamline P02.2 at PETRA III (Hamburg, Germany) and at beamline ID27 at ESRF (Grenoble, France). In addition to  $\mu$ -XRD and  $\mu$ -XRF, *ex-situ* measurements were made on the recovered sample material using transmission electron microscopy (TEM) and provided further insights into the reaction kinetics of carbonate-silicate reactions.

Our investigations show that CaCO<sub>3</sub> is unstable in presence of mantle silicates above 1700 K and a reaction takes place in which magnesite plus CaSiO<sub>3</sub>-perovskite are formed. In addition, we observed that a high content of iron in the carbonate-silicate system favours dolomite formation during the reaction. The subduction of natural carbonates with significant amounts of Sr leads to a comprehensive investigation of the stability not only of CaCO<sub>3</sub> phases in contact with mantle silicates but also of SrCO<sub>3</sub> (and of Sr-bearing CaCO<sub>3</sub>). We found that SrCO<sub>3</sub> reacts with (Mg,Fe)SiO<sub>3</sub>-perovskite to form magnesite and gained evidence for the formation of SrSiO<sub>3</sub>-perovskite. Although, the analysis of this phase is based on very limited data.

To complement our study on the stability of  $\text{SrCO}_3$  at conditions of the Earth's lower mantle, we performed powder X-ray diffraction and single crystal X-ray diffraction experiments at ambient temperature and up to 49 GPa. We observed a transformation from  $\text{SrCO}_3$ -I into a new high-pressure phase  $\text{SrCO}_3$ -II at around 26 GPa with  $Pm\bar{m}n$  crystal structure and a bulk modulus of 103(10) GPa. This information is essential to fully understand the phase behaviour and stability of carbonates in the Earth's lower mantle and to elucidate the possibility of introducing Sr into mantle silicates by carbonate-silicate reactions.

Simultaneous recording of  $\mu$ -XRD and  $\mu$ -XRF in the  $\mu\text{m}$ -range over the heated areas provides spatial information not only about phase reactions but also on the elemental redistribution during the reactions. A comparison of the spatial intensity distribution of the XRF signal before and after heating indicates a change in the elemental distribution of Sr and an increase in Sr-concentration can be found around the newly formed  $\text{SrSiO}_3$ -perovskite. With the help of additional TEM analyses on the quenched sample material the elemental redistribution was studied in a three dimensional space and at a sub-micrometer scale. Contrary to expectations from combined  $\mu$ -XRD and  $\mu$ -XRF measurements, we found that La and Eu were not incorporated into the silicate phases, instead they tend to form either isolated oxide phases (e.g.  $\text{Eu}_2\text{O}_3$ ,  $\text{La}_2\text{O}_3$ ) or hydroxyl-bastnäsite ( $\text{La}(\text{CO}_3)(\text{OH})$ ). In addition, we observed the transformation from  $(\text{Mg,Fe})\text{SiO}_3$ -perovskite to low-pressure clinoenstatite during pressure release. The monoclinic structure of this phase allows the incorporation of Ca as shown by additional EDX analyses and, to a minor extent, Sr too.

Based on our experiments, we can conclude that a detection of the trace elements *in-situ* at high pressure and high temperature remains challenging. However, our first findings imply that silicates may incorporate the trace elements provided by the carbonates and indicate that carbonates may have a major effect on the trace element contents of mantle phases.



# Presentations

The content of this thesis has been presented at scientific conferences in the following contributions:

Biedermann, N., Appel, K., Spiekermann, G., Morgenroth, W., Bayarjargal, L., Fruhner, C.-J., Pakhomova, A., Bykov, M., Garbarino, G., Wirth, R. and Wilke, M. (2019). Reactions between  $\text{CaCO}_3$  and bridgmanite at mantle conditions and the role of carbonates in the Earth's deep interior. European High Pressure Research Group (EHPRG) International Meeting on High Pressure Science and Technology, Prague, Czech Republic.

Biedermann, N., Appel, K., Spiekermann, G., Morgenroth W., Pakhomova, A. and Wilke, M. (2017). *In-situ* stability of carbonates in presence of mantle phases, Foundations of Crystallography 70: C1107.

Biedermann, N. (2017). Stability of carbonates at lower mantle conditions - a possible candidate for carbon storage in the Earth's deep interior. Third DCO Early Career Scientist Workshop, Nicolosi, Italy.

Biedermann, N., Appel, K., Spiekermann, G., Morgenroth W., Pakhomova, A., Wirth, R. and Wilke, M. (2017). Trace-element fractionation processes between carbonates and silicates at mantle conditions, Goldschmidt Abstracts. 2017:342.

Biedermann, N., Appel K., Spiekermann G., Morgenroth W., Pakhomova, A., Bykov, M., Wirth, R. and Wilke, M. (2017). Carbonate-silicate reactions under mantle conditions. The role of carbonates as possible trace-element carriers in the deep Earth. DMG Annual Meeting GeoBremen, Bremen, Germany.

Biedermann, N., Wilke, M. and Appel, K. (2016). Trace element distribution between Earth mantle phases and carbonates at HP/HT, International School of Crystallography (ISCoC), Erice, Italy.



# List of Content

<b>Acknowledgements</b>	<b>v</b>
<b>Kurzfassung</b>	<b>vii</b>
<b>Abstract</b>	<b>ix</b>
<b>Presentations</b>	<b>xi</b>
<b>List of Figures</b>	<b>xv</b>
<b>List of Tables</b>	<b>xvii</b>
<b>1 Introduction</b>	<b>1</b>
1.1 Motivation and aim of this study . . . . .	1
1.2 The deep carbon cycle . . . . .	4
1.2.1 The role of CaCO <sub>3</sub> and SrCO <sub>3</sub> in the Earth's mantle . . . . .	5
1.2.2 Evidence for carbonate-silicate reactions in the deep Earth . . . . .	6
1.3 Chemical composition of the Earth's lower mantle . . . . .	8
1.4 Studying element transport processes in laser-heated diamond anvil cells . . . . .	9
<b>2 Experimental methods</b>	<b>11</b>
2.1 Sample preparation and synthesis of trace element doped carbonates . . . . .	11
2.1.1 Synthesis of Sr- and La-doped calcite using the IHPV . . . . .	12
2.1.2 Pre-characterization of the samples . . . . .	13
2.2 Diamond anvil cell technique and sample loading . . . . .	15
2.3 High-pressure single crystal X-ray diffraction experiments . . . . .	19
2.4 Laser-heated and resistively heated diamond anvil cell experiments . . . . .	21
2.4.1 Offline laser heating . . . . .	21
2.4.2 <i>In-situ</i> laser heating . . . . .	22
2.4.3 Resistively heated DAC experiments . . . . .	24
2.5 Combined $\mu$ -XRD and $\mu$ -XRF data acquisition . . . . .	25
2.5.1 Introduction to XRD and XRF . . . . .	25
2.5.2 XRD and XRF data processing . . . . .	26
2.6 TEM analyses on recovered sample material . . . . .	29

<b>3</b>	<b>EoS and high-pressure phase behaviour of SrCO<sub>3</sub></b>	<b>31</b>
3.1	Introduction . . . . .	31
3.2	Methods . . . . .	33
3.2.1	Synthesis of sample material . . . . .	33
3.2.2	High-pressure X-ray diffraction experiments . . . . .	33
3.3	Results and Discussion . . . . .	35
3.3.1	Phase transitions of SrCO <sub>3</sub> during compression . . . . .	35
3.3.2	Compressibility of strontianite (SrCO <sub>3</sub> -I) and SrCO <sub>3</sub> -II . . . . .	37
3.3.3	Crystal structure of post-aragonite SrCO <sub>3</sub> -II . . . . .	42
3.4	Conclusions . . . . .	44
<b>4</b>	<b>Results on carbonate-silicate reaction experiments</b>	<b>45</b>
4.1	Phase stability of CaCO <sub>3</sub> and SrCO <sub>3</sub> in presence of mantle silicates . . .	45
4.1.1	XRD measurements on reactions between CaCO <sub>3</sub> (:M) and silicates	45
4.1.2	XRD measurements on reactions between SrCO <sub>3</sub> and silicates . .	55
4.1.3	Summary of the XRD results on carbonate-silicate reactions . . .	59
4.2	Elemental redistribution processes in carbonate-silicate reactions . . . .	61
4.2.1	XRF calibration on silicate glass reference materials . . . . .	61
4.2.2	XRF measurements on Sr- and La-doped samples . . . . .	63
4.2.3	Optical fluorescence experiments on Eu-doped samples . . . . .	67
4.3	TEM analysis of recovered samples from carbonate-silicate reactions . .	69
<b>5</b>	<b>Discussion</b>	<b>73</b>
5.1	The fate of CaCO <sub>3</sub> and SrCO <sub>3</sub> in presence of mantle silicates . . . . .	73
5.1.1	Carbonates reacting with (Mg,Fe) <sub>2</sub> SiO <sub>4</sub> . . . . .	74
5.1.2	Carbonates reacting with (Mg,Fe)SiO <sub>3</sub> . . . . .	76
5.1.3	Decomposition and melting of CaCO <sub>3</sub> and SrCO <sub>3</sub> . . . . .	77
5.2	Elemental redistribution of Sr, La and Eu during carbonate-silicate reactions at conditions of the Earth's mantle . . . . .	79
5.2.1	Incorporation of Ca <sup>2+</sup> and Sr <sup>2+</sup> into (Mg,Fe)SiO <sub>3</sub> high pressure polymorphs during carbonate-silicate reactions . . . . .	80
5.3	Limitations of the current study . . . . .	83
<b>6</b>	<b>Conclusions and geological implications</b>	<b>87</b>
<b>7</b>	<b>Outlook</b>	<b>89</b>
	<b>References</b>	<b>93</b>
<b>A</b>	<b>Structure refinement of synthesis NB12 (CaCO<sub>3</sub>:Sr<sup>2+</sup>)</b>	<b>107</b>
<b>B</b>	<b>Refinement of XRD patterns from chapter 4</b>	<b>109</b>
<b>C</b>	<b>Fitted XRF spectra from chapter 4</b>	<b>118</b>
<b>D</b>	<b>EDX analyses on recovered sample material using TEM and SEM</b>	<b>124</b>

# List of Figures

1.1	The deep carbon cycle at the subduction zone . . . . .	4
1.2	Phase diagram of $\text{CaCO}_3$ . . . . .	6
1.3	Phase diagram of the reaction $\text{CaCO}_3 + \text{MgSiO}_3$ vs. $\text{MgCO}_3 + \text{CaSiO}_3$ . . . . .	7
1.4	Mineral composition and phase transformations in Earth's mantle . . . . .	8
2.1	Schematic cross section of an IHPV . . . . .	12
2.2	SEM images of carbonate starting materials NB10 and NB12 . . . . .	15
2.3	BX90 diamond anvil cell . . . . .	16
2.4	Different types of sample loading . . . . .	19
2.5	Experimental setup at ECB beamline P02.2, PETRA III . . . . .	22
2.6	$\text{CO}_2$ -laser heating system and experimental setup at beamline ID27, ESRF . . . . .	23
2.7	Resistive heated DAC . . . . .	24
2.8	Diffraction based on Bragg's law . . . . .	25
2.9	Principle of X-ray fluorescence . . . . .	26
2.10	Procedure for constructing XRD-contrast image in <i>XDI</i> . . . . .	28
2.11	Procedure for constructing an element map in <i>PyMca</i> . . . . .	29
3.1	DAC at 25.9 GPa loaded with $\text{SrCO}_3$ . . . . .	34
3.2	Powder XRD patterns of $\text{SrCO}_3$ at various pressures . . . . .	36
3.3	XRD pattern of post-aragonite $\text{SrCO}_3$ -II . . . . .	37
3.4	Crystal structures of $\text{SrCO}_3$ -I and $\text{SrCO}_3$ -II . . . . .	39
3.5	Compressibility of the unit cell parameters in $\text{SrCO}_3$ . . . . .	41
3.6	P-V-diagram and EoS for $\text{SrCO}_3$ -I and $\text{SrCO}_3$ -II . . . . .	42
3.7	A fragment of $\text{SrCO}_3$ -II crystal structure . . . . .	44
4.1	Selected XRD patterns of run DAC19 . . . . .	47
4.2	XRD-map plot of $\text{CaSiO}_3$ in DAC18 after heating . . . . .	48
4.3	XRD patterns of run DAC18 . . . . .	48
4.4	XRD patterns of run DAC12, DAC24 and DAC29 . . . . .	51
4.5	XRD patterns of run DAC11 . . . . .	53
4.6	Phase diagram of $\text{MgSiO}_3$ - $\text{FeSiO}_3$ compositions . . . . .	54
4.7	XRD patterns of DAC08 and DAC16 . . . . .	55
4.8	XRD patterns of run DAC04 . . . . .	57
4.9	XRD patterns of DAC15 and DAC27 . . . . .	59
4.10	XRF spectra collected on standard silicate glasses . . . . .	62

4.11	Minimum detection limits for elements from two standard glasses . . . . .	62
4.12	XRF spectra of run DAC04, DAC08 and DAC11 . . . . .	63
4.13	Two-dimensional distribution of Re, La, Ag, Sn, Te and I in cell DAC08	64
4.14	La-K $\alpha$ intensity maps of run DAC08 . . . . .	65
4.15	XRF line scans of Sr emission lines across the heated areas from DAC04, DAC11, DAC12 and DAC16 . . . . .	66
4.16	XRF intensity map and XRF line scan of Sr in run DAC13 . . . . .	67
4.17	Optical fluorescence intensity maps of Eu <sup>3+</sup> in run DAC24 . . . . .	68
4.18	TEM on recovered sample materials . . . . .	70
5.1	Reaction diagram of CaCO <sub>3</sub> and SrCO <sub>3</sub> in presence of mantle silicates .	74
5.2	P-T-phase diagram of CaCO <sub>3</sub> . . . . .	78
5.3	TEM images of run DAC23 . . . . .	81
5.4	Electron diffraction images of (Mg,Fe)SiO <sub>3</sub> low-P clinoenstatite . . . . .	82
5.5	Colour map of the recovered sample from run DAC27 measured by EDX	82
5.6	Spatial distribution of the laser power and corresponding temperature variation . . . . .	84
7.1	Schematic drawing of the experimental setup in this study and an opti- mized setup . . . . .	90

# List of Tables

2.1	EMP analyses of silicate starting materials . . . . .	14
2.2	EMP analyses of the carbonate starting materials NB10 and NB12 . . . .	14
3.1	<i>d</i> -spacings of post-aragonite SrCO <sub>3</sub> -II . . . . .	38
3.2	Lattice parameters of SrCO <sub>3</sub> derived from powder XRD . . . . .	39
3.3	Details of single crystal structure refinements of SrCO <sub>3</sub> -I and SrCO <sub>3</sub> -II .	40
3.4	Literature data on aragonite-type and post-aragonite-type carbonates .	43
3.5	Atomic coordinates and anisotropic displacement paramters of SrCO <sub>3</sub> -II	43
4.1	P-T-conditions and run products of DAC18 and DAC19 . . . . .	46
4.2	P-T-conditions and run products of DAC12, DAC24 and DAC29 . . . .	50
4.3	P-T-conditions and run products of DAC08, DAC11, DAC16 and DAC23	52
4.4	P-T-conditions and run products of DAC04 and DAC13 . . . . .	56
4.5	P-T-conditions and run products of DAC15 and DAC27 . . . . .	59
5.1	Theoretical mass balance calculation for the trace elements in Ca-Pv . .	85





# Chapter 1

## Introduction

### 1.1 Motivation and aim of this study

The role of carbonates in the deep Earth is attracting considerable interest due to their great impact on the deep carbon cycle (Li et al., 2019; McCammon et al., 2020). It is possible that 90% of the Earth's carbon content is stored in the Earth's deep interior (Dasgupta and Hirschmann, 2010) and that 0.9 - 1.8 Tmol/year of carbon is subducted, mainly in the form of carbonate-rich sediments (Javoy, 1997). Knowledge about carbon circulation in the mantle is very limited, but communities such as the Deep Carbon Observatory (DCO) have attempted to enlarge our understanding on phase relations and element's movement in the deep Earth. Evidence for the presence of a deep carbon cycle is given by the existence of carbonatite melts causing metasomatism in the upper mantle (Litasov et al., 2013), CO<sub>2</sub> in peridotitic and eclogitic systems with implications for deep melting of subducting slabs (Ghosh et al., 2009; Litasov, 2011; Thomson et al., 2016), mantle minerals hosting dissolved carbon (Shcheka et al., 2006) and the formation of diamonds. Decarbonation reactions and melting of carbonated mafic assemblages are thought to be the dominant processes mobilizing carbon from subducting slabs, transporting up to 50% of recycled carbon down into the deep mantle (Dasgupta and Hirschmann, 2010). Findings of carbonate inclusions in diamonds deriving from the transition zone are a rarity and their origin is still under debate but it also manifest the importance of deep Earth carbonates (Brenker et al., 2007) as one of the main mechanism for carbon storage in the lower mantle.

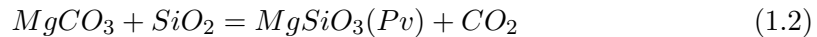
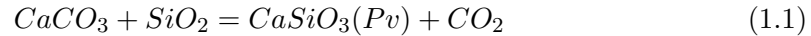
Our understanding of the physical and chemical behaviour of carbonates at conditions relevant to the Earth's mantle is incomplete and fragmentary. Recent studies have shown that carbonates are stable at mantle conditions (Isshiki et al., 2004; Oganov et al., 2008; Merlini et al., 2012; Solopova et al., 2015; Cerantola et al., 2017; Bayarjargal et al., 2018), where they may react with silicates to form new phases. These reactions will redistribute elements, such as calcium (Ca), magnesium (Mg), iron (Fe) and species such as carbon dioxide (CO<sub>2</sub>) but also trace elements, that are carried by the carbonates. The trace elements of most interest are strontium (Sr) and rare earth elements (REE) which have been found to be important constituents in the composition of the primitive lower mantle (Kaminski and Javoy, 2015) and in carbonate-bearing

mantle peridotites (Ionov et al., 1996) as well as in mineral inclusions found in super-deep diamonds (Brenker et al., 2007; Kaminsky, 2012). In the case of Sr, we further assume analogous chemical behaviour of  $\text{Sr}^{2+}$  and  $\text{Ca}^{2+}$  since the size of the cation radii and the elastic strain models are similar (Blundy and Wood, 1994; Wood and Blundy, 2003). The subduction of natural carbonates with significant amounts of Sr leads to a comprehensive investigation of the stability not only of  $\text{CaCO}_3$  phases in contact with mantle silicates but also of strontianite, the Sr-endmember of the aragonite-type carbonates.

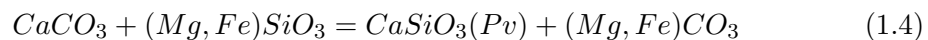
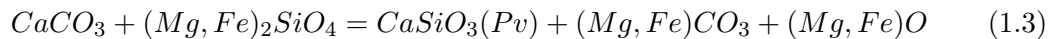
Hence, the present study concerns the chemical behaviour of doped  $\text{CaCO}_3$ - and  $\text{SrCO}_3$ -phases in presence of silicates that are relevant for lower mantle conditions. The main questions addressed are:

1. What are the crystal structures of stable (high-pressure and high temperature) post-aragonite phases of  $\text{CaCO}_3$  and  $\text{SrCO}_3$ ?
2. What do we know about carbonate-silicate reactions, especially the reaction between silicates and  $\text{CaCO}_3$  or  $\text{SrCO}_3$  at relevant lower mantle conditions?
3. Are carbonates possible trace element carriers into the Earth's lower mantle? If so, what is the main mechanism for this process?

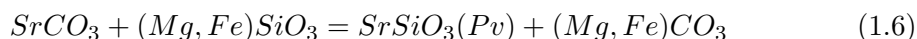
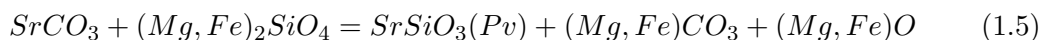
To answer these questions, one needs to consider possible decarbonation reactions in excess of  $\text{SiO}_2$ . This is particularly important when one takes into account that there is material mixing between carbonates and the basaltic part of subducting slabs, which is rich in  $\text{SiO}_2$  (Oganov et al., 2008). Possible reactions are:



These reactions demonstrate whether or not free  $\text{CO}_2$  can be present in the lower mantle and were already studied (Takafuji et al., 2006; Kakizawa et al., 2015; Li et al., 2018; Drewitt et al., 2019; Litasov and Shatskiy, 2019). To determine the stability of carbonates with a focus on Ca-rich lithologies and at more relevant lower mantle conditions, two more reactions have to be considered:



For  $\text{SrCO}_3$ , we consider analogous chemical behaviour and propose the two following reactions for lower mantle conditions:



To enlarge our understanding of the stability of carbonates with a focus on the trace element budget in the Earth's mantle and on the importance of carbonates as possible trace element carriers, experiments on a high sensitivity level are necessary. This thesis aims to clarify whether it is possible to incorporate Sr (representing alkaline earth elements) and La as well as Eu (representing light rare earth elements) into mantle silicates during carbonate-silicate reactions. To track changes in the present system during reaction, a combination of synchrotron radiation based  $\mu$ -X-ray diffraction ( $\mu$ -XRD) and  $\mu$ -X-ray fluorescence ( $\mu$ -XRF) in the  $\mu\text{m}$ -range followed by transmission electron microscopy (TEM) on the recovered sample material was chosen.  $\mu$ -XRD allows monitoring of structural changes whereas  $\mu$ -XRF gives chemical information. The two methods are also applicable to high pressure and high temperature, if they are combined with a laser-heated diamond anvil cell (LHDAC). So far, there are a few studies that have investigated elemental partitioning at high-pressure and high-temperature conditions with *in-situ*  $\mu$ -XRF (Borchert et al., 2009, 2010b,a; Wilke et al., 2010; Petitgirard et al., 2012). The studies focused on the elemental partitioning of trace elements between silicates and iron melts as well as between haplogranitic melts and aqueous solutions. Knowledge is missing on the element mobility between co-existing mantle phases in a sub-solidus state.

Accordingly, the following chapter 1 gives a general overview on the stability of carbonates in the deep Earth and presents the chemical composition of the mantle that is affected by subducting processes. A detailed description of the applied experimental procedures is given in chapter 2 with a focus on sample preparation and synthesis (section 2.1), the generation of high pressure and high temperature conditions using laser-heated and resistively heated DACs (sections 2.2 - 2.4) and the application of combined  $\mu$ -XRD-XRF measurements (section 2.5). The analysis of the recovered sample material with TEM is presented in section 2.6 and builds a fundamental part of this study. Powder X-ray diffraction and single-crystal X-ray diffraction experiments have been performed on pure  $\text{SrCO}_3$  in order to understand the high-pressure phase behaviour in more detail and are presented in chapter 3 with a description of the experimental approach of single-crystal XRD in section 2.3. The results from these experiments were chosen for publication. In chapter 4, the results from carbonate-silicate reaction experiments are presented and are discussed in chapter 5. Our conclusions and geological implications are drawn in chapter 6 with an outlook of future research potential based on the results from this study.

## 1.2 The deep carbon cycle

Carbon is one of the most important elements for us as human beings and contributes essentially to the sustainability of life on Earth. Due to the current debate about the global climate change, most people know that there is carbon in the atmosphere but not many are aware, that the amount of carbon in the Earth's mantle is thought to be one million times higher ( $0.8 - 12.5 \cdot 10^{23}$  g carbon in the mantle (Dasgupta and Hirschmann, 2010) compared to  $11.6 \cdot 10^{17}$  g carbon in the atmosphere (Sleep and Zahnle, 2001)). Estimating the amount of carbon fluxes between the different Earth reservoirs as well as the storage of carbon is important for the origin and evolution of life. Accordingly, the Earth's deep carbon cycle describes the cycling, behaviour and storage of carbon in the Earth's mantle and core (Fig. 1.1). Subducting slabs are the main carrier for introducing carbon into the deep Earth. The most reliable estimate on the amount of carbon added to the mantle through subducted plates is  $3.1 \cdot 10^{13}$  g per year, mostly in form of carbonates (Dasgupta and Hirschmann, 2010). Various processes at high temperature and high pressure lead to chemical reactions that also release  $\text{CO}_2$  from the subducting slabs back to the Earth's crust and surface. However, not all of the carbon degasses and part of the carbon can be reintroduced into the mantle, where it is stored within several phases, including diamond, carbonatitic melts and carbonate minerals (Manning, 2014). Very little is known about the physical and chemical behaviour of carbon and carbon-bearing phases at extreme conditions and questions arise on how carbon can move among these deep reservoirs.

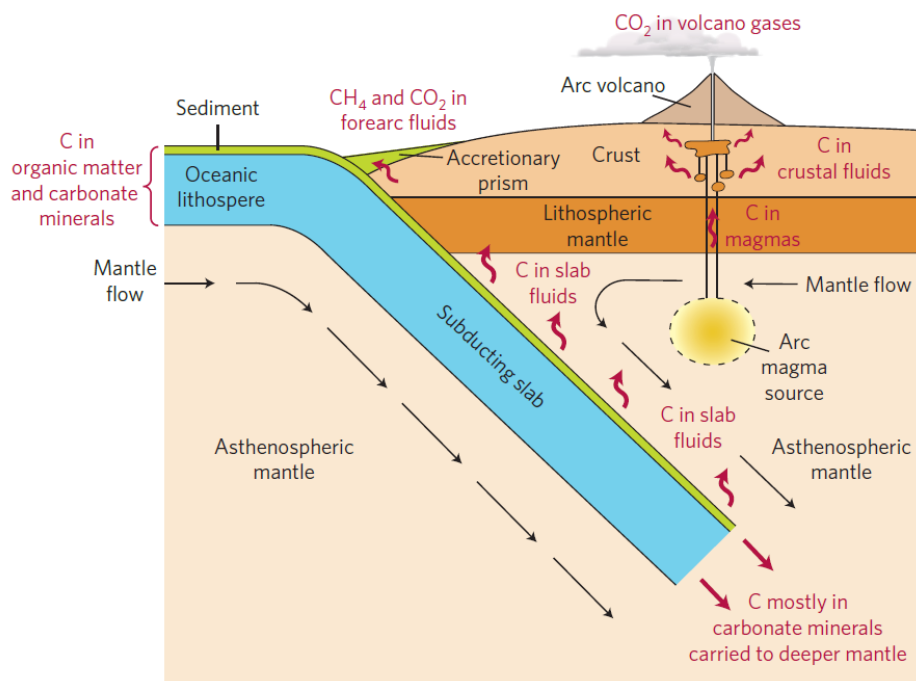


Figure 1.1: The deep carbon cycle at the subduction zone (Manning, 2014). Carbon-bearing sediments are transported into the deeper Earth by subducting slabs where carbon is released back to Earth's surface through fluids and arc volcanoes.

### 1.2.1 The role of $\text{CaCO}_3$ and $\text{SrCO}_3$ in the Earth's mantle

Natural carbonates are solid solutions with the general formula  $\text{XCO}_3$  and where X can be occupied by various divalent cations such as  $\text{Mg}^{2+}$ ,  $\text{Ca}^{2+}$ ,  $\text{Sr}^{2+}$ ,  $\text{Ba}^{2+}$ ,  $\text{Pb}^{2+}$ ,  $\text{Fe}^{2+}$  or  $\text{Mn}^{2+}$  (Deer et al., 1992). Carbonates in the mantle occur in at least two different lithologies. Ca-rich carbonates are expected in subduction zone related eclogitic lithologies (Dasgupta and Hirschmann, 2010; Hazen et al., 2013), whereas ferromagnesian carbonates are likely to occur in peridotite-based lithologies (Canil and Scarfe, 1990). Dolomite ( $\text{CaMg}(\text{CO}_3)_2$ ) is considered to be the major constituent in subducted carbonates. At pressures below 7 GPa and at temperatures between 700 and 1400 K dolomite decomposes to aragonite and magnesite (Martinez et al., 1996). Hence, dolomite is normally not considered to be a potential carrier of carbon into the deep Earth. Instead, calcite and its high-pressure polymorph aragonite as well as magnesite are the carbonate phases of interests according to the deep carbon cycle. Numerous studies on the phase behaviour of  $\text{CaCO}_3$  at high pressure observed a phase transition from orthorhombic aragonite into monoclinic  $\text{CaCO}_3$ -VII at around 30 GPa and into post-aragonite structure  $Pm\bar{m}n$  at around 40 GPa (Gavryushkin et al., 2017; Bayarjargal et al., 2018). A phase diagram of  $\text{CaCO}_3$  is given in Fig. 1.2. Experiments and *ab initio* calculations predict a phase stability of post-aragonite  $\text{CaCO}_3$  between 35-135 GPa with further transformation to structures with tetrahedrally coordinated carbon atoms (Santillán and Williams, 2004; Ono, 2005; Oganov et al., 2006, 2008; Santos et al., 2019). Those studies demonstrate that carbonates may be stable in the Earth's mantle and hence they are potential reaction partners for silicates. Especially magnesite and the recently discovered formation of monoclinic  $\text{CaCO}_3$ -VII (Gavryushkin et al., 2017; Bayarjargal et al., 2018) affect the stability of carbonates during subduction processes. Magnesite is predicted to be the most stable carbonate phase up to about 115 GPa where it transforms to an unknown structure (Isshiki et al., 2004; Solopova et al., 2015) and  $\text{CaCO}_3$ -VII was found to be stable at conditions close to the mantle geotherm.

Until now, the role of  $\text{SrCO}_3$  in the deep mantle has received little attention due to its low abundance. The chemical component  $\text{SrCO}_3$  is often present as a major constituent in natural aragonite, especially in biogenic aragonite (Milliman et al., 1974), and also in alkali-carbonates formed during mantle evolution (Shatskiy et al., 2015). Chemical and physical properties of the carbonate mineral strontianite at ambient conditions are well known (Villiers, 1971; Antao and Hassan, 2009; Nguyen-Thanh et al., 2016; Biedermann et al., 2017b) whereas only minor knowledge exists for the high-pressure polymorphs of  $\text{SrCO}_3$  (Ono et al., 2005; Wang et al., 2015; Biedermann et al., 2017a; Efthimiopoulos et al., 2019). A high-pressure phase transition in  $\text{SrCO}_3$  occurs at around 26 GPa where strontianite with space group  $Pm\bar{c}n$  transforms into a post-aragonite phase with space group  $Pm\bar{m}n$  (see chapter 3). This phase transition is characteristic for most aragonite-type structured carbonates (e.g. aragonite, strontianite, witherite). The properties of the carbonates substantially change across this transition and, as a consequence, along the subduction processes as well. Knowing the properties of the post-aragonite  $Pm\bar{m}n$  high-pressure phase across its full compositional

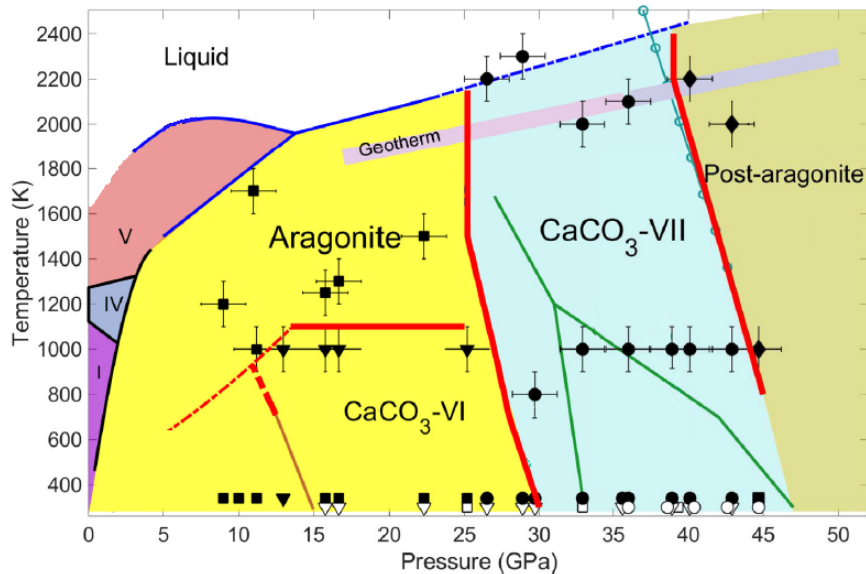


Figure 1.2: Phase diagram of  $\text{CaCO}_3$  modified after Bayarjargal et al. (2018). Colour fields mark the different phases. Thick red lines and dashed red lines mark the phase boundaries. Square symbols represent aragonite, triangles are for  $\text{CaCO}_3$ -VI, circles represent  $\text{CaCO}_3$ -VII, and diamonds represent post-aragonite obtained before (white symbols) and after laser-heating (black symbols). Different phase boundaries are added to this study: The brown thin line represents the phase boundary for the phase transition between  $\text{CaCO}_3$ -III and  $\text{CaCO}_3$ -VI by Koch-Müller et al. (2016), the dark green lines show the phase stability field for  $\text{CaCO}_3$ -VII from Gavryushkin et al. (2017) and the cyan line with circles represents the phase boundary between  $\text{CaCO}_3$ -VII and post-aragonite measured by *in-situ* XRD experiments (Li et al., 2018). The blue line shows melting curves and phase boundary from Li et al. (2017).

range is essential to evaluate the effects of chemical substitution in the system of deep Earth carbonates at relevant conditions.

### 1.2.2 Evidence for carbonate-silicate reactions in the deep Earth

The current knowledge on carbonate-silicate reactions at conditions of the Earth's mantle is largely based on experiments where carbonates (mostly  $\text{MgCO}_3$  and  $\text{CaCO}_3$ ) have reacted with free  $\text{SiO}_2$ . These studies are only of limited geochemical relevance for the lower mantle since there is no free  $\text{SiO}_2$  in the subduction zone. However, experiments in the binary system  $\text{MgCO}_3$ - $\text{SiO}_2$  have shown that magnesite is expected to break down to  $\text{CO}_2$  or diamond by reacting with silica-phases in subducting processes although the details of their phase relations have not yet been clarified (Kakizawa et al., 2015; Maeda et al., 2017). Comparable observations were made on the system  $\text{CaCO}_3$  in reaction with basaltic glasses and a decarbonation reaction in the form of  $\text{CaCO}_3 + (\text{Mg,Fe})\text{SiO}_3 = \text{CaSiO}_3(\text{Pv}) + (\text{Mg,Fe})\text{O} + \text{CO}_2$  was predicted (Seto et al., 2008; Drewitt et al., 2019). Based on *ab initio* calculations and quasi-harmonic approximations, the stability of  $\text{CaCO}_3$  was studied in presence of  $\text{MgSiO}_3$  and results

confirm a reaction into  $\text{MgCO}_3$  and  $\text{CaSiO}_3$  at conditions between 25 - 84 GPa and 300 - 3500 K (Zhang et al., 2018; Santos et al., 2019). These studies indicate that at lower mantle conditions the main carbonate phase is  $\text{MgCO}_3$ .

However, calculations at high temperature and pressures above 84 GPa from Santos et al. (2019) indicate that  $\text{CaCO}_3 + \text{MgSiO}_3$  is more stable than  $\text{MgCO}_3 + \text{CaSiO}_3$  (Fig. 1.3). In addition, experiments on dolomite in reaction with iron at conditions near the core-mantle-boundary (CMB) show a decomposition of  $\text{MgCO}_3$  into diamond,  $\text{Fe}_7\text{C}_3$  and magnesiowüstite ( $(\text{Mg,Fe})\text{O}$ ), whereas  $\text{CaCO}_3$  is preserved (Dorfman et al., 2018). Consequently and due to the resistance against redox break down,  $\text{CaCO}_3$  could be the main carbonate phase in the deeper part of the lower mantle where the conditions have a lower oxygen fugacity.

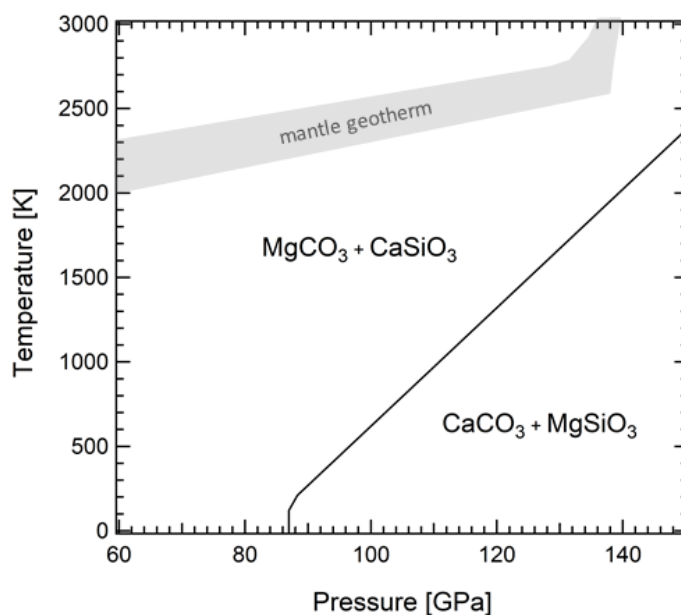


Figure 1.3: Phase diagram of the stability of the reaction  $\text{CaCO}_3 + \text{MgSiO}_3$  versus  $\text{MgCO}_3 + \text{CaSiO}_3$  after Santos et al. (2019). The mantle geotherm is from Brown and Shankland (1981).

So far, no studies exist on the reaction between  $\text{SrCO}_3$  and mantle silicates. Analysing the phase stability of strontianite ( $\text{SrCO}_3$ ) or Sr-bearing  $\text{CaCO}_3$  in presence of mantle silicates is motivated by the idea that a reaction between them could be a possible mechanism for the introduction of Sr as a trace element into mantle silicates. According to the size of  $\text{Sr}^{2+}$  and the elastic strain model (Blundy and Wood, 1994; Wood and Blundy, 2003) we can assume that a  $\text{Sr}^{2+}$  cation may substitute for  $\text{Ca}^{2+}$  in  $\text{CaSiO}_3$ -perovskite. Indeed, significant amounts of Sr in  $\text{CaSiO}_3$  inclusions from ‘super-deep’ diamonds were observed (Brenker et al., 2007). Although strontianite plays only a minor role in the carbonate chemistry at mantle conditions, the occurrence of pressure- and temperature-induced structural changes might allow the formation of solid solutions between endmembers at mantle conditions that are immiscible at ambient conditions.

### 1.3 Chemical composition of the Earth's lower mantle

Chemical and structural models of the most abundant minerals in the Earth's lower mantle have been constructed based on laboratory experiments confirmed by seismological models and result in a composition of mainly three mineral phases:  $(\text{Mg,Fe})(\text{Si,Al})\text{O}_3$  perovskite,  $\text{Ca}(\text{Si,Al})\text{O}_3$  perovskite and  $(\text{Mg,Fe})\text{O}$  magnesiowüstite (Fig. 1.4). The other major and minor elements occurring in the lower mantle are considered to either form accessory mineral phases ( $\text{Na}^+$  in aluminous calcite ferrite structure type phase  $\text{Na}_3\text{Al}_3\text{Si}_3\text{O}_{12}$ , (Ono et al., 2001; Litasov and Ohtani, 2010)) or to be dissolved in the three main phases (e.g.  $\text{Ti}^{4+}$  in  $\text{CaTiO}_3$ -perovskite, (Irifune, 1994)).

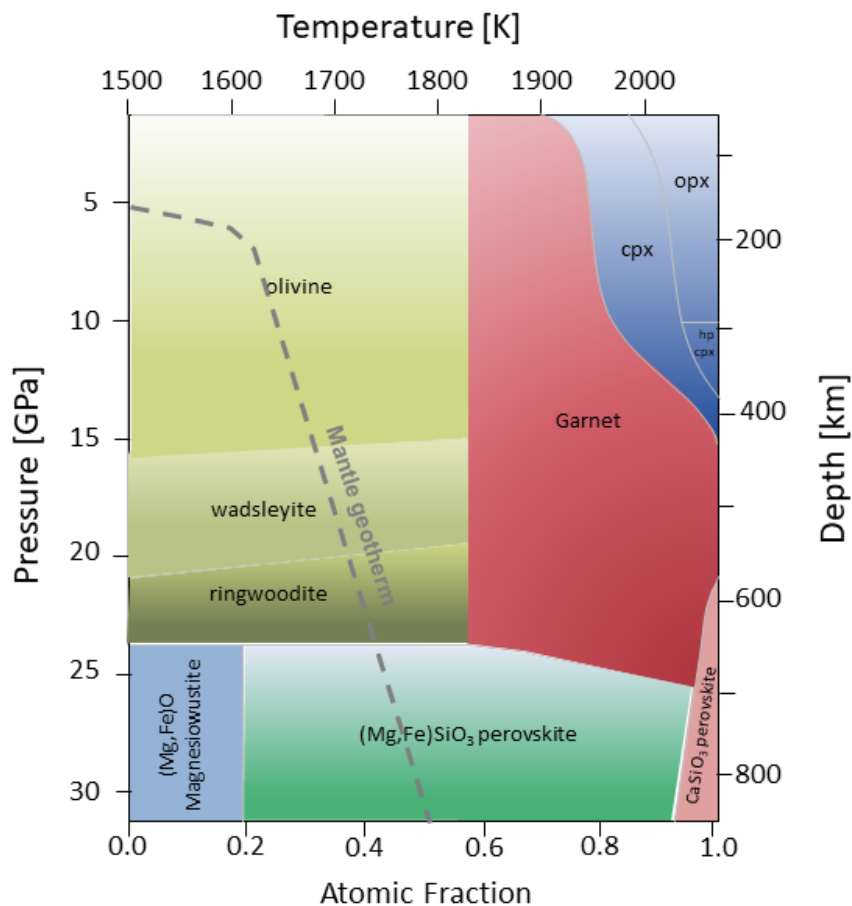


Figure 1.4: Mineral composition and phase transformations in the Earth's upper mantle and uppermost lower mantle after Stixrude and Lithgow-Bertelloni (2007). The dashed grey line represents the mantle geotherm from Helffrich and Wood (2001).

In general, the incorporation of trace elements is controlled by the crystal chemistry and the elements are incorporated in different crystal sites according to their ionic radius and charge (Blundy and Wood, 1994). Partitioning experiments indicate that geochemically important trace elements, such as Sr, Y or REEs, enter preferentially into the  $\text{CaSiO}_3$  perovskite phase rather than into  $(\text{Mg,Fe})\text{SiO}_3$  perovskite or  $(\text{Mg,Fe})\text{O}$  (Kato et al., 1988; Dalou et al., 2009). When  $\text{CaCO}_3$  reacts with the silicate phases,  $\text{CaSiO}_3$ -perovskite is formed and has been found to be the dominant host for Ca in the



deep mantle (Stixrude and Lithgow-Bertelloni, 2007). The incorporation of  $\text{Sr}^{2+}$ ,  $\text{Eu}^{3+}$  and  $\text{La}^{3+}$  takes place on the (divalent) A-site of  $\text{CaSiO}_3$ -perovskite which exhibits a 12-fold coordination. The substitution of trivalent lanthanum and europium for  $\text{Ca}^{2+}$  is coupled with an Al-coupled substitution at the Si-site or by the formation of Ca-vacancies such as  $3 \text{Ca}^{2+} \leftrightarrow 2 \text{La}^{3+}/\text{Eu}^{3+} + \square$  to balance the charge as reported by Corgne and Wood (2005). Besides of REEs,  $\text{CaSiO}_3$ -perovskite can also incorporate highly charged trace elements like  $\text{U}^{4+}$  or  $\text{Th}^{4+}$  and is therefore a major reservoir for heat-producing elements (Corgne and Wood, 2005).  $\text{CaSiO}_3$ -perovskite inclusions in diamonds that are believed to be originated from lower mantle also show strong enrichment in Sr (Stachel et al., 2000) which supports our idea of having Sr as an important trace element in the Earth's lower mantle.

## 1.4 Studying element transport processes in laser-heated diamond anvil cells (LHDAC)

So far, generic processes leading to trace element patterns observed in phases found in natural diamond inclusions originating from the lower mantle, e.g. Brenker et al. (2007), remain unclear due to the lack of knowledge on trace element partitioning and the difficulty of experimental *in-situ* studies at such extreme P-T-conditions. Our knowledge of carbonates as possible candidates for carrying trace elements into the Earth's deep interior is largely based on very limited data. Simultaneous investigation of (doped) carbonate fractionation in reaction with mantle silicates and the incorporation of trace elements into newly formed silicate perovskite phases improves our understanding not only of the trace element budget in the Earth's mantle, but also of the possibility of carbonates as important trace element carriers. The trace element composition of the mantle is thus important since it is often used as a fingerprint for the source reservoir.

In general, high-pressure and/or high-temperature induced phase transitions or chemical reactions can provoke an elemental fractionation and/or partitioning between co-existing phases which is generally described as the change in concentration ratio by a specific process. New approaches and developments, such as laser-heated diamond anvil cells (LHDAC) in combination with *in-situ* X-ray fluorescence allow us to study the chemical behaviour of REE and Sr at mantle conditions with high sensitivity. So far, there are a few studies that have investigated elemental partitioning at high-pressure and high-temperature conditions with *in-situ* XRF (Borchert et al., 2009, 2010b,a; Wilke et al., 2010; Petitgirard et al., 2012). They studied the elemental partitioning of trace elements between silicates and iron melts as well as between haplogranitic melts and aqueous solutions. Basically, knowledge on the element mobility during solid-solid interactions, such as carbonate-silicate reactions, at high pressure and high temperature, is missing.



## Chapter 2

# Experimental methods

This chapter focuses on the methodological aspects as well as the experimental approach to study carbonate-silicate reactions at Earth mantle conditions. The laser-heated or resistively heated diamond anvil cell in combination with synchrotron radiation has become a major tool to study chemical reactions at high pressure and high temperature as they allow the analyses of the phases *in-situ* with high sensitivity. A combination of  $\mu$ -XRD and  $\mu$ -XRF was chosen to investigate the chemical redistribution processes between carbonates and mantle silicates upon heating and will be explained in sections 2.4 and 2.5. In order to follow an elemental redistribution, we have synthesized with trace elements doped carbonate starting materials as described in section 2.1 prior to carbonate-silicate reaction experiments. Section 2.2 presents the various procedures of sample loading that have been tested and outlines the importance of good sample handling for LHDAC experiments. A general introduction on single-crystal XRD data collection is given in section 2.3 because it builds a fundamental part in the study of the high-pressure phase behaviour of  $\text{SrCO}_3$ . Finally, transmission electron microscopy (TEM) on the recovered sample material was used as a tool to investigate the elemental redistribution in three-dimensional space (section 2.6). Attention is also given on the difficulties of recovering the sample from the diamond anvil cell for post-heating TEM analyses.

### 2.1 Sample preparation and synthesis of trace element doped carbonates

For carbonate-silicate reaction experiments different silicate starting materials with various Fe-contents were used. Furthermore, to study an elemental redistribution of specific trace elements, we synthesized carbonate starting materials doped with trace amounts of Sr or La ( $\text{CaCO}_3\text{:Sr}^{2+}$ ,  $\text{CaCO}_3\text{:La}^{3+}$ ) in an internally heated pressure vessel. Eu-doped calcite powder samples ( $\text{CaCO}_3\text{:Eu}^{3+}$ ) were provided by the University of Frankfurt, from the Institute for Geosciences and have been synthesized after Pan et al. (2003). A detailed description of the synthesis of  $\text{CaCO}_3\text{:Eu}^{3+}$  can be found in Fruhner (2019). All samples were pre-characterized in terms of composition and homogeneity using electron microprobe analysis and scanning electron microscopy.

### 2.1.1 Synthesis of Sr- and La-doped calcite using the internally heated pressure vessel (IHPV)

We performed synthesis experiments of homogeneously doped calcite crystals using a Harwood-type internally heated pressure vessel (Fig. 2.1) in the High Pressure Laboratory for Geomaterial Sciences at the GeoForschungsZentrum (GFZ) Potsdam, Germany. Commercial powders of  $\text{CaCO}_3$ ,  $\text{SrCO}_3$  and  $\text{La}_2(\text{CO}_3)_3 \cdot x\text{H}_2\text{O}$  ( $x = 2.0\text{--}5.0$ ) were dried overnight at  $200\text{ }^\circ\text{C}$  prior to being weighed. Mixtures of  $\text{CaCO}_3$  together with  $\text{SrCO}_3$  or  $\text{La}_2(\text{CO}_3)_3$  in respective proportions (depending on the solubility of the elements in calcite) were ground and homogenized in an agate mortar. 200 - 300 mg of carbonate mixtures were then transferred into a platinum capsule. After loading the capsules, they were welded shut and stored again at  $100\text{ }^\circ\text{C}$  overnight. To ensure complete sealing of the capsules the weight was recorded before and after the storage as well as after the synthesis experiment and indeed no weight loss was measured. The advantage of using an IHPV over piston cylinder apparatuses is the comparatively large sample chamber, allowing to run simultaneously 5 - 10 sample capsules. Therefore, capsules with different carbonate mixtures were placed into the sample chamber in the internal furnace and then loaded into the pressure autoclave in which Ar is used as a pressurizing medium. The pressure was raised to the target pressure of 700 MPa and once stabilized, the temperature was raised to its target value of  $1200\text{ }^\circ\text{C}$ . The pressure was measured and continuously recorded by a strain gauge to an accuracy of  $\pm 5$  MPa.

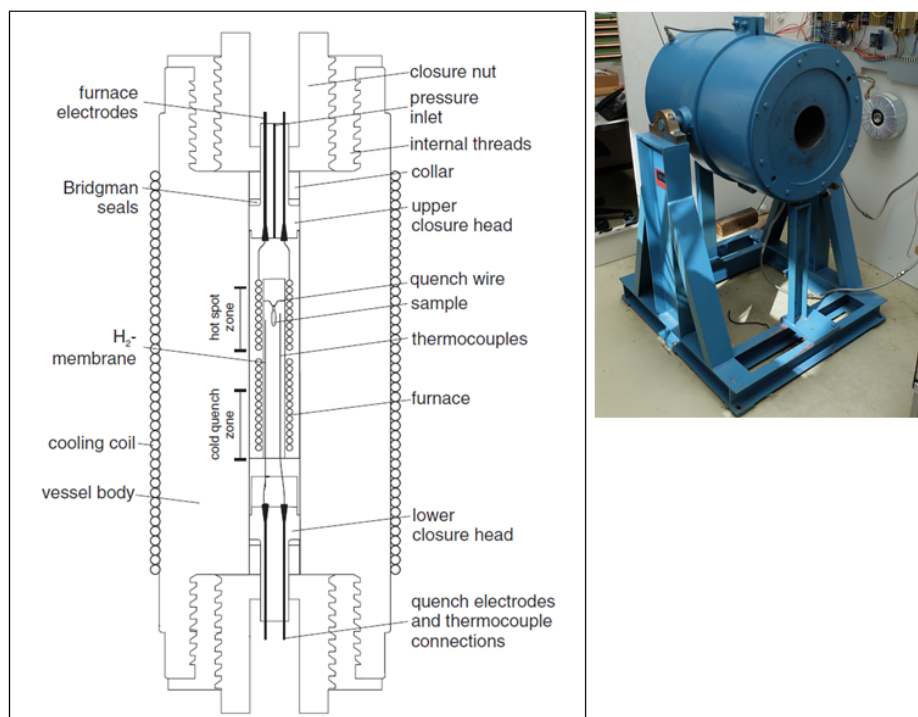


Figure 2.1: Schematic cross section of an IHPV with similar design from University of Hannover, Germany, Institute for Mineralogy (Berndt et al., 2002). For easier insertion of the furnace and the sample holder, the vessel can be turned around into a horizontal position as shown in the picture on the right hand side.

Temperature measurements were conducted with four S-type thermocouples placed at the top, middle and bottom of the furnace as well as one thermocouple placed very close to the capsule. The thermocouples were calibrated against the melting point of NaCl (Borchert et al., 2010b) and showed a thermal gradient along the capsule of  $\pm 10^\circ\text{C}$ . The duration of the synthesis experiment was 75 h. After switching off the furnace, the samples were quenched isobarically with quench rates of 150-200 $^\circ\text{C}/\text{min}$  to ambient conditions. After that, the pressure was released to ambient conditions.

### 2.1.2 Pre-characterization of the samples

#### Electron microprobe (EMP) analysis

For the characterization of the silicate starting materials electron microprobe analysis were conducted on a JEOL JXA-8200 equipped with a LaB<sub>6</sub> cathode at the University of Potsdam in the Institute for Geosciences. A portion of each sample powder was mixed in epoxy, then polished and finally carbon-coated to ensure conductivity. Measurements were performed in line scans over the mounted sample at a voltage of 15 kV and a beam current of 10 nA. In total, 6 different silicate phases with various Fe-contents were characterized: pure MgSiO<sub>3</sub> glass provided by Dr. S. Petitgirard (Petitgirard et al., 2015), a natural orthopyroxene with Fe-contents of 57.3 wt%, natural olivine with 16.4 wt% of Fe and an hydrous wadsleyite provided by Prof. M. Koch-Mueller with a Fe-content of 11.4 wt% (sample MA-316 in Mrosko et al. (2015)). In addition, to be closer to the actual mantle conditions, we used a natural Fe-bearing olivine from San Carlos ((Mg<sub>0.9</sub>Fe<sub>0.1</sub>)<sub>2</sub>SiO<sub>4</sub>) provided by Prof. L. Dubrovinsky from the Bayerisches Geoinstitut (BGI) for our XRD-XRF studies and for optical fluorescence measurements (see section 4.2.3) and a natural enstatite with only 2.8 wt% of Fe. All microprobe analysis of the silicates, except for the Fe-bearing olivine from San Carlos, can be seen in Tab. 2.1.

Microprobe analysis of the carbonate starting materials after synthesis were performed on a JEOL Hyperprobe JXA-8500F with a thermal field-emission cathode at the GFZ Potsdam. Measurements were taken at 15 kV and 10 nA. Results of the analysis indicated a homogeneous distribution of the dopants La and Sr at a level of 1.53(9) wt% for La<sub>2</sub>O<sub>3</sub> and 2.4(4) wt% for SrO in the calcite crystals (see Table 2.2). The doping level of Sr in calcite is usually relatively high as reported by Carlson (1980). The doping level for La was tested by additional runs that determined the solubility of the rare earth elements in presence of a REE-hydroxyl-bastnäsite and REE-oxide phases. At 1050 $^\circ\text{C}$  and 700 MPa REE-hydroxyl-bastnäsite co-existed with homogeneous calcite crystals with a REE/Ca ratio of 0.005. Based on this knowledge, we adapted the doping level for the synthesis of La-doped carbonates to avoid the formation of REE-hydroxyl-bastnäsite. In case of the Sr-doped calcite that has a Sr/Ca ratio of 0.024, the composition is also confirmed by X-ray diffraction and results from this can be found in the Appendix A.

Table 2.1: Microprobe analyses of the silicate starting materials.

	MgSiO <sub>3</sub> glass <sup>1</sup>	(natural) enstatite	ortho- pyroxene	olivine	wadsleyite (hydrous) <sup>2</sup>
SiO <sub>2</sub> [wt%]	50.77	59.5(12)	52.8(4)	40.51(3)	39.3(5)
Al <sub>2</sub> O <sub>3</sub> [wt%]	-	1.51(4)	1.092	1.1(3)	0.021(8)
MgO [wt%]	49.18	37.3(3)	19.2(3)	48.9(4)	45.9(6)
FeO [wt%]	-	1.08(3)	28.6(15)	9.5(9)	10.6(2)
MnO [wt%]	-	0.01(1)	0.3(2)	0.126	
NiO [wt%]	-	0.013(13)	0.08(2)	0.36(1)	
CaO [wt%]	-	-	1.72(5)		
H <sub>2</sub> O [wt%]					1.7(2)
Total	99.95	99.4(6)	102.1(10)	99.4(6)	95.7(3)
Mg	1	0.971(3)	0.38(1)	1.660(6)	1.77(1)
Fe	0	0.0282(7)	0.57(1)	0.32(1)	0.23(1)

The number in parentheses refers to  $1\sigma$ ; cations per formula unit are calculated on the base of 3 oxygens for pyroxene and 4 oxygens for olivine; <sup>1</sup>Petitgirard et al. (2015), <sup>2</sup>sample MA-316 in Mrosko et al. (2015)

Table 2.2: Chemical analysis and doping level of the synthesized carbonate samples NB10 and NB12 that were used for carbonate-silicate reactions. Experimental conditions for both runs were 1200° C, 700 MPa, duration 75 h.

sample	NB10 CaCO <sub>3</sub> :La <sup>3+</sup>	NB12 CaCO <sub>3</sub> :Sr <sup>2+</sup>
CaO [wt%]	53.7(6)	49.76
La <sub>2</sub> O <sub>3</sub> [wt%]	1.53(9)	0.02(2)
SrO [wt%]	-	2.4(4)
CO <sub>2</sub> [wt%]	44.8(6)	46.6(6)
Total	100.00	100.00(1)
Ca	0.9951(3)	0.976(4)
La	0.0049(3)	-
Sr	-	0.024(4)

The number in parentheses refers to  $1\sigma$ ; cations per formula unit are calculated on the base of 3 oxygens

### Scanning electron microscopy

Additional to EMP analysis, further characterization of the carbonate starting materials were performed with a JSM-6510 scanning electron microscope at the GFZ Potsdam, using an acceleration voltage of 15 to 30 kV. Images of the synthesis NB10 show the presence of La<sub>2</sub>O<sub>3</sub> along intergranular boundaries between the La-doped calcite crystals, indicating the formation of La-excess phases (Fig. 2.2). In addition, relicts of a fluid

(most probably  $\text{CO}_2$ ) are visible as well and might indicate a decomposition of the  $\text{La}_2(\text{CO}_3)_3 \cdot x\text{H}_2\text{O}$  ( $x = 2.0 - 5.0$ ) starting material at conditions of 700 MPa and 1200 °C.

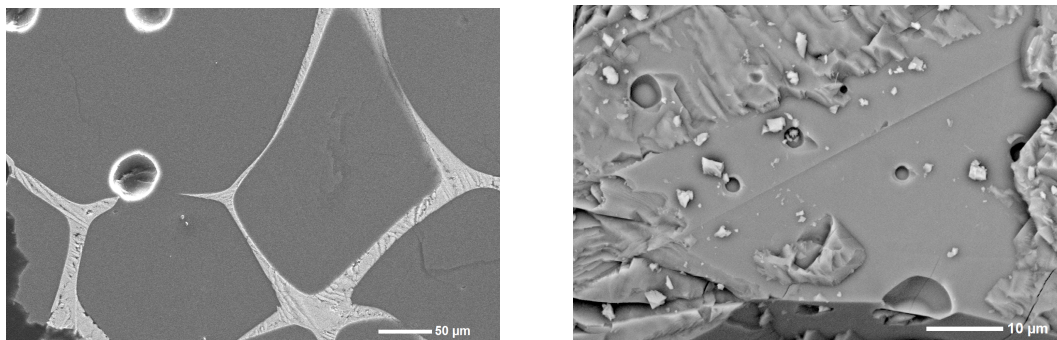


Figure 2.2: SEM images of a) La-doped calcite crystals obtained from synthesis NB10 with formation of  $\text{La}_2\text{O}_3$  along intergranular boundaries and b) of Sr-doped calcite crystals obtained from synthesis NB12 (see for chemical analysis Tab.2.2).

## 2.2 Diamond anvil cell technique and sample loading

The development of the diamond anvil cell (DAC) began in the late 1950s. Since then, the DAC has become one of the most powerful tools for generating high-pressure conditions. Today, a DAC capable of generating megabar pressure easily fits into your hand and makes it possible to perform *in-situ* studies at extreme conditions using hard X-ray diffraction, spectroscopy and other techniques. The basic principle of a DAC consists of a sample placed between flat parallel faces of two opposed diamond anvils. When force is applied to the diamonds, the sample gets pressurized. A metal (Re or steel) gasket with an indentation and a hole forming a sample chamber is always placed between the diamonds in order to seal and form the sample chamber and to separate the diamonds from each other. Different designs of DACs have been developed for commercial use but also for specific applications in academic research. In this work, the combination of XRD and XRF requires a wide opening angle of the cell in order to place a fluorescence detector accurately and to collect Bragg reflections up to a high  $Q$  range. Therefore, cells of the BX90 type (Kantor et al., 2012) were used, which have axial openings on four sides with 90° distance in between and additional conical opening which is needed for double-sided laser heating (Fig. 2.3). In some cases, we also used high-precision DACs of the type "Boehler Almax" suitable for laser heating and pressures up to 100 GPa (Boehler, 2006). Diamonds with Boehler-Almax (BA) design and conical tungsten-carbide seats produced by Almax easyLab that match perfectly with the diamonds, were mounted into the DAC providing an X-ray aperture of up to  $\sim 85^\circ$ . We used an asymmetric diamond anvil pair consisting of one BA diamond with 300  $\mu\text{m}$  culet mounted on the downstream site and a second one with 200  $\mu\text{m}$  culet size at the upstream site. This anvil geometry indents and deforms the Re gasket to a greater extent towards the smaller anvil positioned at the upstream site. By grinding

off the indentation wall of the gasket at the downstream site, the amount of Re is further decreased. In addition, this configuration also allows access to the XRF signal downstream from the beam above the Re gasket.

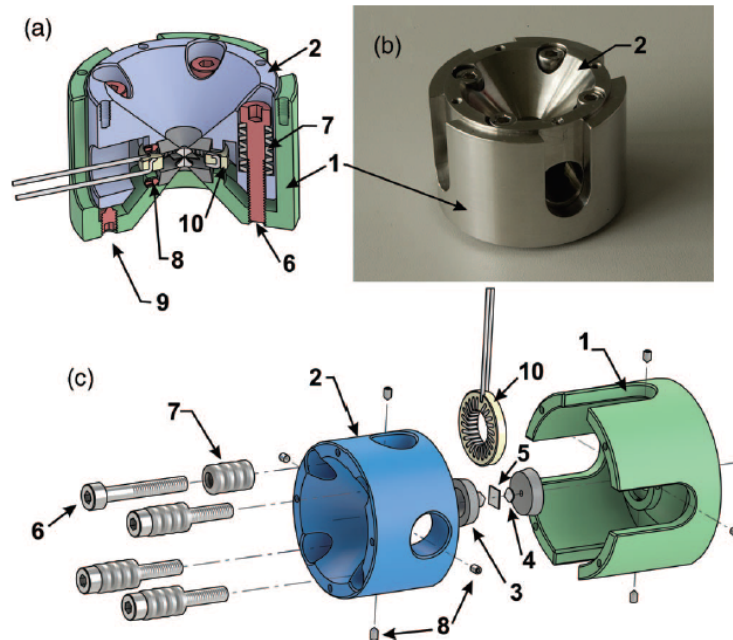


Figure 2.3: BX90 diamond anvil cell design after Kantor et al. (2012). (a) Section view, (b) photograph of a loaded cell, (c) exploded view. 1. Outer cylinder part, 2. inner piston part, 3. WC seats, 4. diamond anvils, 5. Re gasket, 6. screws for generating loading force, 7. pack of conical spring washers (Belleville springs), 8. setscrews for diamond anvils alignment, 9. safety setscrews, 10. optional miniature resistive heater.

A pressure transmitting medium (PTM) is inserted into the gasket in most experiments and is used to transmit the axial stress applied by the diamond anvils to the sample and to generate (quasi-)hydrostatic conditions in the sample chamber. Ideally, the PTM suppresses the shear stress over the entire pressure range. However, hydrostaticity above 15 GPa is not fulfilled because fluids eventually solidify under pressure, leading to the formation of differential stresses in the sample chamber (Klotz et al., 2009). DACs in combination with a laser-heating system require a thermal insulator, in addition to the PTM, which isolates the sample from the diamonds and ensures efficient heating of the sample. There are many kinds of thermal insulators (which also serve as a PTM) with low thermal conductivity and very low absorbance of the laser radiation in the X-ray regime. In our study, we tried to avoid using non-inert thermal insulators like MgO or KCl, as they may react with the sample material. The best PTM and thermal insulator for our purpose is argon, which was loaded into the cell with a gas-loading system installed at the beamlines P02.2 at PETRA III, DESY, Hamburg, Germany and at ID27 at ESRF, Grenoble, France. The pressure in the cell is measured using a pressure standard which is loaded as an additional compound into the cell. The most common pressure standard is ruby, Cr-doped  $\text{Al}_2\text{O}_3$ . The shift with



pressure of the R<sub>1</sub> fluorescence line in ruby is used to calculate the pressure in the cell (Mao et al., 1986; Chijioke et al., 2005):

$$P[\text{GPa}] = \frac{A}{B}[(\lambda/\lambda_0)^B - 1] \quad (2.1)$$

where  $P$  is the pressure and  $\lambda$  is the wavelength of the ruby R<sub>1</sub> line with  $\lambda_0 = 694.24$  nm as the zero pressure value at 298 K.  $A = 1904$  GPa and  $B = 7.665$  are the least-square-fit parameters for the calibration of the ruby fluorescence shift measured in argon up to 80 GPa (Mao et al., 1986). Non-hydrostatic stress applied to the ruby crystal could cause line broadening and the uncertainty of pressure measurement in argon is usually assumed to be less than 2% of the pressure (Mao et al., 1986). The disadvantage of using ruby fluorescence for pressure measurement is a large temperature dependence. Thus above 800 K, the ruby fluorescence cannot be used for proper calculation. Therefore, in the present study the pressure was measured only before and after heating and the average between the two values were used as experimental pressure. The software PeakFit (SYSTAT Software Inc., 2002) was used to fit the positions of the ruby fluorescence lines by using constant baseline subtraction and a symmetric peak shape (Gaussian + Lorentzian area model).

An alternative way to determine the pressure in the cell is to use the laser-induced fluorescence of the diamond. This method has the advantage, that no further compound has to be loaded into the cell and it prevents the chemical system from additional contamination. The high-frequency edge of the Raman band  $\nu$ , which corresponds to the Raman shift of the diamond culet face (that is the wall of the sample chamber), is used to determine the pressure in the sample chamber (Akahama and Kawamura, 2004):

$$P[\text{GPa}] = 3.585(3) \cdot 10^{-4} \nu^2 - 0.5281(4) \nu + 66.9(7). \quad (2.2)$$

The errors in brackets correspond to the estimated standard deviation of a least-square fit to the data by the ruby and Pt scale (Akahama and Kawamura, 2004). The frequency is measured in the center of the sample chamber and the accuracy for the determination is  $\pm 2$  cm<sup>-1</sup>. A standard deviation of 0.66 GPa is given for pressures of up to 200 GPa (Akahama and Kawamura, 2004).

Different ways of sample arrangements were tested to develop successful and promising experimental protocols. Depending on the experimental setup, we can distinguish three different types of loading.

### **Carbonate-silicate powder mixtures**

Homogeneously mixed powders were used to study the reaction between carbonates and mantle silicates at high pressure and high temperature and to ensure a good reactivity between them. In the experimental runs DAC18 and DAC19, crystals from the synthesis of Sr-doped calcite starting material (NB12) and fragments of the MgSiO<sub>3</sub> glass were ground to fine powders in an agate mortar and dried overnight at 100 °C, separately.

The powders were then mixed with 1:1 mole fraction and ground in an agate mortar for 20 min in ethanol to homogenize the mixture. For the experiment run DAC27, SrCO<sub>3</sub> powder from Sigma Aldrich Chemical Company (99.995% purity) was mixed with 50 % of finely ground natural enstatite powder. In both cases, high-pressure was applied using a BX90 diamond anvil cell with culets sizes of 200  $\mu\text{m}$  and 300  $\mu\text{m}$ . The powder mixture was loaded into a sample chamber with a diameter of 80 - 100  $\mu\text{m}$  and a thickness of 20 - 30  $\mu\text{m}$  drilled into a rhenium gasket. No pressure standard and no PTM were loaded in order to prevent reactions with other components and contamination of the chemical system. A picture of the cell loaded with carbonate-silicate powder mixtures is shown in Fig. 2.4a.

### **Silicate single crystal embedded into a carbonate powder layer**

To follow a spatial redistribution of the trace elements during carbonate-silicate-reactions, we needed to adapt the sample loading as the spatial resolution of the X-ray beam is above the typical grain size of powder samples, e.g. 1  $\mu\text{m}$ . The carbonate starting materials were prepared in the same way as described before and were loaded into a 80 - 100  $\mu\text{m}$  diameter hole of a rhenium gasket as a powder. Instead of silicate powder samples, a small silicate single crystal with average widths of 20 - 50  $\mu\text{m}$  and a thickness of < 20  $\mu\text{m}$  was placed on top of the carbonate powder layer. While closing the DAC, the silicate single crystal was further pushed into the powder layer and thus completely surrounded by the carbonate phase (Fig. 2.4b). Argon was then loaded as a PTM and thermal insulator. This type of sample arrangement has been realized in seven runs (DAC04, DAC11, DAC13, DAC15, DAC16, DAC23 and DAC24). During the experiments, the exact location of the single crystal was determined by using the silicate XRF signal. Following the reaction between the two phases at the interface, the migration of the trace elements from the carbonate into the newly formed silicate phase could be observed by X-ray fluorescence and also by optical fluorescence techniques.

### **Silicate single crystal and carbonate single crystal**

Further improvements were made on the shape and loading of the starting material and were tested in the runs DAC08 and DAC12. Single crystals of La-doped calcite and of orthopyroxene (DAC08) as well as of Sr-doped calcite together with a single crystal of olivine (DAC12) were polished down to a thickness of < 20  $\mu\text{m}$  and then cut into platelets with a shape of half circles with a radius of  $\sim 35 \mu\text{m}$ . The cutting was done by Dr. M. Bykov using a FEI SCIOS dual-beam focused ion beam at the DESY NanoLab. The half circles were loaded into a 70  $\mu\text{m}$  big sample chamber laser-drilled into a rhenium gasket. When the cell was carefully closed, the crystals were in close contact to each other (Fig. 2.4c). Finally, argon served as a PTM and thermal insulator. Compared to the sample arrangements described above, three distinct areas could be now separated by the XRF: a) one with only carbonate, b) a second one with only silicate and a third where both phases are in close contact and carbonate-silicate reactions take place.

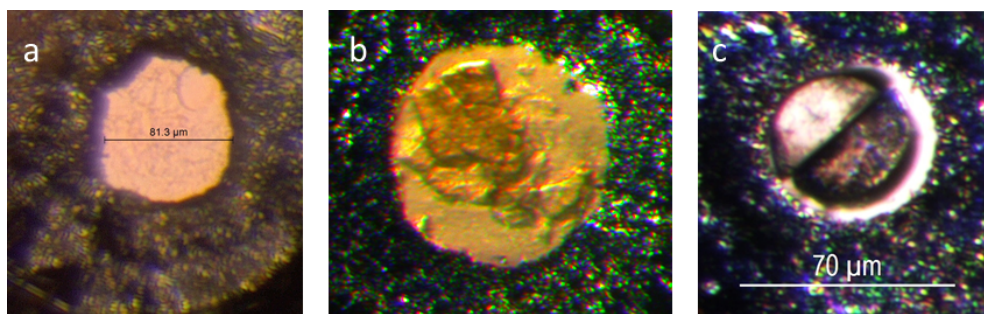


Figure 2.4: Different types of sample arrangements. a) Carbonate-silicate powder mixture, b) silicate single crystal embedded into a carbonate powder layer and c) silicate single crystal and carbonate single crystal loaded in one cell.

### 2.3 High-pressure single crystal X-ray diffraction experiments

Single crystal X-ray diffraction at high pressure serves as an ultimate probe for the characterization of minerals at conditions of the Earth's deep interior. They give direct information on the behaviour of the high pressure phase of the samples and provide data for volume/density changes under pressure hence volume compressibility (which is the inverse of the bulk modulus). These changes are important for interpreting seismic observations since the density and the bulk modulus under compression control the velocity of seismic waves in the mantle.

In a high pressure experiment, the crystal is affected by stresses that cause strains propagating through the sample and deteriorating it. Nearly perfect crystals with low mosaicity are essential for high-pressure studies as they deteriorate more slowly (Bykova, 2015). Single crystals of strontianite ( $\text{SrCO}_3$ ) were synthesized (see for details chapter 3) and most of the crystals were twinned or had a high mosaicity. Therefore, the selection of an appropriate single crystal has been carried out prior to the performance of the actual experiment: Several crystals from the synthesis of  $\text{SrCO}_3$  were placed into one DAC with large culets of  $500 \mu\text{m}$  and fast scanning with the collection of single crystal XRD for each individual crystal was performed. From the given XRD patterns, we evaluated the crystal quality and picked the most promising crystal for our high-pressure study.

The selected crystal was pressurized using a symmetric piston-cylinder diamond anvil cell of the "Mao-Bell"-type (Mao, 1997) connected to a membrane for controlled pressure increase. The software *CrysAlis PRO* (Rigaku Oxford Diffraction, 2019) was used for single crystal XRD data processing and data reduction. The actual XRD images were converted into *CrysAlis PRO* format called ESPERANTO. An instrument model was inserted for calibration of sample-to-detector distance, the detector's origin, offsets of the goniometer angles and rotation of the X-ray beam and the detector around the instrument axis. We used  $\text{CeO}_2$  powder and an orthoenstatite crystal ( $(\text{Mg}_{1.93}\text{Fe}_{0.06})(\text{Si}_{1.93}\text{Al}_{0.06})\text{O}_6$ , *Pbca*,  $a = 8.8117(2) \text{ \AA}$ ,  $b = 5.18320(10) \text{ \AA}$ ,  $c = 18.2391(3) \text{ \AA}$ ) for calibration of the diffractometer and for refinement of the instru-

ment model. XRD data collection is performed in *oscillation mode* where the diffraction is recorded while rotating the sample about a single  $\omega$ -axis and over the entire opening angle of the DAC in small steps of  $0.5^\circ$ . The exposure time is adjusted according to the dynamic range of the detector. To avoid oversaturation of the detector, a test is made prior to the actual measurement, where the threshold intensity  $T_r$  for saturated reflections is defined (see for more details Bykova (2015)).

Processing of the single crystal XRD data includes an automatic indexing of the reflections to metric parameters while eliminating reflexes coming from the diamond, the PTM and the gasket material. Once the unit cell parameters are extracted, data reduction can be done with insertion of the correct data range, the opening angle for the DAC, an integration box size, a profile fitting mode and a background evaluation mode. The final data is stored in a *.hkl*-file which contains a list of all observed reflections and a *.cif*-file is created with structural information and a detailed description of the data collection and the integration procedure. The *.hkl*-file together with an instruction file called *.ins*-file is used for the structure solution in SHELXS (Sheldrick, 2007) and for the refinement in SHELXT (Sheldrick, 2015). The instruction file contains information on the space group, the unit cell parameters with standard deviations, the wavelength, the number of formula per unit cell, the lattice type, symmetry operators and the chemical composition. The structure solution is performed by calculating atomic positions and thermal parameters in isotropic or anisotropic approximation based on a set of squared experimental structural amplitudes  $F_{hkl}^2$  (Bykova, 2015).

$$F_{hkl}^2 = \frac{I_{hkl}}{k \cdot Lp \cdot A} \quad (2.3)$$

where  $I_{hkl}$  are the intensities from the *hkl*-reflections of the phase,  $k$  is a scale factor,  $Lp$  is the Lorentz-polarization correction and  $A$  is the transmission factor.  $F_{hkl}^2$  is related to the structure factor  $\mathbf{F}_{hkl}$  which is a complex parameter and its amplitudes is derived from the X-ray diffraction experiment. The atomic coordinates of the derived phase can be then directly calculated, since the electron density in a position  $x,y,z$  of the unit cell  $\rho_{xyz}$  is related to the structure factor by an inverse Fourier transform:

$$\rho_{xyz} = \frac{1}{V} \sum \mathbf{F}_{hkl} \exp[-2\pi i(hx + ky + lz)] \quad (2.4)$$

where  $V$  is the unit cell volume. Once the initial structural model is obtained, it is refined against the experimental data by a least-squares minimization of adjustable parameters. The quality of the agreement between model and experimental data is defined by the residual R-factors  $R_1$  and  $wR_2$ . Our results on the structure solution of the low-pressure phase SrCO<sub>3</sub>-I and the post-aragonite phase SrCO<sub>3</sub>-II can be found in detail in chapter 3.

## 2.4 Laser-heated and resistively heated diamond anvil cell experiments

The diamond anvil cell technique coupled with a laser heating system is an important technique in geoscience to study materials at conditions of the Earth's mantle. In this section, the setup of two laser-heating systems with a) an Yb-fiber laser and b) a pulsed CO<sub>2</sub>-laser will be presented. In preparation of the *in-situ* experiments at the X-ray beamline, we performed offline laser heating experiments which will be described first. In addition, we will compare laser-heated diamond anvil cell (LHDAC) experiments with experiments that have been resistively heated.

### 2.4.1 Offline laser heating

We performed offline laser-heating experiments combined with analysis of the recovered run products. These first experiments aimed at gaining know-how on the laser-sample interaction as well as on testing appropriate P-T-conditions for ensuing *in-situ* experiments at the X-ray beamline. The test experiments were performed on two different laser-heating systems: a portable Yb-fiber laser-heating system built and operated by the TU Dortmund and the University of Potsdam (Spiekermann et al., 2020) and a pulsed CO<sub>2</sub>-laser-heating system (*Coherent*, Diamond K-250) in the central laser-heating facility of the DFG-funded Research Unit *CarboPaT* (Bayarjargal et al., 2018). Three sample assemblages were chosen for testing: i) mixture of 75 wt% San Carlos olivine and 25 wt% SrCO<sub>3</sub> powder; ii) single crystal of San Carlos olivine embedded in a powder of SrCO<sub>3</sub> or Sr-doped calcite (from synthesis NB12) and iii) single crystal of San Carlos olivine in contact with a crystal of SrCO<sub>3</sub> or Sr-doped calcite (from synthesis NB12). All three loadings were pressurized up to about 45 GPa. In the latter two assemblages, the sample could not be heated with the fiber laser due to the weak coupling of the 1070 nm-laser to the olivine crystal which has a low Fe-content and a high transparency. In the first case, we could heat the sample up to 2500 K. There was a strong change of the laser-sample coupling behaviour at around 1800 K. We interpreted this to be the phase transformation of olivine to Mg,Fe-perovskite plus ferropericlase.

Heating transparent materials, like iron-free silicates, with a Yb-fiber laser is challenging, because of the low absorption at the near-infrared wavelength of 1070 nm. The light of the laser passes through the crystal lattice without enough absorption to the atoms. Hence, the sample material does not heat up. In contrast, the absorption of silicate minerals at the wavelength of 10.6  $\mu\text{m}$  emitted by a CO<sub>2</sub>-laser is high enough due to phonon absorption to efficiently heat the sample material (Boehler and Chopelas, 1991). The CO<sub>2</sub>-laser heats the sample more easily and penetrates deeper into the sample (several tens of  $\mu\text{m}$ ) which releases the need of double-sided heating. However, it also puts higher strain on the diamonds if the sample is not well isolated and causes the diamond more likely to break during the experiment. These first investigations showed that experiments using a Yb-fiber laser for heating have to be performed with Fe-bearing minerals whereas experiments with a CO<sub>2</sub>-laser are not restricted by the Fe content in the sample.

### 2.4.2 *In-situ* laser heating

#### LHDAC experiments at the Extreme Conditions Beamline P02.2 at PETRA III, Hamburg, Germany

To study elemental distribution processes between carbonates and silicates, we performed experiments at the Extreme Conditions Beamline (ECB) at P02.2 at PETRA III. We made use of the high energy photons of 42.7 keV. Focusing of the X-ray beam with KB-mirrors yields a focal spot size on the sample of  $2\ \mu\text{m}$  (horizontal)  $\times$   $2\ \mu\text{m}$  (vertical). The ECB is equipped with a flat panel Perkin Elmer detector (XRD-1621) for XRD data collection and a 200 W Yb-fiber laser with a wavelength of 1072 nm. The two laser beams are collinear to the X-ray beam and to the compression axis of the DAC allowing on-axis double-sided heating (Liermann et al., 2015) (Fig. 2.5). Due to large temperature gradients in depth and radial directions during laser heating, the laser spot has been defocused to a size of 20 - 30  $\mu\text{m}$  which results in a much flatter profile (Boehler, 2000). In addition, XRD images were collected during heating always in the center of the defocused heating spot to minimize the impact of large temperature gradients. The temperature is recorded by a Czerny-Turner spectrograph with an iCCD camera collecting the thermal radiation of the hot sample through a dedicated beam path (Liermann et al., 2015). Simultaneously to XRD, the signal for XRF was measured at  $\sim 20^\circ$  from the direct X-ray beam on the downstream site (see Fig. 2.5) by using a confocal setup with a collimating polycapillary mounted on a Vortex silicon drift detector. The characteristics of this polycapillary collimator are well described in a study by Wilke et al. (2010). So far, the detector capillary has only been used for excitation energies up to 33 keV (Borchert et al., 2009, 2010b,a; Andraut et al., 2012; Petitgirard et al., 2012; Wilke et al., 2012). Our study provides first experimental data on using this confocal optic for XRF with an energetically higher incident beam of 42.7 keV.

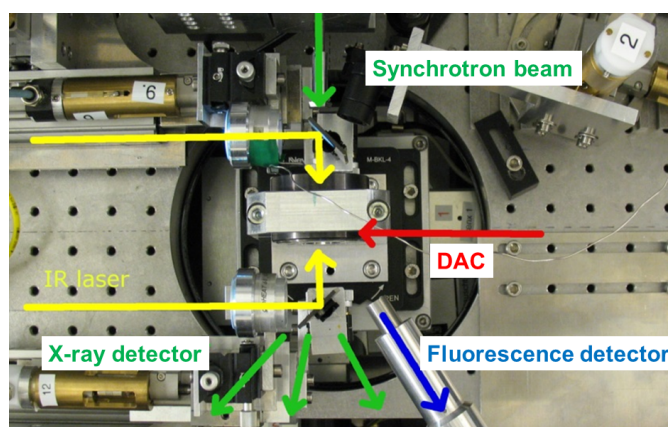


Figure 2.5: Photograph of the experimental setup at beamline P02.2 at PETRA III (courtesy of W. Morgenroth). In green are the incident X-ray beam and the diffracted X-rays to the Perkin Elmer detector. In yellow is the path for double-sided laser heating. A fluorescence detector is placed at the downstream site at  $\sim 20^\circ$  from the direct X-ray beam.

### LHDAC experiments at beamline ID27 at ESRF, Grenoble, France

Further experiments were performed at beamline ID27 at the ESRF using the CO<sub>2</sub>-laser heating system with a maximum power of 200 W (Petitgirard et al., 2014) enabling efficient heating of the low-iron bearing sample material. XRD data were collected with a MAR CCD 345 detector and the XRF signal was measured with an equivalent Vortex detector and polycapillary in front of it as described in the previous paragraph. The layout of the CO<sub>2</sub>-laser and the experimental setup can be seen in Fig. 2.6. The CO<sub>2</sub>-laser was positioned at the upstream site in off-axis mode at 18° from the incoming X-ray beam direction. Imaging of the sample is done by a Schwarzschild reflective objective that transmits the image to a spectrometer equipped with a Pixis 100 CCD camera (Petitgirard et al., 2014). The temperature is measured using the light emitted from the hot sample collected at the hot spot of the CO<sub>2</sub>-laser radiation. To avoid absorption of the X-rays, the emitted light is guided through two pinholes that have been drilled into a mirror which is placed in front of the spectrometer. Temperatures are then calculated from corrected emission spectra using either the Planck or Wien function to fit the data (Petitgirard et al., 2014).

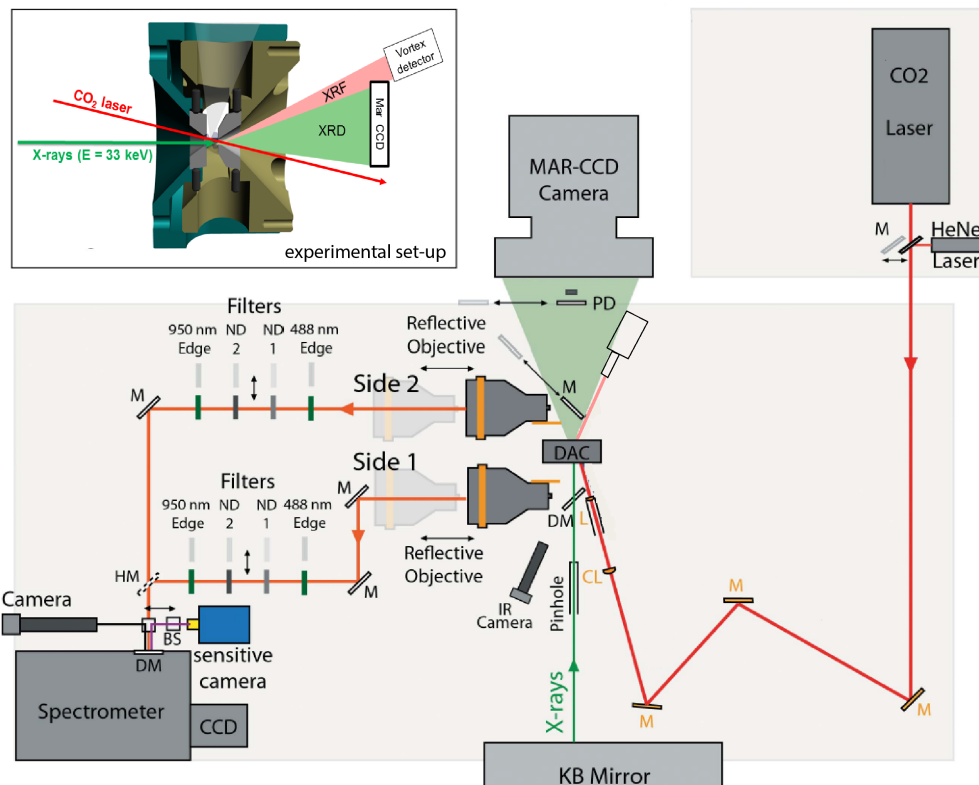


Figure 2.6: Schematic layout of the CO<sub>2</sub>-laser heating system and the experimental setup (upper left corner) at beamline ID27 at ESRF modified after Petitgirard et al. (2014). In green are the incident X-ray beam and the X-ray cone of diffraction to the MAR CCD camera. The CO<sub>2</sub>-laser shown in red is focused on the sample in the DAC in off-axis geometry at 18° from the incoming beam direction. In orange is the path for (double-sided) temperature measurement. A fluorescence detector is placed at ~20° from the X-ray beam direction on the downstream site.



### 2.4.3 Resistively heated DAC experiments

To minimize the effect of temperature gradients (see also section 5.3) which usually occurs in LHDAC experiments, we performed resistive heating of the sample in four different experiment runs. For that purpose, a membrane-driven four pin DAC equipped with diamonds with a culet size of 300  $\mu\text{m}$  were used. A Re gasket with 80  $\mu\text{m}$  hole was used as a sample chamber. Heating of the sample is achieved by using a graphite heater built manually that surrounds the gasket assembly. The graphite heater consists of two pieces of flexible graphite foil with a thickness of 1 mm. Prior to sample loading, the graphite foil is indented between the diamonds using a steel gasket on the same position as the initial Re gasket. This process shapes the graphite foil in a way that there is a close contact between the heater and the diamonds. The temperature was measured with two R-type thermocouples (Pt-Pt13Rh) that were positioned on the diamond facet between diamond tip and cylinder site of the cell (Fig. 2.7). The optimum achievable accuracy in temperature measurements of the thermocouples is  $\pm 5$  K (Liermann et al., 2009). However, during the experiments, we recognized a difference of 60 K between the thermocouples. In addition to the sample assemblage, a piece of platinum was placed into the sample chamber for proper pressure calibration by using the well known equation of state for platinum during heating. To avoid the oxidation of the sample and diamonds, the entire DAC was put into a vacuum chamber designed at the ECB P02.2, PETRA III (Liermann et al., 2015).

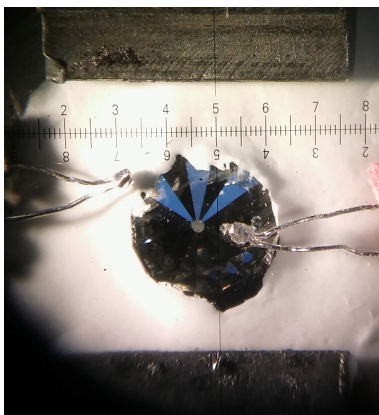


Figure 2.7: Top view of the resistive heated DAC with positions of the thermocouples.

Because of the complexity of the sample assembly in resistively heated DACs, many problems can arise during heating such as creep deformation of the material or welding of the gasket to the anvils (Dubrovinskaia and Dubrovinsky, 2003). Also maintaining constant pressure during heating is difficult because of differences in the thermal expansion of the seats and other mechanical parts in the cell that lead to a variation of the pressure during heating. For example, heating of 1000 K with a graphite heater can double the pressure in the DAC (Dubrovinskaia and Dubrovinsky, 2003). Due to these challenges, only one experiment run (DAC29) out of four was successful. We reached a temperature of 1273 K at a maximum pressure of 35 GPa and we were able to recover the sample material of DAC29 after quenching for additional post-heating analysis.



## 2.5 Combined $\mu$ -XRD and $\mu$ -XRF data acquisition

### 2.5.1 Introduction to XRD and XRF

X-ray diffraction as well as X-ray fluorescence have become commonly used techniques for the identification and characterization of materials. In general, diffraction describes the interaction between electromagnetic radiation (e.g. X-rays) and atoms which are periodically ordered in material. From a crystallographic point of view, diffraction is described as the reflection of an X-ray beam on families of equivalent crystallographic planes labelled by Miller- or  $hkl$ -indices and separated by specific lengths called  $d$ -spacings. The maxima of scattered intensity correspond to scattering angles ( $2\theta$ ) and the connection between wavelength,  $d$ -spacing and diffraction angle is called Bragg's law which is defined as:

$$2d \cdot \sin\theta = n\lambda. \quad (2.5)$$

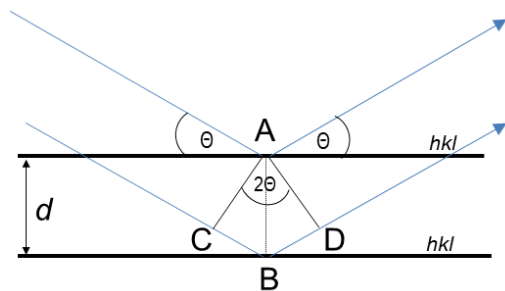


Figure 2.8: Diffraction of an X-ray beam (blue arrows) by crystallographic planes  $hkl$  with same  $d$ -spacing based on Bragg's law.

In a routine X-ray diffraction experiment, a crystal is mounted on a goniometer and is illuminated by a monochromatic X-ray beam. The geometrical distribution of the reflections (diffraction spots) is used to derive an orientation of the crystal with respect to the goniometer axis. The positions of the reflections as a function of the diffraction angle are used to determine lattice parameters and – if the composition is known – also the mineral density which is important for modelling the Earth's deep interior. Since diffraction is a scattering process on electrons, it depends on the electron density

distribution of the crystal. In addition, the intensity of scattering of a diffraction peak is given by the structure factor (Lavina et al., 2014). The intensity of the reflections also depends on the experimental geometry and setup (instrument parameters).

In the energy regime of X-rays (500 eV - 500 keV) electromagnetic radiation interacts with matter and is absorbed through the photo electric effect in which an X-ray photon is absorbed by an electron on a specific quantum core level of an atom (Fig. 2.9). Following this absorption event, the atom is put in an excited state with one of the core levels left empty (core-hole). An outer shell electron fills the core hole and ejects an X-ray photon of well defined energy that corresponds to the energy difference of the electrons. This process is called X-ray fluorescence (XRF) and fluorescence energies are characteristic for each element. They can be used to identify the absorbing atom and to quantify its concentration, thus making XRF to a sensitive multi-element analysis. X-ray fluorescence can be triggered by any electromagnetically interacting particles, including X-rays themselves. If a conventional X-ray tube is used for excitation, a large background due to scattered radiation (Rayleigh and Compton scattering) is produced

(Haller and Knoechel, 1996) and the signal-to-noise ratio for XRF is very low. By using synchrotron radiation with a collimated and monochromatic beam instead of an X-ray tube, the sensitivity is greatly enhanced also due to the possibility of micro-focussing. The size of the focussed beam determines the spatial resolution which can be in the single digit micrometer range and which is necessary to probe small samples during LHDAC experiments. An increase in the sensitivity is further achieved by using a collimating polycapillary suited for the given energy range which reduces the signal that comes from elastic and inelastic scattering of the incoming X-ray beam by the diamond anvils as well as from excitation of fluorescence from the cell body. Considering all the named aspects, synchrotron-based XRF is one of the few elemental probes to investigate materials at extreme conditions and therefore important for studying elemental redistribution processes in carbonate-silicate reactions at conditions of the Earth's mantle.

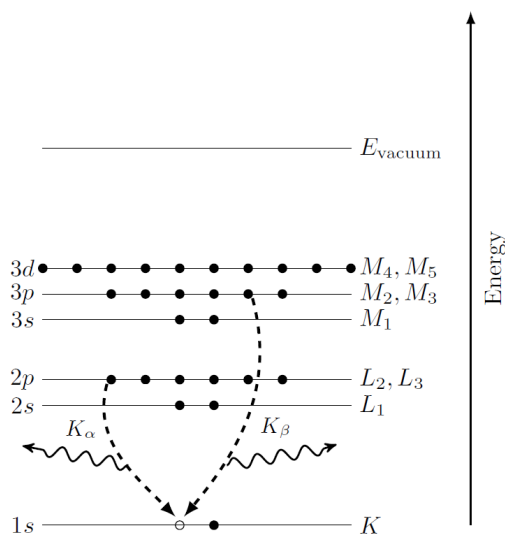


Figure 2.9: The excited atomic state will decay by X-ray fluorescence where an electron is moved from a less tightly bound orbital to core hole level and the energy difference is given to the emitted photon ( $K_\alpha$  or  $K_\beta$ ) (Newville, 2014).

### 2.5.2 XRD and XRF data processing

Combining XRD and XRF for scanning the sample material allows us to collect structural information as well as chemical redistribution between the phases at the same time. Both methods are applicable to DAC experiments and laser heating, thus making it possible to study materials at Earth's mantle conditions with a high precision and accuracy. However, limitations are given in the depth resolution as both methods produce averages upon the entire depth of the sample. The produced raw data from XRD and XRF measurements are processed and analysed individually.

In the case of XRD data analyses, all XRD images have been converted precedently into azimuthally integrated XRD patterns using the program *DIOPTAS* (Prescher and Prakapenka, 2015). Refinement and fitting of the XRD patterns were carried out with

the program *Fullprof* (Rodriguez-Carvajal, 2008). A profile matching tool called Le Bail fit (Le Bail et al., 1988) was used to get a whole-pattern decomposition of the XRD patterns. This fitting procedure requires approximate unit cell and resolution parameters of the present mineral phases, which are derived from pre-processed XRD data using *DIOPTAS* and the respective known equation of states (EoS). All mineral phases and corresponding EoS which were applied to the Le Bail fit are listed in the Appendix B. A Thompson-Cox-Hastings (TCH) pseudo-Voigt peak shape function was used for fitting the peaks and background parameters were refined individually using linear interpolations between a set of points selected manually. The selection of parameters to be refined was chosen carefully and others were kept fixed to physically reasonable constraints (e.g. constant scale factors for individual phases over the refinement).

In addition to single point XRD images with acquisition times of 5-10s during heating, XRD maps over the heated area before and after heating were recorded on appropriate loadings (see section 2.2) to scan the sample material with an acquisition time per point of 3s. These data were analysed using the program *XDI* (Hrubiak, 2016). This program builds an XRD contrast image of the sample by integrating diffraction images obtained from a two dimensional grid scan. It is especially developed for data analysis derived from diamond anvil cell experiments and therefore provides additional functions for pressure measurement and 2-D phase identification (Hrubiak, 2016). The data processing with *XDI* is divided into three main steps: Setup, single point integration and imaging. In the first step, XRD processing parameters, like sample-detector calibration, X-ray wavelength and area detector pixel dimension, are imported. In the next step, a single XRD file from a 2-D-grid is integrated for masking and phase identification.

At this point, we also used preliminary results for phase identification from refinements of XRD single point images. The background is subtracted by a pre-measured background XRD image and improves the analysis of weak features in the pattern. The obtained parameters are then used for processing of all XRD files corresponding to the given 2-D-grid scan (Fig. 2.10b). The resulted XRD map has now a multi-dimensional data structure with azimuthal information and 1-D-XRD pattern of each single point in the 2-D-grid. XRD-contrast images can be built easily by selecting a  $2\theta$  range of interest manually or automatically (Fig. 2.10c,d). Furthermore, the automatic  $2\theta$  selection can build a XRD-contrast image by combining multiple  $2\theta$  intervals (e.g. single peaks) which belong to the currently loaded phase. This allows a precise localization of the different phases. Furthermore, the heated areas are clearly separated from unheated areas.

In addition to XRD-measurements in the maps, the XRF signal was recorded with a different exposure time of 10 s by using a confocal setup with a collimating polycapillary half-lens mounted on a Vortex silicon drift detector (Wilke et al., 2010). The program *PyMca* written by Solé et al. (2007) is a collection of Python tools to visualize and analyse energy-dispersive XRF data and was used for data analysis. In order to analyse the data as XRF data, one needs to calibrate the spectrum and assign the energy to each

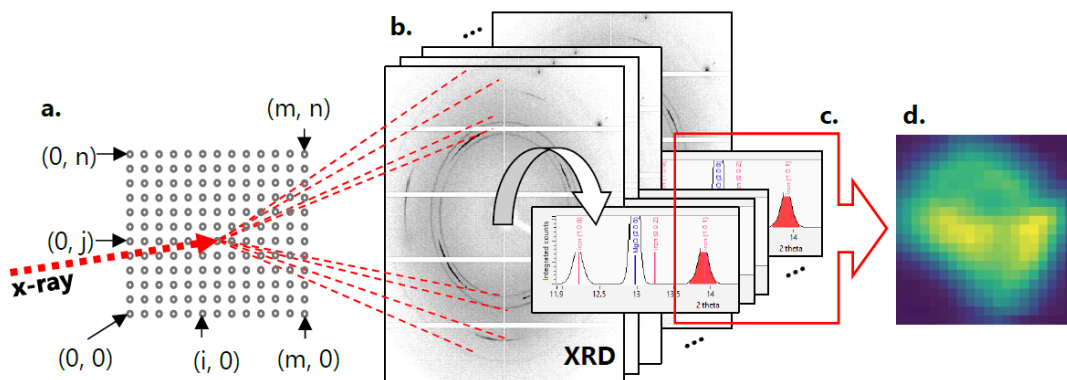


Figure 2.10: Procedure for constructing an XRD-contrast image in *XDI*: a) experimental setup with incident X-ray beam shown as dashed red line onto a 2-dimensional grid with  $m \times n$ -points. b) A batch of XRD images recorded on a X-ray area detector at each point of the 2-D-grid in a). c) A batch of 1-dimensional XRD patterns obtained by integration of the XRD images in b). d) XRD-contrast image is built by integrating the scattered photon counts from selected  $2\theta$  range in c). for each point on the 2-D-scan. (Hrubiak, 2016)

channel of the given amplitude pattern. The spectrum is calibrated by identifying peaks from a standard sample (NIST SRM 610 or NIST SRM 612), that was measured at the same experimental conditions but with longer acquisition times (e.g. 100 s), and where the energy of the peaks is known. In our study, we also used the excitation energy for initial calibration (Fig. 2.11a). For XRD-XRF-map-measurements performed at beamline ID27, at the ESRF, the excitation energy was 33.2 keV whereas the excitation energy for measurements at beamline P02.2 at PETRA was 42.7 keV.

After calibrating, the peaks in the spectrum are then directly correlating to the elements present in the sample (Fig. 2.11b). PyMca offers peak search routines which give a good first guess of the elements in the measured spot. Since our sample material contains a manageable number of elements, this already has identified all the peaks in the spectrum and could be used for building a fit configuration file. This fit configuration file is used to fit all XRF spectra in the same XRF map using the *batch fitting* mode. The fit configuration file used for our study on  $\text{SrCO}_3$ ,  $\text{CaCO}_3\text{:Sr}^{2+}$  and  $\text{CaCO}_3\text{:La}^{3+}$  in contact with silicates as well as the results of the fitting can be found in the Appendix C. In the *batch fitting* mode, a file is created which contains the intensities for all elements and their corresponding fluorescence lines at each individual point of the XRF map. In a next step, the intensities have been normalized to the incident intensity of the X-ray beam. Finally, using the *RGB correlator*, different colours are assigned to the characteristic peaks of the elements. An example is shown in Fig.2.11c. The program allows a differentiation of the overlapping peaks to element specific peaks (e.g. Eu-L-lines are usually overlapped by Fe- $K_\alpha$ -line) and it is possible to select sub-groups (e.g. L3) in addition to the groups (e.g. L-lines). These two features are essential to detect a possible redistribution of REEs in an environment where iron is present.

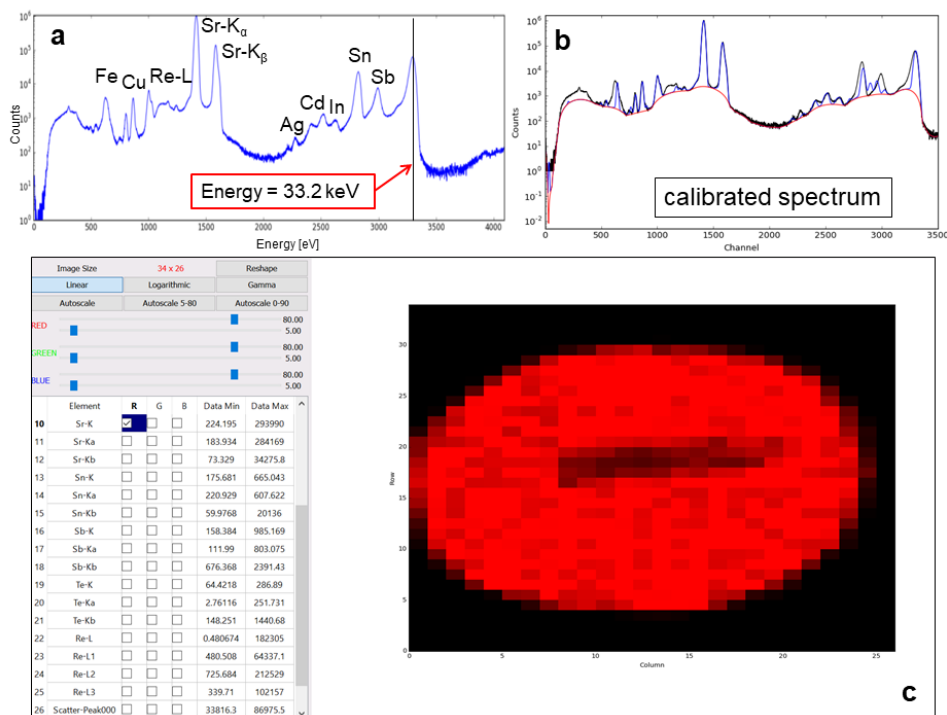


Figure 2.11: Procedure for constructing an element map in *PyMca* using the *RGB correlator*. a) Calibration of the spectrum using the strongest scattering peak which corresponds to the excitation energy of 33.2 keV. b) the calibrated spectrum with fitting results after insertion of the fit configuration file for samples with  $\text{SrCO}_3$  + silicate, measured at ID27 at 33.2 keV (see Appendix C for details). c) In the *RGB correlator*, the different fluorescence lines with corresponding fit areas are assigned to a certain colour and are plotted in the XRF map.

## 2.6 TEM analyses on recovered sample material

To study carbonate-silicate reactions at a sub-micrometer scale and to obtain information in three-dimensional space, additional analytical observations with transmission electron microscopy (TEM) were carried out. Analysing the recovered sample material with TEM involves several challenges. First, the remaining sample including the gasket needs to be unloaded from the DAC without destroying or losing it. Secondly, the recovered sample material has to be prepared for TEM measurements such that a region from the heated interface between the carbonate and silicate phase can be investigated. The selected region must be thin enough for electron transmission.

In all cases, where the diamonds survived the experiment, we were able to recover the sample material for *ex-situ* TEM analyses. A thin foil ( $<$  about 100 nm thickness) with a size of approx.  $10 \times 30 \mu\text{m}^2$  was cut out of each recovered sample using the focused ion beam (FIB) preparation technique. This work was done partially by Dr. M. Bykov using a FEI SCIOS dual-beam FIB at the DESY NanoLab and by A. Schreiber with a FEI FIB200TEM device at the GFZ Potsdam.

The electron microscopic analyses were performed with a FEI TECNAI G2 F20 X-Twin (200 kV) microscope at the GFZ Potsdam by Dr. R. Wirth. The TEM is equipped with a field emission gun electron source, an energy-dispersive X-ray (EDX) detector for chemical analyses and a high-angle annular dark-field (HAADF) detector for Z-contrast imaging. EDX spectra were obtained in STEM mode (Brydson et al., 2014) with 200 kV acceleration voltage, 60 s acquisition time and 20 keV spectrum range. Additional to EDX, images were taken in bright field mode in order to visualize the crystallinity of the recovered sample material and to define amorphous phases.

## Chapter 3

# Equation of state and high-pressure phase behaviour of SrCO<sub>3</sub>

In order to interpret the results of our carbonate-silicate reactions experiments we investigated the high-pressure phase transition of strontianite (SrCO<sub>3</sub>), which is an important component in our study and whose high-pressure stability is not yet well understood. We performed powder X-ray diffraction experiments at ambient temperature as well as single-crystal X-ray diffraction to resolve a long standing discussion on the correct space group of the post-aragonite phase. We were able to confirm the existence of SrCO<sub>3</sub> in the low pressure aragonite-type space group setting *Pmcn* (62) up to about 26 GPa. Above this pressure, SrCO<sub>3</sub> transforms into a high-pressure phase with post-aragonite crystal structure with space group *Pmnn* (No. 59, origin choice 2). The occurrence of pressure-induced structural changes in the carbonates can have an effect on the stability as well as on the reaction between carbonates and mantle silicates. It is therefore important to consider all possible high-pressure polymorphs as they become more relevant at Earth's mantle conditions. Our results unequivocally show the existence of a *Pmnn* structure in SrCO<sub>3</sub> above 26 GPa and provide important structural parameters for this phase. A manuscript elaborating the contents of this chapter has been submitted to *European Journal of Mineralogy* and was published on the 3<sup>rd</sup> November 2020.

### 3.1 Introduction

The most abundant carbonates entering the subduction zone are Ca-, Mg- and Fe-carbonates. At the PT-conditions expected for subduction zones and the Earth's mantle, carbonates undergo pressure- and temperature-induced structural changes: CaCO<sub>3</sub>, for instance, undergoes several phase transitions, with some of them becoming more relevant to Earth's mantle conditions (Martinez et al., 1996; Santillán and Williams, 2004; Ono, 2005; Oganov et al., 2006; Bayarjargal et al., 2018); other studies have shown the stability and phase transitions of dolomite (Zucchini et al., 2017; Solomatova and

Asimow, 2017; Efthimiopoulos et al., 2017) which is thought to be the main carbonate phase in subducted slabs. Regarding  $\text{CaCO}_3$ , numerous studies on the phase behaviour of aragonite-type  $\text{CaCO}_3$  at high pressure reported a phase transition from orthorhombic aragonite (space group  $Pm\bar{c}n$ ) into monoclinic  $\text{CaCO}_3$ -VII at around 30 GPa and into post-aragonite structure  $Pm\bar{m}n$  at around 40 GPa (Gavryushkin et al., 2017; Bayarjargal et al., 2018). Meanwhile, strontianite, which is isostructural to aragonite at room pressure and room temperature conditions and very common in natural carbonates, is considered to have similar phase transitions which are shifted to lower pressure due to larger ionic radius of  $\text{Sr}^{2+}$  (1.31 Å) in comparison with  $\text{Ca}^{2+}$  (1.18 Å) (Shannon, 1976). Recent findings on mineral inclusions in transition-zone diamonds showed significant amounts of strontium (Brenker et al., 2007; Kaminsky, 2012), which motivated our investigations of  $\text{SrCO}_3$  as a possible stable phase in deep Earth.

Whilst most of the physical properties of  $\text{SrCO}_3$  are well known at ambient conditions (Villiers, 1971; Antao and Hassan, 2009; Nguyen-Thanh et al., 2016; Biedermann et al., 2017b), they have rarely been measured by powder X-ray diffraction at high pressure (Ono et al., 2005; Wang et al., 2015) with some of them being based on density functional theory (DFT) calculations (Biedermann et al., 2017a; Efthimiopoulos et al., 2019). However, up to now, no single crystal X-ray diffraction data was measured on  $\text{SrCO}_3$ , thus making it difficult to analyse structural changes at conditions of the Earth's mantle. At ambient pressure,  $\text{SrCO}_3$  has an aragonite-type crystal structure with space group  $Pm\bar{c}n$  (62). This crystal structure consists of planar trigonal  $[\text{CO}_3]^{2-}$  oxyanions parallel to (001). The cations (e.g.  $\text{Ca}^{2+}$  or  $\text{Sr}^{2+}$ ) are surrounded by six  $\text{CO}_3^{2-}$  ions in a trigonal prismatic arrangement parallel to the  $c$ -axis, whereas the carbonate groups are octahedrally surrounded by six cations. Sr atoms are nine-fold coordinated in the aragonite-type structure of  $\text{SrCO}_3$ . The higher coordination number of the cation correlates with a larger ionic radius in the aragonite-group minerals (e.g.  $\text{Sr}^{2+}$ ,  $\text{Ba}^{2+}$ ,  $\text{Pb}^{2+}$ ) compared to the calcite-group minerals, where the cation is only six-fold coordinated.

A few studies on the pressure-induced phase transitions in  $\text{SrCO}_3$  have been performed (Lin and Liu, 1997; Arapan and Ahuja, 2010; Wang et al., 2015; Biedermann et al., 2017a; Efthimiopoulos et al., 2019). They partially disagree regarding both the stability field as well as the structure of the high-pressure phases. Lin and Liu (1997) suggested a phase transition of  $\text{SrCO}_3$  to post-aragonite between 32 and 35 GPa by Raman spectroscopy and proposed a space group setting of  $P2_122$  for this phase. In comparison, Ono et al. (2005) observed a post-aragonite phase by powder X-ray diffraction of  $\text{SrCO}_3$  already at 14.5 GPa and at 40 GPa for  $\text{CaCO}_3$  (Ono, 2005). In a later study, Ono (2007) could show that the post-aragonite modification in  $\text{BaCO}_3$  has to be the same post-aragonite structure as of  $\text{CaCO}_3$  and  $\text{SrCO}_3$ , and had to be described in space group setting  $Pm\bar{m}n$ . More recently, Wang et al. (2015) reported a possible high-pressure induced transition at room temperature of  $\text{SrCO}_3$  from  $Pm\bar{c}n$  to  $P2_12_12$  between 22.2 and 26.9 GPa and of  $\text{BaCO}_3$  from  $Pm\bar{c}n$  to  $Pm\bar{m}n$  between 9.8 and 11.2 GPa. A similar pressure range for a transition to the post-aragonite phase in  $\text{SrCO}_3$  was proposed by Biedermann et al. (2017a) using experimental and computational Ra-



man spectroscopy. Later on, the boundary of this phase transition was extended to high-temperature conditions using mid-infrared absorbance and Raman spectroscopy in combination with DFT based calculations (Efthimiopoulos et al., 2019).

The variety of experimental conditions and techniques in the cited studies leads to results that are difficult to compare and sometimes even contradictory. To clarify these controversies we investigated the structure of pure  $\text{SrCO}_3$  up to 49 GPa at ambient temperature by powder and single crystal X-ray diffraction. This method allows us to precisely determine the crystal structure and to finally resolve the disagreement concerning the correct space group symmetry for the post-aragonite phase.

## 3.2 Methods

### 3.2.1 Synthesis of sample material

For powder X-ray diffraction experiments, we used commercial  $\text{SrCO}_3$  powder from Sigma Aldrich Chemical Company (99.995% purity). The single crystals of pure  $\text{SrCO}_3$  strontianite were grown in a Walker-type multi-anvil apparatus at 4 GPa and 1273 K for 24 h using the same  $\text{SrCO}_3$  powder as a starting material. The same synthesis has been used in previous studies (Biedermann et al., 2017a,b). The chemical composition of the synthesized sample was determined using a JEOL Hyperprobe JXA-8500F with a field emission cathode at the GFZ Potsdam. Analysis was conducted with an acceleration voltage of 15 kV, a 10 nA beam current and a  $<10 \mu\text{m}$  focused beam size. As reference standard materials we used dolomite for CaO and strontianite for SrO. The chemical analysis gave a concentration for  $\text{Ca}^{2+}$  below the detection limit of 130 ppm. In addition, the morphology and chemical composition of the single crystals were studied with scanning electron microscopy. Most of the synthesized single crystals of  $\text{SrCO}_3$  were twinned which is very common for aragonite-type carbonates as they exhibit pseudo-hexagonal morphologies with mirror plane (110) as twin plane (Bragg, 1924).

### 3.2.2 High-pressure X-ray diffraction experiments

#### Powder X-ray diffraction experiments

For high-pressure X-ray diffraction studies,  $\text{SrCO}_3$  powder was pressurized up to 49 GPa in a membrane-driven Mao-Bell-type diamond anvil cell (Mao, 1997) equipped with  $400 \mu\text{m}$  culets. Drilled pre-indented rhenium gaskets with hole diameter of  $200 \mu\text{m}$  served as sample chambers. The pressure transmitting medium (PTM) neon and a ruby sphere were loaded in addition to the sample. The pressure in the cell was measured with an online HR-2000 spectrometer (Ocean Optics) using the well-known  $R_1$ -line fluorescence band shift of ruby described by Mao et al. (1986) before and after each measurement where the average is used as experimental pressure. In addition, the equation of state of neon was used for additional pressure calibration (Hemley et al., 1989). The powder and single crystal XRD experiments were carried out at the beamline P02.2 at PETRA III, DESY (Hamburg) (Liermann et al., 2015). The X-ray

wavelength was  $\lambda = 0.2906 \text{ \AA}$  and the beam size was  $2 \times 2 \mu\text{m}^2$  at FWHM. For data collection, we used a fast flat panel detector XRD1621 from Perkin Elmer (2048 pixels  $\times$  2048 pixels with  $200 \times 200 \mu\text{m}^2$  pixel size). The two dimensional X-ray images were integrated using the Fit2D program (Hammersley, 2016). Refinements of the powder X-ray diffraction data were performed using the GSAS and EXPGUI software packages (Larson and Von Dreele, 2004).

### Single crystal X-ray diffraction experiments

In the case of high-pressure single crystal X-ray diffraction experiments, a small crystal of  $\text{SrCO}_3$  (25-30  $\mu\text{m}$  in diameter and 10  $\mu\text{m}$  thickness), a piece of tungsten ( $\sim 10 \mu\text{m}$  in diameter) and a ruby sphere ( $\sim 10 \mu\text{m}$  in diameter) were placed into a 150  $\mu\text{m}$  wide cylindrical chamber drilled in a pre-indented rhenium gasket. We used the same type of membrane-driven diamond anvil cells as in the case of powder samples but with smaller culet size of 300  $\mu\text{m}$ . Again, neon was loaded into the cell as a PTM. The single crystal was pressurized up to pressures of 26.3 GPa. A picture of the single crystal loaded into the cell at 25.9 GPa is shown in Fig. 3.1.

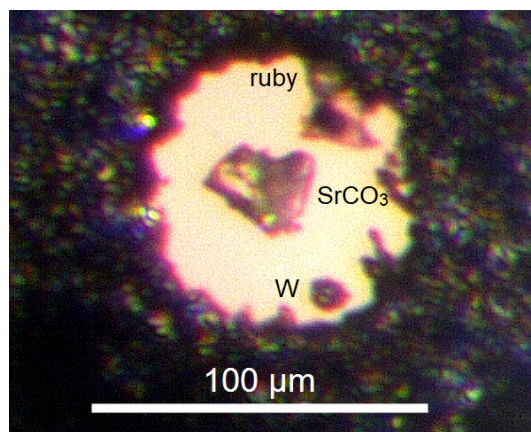


Figure 3.1: Diamond anvil cell at 25.9 GPa loaded with a single crystal of  $\text{SrCO}_3$ , neon as pressure-transmitting medium, a ruby sphere and a piece of tungsten.

The intensities of the reflections for the  $\text{SrCO}_3$  single crystal were integrated in steps of  $= 0.5^\circ$  over the entire opening angle of the cell of  $54^\circ$ . At each pressure point, additional X-ray diffraction wide images (from  $-27^\circ$  to  $+27^\circ$  in omega) were collected to confirm the data quality. A single crystal of orthoenstatite ( $(\text{Mg}_{1.93}\text{Fe}_{0.06})(\text{Si}_{1.93}\text{Al}_{0.06})\text{O}_6$ ,  $Pbca$ ,  $a = 8.8117(2) \text{ \AA}$ ,  $b = 5.18320(10) \text{ \AA}$ ,  $c = 18.2391(3) \text{ \AA}$ ), mounted in the cell without PTM and collected at the same experimental conditions, was used to calibrate the instrument model of the experimental geometry for the whole pressure range from 0 to 26.3 GPa (sample-to-detector distance, the detector's origin, offsets of the goniometer angles and rotation of the X-ray beam and the detector around the instrument axis) using *CrysAlis PRO* software (Rigaku Oxford Diffraction, 2019). The processing of XRD data (the unit cell determination and integration of the reflection intensities) was performed with the same software. Indexing of the unit cell was performed on about 30 reflections manually selected in the reciprocal space viewer (Ewald explorer imple-

mented in CrysAlisPro software). The reflections were selected in order to determine a 3D-lattice in the reciprocal space. The identified unit cell was then refined on the whole set of reflections at the end of the integration.

The selected grain of SrCO<sub>3</sub> was a non-merohedral twin with following twin law:

$$\begin{pmatrix} -0.46 & -0.54 & 0 \\ 1.46 & -0.46 & 0 \\ 0 & 0 & 1 \end{pmatrix} \quad (3.1)$$

The twin law corresponds to two differently oriented grains rotated by about 118° (at 0.5 GPa) around the common *c*-axis. Since the degree of overlap was small (less than 3% out of all reflections) no twin integration was applied in SrCO<sub>3</sub>-I and only the most intense grain (e.g. larger volume) was used for extraction of the reflection intensities. While *00l* reflections belonging to two grains should overlap, they were not present in the refinement since a metallic body of the diamond anvil cell have completely shadowed this type of the reflections. However, after the phase transition above 26 GPa we observed three twin domains related to a three-fold rotation along *a*-axis. Due to a high degree of overlap between reflections (about 10%) we applied simultaneous twin integration, however further structure solution and refinement was performed using the data collected from the most intense twin component. Empirical absorption correction was applied using spherical harmonics, implemented in the SCALE3 AB-SPACK scaling algorithm, which is included in the CrysAlisPro software. The crystal structures of aragonite-type SrCO<sub>3</sub>-I and post-aragonite SrCO<sub>3</sub>-II were determined by the dual space method using SHELXT (Sheldrick, 2015) software. After the structure solution most of the atoms were found and the remaining were located from a series of difference Fourier maps. The crystal structures were refined against F<sup>2</sup> on all data by full-matrix least squares with the SHELXL (Sheldrick, 2015) software. The amount of the collected data allowed us to refine the structures in anisotropic approximation. Details of crystal structure refinements of SrCO<sub>3</sub>-I and SrCO<sub>3</sub>-II are given in Tab. 3.3. The X-ray crystallographic coordinates have been deposited at the Inorganic Crystal Structure Database (ICSD) under deposition number CSD (1944794). These data can be obtained from CCDC's and FIZ Karlsruhe's free service for viewing and retrieving structures ([www.ccdc.cam.ac.uk/structures/](http://www.ccdc.cam.ac.uk/structures/)).

## 3.3 Results and Discussion

### 3.3.1 Phase transitions of SrCO<sub>3</sub> during compression

Powder XRD patterns in the  $2\theta$  range 3 - 22° were collected upon compression up to 49(2) GPa and are presented in Fig. 3.2. No other peaks except those of the sample and the pressure transmitting medium neon (Ne) were observed. Peaks corresponding to the sample at ambient conditions were well indexed to the low-pressure aragonite structure *Pmcn* with the lattice parameters  $a = 5.126(1)$  Å,  $b = 8.472(2)$  Å,  $c = 6.061(1)$  Å and are in agreement with the literature (Wang et al., 2015; Villiers, 1971; Arapan and Ahuja, 2010; Antao and Hassan, 2009). As shown in Fig. 3.2, reflections of SrCO<sub>3</sub> shift

to higher angles with increasing pressure and no structural transformation has occurred until 25.9(3) GPa. A Rietveld refinement for the low-pressure aragonite-type  $\text{SrCO}_3$ -I phase until a pressure of 15.1(2) GPa was used to calculate the lattice parameters and interatomic distances. Above 15 GPa, the broadening of the peaks does not allow reliable refinement of the structure, hence the method of Le Bail fitting was applied in order to derive lattice parameters from powder-XRD measurements between 15 and 49 GPa. Some reflections of  $\text{SrCO}_3$ -I disappear and new peaks appear at 28.5(3) GPa which could not be indexed using the  $Pm\bar{c}n$ -metric of  $\text{SrCO}_3$ . These new peaks increase in intensity at higher pressures and indicate that  $\text{SrCO}_3$  has transformed into a post-aragonite phase.

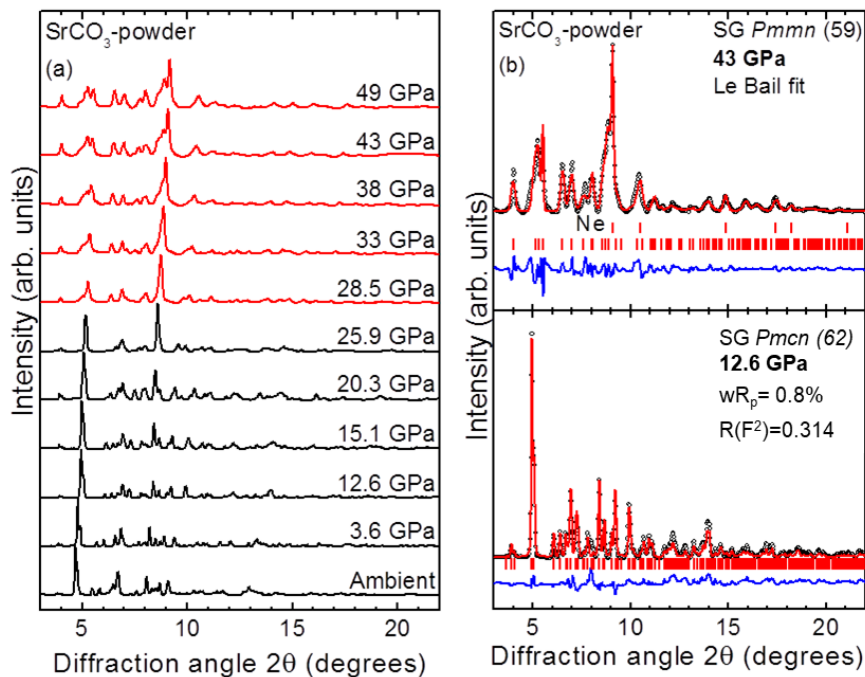


Figure 3.2: (a) Powder XRD patterns of  $\text{SrCO}_3$  at various pressures ( $T = 300$  K,  $\lambda = 0.2906$  Å). The different phases are indicated by black ( $\text{SrCO}_3$ -I) and red ( $\text{SrCO}_3$ -II) colors. (b) Refined XRD patterns for the aragonite-type  $\text{SrCO}_3$ -I phase (12.6 GPa, Rietveld, bottom) and for  $\text{SrCO}_3$ -II (43 GPa, Le Bail, top). Dots correspond to the measured spectra and the red solid lines represent the best refinements. The difference curves between the measured and the refined patterns are depicted too (blue curves). Vertical ticks mark the Bragg peak positions.

Our observations are in good agreement with powder X-ray diffraction studies from Wang et al. (2015) where a phase transition in  $\text{SrCO}_3$  was observed between 22.2 and 26.9 GPa. In contrast, Ono et al. (2005) proposed the presence of a post-aragonite phase in  $\text{SrCO}_3$  already at 14.5 GPa and at high temperature which was also indexed with  $Pm\bar{c}n$  structure. For  $\text{CaCO}_3$ , a phase transformation into post-aragonite was observed at 40 GPa (Ono, 2005) and for  $\text{BaCO}_3$  at 10 GPa (Ono, 2007; Townsend et al., 2013). Our results for  $\text{SrCO}_3$  lie in between these values and comply with the pressure-homologue rule according to which isostructural compounds often exhibit similar phase

transitions but at lower pressures with increasing ionic radius (Shannon, 1976).

Single crystal X-ray diffraction experiments were performed from 0 to 26.3 GPa. In agreement with our results from powder X-ray diffraction, reflections of the single crystal can be unambiguously indexed with the same aragonite-type orthorhombic cell  $Pm\bar{c}n$  between 0 and about 21 GPa. Results taken at 26.3 GPa clearly indicate that  $\text{SrCO}_3$  has fully transformed into the more stable post-aragonite phase with space group  $Pm\bar{m}n$ . A selected XRD pattern derived from a wide scan of the single crystal at this pressure is shown in Fig. 3.3. Additional peaks are indexed for rhenium, tungsten and the pressure transmitting medium neon. Fitted  $d$ -spacings from this study at 26.3 GPa are given in Tab. 3.1 and are in good agreement with previous results from Ono et al. (2005) at 14.5 GPa.

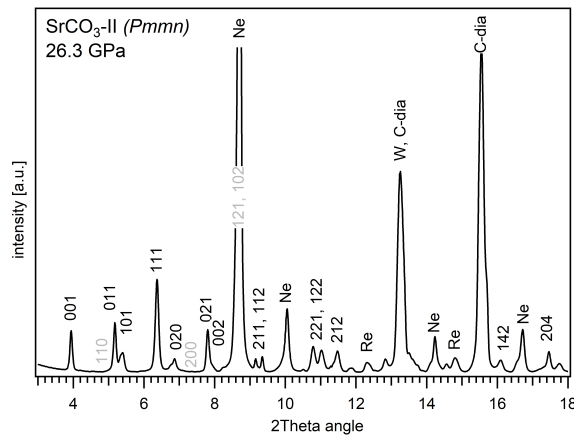


Figure 3.3: A representative XRD pattern of post-aragonite  $\text{SrCO}_3$ -II obtained from single crystal data at 26.3 GPa derived from continuous  $\omega$ -rotation of the DAC from  $-27^\circ$  to  $+27^\circ$  (wide scan image). Reflections corresponding to  $\text{SrCO}_3$ -II that are absent (low energy or overlaid) are marked in grey.

A comparison between the low-pressure phase and the post-aragonite phase is shown in Fig. 3.4. One can see that  $a$ ,  $b$  and  $c$  axis in  $\text{SrCO}_3$ -I ( $Pm\bar{c}n$ ) correspond to  $b$ ,  $c$  and  $a$  axis in  $\text{SrCO}_3$ -II ( $Pm\bar{m}n$ ). The phase transition from  $\text{SrCO}_3$ -I ( $Pm\bar{c}n$ ) to  $\text{SrCO}_3$ -II ( $Pm\bar{m}n$ ) is a first-order phase transition (Ono, 2005) and is likely driven by a shift of half of  $\text{Sr}^{2+}$  cations and  $\text{CO}_3^{2-}$  anions along the  $[100]$  direction. At the same time, a shift by half of the translation of all  $\text{Sr}^{2+}$  cations and  $\text{CO}_3^{2-}$  anions accompanied with a small displacement along  $[001]$  occurs such that the cations and anions line up in one plane parallel to  $(001)$ . These shifts result in more dense packing of cations and anions and in the increase of the  $\text{Sr}^{2+}$  coordination number from 9 to 12.

### 3.3.2 Compressibility of strontianite ( $\text{SrCO}_3$ -I) and $\text{SrCO}_3$ -II

The refined unit cell parameters for the low-pressure phase strontianite ( $\text{SrCO}_3$ -I) and for the high-pressure phase  $\text{SrCO}_3$ -II obtained at different pressures are listed in Tab. 3.2 and 3.3. The evolution of the lattice parameters with pressure is given in Fig. 3.5. Upon compression from 0.5 to 26 GPa, the axes of  $\text{SrCO}_3$ -I change anisotropically with the

Table 3.1: Observed  $d$ -spacings of the post-aragonite phase SrCO<sub>3</sub>-II at 26.3 GPa and room temperature in comparison with those from previous work (Ono et al., 2005).

hkl	<i>this study</i>	<i>Ono et al. (2005)</i>
	$d_{obs}$ [Å] (26.3 GPa)	$d_{obs}$ [Å] (14.5 GPa)
001	4.2320	4.3106
110	3.3436	3.4197
011	3.2136	3.2750
101	3.0966	3.1644
111	2.6236	2.6803
020	2.4695	2.5210
200	2.2715	2.3260
021	2.1329	2.0477
121	1.9307	1.9720
102	1.9181	1.9545
211	1.5849	1.8964

highest compressibility found in direction of the  $c$ -axis, that is perpendicular to the carbonate groups. This anisotropic compression scheme is typical for aragonite-type carbonates (Townsend et al., 2013; Zhang et al., 2013) and reflects the incompressibility of the CO<sub>3</sub> groups in the (001)-plane compared to the SrO<sub>9</sub> polyhedra. The calculated lattice parameters for SrCO<sub>3</sub>-I in this study exhibit quasi-linear pressure-dependence with no obvious discontinuities. A linear fit of the given  $a/a_0$ ,  $b/b_0$  and  $c/c_0$  values against pressure yields a linear compressibility of  $\beta_a$ ,  $\beta_b$  and  $\beta_c$  with  $1.85(2)\cdot 10^{-3}$  GPa<sup>-1</sup>,  $2.62(7)\cdot 10^{-3}$  GPa<sup>-1</sup> and  $6.4(5)\cdot 10^{-3}$  GPa<sup>-1</sup>, respectively, and agrees well with data from Wang et al. (2015).

Across phase transition at about 26 GPa, the length of the  $c$ -axis (=  $a$  in SrCO<sub>3</sub>-II) sharply decreases by  $\sim 10$  % whereas the  $b$ -axis (=  $c$  in SrCO<sub>3</sub>-II) increases. The lattice parameters of SrCO<sub>3</sub>-II are further decreasing with pressure but at lower rates, indicating that the structure of SrCO<sub>3</sub>-II is less compressible than SrCO<sub>3</sub>-I. The linear compressibilities of the high-pressure phase are found to be  $2.223(7)\cdot 10^{-3}$  GPa<sup>-1</sup> for the  $a$ -axis,  $1.29(8)\cdot 10^{-3}$  GPa<sup>-1</sup> for the  $b$ -axis and  $1.05(4)\cdot 10^{-3}$  GPa<sup>-1</sup> for the  $c$ -axis.

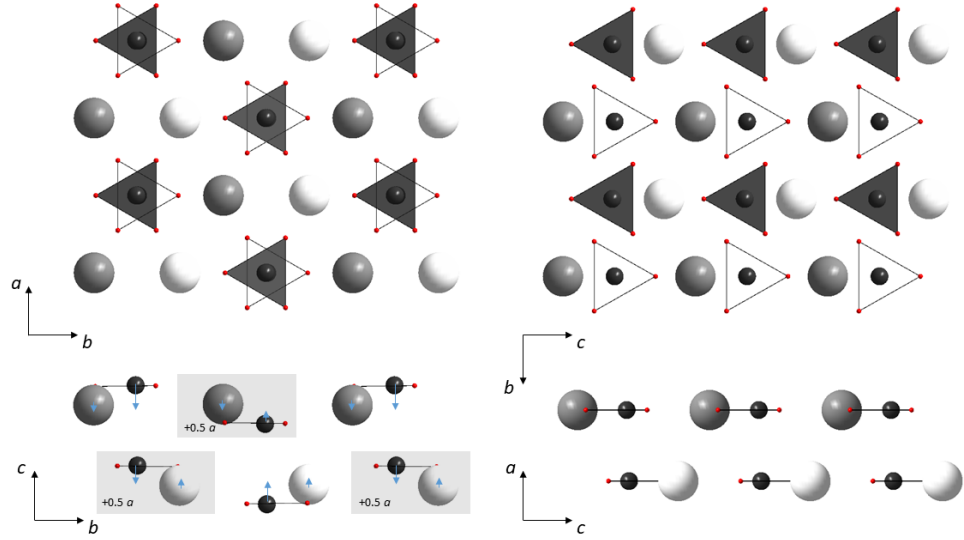


Figure 3.4: Crystal structures of  $\text{SrCO}_3\text{-I}$  (left) and  $\text{SrCO}_3\text{-II}$  (right). Axis  $a$ ,  $b$  and  $c$  in aragonite ( $Pmcn$ ) correspond to  $b$ ,  $(2)c$  and  $a$  axis in post-aragonite ( $Pmnn$ ). Small-sized red spheres correspond to oxygen atoms, black spheres are carbon,  $\text{CO}_3^{2-}$  are additionally highlighted as white and dark grey triangles, white and dark grey spheres are  $\text{Sr}^{2+}$ . Dark grey units (spheres and triangles) and white ones have different position along  $c$ -axis in  $\text{SrCO}_3\text{-I}$  and along  $a$ -axis in  $\text{SrCO}_3\text{-II}$ . During the phase transition from aragonite to post-aragonite half of  $\text{Sr}^{2+}$  and  $\text{CO}_3^{2-}$  ions highlighted by grey rectangles shift by  $0.5[100]$  and then the ions line up in  $(001)$  plane (the directions of displacements are shown by small blue arrows).

Table 3.2: Pressure dependence of lattice parameters of  $\text{SrCO}_3$  at room temperature derived from powder X-ray diffraction.

P[GPa]	$a[\text{\AA}]$	$b[\text{\AA}]$	$c[\text{\AA}]$	$V[\text{\AA}]^3$
<b><math>\text{SrCO}_3\text{-I}</math> in <math>Pmcn</math></b>				
0.0001	5.126(1)	8.472(2)	6.061(1)	263.21(15)
3.6(1)	5.057(1)	8.358(2)	5.840(1)	246.81(15)
12.6(2)	4.978(1)	8.182(2)	5.419(1)	220.73(15)
15.1(2)	4.957(1)	8.121(2)	5.337(1)	216.94(15)
20.3(2)	4.929(1)	8.017(2)	5.186(1)	209.85(15)
25.9(3)	4.892(1)	7.878(2)	5.037(1)	202.32(15)
<b><math>\text{SrCO}_3\text{-II}</math> in <math>Pmnn</math></b>				
28.5(3)	4.521(1)	4.918(1)	4.219(1)	93.79(8)
33(1)	4.459(1)	4.879(1)	4.194(1)	91.25(8)
38(1)	4.393(1)	4.845(1)	4.171(1)	88.79(8)
43(1.5)	4.325(1)	4.811(1)	4.151(1)	86.39(8)
49(2)	4.244(1)	4.782(1)	4.127(1)	83.75(8)

Errors in parentheses are one standard deviation.

Table 3.3: Details of single crystal structure refinements of SrCO<sub>3</sub>-I and SrCO<sub>3</sub>-II between 0.5 and 26.3 GPa.

P [GPa]	0.5(6)	5.2(4)	14.6(6)	20.6(4)	22.7(5)	25.9(4)	26.3(5)
<b>crystal data</b>				<b>SrCO<sub>3</sub>-I</b>			<b>SrCO<sub>3</sub>-II</b>
space group				<i>Pmcn</i> (No.62)			<i>Pmmn</i> (No.59)
<i>a</i> [Å]	5.1034(4)	5.0429(5)	4.9559(2)	4.9059(5)	4.8861(4)	4.8618(7)	4.543(2)
<i>b</i> [Å]	8.4056(8)	8.2858(9)	8.1986(5)	8.1932(8)	8.2025(8)	8.2078(12)	4.939(2)
<i>c</i> [Å]	6.0180(12)	5.7657(15)	5.3755(7)	5.1596(15)	5.0771(15)	4.985(2)	4.232(2)
<i>V</i> [Å <sup>3</sup> ]	258.15(6)	240.92(7)	218.41(3)	207.39(7)	203.48(7)	198.93(9)	94.97(8)
<i>Z</i>	4	4	4	4	4	4	2
<b>refinement</b>							
$\theta$ range for data collection(°)	2.358 to 16.704	2.413 to 17.989	2.501 to 16.767	2.553 to 16.882	2.574 to 17.052	2.599 to 16.950	2.595 to 15.947
Completeness to $d=0.8$ Å, %	0.492	0.602	0.536	0.538	0.570	0.541	0.541
Index ranges	-6 < <i>h</i> < 9	-9 < <i>h</i> < 9	-8 < <i>h</i> < 9	-9 < <i>h</i> < 7	-8 < <i>h</i> < 9	-5 < <i>h</i> < 5	-4 < <i>h</i> < 5
	-10 < <i>k</i> < 15	-15 < <i>k</i> < 15	-15 < <i>k</i> < 12	-15 < <i>k</i> < 12	-15 < <i>k</i> < 14	-15 < <i>k</i> < 13	-7 < <i>k</i> < 8
	-7 < <i>l</i> < 7	-7 < <i>l</i> < 7	-6 < <i>l</i> < 6	-5 < <i>l</i> < 5	-5 < <i>l</i> < 5	-5 < <i>l</i> < 5	-5 < <i>l</i> < 6
Goodness of fit on F <sup>2</sup>	1.064	1.015	0.943	0.989	1.037	1.033	1.369
Reflections collected	485	687	542	400	640	501	256
Independent reflections	355	421	325	289	319	299	142
No. of parameters	29	29	29	29	29	29	19
Final R indices [ <i>I</i> > 2σ( <i>I</i> )], <i>R</i> <sub>1</sub> / <i>wR</i> <sub>2</sub>	0.0288 / 0.0696	0.0232 / 0.0611	0.0240 / 0.0629	0.0322 / 0.0951	0.0383 / 0.1050	0.0358 / 0.0944	0.0708 / 0.1922
R indices (all data) <i>R</i> <sub>1</sub> / <i>wR</i> <sub>2</sub>	0.0316 / 0.0739	0.0266 / 0.0654	0.0272 / 0.0677	0.0379 / 0.1020	0.0496 / 0.1087	0.0509 / 0.1112	0.0759 / 0.1955
<i>R</i> <sub>int</sub>	0.013	0.0164	0.0201	0.0170	0.0474	0.022	0.0140



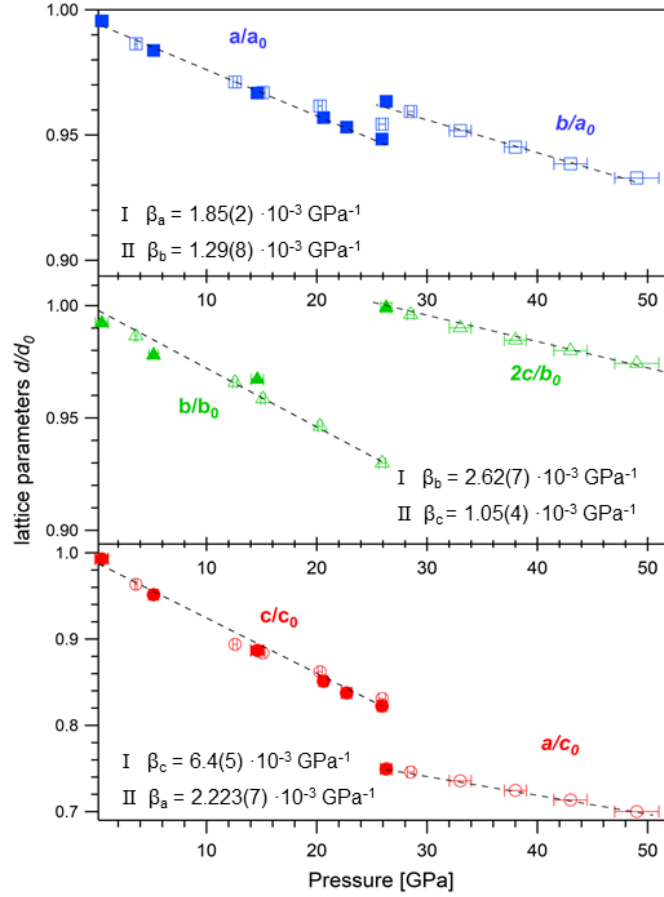


Figure 3.5: Compressibility of the unit cell parameters  $\beta_a$ ,  $\beta_b$  and  $\beta_c$  for SrCO<sub>3</sub>-I and SrCO<sub>3</sub>-II. Open symbols are data derived from powder samples and solid symbols are from single crystal X-ray diffraction. Note that the  $a$ ,  $b$  and  $c$  axis in SrCO<sub>3</sub>-I ( $Pm\bar{c}n$ ) correspond to  $b$ ,  $(2)c$  and  $a$  axis in SrCO<sub>3</sub>-II ( $Pmmn$ ). The lattice parameters at ambient conditions are  $a_0 = 5.126(1)$  Å,  $b_0 = 8.472(2)$  Å and  $c_0 = 6.061(1)$  Å.

The pressure dependence of the molar volume for SrCO<sub>3</sub>-I and SrCO<sub>3</sub>-II is shown in Fig. 3.6a. An f-F-plot (Fig. 3.6b) indicates that a third order Birch-Murnaghan equation of state is necessary to fit the P-V-data of SrCO<sub>3</sub> which is expressed as (Birch, 1947; Angel et al., 2014):

$$P(\text{GPa}) = 3K_0 f_E \left[ (1 + 2f_E)^{\frac{5}{2}} \left( 1 + \frac{3}{2}(K' - 4)f_E \right) \right] \quad (3.2)$$

with  $f_E$  as the Eulerian strain given by

$$f_E = \frac{1}{2} \left[ (V_0/V)^{\frac{2}{3}} - 1 \right] \quad (3.3)$$

and where  $V_0$ ,  $K_0$  and  $K'$  are the (molar) volume, the isothermal bulk modulus and its pressure derivative at room pressure, respectively. The program *EosFit7c* (Angel et al., 2014) was used to fit the data. For the low-pressure phase strontianite (SrCO<sub>3</sub>-I), the following EoS parameters were calculated:  $V_0 = 259.8(3)$  Å<sup>3</sup>,  $K_0 = 62.7(6)$  GPa and  $K'_0 = 3.2(1)$ . Values for  $K_0$  are in good agreement with previous studies

on strontianite (Wang et al., 2015; Biedermann et al., 2017b). The fit results for the high-pressure phase SrCO<sub>3</sub>-II yield  $V_0 = 115(1) \text{ \AA}^3$ ,  $K_0 = 103(10) \text{ GPa}$  and  $K'_0 = 2.3(6)$ , respectively. As indicated in Tab. 3.4, these values are in between the values for BaCO<sub>3</sub>-II with  $K_0 = 84(4) \text{ GPa}$  (Ono, 2007) and for post-aragonite CaCO<sub>3</sub> with 127(14) GPa (Ono, 2005) thus confirming a dependency on the cation radius.

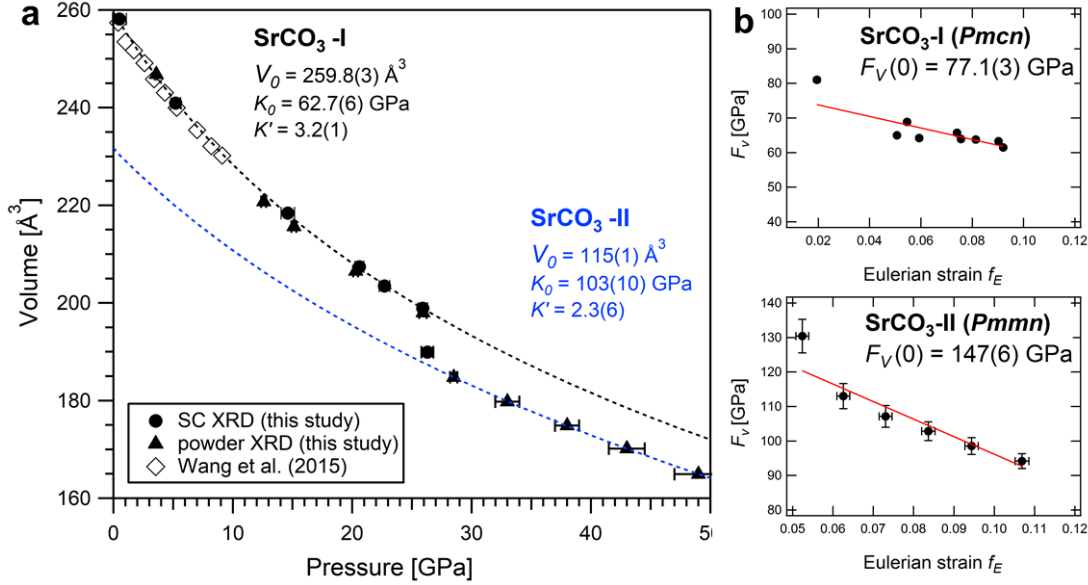


Figure 3.6: a. Isothermal compression of the molar volume plotted together with the best fit after Birch Murnaghan equation of state for SrCO<sub>3</sub>-I (black dashed line) and SrCO<sub>3</sub>-II (blue dashed line). Open symbols are data from Wang et al. (2015) (with methanol-ethanol as PTM) and solid symbols are from this study. Note that for SrCO<sub>3</sub>-II the volume is doubled with respect to two times of the unit cell volume. b. Normalized pressure ( $F_V$ ) as a function of the Eulerian strain ( $f$ ) for SrCO<sub>3</sub>-I and SrCO<sub>3</sub>-II, respectively. The red solid lines are the weighted linear fit through the data at  $P > 3.6 \text{ GPa}$ .

### 3.3.3 Crystal structure of post-aragonite SrCO<sub>3</sub>-II

A detailed refinement of the high-pressure phase was carried out on single crystal X-ray diffraction data at 26.3 GPa. We were able to refine the structure in anisotropic approximation. Fractional atomic coordinates and anisotropic displacement parameters are shown in Tab. 3.5. At this pressure, the post-aragonite phase of SrCO<sub>3</sub> crystallizes in an orthorhombic unit cell with space group *Pmmn* (No. 59, origin choice 2) and with the following unit cell parameters:  $a = 4.543(2) \text{ \AA}$ ,  $b = 4.939(2) \text{ \AA}$ ,  $c = 4.232(2) \text{ \AA}$ ,  $V = 94.97(8) \text{ \AA}^3$ . The atomic arrangement in post-aragonite SrCO<sub>3</sub>-II adopts the structure type of the orthorhombic high-pressure form of RbNO<sub>3</sub>-V (Kalliomäki and Meisalo, 1979). The Sr ion is located on a Wyckoff position  $2b$ , C is on a  $2a$  position, while O1 and O2 atoms occupy  $2a$  and  $4e$  positions, respectively (Tab. 3.3). The same crystal structure was already proposed for high-pressure modifications of CaCO<sub>3</sub> (Ono, 2005) and for BaCO<sub>3</sub> (Ono, 2007; Townsend et al., 2013). However, there are also XRD data

Table 3.4: Comparison of the different literature data for aragonite-type ( $Pm\bar{c}n$ ) and post-aragonite ( $Pm\bar{m}n$  or  $P2_12_12$ ) carbonates at ambient conditions.

	$V_0$ [ $\text{\AA}^3$ ]	$K_0$ [GPa]	$K'_{T_0}$	References
<b>aragonite-type carbonates</b>				
CaCO <sub>3</sub>	227.5(8)	65(4)	4(fixed)	Martinez et al. (1996)
	227.2(10)	67.1(63)	4.7(8)	Ono (2005)
	227.2(10)	73.1(22)	4(fixed)	Ono (2005)
SrCO <sub>3</sub> -I	258.4(3)	62(1)	4(fixed)	Wang et al. (2015)
	258.4(1)	64(4)		Biedermann et al. (2017b)
	259.8(3)	62.7(6)	3.2(1)	This work
BaCO <sub>3</sub>	303.8(1)	50.4(9)	1.9(4)	Holl et al. (2000)
	304.1(3)	44.3(8)	4(fixed)	Holl et al. (2000)
	319.3	47.2	2.4	Ono et al. (2008)
	304.8(3)	48(1)	4(fixed)	Wang et al. (2015)
<b>post-aragonite carbonates</b>				
CaCO <sub>3</sub> post-aragonite	98(2)	127(14)	4(fixed)	Ono (2005)
	102(3)	90(13)	4.94	Oganov et al. (2006)
	109.74	42(7)	7(1)	Oganov et al. (2006)
SrCO <sub>3</sub> -II	115(1)	103(10)	2.3(6)	This work
	111(2)	101(16)	4(fixed)	Ono et al. (2005)
BaCO <sub>3</sub> post-aragonite	129.0(7)	84(4)	4(fixed)	Ono (2007)
	128.1(5)	88(2)	4.8(3)	Townsend et al. (2013)

Table 3.5: Atomic coordinates and anisotropic displacement parameters  $U_{ij}$  [ $\text{\AA}^2 \cdot 10^3$ ] with  $U_{ij}(i \neq j) = 0$  for post-aragonite SrCO<sub>3</sub>-II at 26.3 GPa (space group  $Pm\bar{m}n$ ).

Site	Wyckoff position	x	y	z	$U_{11}$	$U_{22}$	$U_{33}$
Sr	$2b$	0.25	-0.25	0.6186(4)	0.036(2)	0.0096(8)	0.0152(10)
C	$2a$	0.25	0.25	0.991(4)	0.04(2)	0.010(5)	0.007(8)
O1	$2a$	0.25	0.25	0.682(3)	0.029(12)	0.005(4)	0.011(6)
O2	$4e$	0.25	0.025(2)	0.146(2)	0.026(11)	0.012(3)	0.009(4)

suggesting a trigonal symmetry for the post-aragonite phase in CaCO<sub>3</sub> (Santillán and Williams, 2004) and in BaCO<sub>3</sub> (Holl et al., 2000). When adapting the trigonal symmetry reported by Holl et al. (2000) some diffraction peaks of the high-pressure phase of SrCO<sub>3</sub> could not be indexed. We conclude that for SrCO<sub>3</sub> only an orthorhombic description of the crystal structure for the post-aragonite phase is possible.

The  $Pm\bar{c}n$  to  $Pm\bar{m}n$  transition of SrCO<sub>3</sub> is characterized by an increase of the coordination of Sr<sup>2+</sup> from 9 to 12. The relative change in density across this transition is about 5%. The Sr-O interatomic distances vary from 2.418(10) to 2.718(6) Å. Six oxygen atoms with shorter distances (2.418(10), 2.4842(19) and 2.613(10) Å) are located on a plane intersecting Sr, parallel to the  $bc$ -plane. Three oxygen atoms are located below the plane and three atoms above. Note, that in the  $Pm\bar{m}n$ -description, the planar carbonate groups are aligned parallel to the (100)-plane while instead in the

low-pressure  $Pm\bar{c}n$ -structured  $\text{SrCO}_3$ -I phase they are aligned parallel to the (001)-plane. C-O distances in the high-pressure phase of  $\text{SrCO}_3$  are 1.291(13) and 1.31(2) Å and identical within errors with data from Ono (2005) for  $\text{CaCO}_3$ .

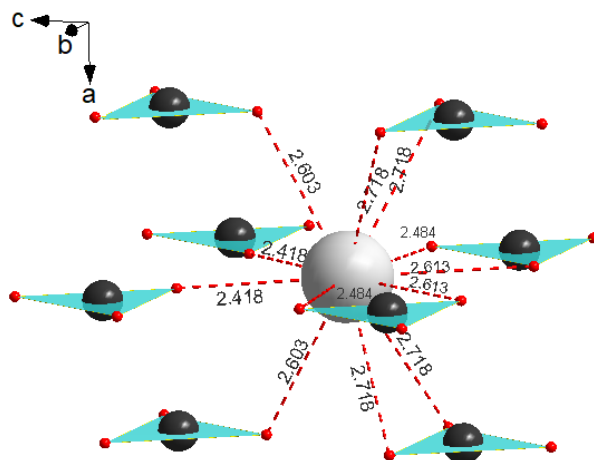


Figure 3.7: A fragment of  $\text{SrCO}_3$ -II crystal structure at 26.3 GPa showing  $\text{Sr}^{2+}$  ion (light grey sphere) surrounded by eight triangular  $\text{CO}_3^{2-}$  anions (C - dark grey spheres, O - red spheres).

### 3.4 Conclusions

Powder X-ray diffraction in combination with single-crystal X-ray diffraction was used for the first time to determine the high-pressure phase behaviour of  $\text{SrCO}_3$  up to 49 GPa at ambient temperature. We observed a transformation from strontianite ( $Pm\bar{c}n$ ) to post-aragonite  $\text{SrCO}_3$ -II ( $Pm\bar{m}n$ ) at around 26 GPa which is in agreement with previous studies that used other techniques, e.g. Raman spectroscopy to detect a phase transition in  $\text{SrCO}_3$  (Biedermann et al., 2017a). We present reliable structural information for post-aragonite  $\text{SrCO}_3$ -II including interatomic distances and anisotropic displacement parameters and finally resolve the discussion about the correct space group setting of the post-aragonite phase in  $\text{SrCO}_3$ . Our results further confirm a bulk modulus of 62.7(6) GPa for strontianite ( $\text{SrCO}_3$ -I) and provide first experimental data for the equation of state for the high-pressure phase  $\text{SrCO}_3$ -II with  $V_0 = 115(1) \text{ \AA}^3$ ,  $K_0 = 103(10) \text{ GPa}$  and  $K'_0 = 2.3(6)$ .

## Chapter 4

# Results on carbonate-silicate reaction experiments

In order to learn about carbonate stability and reactions in presence of silicates, experiments on Sr-, La- and Eu-doped carbonates as well as on the end members calcite ( $\text{CaCO}_3$ ) and strontianite ( $\text{SrCO}_3$ ) in contact with silicates were performed. A combination of XRD and XRF was used to study structural changes as well as the chemical behaviour of the trace elements during reaction at high pressure and high temperature. In the first section, we present X-ray diffraction data and provide further insights to the reactivity of carbonates and the formation of new phases at mantle conditions. According to the chemical systems under investigation, our XRD results are divided into two main groups: silicates of the pseudo-binary system  $(\text{Mg,Fe})\text{SiO}_3$ – $(\text{Mg,Fe})_2\text{SiO}_4$  reacting with (a) (doped)  $\text{CaCO}_3$  and (b) with  $\text{SrCO}_3$ . In the second section, results are presented on the elemental fractionation during reaction based on synchrotron-radiation induced XRF of selected trace elements. Further experimental details have been described in section 2.4.2.

### 4.1 Phase stability of $\text{CaCO}_3$ and $\text{SrCO}_3$ in presence of mantle silicates

#### 4.1.1 XRD measurements on reactions between $\text{CaCO}_3$ (:M) and silicates at conditions of the Earth's mantle

##### Experiments with $\text{CaCO}_3$ : $\text{Sr}^{2+}$ and $\text{MgSiO}_3$ glass as starting materials

First experiments using a powder mixture of pure  $\text{MgSiO}_3$  glass and Sr-doped  $\text{CaCO}_3$  carbonate (NB12) loaded into a BX90 cell have been performed at beamline ID27, at the ESRF in Grenoble, France. The powder mixture itself served as a PTM and no ruby was loaded into the cell. Rhenium was used as a gasket material. We calibrated the pressure using the laser-induced fluorescence of the diamond before and after the run. In addition, the equation of state of Re was used for additional pressure calibration during heating. The cell was pressurized to 35 GPa and then laser-heated to a maximum temperature of 1850 K (DAC19). We increased the temperature in small steps of about

100 K and waited for several minutes until the laser spot has stabilized. We then collected single point XRD images during heating at the center of the hot spot to follow the structural changes of the phases present. The acquisition time was 10 s for each temperature step. The photon energy was 33.2 keV corresponding to a wavelength  $\lambda = 0.3738 \text{ \AA}$ . Results from run DAC19 are displayed in Fig. 4.1 and are listed in Tab. 4.1. Recovery of the sample material after temperature quench and pressure release was not successful and we were not able to perform any TEM-imaging on this particular run.

Table 4.1: P-T-conditions and run products of experiments using amorphous (am)  $\text{MgSiO}_3$  glass and  $\text{CaCO}_3\text{:Sr}^{2+}$  as starting compositions (DAC18 and DAC19). Analytical methods that were used are: Synchrotron-based X-ray diffraction during heating (*in-situ* XRD) and X-ray diffraction mapping only before and after heating (XRD-map).

<b>starting material: amorphous <math>\text{MgSiO}_3</math> glass + <math>\text{CaCO}_3\text{:Sr}^{2+}</math></b>				
run	experiment	P [GPa]	T [K]	run products
<i>XRD-map</i>				
DAC18	DAC18_01	36(2)	300	$\text{MgSiO}_3$ (am) + cc-VII
	DAC18_02	36(2)	2000(100)	brd + Ca-Pv + post-aragonite + mgs + stv + MgO
	DAC18_03	36(2)	2500(100)	brd + Ca-Pv + CaO + MgO
	DAC18_04	36(2)	3000(300)	brd + MgO (+CaO + $\text{CO}_2$ )
<i>in-situ XRD measurements</i>				
DAC19	DAC19_01	35(1)	300	$\text{MgSiO}_3$ (am) + cc-VII
	DAC19_02	35(1)	1510(30)	$\text{MgSiO}_3$ (am) + cc-VII
	DAC19_03	35(1)	1590(30)	$\text{MgSiO}_3$ (am) + cc-VII
	DAC19_04	40(1)	1720(40)	brd + Ca-Pv + post-aragonite + stv
	DAC19_05	40(1)	1800(50)	brd + Ca-Pv + post-aragonite + stv
	DAC19_06	40(1)	1850(50)	brd + Ca-Pv + post-aragonite + stv

Abbreviations: brd = bridgmanite, Ca-Pv =  $\text{CaSiO}_3$ -perovskite, cc = calcite, mgs = magnesite, stv = stishovite

At room temperature and 35 GPa, the starting carbonate has transformed into calcite-VII and a strong broadening of the carbonate reflections is present which implies the presence of non-hydrostatic conditions. After the first few minutes of heating at a temperature of about 1700 K, the diffraction patterns changed substantially and the  $\text{MgSiO}_3$ -glass started to crystallize into the orthorhombic perovskite phase bridgmanite and the intensities of the reflections further increased with increasing temperature. During heating, the pressure in the cell increases from 35 GPa to 40 GPa due to isochoric thermal pressure and calcite-VII transforms into  $\text{CaCO}_3$  post-aragonite, which is the stable phase of  $\text{CaCO}_3$  at these P-T-conditions. Our results in run DAC19 thus confirm an existing phase boundary between calcite-VII and post-aragonite which has been previously published (Bayarjargal et al., 2018; Li et al., 2018). Finally, a reaction between  $\text{CaCO}_3$  and the stable phase bridgmanite is indicated by the appearance of new peaks at 1720 K which can be assigned to the cubic  $\text{CaSiO}_3$ -perovskite phase and to magnesite. In addition to bridgmanite,  $\text{CaSiO}_3$ -perovskite and the carbonates, diffraction peaks belonging to stishovite are also visible. As the starting silicate mate-

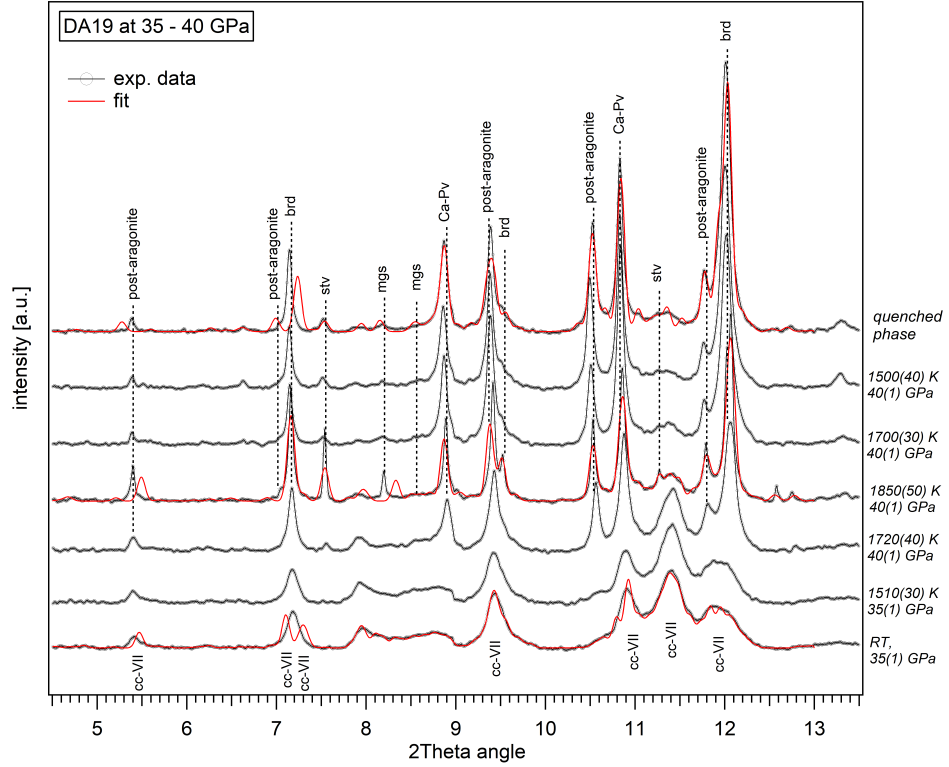


Figure 4.1: Selected XRD patterns of run DAC19 ( $\text{MgSiO}_3$  (am) +  $\text{CaCO}_3\text{:Sr}^{2+}$ ) taken at 35-40 GPa during heating. Fitted spectra at room temperature (RT) and 35 GPa, at a temperature of 1850 K and 40 GPa and after temperature quench are highlighted in red. Abbreviations for the phases are explained in Tab. 4.1.

rial is free of iron and no MgO was detected during heating which could be evidence for decomposition of  $\text{MgSiO}_3$  ( $\text{MgSiO}_3 \rightarrow \text{MgO} + \text{SiO}_2$ ), the occurrence of stishovite at high temperature and in the temperature quenched run products remains unclear. The starting carbonate material also contained trace amounts of Sr with an initial composition of  $\text{Ca}_{0.976}\text{Sr}_{0.024}\text{CO}_3$ . XRD images during heating do not show any evidence for Sr-bearing phases like SrO or  $\text{SrSiO}_3$ -perovskite. According to the sample geometry consisting of a powder mixture, the application of spatially resolved XRF is not feasible. Therefore, the behaviour of the trace element Sr remains unclear and the question whether Sr is still incorporated into the carbonate or might be distributed into the newly formed  $\text{CaSiO}_3$ -perovskite phase could not be answered in this run.

Additional experiments were performed in run DAC18 at 36 GPa with the same powder mixture as used in run DAC19. The sample assemblage was laser-heated at three different spots to temperatures of about 2000 K, 2500 K and 3000 K, respectively. An XRD-map of the heated cell at 36 GPa with a size of  $70 \mu\text{m} \times 100 \mu\text{m}$  was measured with acquisition settings of 3 s per point and a step size of  $2 \mu\text{m} \times 2 \mu\text{m}$  (see Fig. 4.2). XRD-patterns taken from the XRD-map at the center of each heating spot are shown in Fig. 4.3 and document a reaction between  $\text{CaCO}_3\text{:Sr}^{2+}$  and  $\text{MgSiO}_3$  at around 2000 K by the appearance of reflections corresponding to  $\text{CaSiO}_3$ -perovskite and magnesite. Again, stishovite was detected after heating to a temperature of 2000 K and this time

evidence is also found for the formation of MgO. This observation supports the hypothesis that the starting material consisting of  $\text{MgSiO}_3$  glass has partially decomposed into  $\text{MgO} + \text{SiO}_2$  prior to the formation of bridgmanite. Above this temperature, e.g. at 2500 K and at 3000 K, reflections corresponding to CaO B2-phase and MgO were observed in the temperature quenched run products and no magnesite was detected.

Figure 4.2: XRD-map plot of  $\text{CaSiO}_3$ -perovskite in run DAC18 after heating. Selected  $2\theta$ -range for building the map is marked in red in the XRD pattern at the bottom. The cell was heated in three different spots (yellow circles) up to a temperature of 2000(100) K (spot 1), 2500(100) K (spot 2) and 3000(300) K (spot 3). XRD patterns at the center of each hot spot are extracted and are shown in Fig.4.3. A photograph of the cell taken after the experiment is shown as an inset.

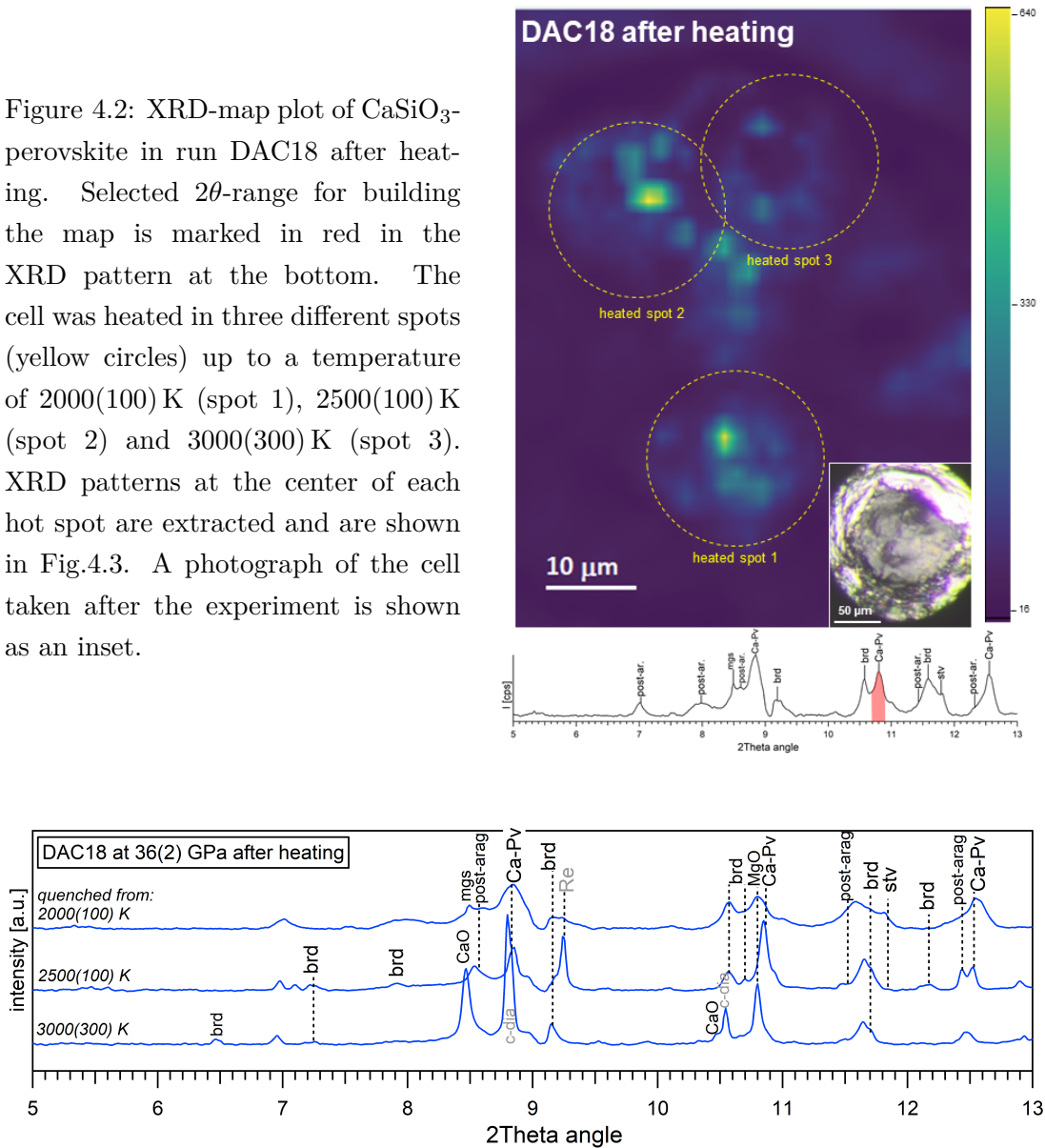


Figure 4.3: XRD patterns extracted from the XRD-map of run DAC18 (Fig. 4.2) in the center of the heated spots. The maximum temperature in the heated spots 1,2 and 3 were 2000(100) K, 2500(100) K and 3000(300) K, respectively. Phases formed during a reaction between  $\text{CaCO}_3$ :<sup>2+</sup> and  $\text{MgSiO}_3$  are marked in black. Phases that do not belong to the sample material (e.g. Re, C-dia) are marked in grey.



## Experiments with (doped) $\text{CaCO}_3$ and olivine $((\text{Mg,Fe})_2\text{SiO}_4)$ as starting materials

To perform experiments that are more representative to natural Earth mantle conditions with 6-8 wt% of Fe (Javoy et al., 2010), two additional BX90 cells were loaded with olivine single crystals (16 wt% of Fe) embedded into a powder layer of either  $\text{CaCO}_3:\text{Sr}^{2+}$  (DAC29) or  $\text{CaCO}_3:\text{Eu}^{3+}$  (DAC24). A third cell was loaded with two single crystals, one of olivine and another one of  $\text{CaCO}_3:\text{Sr}^{2+}$ , shaped into two half circles (DAC12). These configurations allow us to follow the spatial distribution of the trace elements during reaction by using combined XRD-XRF-measurements and map the sample material before and after heating. Further analysis on the recovered sample material using TEM provides additional information on the incorporation of trace elements into the run products. Results on this are presented in section 4.3. Measurements have been performed at beamline P02.2 at PETRA III with an X-ray energy of 42.7 keV and at beamline ID27, ESRF, using an X-ray energy of 33.2 keV. Due to the high transparency of the sample material,  $\text{CO}_2$ -laser heating was performed either online at beamline ID27 (in case of DAC12) or offline using the  $\text{CO}_2$ -laser system at the central laser heating facility of the Research Unit *CarboPaT* complemented with post-heating  $\mu$ -XRD analysis at beamline P02.2 (in case of DAC24). To thermally insulate the sample material from the diamonds during laser heating, KCl or Ar were loaded additionally to the sample volume of the cell. The pressure in the cell was then measured using the diamond fluorescence before and after the experiment where the average is used as experimental pressure. We complemented our results from laser heating with one experiment which has been resistively heated (DAC29). For that purpose, a small grain of Pt was loaded into the cell in addition to the sample assemblage for additional pressure calibration during resistive heating.

The acquisition settings for XRD-XRF maps differ from *in-situ* XRD measurements as the collection time for a single XRD image in the map was below 3 s in addition to 10 s for the XRF spectrum. However, Bragg peaks corresponding to the starting sample material and of the newly formed phases during heating could be indexed. The XRD patterns of DAC12, DAC24 taken at the heated spots, and of DAC29, which has been resistively heated, are listed in Tab. 4.2 and are shown in Fig. 4.4. Results on the elemental distribution measured by XRF mapping are presented in section 4.2.

Offline laser-heating experiments at a temperature of 1990 K (DAC24) indicate a transformation from olivine into Fe-bearing bridgmanite  $((\text{Mg,Fe})\text{SiO}_3)$  and ferropericlase  $((\text{Mg,Fe})\text{O})$ . Furthermore, a reaction between the carbonate and bridgmanite has formed cubic  $\text{CaSiO}_3$ -perovskite plus magnesite which is consistent with our observations on run DAC18 and run DAC19 (Fig. 4.1 and Fig. 4.3). At the highest temperatures of 3000 K (DAC12\_02) flash heating has occurred due to irregularities in sample surface with a sudden change in the emissivity of the sample. Thus, the actual maximum temperature on the sample of run DAC12 could have been even higher than 3000 K. In addition, reflections corresponding to CaO B2-phase were observed. Due to the present sample geometry with two separate grains of olivine and  $\text{CaCO}_3:\text{Sr}^{2+}$  in run DAC12, we

suggest that a reaction between bridgmanite and  $\text{CaCO}_3$  did not occur as both phases were not in close contact. Instead, a decomposition reaction of  $\text{CaCO}_3$  has occurred which must also produce  $\text{CO}_2$  or  $\text{C} + \text{O}_2$ . At P-T-conditions of experiments reported here,  $\text{CO}_2$  would be present in the four-fold coordinated  $P2_12_12_1$  structure (phase V) as reported by Iota et al. (2006). The detection of  $\text{CO}_2$ -V with XRD is challenging due to the low scattering efficiency and we were not able to identify any diffraction lines attributed to  $\text{CO}_2$  in the XRD patterns of run DAC12 (focussed onto the carbonate phase) or DAC18 where the temperature was high enough for  $\text{CaCO}_3$ -decomposition.

Resistive heating of cell DAC29 reached a maximum temperature of 1273 K at 35 GPa and results from this run are plotted in comparison to our diffraction patterns from LHDAC experiments (Fig. 4.4). The reflections in the XRD patterns are very broad due to highly non-hydrostatic conditions in the cell caused by the absence of a PTM. We observed a transformation of the carbonate phase from calcite-I into calcite-VII at high pressure and high temperature. A more heterogeneous phase transition has occurred in the silicate crystal where parts of the silicate grain have transformed into a phase assemblage of Fe-bearing bridgmanite + (Mg,Fe)O while others remained as olivine. Contrary to our findings in LHDAC experiments, where the temperature was high enough to observe a reaction between carbonates and silicates, no formation of  $\text{CaSiO}_3$ -perovskite or magnesite was detected in this particular run.

Table 4.2: P-T-conditions and run products of experiments using olivine ( $(\text{Mg,Fe})_2\text{SiO}_4$ ) and doped  $\text{CaCO}_3$  as starting compositions. In laser-heated experiments (DAC12, DAC24) a pressure transmitting medium (PTM) was used and is marked. XRD-XRF-maps were conducted over the sample material before and after heating as well as TEM analyses on recovered samples from run DAC24 and DAC29.

starting material: $(\text{Mg,Fe})_2\text{SiO}_4 + \text{CaCO}_3:\text{Sr}^{2+}$					
run	experiment	P [GPa]	T [K]	PTM	run products
<i>XRD-XRF map</i>					
DAC12	DAC12_01	33(2)	300	Ar	ol + cc-VII
	DAC12_02	57(5)	3000(300)	Ar	brd + fp + CaO (+ $\text{CO}_2$ )
DAC29	DAC29_01	28(1)	300	-	ol + cc-VII
	DAC29_02	35(1)	1273(60) <sup>1</sup>	-	brd + fp + cc-VII
<i>TEM analyses</i>					
DAC29 <sup>1</sup>	DAC29_03		<i>quench</i>		ol + cc + dol + Mg,Al,O phases

<sup>1</sup>This cell was resistively heated.

starting material: $(\text{Mg,Fe})_2\text{SiO}_4 + \text{CaCO}_3:\text{Eu}^{3+}$					
run	experiment	P [GPa]	T [K]	PTM	run products
<i>XRD-XRF map</i>					
DAC24	DAC24_01	32(1)	1990(90)	KCl	brd + fp + Ca-Pv + mgs + cc-VII
<i>TEM analyses</i>					
DAC24	DAC24_02		<i>quench</i>		brd + fp + mgs + cc + $\text{Eu}_2\text{O}_3$

Abbreviations: brd = bridgmanite, Ca-Pv =  $\text{CaSiO}_3$ -perovskite, cc = calcite, dol = dolomite, fp = ferropiclasite, mgs = magnesite, ol = olivine, stv = stishovite

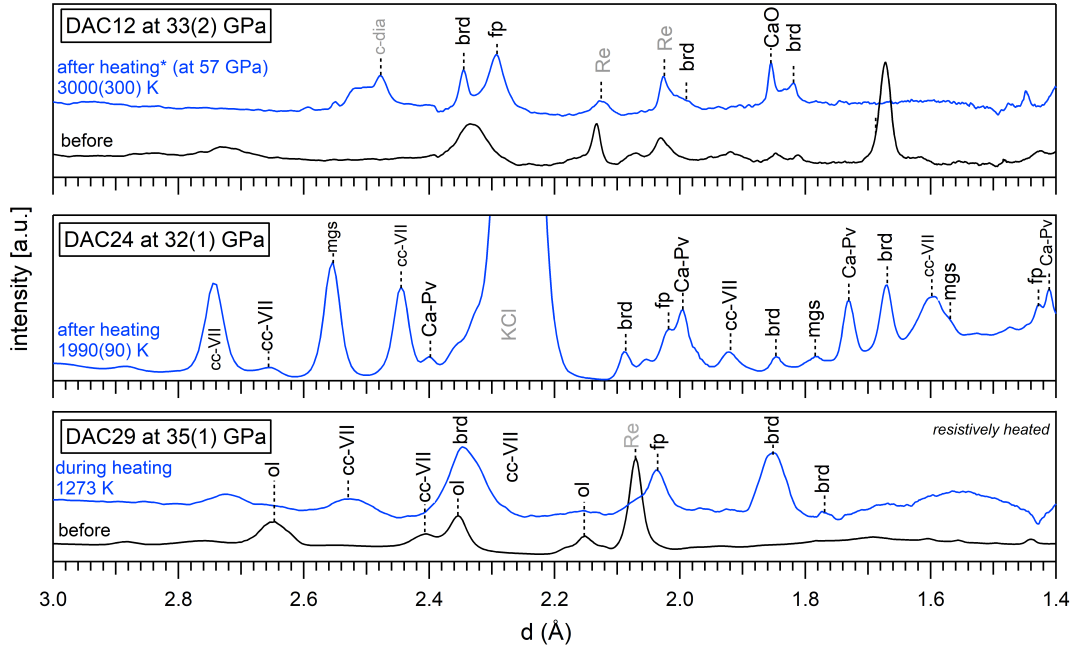


Figure 4.4: XRD patterns before and after heating of experiments using doped  $\text{CaCO}_3$  and olivine ( $(\text{Mg,Fe})_2\text{SiO}_4$ ) as starting compositions, namely DAC12 with  $\text{CaCO}_3:\text{Sr}^{2+}$ , DAC24 with  $\text{CaCO}_3:\text{Eu}^{3+}$  and DAC29 with  $\text{CaCO}_3:\text{Sr}^{2+}$  at pressures between 32 to 35 GPa. Intensities are plotted against  $d$ -values for better comparison. The blue curves mark XRD patterns recorded after heating whereas the black curves represent XRD patterns measured before heating. Phases that do not belong to the sample material (e.g. Re, C-dia, KCl) are marked in grey. Note that in experiment run DAC12 the pressure suddenly increased after laser heating to about 57 GPa. Abbreviations of the phases are explained in Tab.4.2.

### Experiments with doped $\text{CaCO}_3$ and orthopyroxene ( $(\text{Mg,Fe})\text{SiO}_3$ ) as starting materials

Further investigations on the stability of  $\text{CaCO}_3$  in contact with  $(\text{Mg,Fe})\text{SiO}_3$ -silicates were made in run DAC08, DAC11, DAC16 and DAC23. Two cells were loaded with a single crystal of high-Fe bearing orthopyroxene (57 wt% of Fe) embedded into a powder layer of  $\text{CaCO}_3:\text{Sr}^{2+}$  (DAC11) or in close contact with a single crystal of  $\text{CaCO}_3:\text{La}^{3+}$  (DAC08). In addition to the sample, Ar was loaded as a PTM. Laser-heating experiments with *in-situ* XRD analyses of these cells were performed at beamline P02.2, PETRA III, using a Yb-fiber laser and with an photon energy of 42.7 keV. A third and fourth cell were loaded with the same carbonate powders and Ar but with natural enstatite single crystals that contained only 2.8 wt% of Fe (low-Fe, DAC16 and DAC23). Due to the high transparency of the silicate grains, the runs DAC16 and DAC23 have been performed with the  $\text{CO}_2$ -laser heating system available at beamline ID27, at the ESRF. A list of the run products is given in Tab.4.3 and XRD patterns are shown in Fig. 4.5 and Fig. 4.7. Offline heating experiments were performed in run DAC23 at a pressure of 26 GPa and at 1600 K. We only used TEM for the analyses of the

recovered sample material and the results are presented in section 4.3 and are discussed in section 5.2.1.

Table 4.3: P-T-conditions and run products of experiments using high-Fe bearing or low-Fe bearing (Mg,Fe)SiO<sub>3</sub> together with doped CaCO<sub>3</sub> as starting phases. In all cases, Ar was used as a PTM. Ruby for pressure calibration was loaded in DAC11 and DAC16. Different analytical methods were used to analyse the run products: Synchrotron-based XRD during heating (in-situ XRD), combined XRD-XRF mapping only before and after heating (XRD-XRF map) and transmission electron microscopy (TEM analyses).

starting material: (Mg,Fe)SiO <sub>3</sub> + CaCO <sub>3</sub> :La <sup>3+</sup>				
run	experiment	P [GPa]	T [K]	run products
<i>in-situ XRD measurements</i>				
DAC08	DAC08_01	42(2)	1566(25)	opx + post-ar. + dol-III + ba
(high Fe)	DAC08_02	42(2)	1743(45)	brd + mw + post-ar. + dol-III + ba
	DAC08_03	42(2)	2159(23)	brd + mw + post-ar. + dol-III + ba
<i>TEM analyses</i>				
DAC23	DAC23_01		<i>quench</i> <sup>1</sup>	cen + cc + La <sub>2</sub> O <sub>3</sub>
(low Fe)				

<sup>1</sup>quenched from 26(1) GPa and 1600(100) K

starting material: (Mg,Fe)SiO <sub>3</sub> + CaCO <sub>3</sub> :Sr <sup>2+</sup>				
run	experiment	P [GPa]	T [K]	run products
<i>in-situ XRD measurements</i>				
DAC11	DAC11_01	32(1)	1776(34)	brd + Ca-Pv + cc-VII + dol-II
(high Fe)	DAC11_02	29(1)	1929(21)	brd + Ca-Pv + cc-VII + dol-II
	DAC11_03	29(1)	1931(53)	brd + Ca-Pv + cc-VII + dol-II
	DAC11_04	29(1)	2187(248)	brd + Ca-Pv + cc-VII + dol-II + stv + mw
	DAC11_05	29(1)	2136(211)	brd + Ca-Pv + cc-VII + dol-II + stv + mw
	DAC11_06	29(1)	2072(213)	brd + Ca-Pv + cc-VII + dol-II + stv + mw
	DAC11_07	29(1)	2000(162)	brd + Ca-Pv + cc-VII + dol-II + stv + mw
	DAC11_08	29(1)	1882(195)	brd + Ca-Pv + cc-VII + dol-II + stv + mw
<i>XRD-XRF map</i>				
DAC16	DAC16_01	38(1)	300	oen + cc-VII
(low Fe)	DAC16_02	32(1)	2000(100)	brd + Ca-Pv + cc-VII (+ mgs)
	DAC16_03	32(1)	2100(100)	brd + Ca-Pv + cc-VII (+ mgs)
<i>TEM analyses</i>				
DAC11	DAC11_09		<i>quench</i>	brd + stv + mw + Ca-Pv + cen + dol + cc
(high Fe)				

Abbreviations: ba = (hydroxyl)-bastnäsit La(CO<sub>3</sub>)(OH), brd = bridgmanite, Ca-Pv = CaSiO<sub>3</sub>-perovskite, cc = calcite, dol = dolomite, oen = (nat.) orthoenstatite, cen = clinoenstatite, mgs = magnesite, mw = magnesiowüstite, opx = orthopyroxene, stv = stishovite

*In-situ* XRD measurements which were taken at the heated spot of run DAC11 at 29-32 GPa are displayed in Fig. 4.5. Fitting the thermal radiation of the hot sample gave reasonable values for the temperature in the first 2-3 minutes of heating. At the same time, the cell has moved during heating due to warming up and the position on the sample slightly shifted. The movement has affected the fitting of the ther-

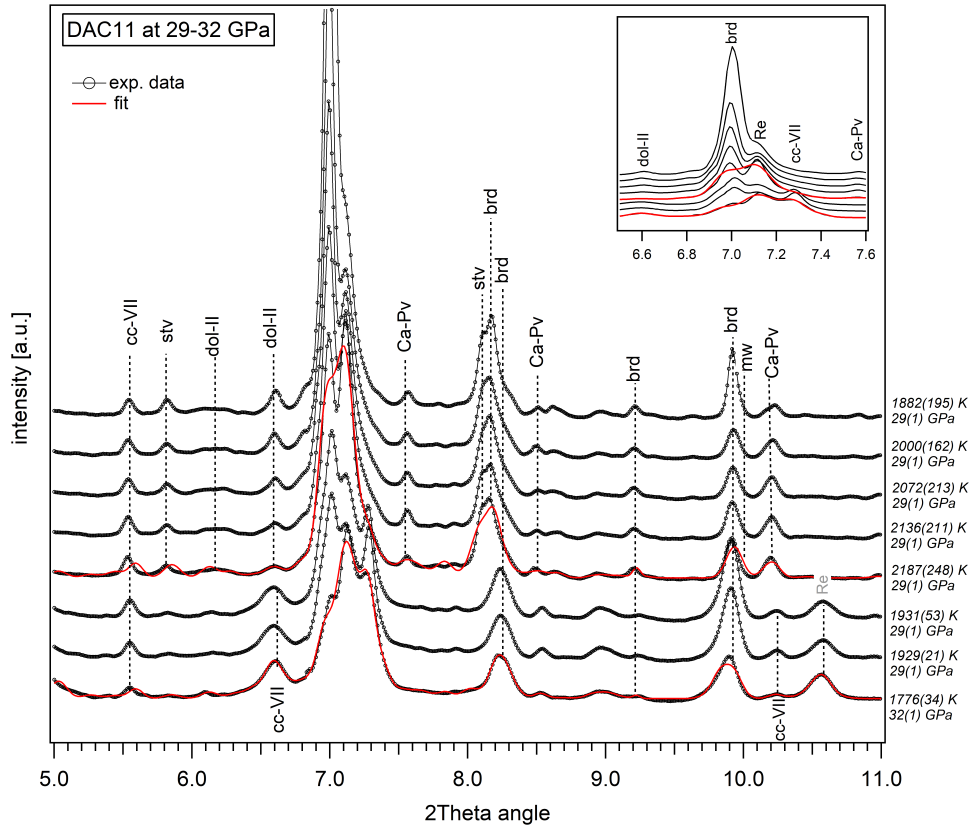


Figure 4.5: XRD patterns of run DAC11 ( $\text{opx} + \text{CaCO}_3:\text{Sr}^{2+}$ ) at 29-32 GPa during heating from 1800 K up to a maximum temperature of 2200 K. Note that the sample has moved during heating and fits for temperatures above 2000 K are less accurate. The red line indicates the fitted XRD pattern at 1776(34) K and on the new position at 2187(248) K. A detailed view on the evolution of the peaks between  $2\theta$  angles of  $6.6^\circ$  and  $7.6^\circ$  is given as an inset with insertion of the fits shown as red lines for the first and second position. Abbreviations for the phases are explained in Tab. 4.3.

mal radiation and errors for the calculated temperatures of experiments DAC11\_04 to DAC11\_08 are higher (see Tab. 4.3). Refined XRD data for the first position on the sample at 1800 K and for the second position at a temperature of 2200 K are therefore highlighted in Fig. 4.5. However, it can be seen that the starting silicate material transformed from orthopyroxene to orthorhombic Fe-bearing bridgmanite at around 1800 K. Intensities of the reflections for bridgmanite increase with higher temperatures whereas others, especially intensities for calcite-VII, are decreasing. This observation is taken as an evidence for an ongoing reaction between calcite-VII and the silicate phase in the heated spot. Intensities for  $\text{CaSiO}_3$ -perovskite are found at the maximum temperature of 2200 K and unequivocally prove that calcite-VII has reacted with Fe-bearing bridgmanite. Additional reflections for dolomite-II, stishovite and magnesiowüstite could be indexed which is different with respect to experiments where lower Fe-contents in the starting silicate material are present (e.g. DAC18, DAC19, DAC12, DAC24 and DAC29).

As reported by Dorfman (2016), the solubility of  $\text{FeSiO}_3$  in bridgmanite is limited. Computed phase boundaries give an approximate incorporation of about 28%  $\text{FeSiO}_3$  in bridgmanite at 40 GPa (Dorfman, 2016) for  $\text{Fe}/(\text{Fe}+\text{Mg})$ -ratios in the orthopyroxene between 0.3 and 0.8. A phase diagram for  $\text{MgSiO}_3$ – $\text{FeSiO}_3$  compositions at 2000 K is given in Fig. 4.6 with the addition of the compositions for the used silicate starting materials shown in red. We can see that for orthopyroxene (with initial Fe-contents of 57 wt%), stishovite and magnesiowüstite are formed in equilibrium with bridgmanite. It seems that the high content of Fe has also an effect on the structure of the newly formed carbonate, and triclinic dolomite, containing a significant amount of Fe, is formed in addition to rhombohedral magnesite.

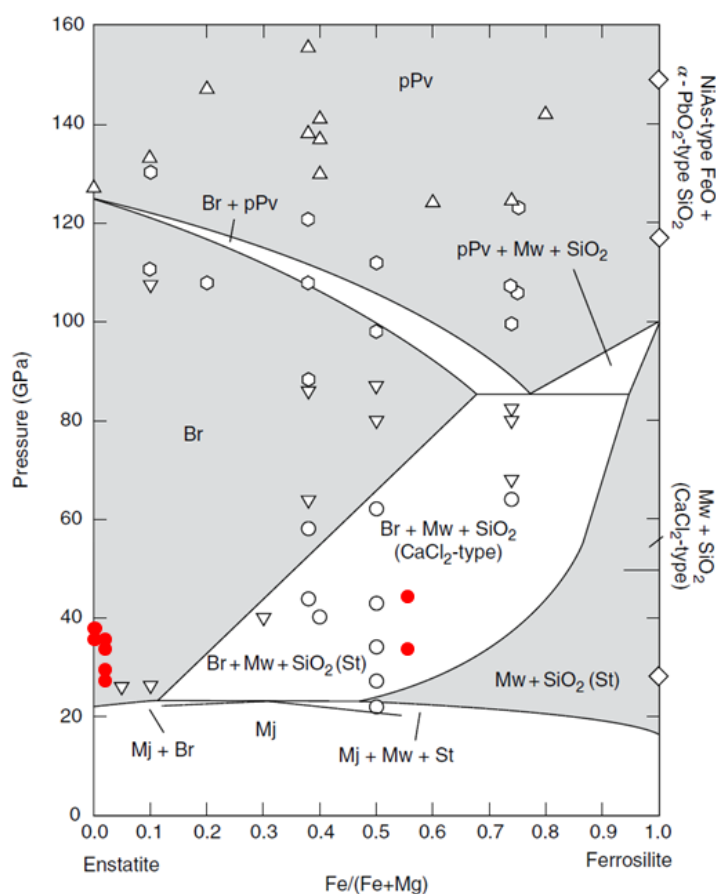


Figure 4.6: Phase diagram of  $\text{MgSiO}_3$ – $\text{FeSiO}_3$  (enstatite–ferrosilite) compositions at lower mantle pressures and  $\sim 2000$  K (Dorfman, 2016). Compositions of the used silicate starting materials are highlighted in red with  $\text{En}_{100}\text{Fe}_0$  for the  $\text{MgSiO}_3$  glass,  $\text{En}_{97}\text{Fe}_3$  for natural enstatite and  $\text{En}_{43}\text{Fe}_{57}$  for orthopyroxene.

*In-situ* XRD analyses and XRD-map measurements of run DAC08 and DAC16 confirm a reaction between  $\text{CaCO}_3$  and  $(\text{Mg},\text{Fe})\text{SiO}_3$  at 42 GPa and 1743 K as well as at 35 GPa and 2000 K, respectively (Fig. 4.7). In both runs we could observe reflections corresponding to  $\text{CaSiO}_3$ -perovskite. The detection of magnesite is rather difficult to see due to the low peak intensities of the diffraction lines. Again, the formation of Fe-bearing dolomite could be observed in run DAC08 where  $\text{CaCO}_3:\text{La}^{3+}$  has reacted with high-Fe bearing orthopyroxene.

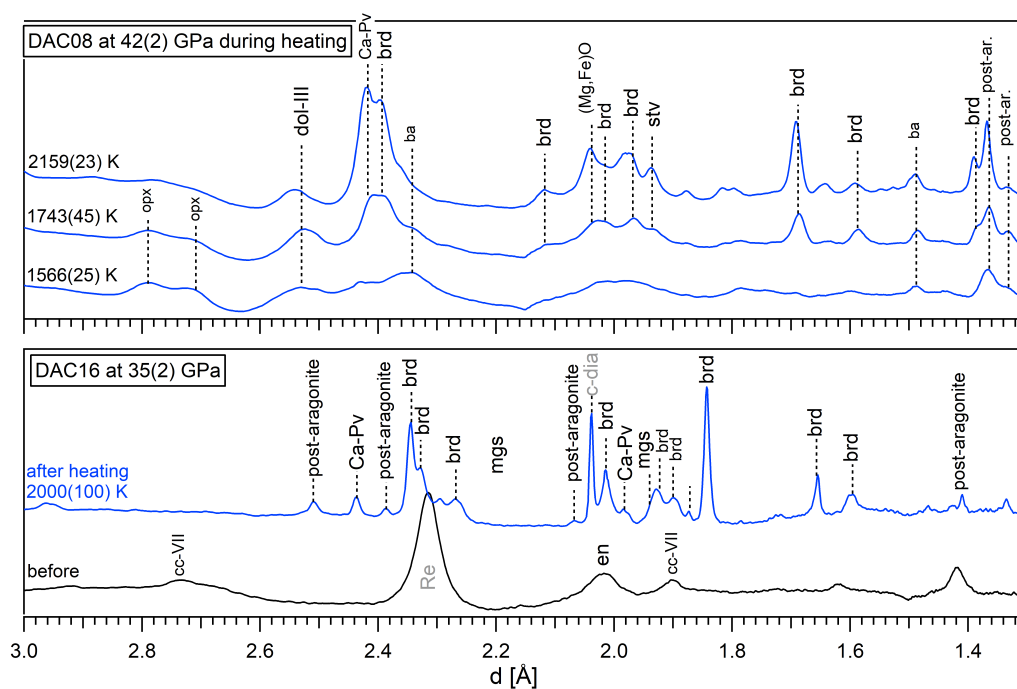


Figure 4.7: XRD patterns of run DAC08 at 42(2) GPa during heating at 1566(25) K, 1743(45) K and 2159(23) K and of run DAC16 before and after heating at a temperature of 2000(100) K. Intensities are plotted against  $d$ -values for better comparison. Abbreviations of the phases are explained in Tab.4.3.

#### 4.1.2 XRD measurements on reactions between $\text{SrCO}_3$ and silicates at conditions of the Earth's mantle

Four runs were performed on pure  $\text{SrCO}_3$  samples in contact with (hydrous) wadsleyite (DAC04), olivine (DAC13) or natural enstatite (DAC15, DAC27). The chosen sample geometry for the cells, except for DAC27, consisted of a silicate single crystal embedded into a  $\text{SrCO}_3$  powder layer. KCl or Ar were used to thermally insulate the sample material from the diamonds and to serve as a PTM. Run DAC27 was loaded with a powder mixture of natural enstatite and  $\text{SrCO}_3$  and only post-heating XRD analyses at beamline P02.2 (PETRA III) were performed. LHDAC experiments DAC13 and DAC15 were carried out at beamline ID27 (ESRF), using the  $\text{CO}_2$ -laser heating system and with an excitation energy of 33.2 keV. *In-situ* XRD analyses of run DAC04 were conducted at beamline P02.2 (PETRA III) at higher excitation energies of 42.7 keV and using a Yb-fiber laser for heating. A list of the conducted experiments together with details on the XRD analyses can be found in Tab.4.4 and Tab.4.5. The aim of these experiments was to study the phase stability in the  $\text{SrO-MgO-FeO-SiO}_2\text{-CO}_2$  system at lower mantle conditions and to observe the formation of  $\text{SrSiO}_3$ -perovskite, which is an isostructural phase to  $\text{CaSiO}_3$ -perovskite.

## Experiments with $\text{SrCO}_3$ and $(\text{Mg,Fe})_2\text{SiO}_4$ as starting materials

*In-situ* XRD measurements of run DAC04 show the evolution of the present phases during heating and are displayed in Fig. 4.8. The cell was loaded with single crystals of (hydrous) wadsleyite with 11.4 wt% of Fe (sample MA-316 from Mrosko et al. (2015)) embedded into a  $\text{SrCO}_3$  powder layer. Wadsleyite belongs to the group of nominally anhydrous minerals (NAM) which can incorporate hydrogen as a hydroxyl group via point defects with incorporations of up to 3 wt%  $\text{H}_2\text{O}$  (Kohlstedt et al., 1996; Mrosko et al., 2015). As shown in Mrosko et al. (2015), the presence of hydrogen extends the stability field of wadsleyite towards lower and higher pressures of about  $\sim 0.5$  GPa. However, it has also an influence on the reactivity and usually reactions in the deep mantle occur at lower temperatures when hydrogen is incorporated in the solid phases. The results on the stability of  $\text{SrCO}_3$  in presence of mantle silicates based on run DAC04 might show a reaction at lower temperatures than in a  $\text{H}_2\text{O}$ -free system and should be therefore treated with caution. In addition, KCl was used as a PTM and thermal insulator, which is also hygroscopic. The pressure was measured with the diamond fluorescence method using Raman spectroscopy as well as with the known equation of state of KCl.

Table 4.4: P-T-conditions and run products of experiments using  $(\text{Mg,Fe})_2\text{SiO}_4$  and  $\text{SrCO}_3$  as starting phases with different pressure transmitting media. Ruby was used in run DAC13 for pressure calibration before and after heating.

starting material: $(\text{Mg,Fe})_2\text{SiO}_4 + \text{SrCO}_3$					
run	experiment	P [GPa]	T [K]	PTM	run products
<i>in-situ XRD measurements</i>					
DAC04	DAC04_01	25(1)	300	KCl	wads(hy) + $\text{SrCO}_3\text{-II}$ + shy B
	DAC04_02	29(1)	1494(56)	KCl	wads(hy) + $\text{SrCO}_3\text{-II}$ + shy B
	DAC04_03	29(1)	1738(72)	KCl	brd (+ fp) + $\text{SrCO}_3\text{-II}$
	DAC04_04	29(1)	1826(84)	KCl	brd + fp + $\text{SrCO}_3\text{-II}$ + Sr-Pv + mgs
	DAC04_05	29(1)	1656(69)	KCl	brd + fp + $\text{SrCO}_3\text{-II}$ + Sr-Pv + mgs
	DAC04_06	29(1)	1964(111)	KCl	brd + fp + $\text{SrCO}_3\text{-II}$ + Sr-Pv + mgs
	DAC04_07	29(1)	2004(110)	KCl	brd + fp + $\text{SrCO}_3\text{-II}$ + Sr-Pv + mgs
	DAC04_08	29(1)	2088(100)	KCl	brd + fp + $\text{SrCO}_3\text{-II}$ + Sr-Pv + mgs
<i>XRD-XRF map</i>					
DAC13	DAC13_01	23(1)	300	Ar	ol + $\text{SrCO}_3\text{-I}$
	DAC13_02	23(1)	1850(150)	Ar	brd (+ fp) + Sr-Pv + $\text{SrCO}_3\text{-II}$ + mgs
	DAC13_03	23(1)	2400(100)	Ar	brd (+ fp) + SrO
<i>TEM analyses</i>					
DAC04	DAC04_09		<i>quench</i>		brd + fp + $\text{SrCO}_3$ + Sr-Pv(am) + $\text{K}_2\text{CO}_3^1$

<sup>1</sup>PTM has reacted with carbonate, Abbreviations: brd = bridgmanite, fp = ferropericlasite, mgs = magnesite, ol = olivine, shy B = superhydrous phase B ( $\text{Mg}_{10}\text{Si}_3\text{O}_{14}(\text{OH})_4$ ), Sr-Pv =  $\text{SrSiO}_3$ -perovskite, wads = (hydrous) wadsleyite.



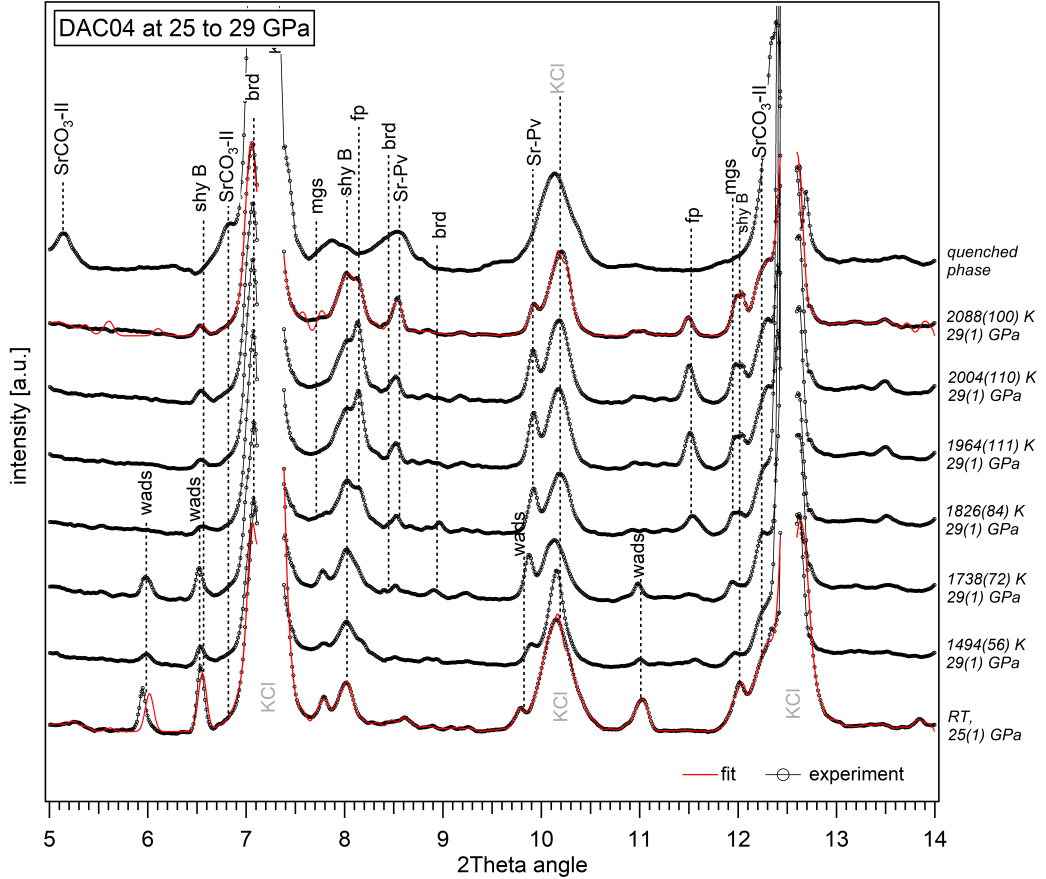


Figure 4.8: XRD patterns of run DAC04 (hy-wds +  $\text{SrCO}_3$ ) at 25(1) and 29(1) GPa during heating up to a maximum temperature of 2088(100) K. The red lines indicate the fitted XRD patterns (Le Bail) at room temperature (RT) and at a maximum temperature of 2088 K.

XRD patterns at ambient temperature but at pressures of 25 GPa show, in addition to (hydrous) wadsleyite and  $\text{SrCO}_3\text{-II}$ , the presence of superhydrous phase B ( $\text{Mg}_{10}\text{Si}_3\text{O}_{14}(\text{OH})_4$ ) which comes from the wadsleyite synthesis (Mrosko et al., 2015). The nominal pressure in the sample chamber increased from 25 to 29 GPa due to isochoric thermal pressure when temperature was applied to the system. We then collected XRD data with acquisition settings of 10 s per step at this higher pressure. The temperature was increased stepwise with 100 K per step and with dwell times of about 2-3 minutes. XRD patterns in Fig. 4.8 document the transformation from (hydrous) wadsleyite into the more stable phase assemblage Fe-bearing bridgmanite and (Mg,Fe)O at around 1740 - 1830 K indicated by the rise of a new peak at a  $2\theta$  angle of  $\sim 7^\circ$  which corresponds to the 112-reflection of bridgmanite on the shoulder of the strong 110-reflection from KCl. Diffraction peaks belonging to (Mg,Fe)O are rather weak but reflections with  $hkl$ -indices 200 and 220 are visible at  $2\theta$ -angles between  $8.2^\circ$  and  $11.6^\circ$ . The main carbonate phase at high pressure and high temperature is the post-aragonite phase  $\text{SrCO}_3\text{-II}$  and was fitted with the refined crystals structure from chapter 3 as starting values. Finally, a reaction between  $\text{SrCO}_3\text{-II}$  and the silicate is observed at

1826 K by the formation of magnesite and a hexagonal structured SrSiO<sub>3</sub>-perovskite phase (6H-BaTiO<sub>3</sub> type). This SrSiO<sub>3</sub>-perovskite structure has been previously described by Yusa et al. (2005) and was found to be stable at 25 GPa and 1450(150) K.

A second diamond anvil cell was prepared loading olivine single crystals in contact with SrCO<sub>3</sub> powder as starting materials (DAC13). Results from this experiment are listed in Tab. 4.4 and XRD data were measured only before heating and on temperature quench run products with acquisition times of 3 s per point. In run DAC13, the risk of contamination by water has been minimized in two ways: instead of using KCl, the PTM was changed to Ar and the used olivine crystal is free of H<sub>2</sub>O (see section 2.1.2 for chemical analyses). The pressure in the cell was increased to 23(1) GPa where SrCO<sub>3</sub> exist in the low-pressure phase with space group *Pmcn*. Thanks to the refinement of the high-pressure phase of SrCO<sub>3</sub>-II, we could detect that during heating at a temperature of about 1850 K SrCO<sub>3</sub> has transformed into the same *Pmnn*-phase as presented in chapter 3. We suggest that annealing of the sample material has lead to a stabilization of the high-pressure phase SrCO<sub>3</sub>-II already at lower pressure compared to our results from chapter 3 where data was collected during compression only at room temperature. In addition and during heating, olivine transformed into Fe-bearing bridgmanite and (Mg,Fe)O and bridgmanite reacted with SrCO<sub>3</sub>-II producing magnesite and the same hexagonal SrSiO<sub>3</sub>-perovskite phase as in DAC04.

### Experiments with SrCO<sub>3</sub> and natural enstatite as starting material

XRD-map measurements of run DAC15 and DAC27, performed only before and after heating, are listed in Tab. 4.5 and XRD patterns extracted from the XRD-maps at the center of the heated spots are shown in Fig. 4.9. A powder mixture was loaded into DAC27, whereas the sample configuration in run DAC15 consisted of a natural enstatite single crystal embedded into a SrCO<sub>3</sub> powder layer. Run DAC27 was conducted as an offline experiment using the Yb-fiber laser heating system at the University of Potsdam with post-heating XRD-map measurements at beamline P02.2 at PETRA III. Although the Fe content in the starting sample material is very low, we were able to heat the sample assemblage with the current system up to temperatures of 2300 K. By comparing both XRD patterns for cell DAC15, we could observe that SrCO<sub>3</sub>-I has transformed into *Pmnn*-structured SrCO<sub>3</sub>-II phase during heating at a pressure of 26 GPa. Furthermore, both experiments show in addition to SrCO<sub>3</sub>-II and bridgmanite the appearance of reflections that belong to the same hexagonal structured SrSiO<sub>3</sub>-perovskite phase as in run DAC04.

Table 4.5: P-T-conditions and run products of experiments using natural enstatite and SrCO<sub>3</sub> as starting compositions.

starting material: MgSiO <sub>3</sub> + SrCO <sub>3</sub>				
run	experiment	P [GPa]	T [K]	run products
<i>XRD-XRF map</i>				
DAC15	DAC15_01	26(1)	300	oen + SrCO <sub>3</sub> -I
	DAC15_02	26(1)	1900(100)	brd + Sr-Pv + mgs + SrCO <sub>3</sub> -II
DAC27	DAC27_01	27(2)	2300(100)	brd + stv + mgs + SrCO <sub>3</sub> -II
<i>TEM post-analyses</i>				
DAC27	DAC27_02	<i>quench</i>		brd + cen + stv + SrCO <sub>3</sub> -I + mgs

Abbreviations: brd = bridgmanite, mgs = magnesite, cen = clinoenstatite, oen = orthoenstatite, Sr-Pv = SrSiO<sub>3</sub>-perovskite, stv = stishovite

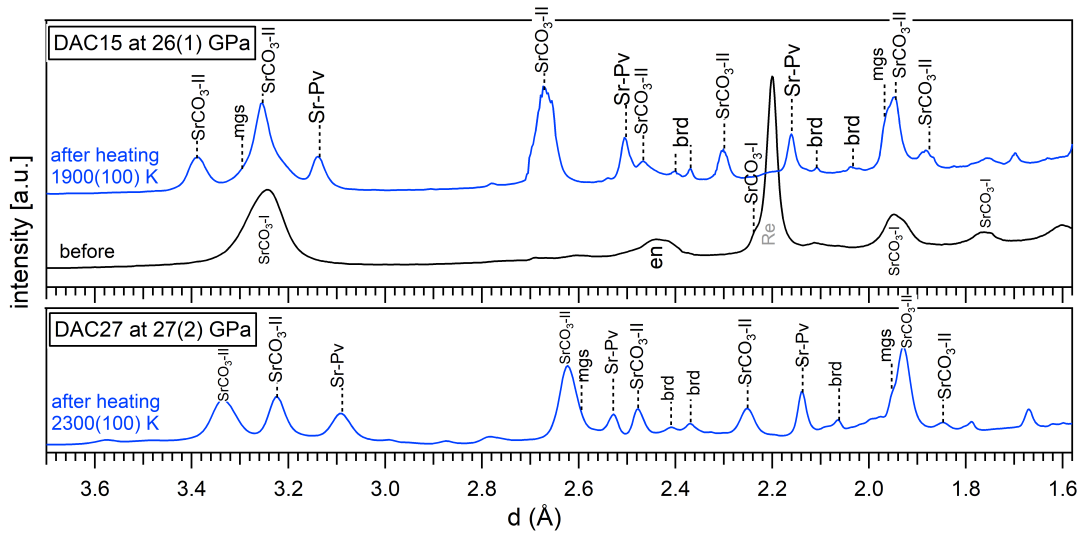


Figure 4.9: XRD patterns extracted from XRD-XRF maps before and after heating of experiments with SrCO<sub>3</sub> and natural enstatite as starting materials at pressures between 26 and 27 GPa. Intensities are plotted against  $d$ -values for better comparison. The blue curves mark XRD patterns recorded after heating at the center of the heated spot whereas the black curve represents XRD pattern measured before heating of DAC15. Phases that do not belong to the sample material (e.g. Re) are marked in grey. Abbreviations of the phases are explained in Tab. 4.5.

### 4.1.3 Summary of the XRD results on carbonate-silicate reactions

We investigated the stability of CaCO<sub>3</sub> and SrCO<sub>3</sub> at high pressure and high temperature in contact with silicates in the pseudo-binary system (Mg,Fe)<sub>2</sub>SiO<sub>4</sub>–(Mg,Fe)SiO<sub>3</sub>. Results from experiments where carbonates reacted with olivine ((Mg,Fe)<sub>2</sub>SiO<sub>4</sub>) show a transformation from olivine into Fe-bearing bridgmanite and ferropericlase at high pressure and high temperature. Furthermore, a reaction between CaCO<sub>3</sub> and bridgmanite has formed cubic CaSiO<sub>3</sub>-perovskite plus magnesite but the onset for this reaction is not well constrained since only two experiments have been conducted on this particular system. In the case of SrCO<sub>3</sub> reacting with (Mg,Fe)<sub>2</sub>SiO<sub>4</sub>, we could observe the onset

of carbonate-silicate reaction by the formation of  $\text{SrSiO}_3$ -perovskite and magnesite at 1720 K and 29 GPa. However, these results are based on data in a  $\text{H}_2\text{O}$ -bearing system. Therefore a reactivity between the two phases could be promoted already at lower temperatures compared to  $\text{H}_2\text{O}$ -free systems as the incorporation of hydrogen affects the stability of the silicate phase.

A more detailed view is given on carbonates reacting with orthopyroxene  $(\text{Mg,Fe})\text{SiO}_3$ . Orthopyroxene usually transforms into Fe-bearing bridgmanite at high pressure and high temperature. If the Fe content in the orthopyroxene is higher than 25 wt%, orthopyroxene transforms into the phase assemblage bridgmanite +  $(\text{Mg,Fe})\text{O}$  +  $\text{SiO}_2$  as shown in the two experiments DAC08 and DAC11. We could identify the formation of  $\text{CaSiO}_3$ -perovskite and magnesite documenting a reaction between  $\text{CaCO}_3$  and bridgmanite at pressures between 33 and 42 GPa and temperatures above 1770 K. A reaction between  $\text{SrCO}_3$  and bridgmanite was found by forming magnesite and evidence is given also for the formation of  $\text{SrSiO}_3$ -perovskite. However, the existence of  $\text{SrSiO}_3$ -perovskite at high-pressure remains unclear since a refinement of the data is based only on a recent study from Yusa et al. (2005) and an equation of state for this phase is not available. The role of Fe in the carbonate-silicate system is still under investigation. We observed that a high content of Fe favours dolomite formation in addition to magnesite during the reaction. Our XRD study only provides qualitative data on the Fe-content in the run products and additional experiments are needed to better constrain the Fe-partitioning in carbonate-silicate reactions.

## 4.2 Elemental redistribution processes in carbonate-silicate reaction experiments

In order to follow elemental redistribution at *in-situ* conditions, synchrotron-radiation induced  $\mu$ -XRF was used which makes it possible to perform a qualitative and quantitative analysis of the elements present in a diamond anvil cell at a high spatial resolution and with high sensitivity. Using confocal detection schemes, the sensitivity of  $\mu$ -XRF is further enhanced and produces detection limits in the ppm range. A detailed description on the experimental setup is given in section 2.4. For the two beamlines ID27(ESRF) and P02.2 (PETRA III), the sensitivity of the current experimental conditions has been evaluated by the measurement of homogeneous reference materials and is presented precedently.

### 4.2.1 XRF calibration on silicate glass reference materials

Prior to the actual measurements on the sample material, we performed calibration measurements on standard silicate glasses with nominal concentrations for a suite of trace elements at the concentration level of about 500 ppm (NIST SRM 610) and of 50 ppm (NIST SRM 612) (Pearce et al., 1997). The standard glasses were ground to fine powders and then placed into a DAC equipped with a Re gasket simulating conditions that will be present in the actual experiment. Fig. 4.10 presents the XRF spectra of the standard glasses with acquisition times of 100 s. Using excitation energies of 33.2 keV and 42.7 keV, we observed  $K_\alpha$  fluorescence lines of elements with atomic numbers from 23 (V) to 53 (I). Fluorescence lines from elements with  $Z \geq 54$  are rarely visible due to a very high background between 0 and 6 keV and a broad inelastic scattering between 30 and 40 keV that overlays the fluorescence peaks of the elements. The exact concentrations for the elements of interest in the standard glass NIST SRM 610 are 494(35) ppm for Sr, 440(19) ppm for La and 447(13) ppm for Eu. The standard glass NIST SRM 612 contains 73.5(5) ppm of Sr, 35(1) ppm of La and 34(2) ppm of Eu (Pearce et al., 1997). Intensities for the peaks of the detected elements were determined by fitting the spectra using the program PyMCA (Solé et al., 2007). The minimum detection limit ( $C_{mdl}$ ) was calculated, which is defined as the lowest concentration of an element that can be detected by the given experimental configuration of the material after equation (Petitgirard et al., 2012; Haller and Knoechel, 1996):

$$C_{mdl,i} = \frac{3 \cdot \sqrt{I_B}}{I_i} \cdot \frac{\sqrt{t}}{\sqrt{1000}} \cdot C_i \quad (4.1)$$

where  $I_B$  is the intensity of the background,  $I_i$  the intensity of the fluorescence line of element  $i$  calculated from an analytic area over  $3\sigma$  (in this case only  $K_\alpha$  fluorescence lines are used),  $t$  is the acquisition time and  $C_i$  is the actual concentration of element  $i$ . Due to the constraints on the sensitivity of certain elements as mentioned in the first paragraph, only reliable  $C_{mdl}$  of elements with  $Z$  from 37 to 51 were determined (Fig. 4.11).

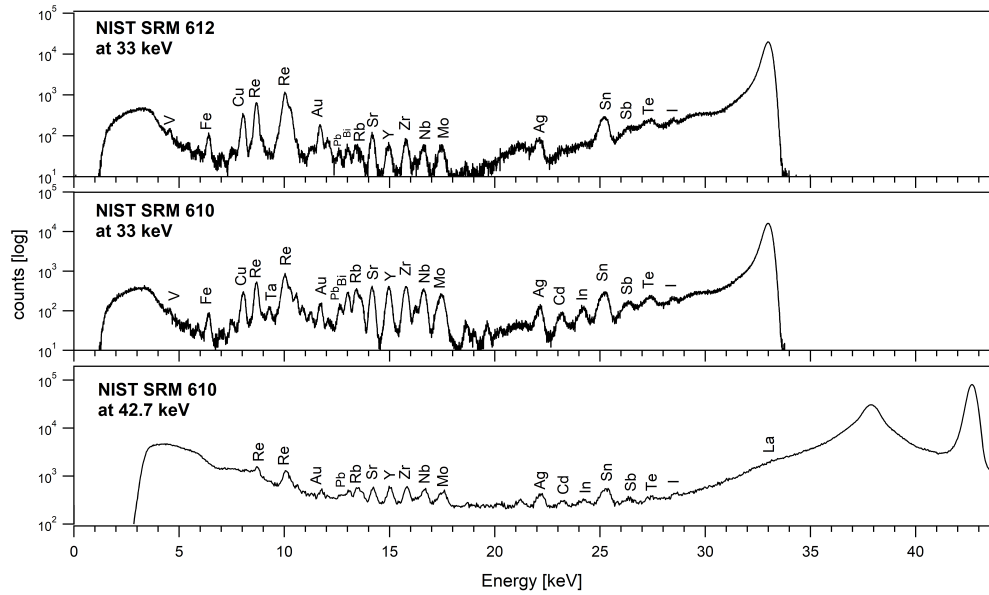


Figure 4.10: XRF spectra with acquisition times of 100 s collected on standard silicate glasses NIST SRM 610 and NIST SRM 612 in a diamond anvil cell with an X-ray excitation energy of 33.2 keV and 42.7 keV. Note that at higher excitation energy the Compton scattering of the incoming beam passing through the diamond anvil increases. Re was used as a gasket material. No pressure medium was loaded and measurements were performed at ambient pressure.

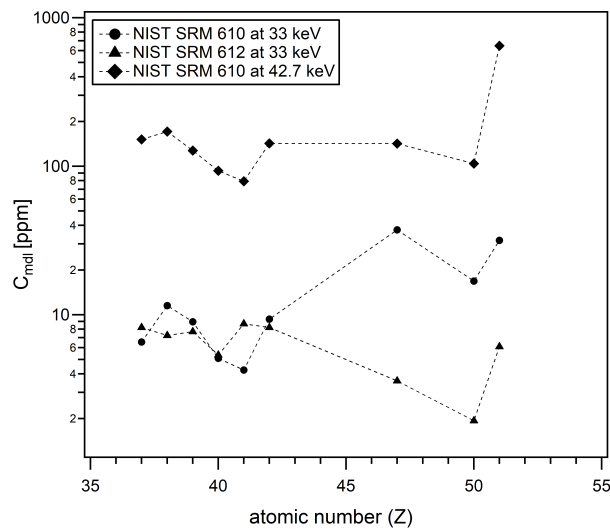


Figure 4.11: Minimum detection limits ( $C_{mdl}$ ) for various elements from two standard glasses in a diamond anvil cell equipped with a Re gasket (NIST SRM 610 and NIST SRM 612) at excitation energies of 33.2 keV and 42.7 keV.

While using the setup at beamline ID27, ESRF, with an excitation energy of 33.2 keV, the detection limits for the elements with atomic numbers ( $Z$ ) between 37 and 42 in the standard glasses were  $\leq 15$  ppm and usually higher for elements with  $47 < Z < 51$ . The reason for this higher detection limit is a contribution of Compton scattering from the diamonds, that overlays the  $K_{\alpha}$  lines at energies above 20 keV. In

addition, contamination of the fluorescence signal from the detector gives inaccurate concentration levels for the elements Ag, Sn, Sb, Te and I as they are being contained as impurities (Appendix C). The minimal detectable concentration level for Sr is 7.25 ppm using an excitation energy of 33.2 keV.

Experiments on beamline P02.2. at PETRA III were performed at a higher excitation energy of 42.7 keV which is above the K-edge of La. However, the signal-to-noise ratio for our measurements at this beamline are poor in comparison to our measurements at beamline ID27 suggesting a misalignment between fluorescence detector and sample. In addition, we were not able to observe the La- $K_\alpha$  line in the standard glasses. Therefore, we could only assume a detection limit for La above 500 ppm.

#### 4.2.2 XRF measurements on Sr- and La-doped samples

The XRF-signal over the heated area of the sample material was recorded simultaneously to XRD before and after heating. Typical XRF-spectra of the carbonate sample materials with various contents of Sr and La are given in Fig. 4.12. Fluorescence lines for Sr and Re are clearly visible. The detection of La is rather difficult because of the strong Compton peak in the energy region of La- $K_\alpha$ . However, concentrations of La in  $\text{CaCO}_3:\text{La}^{3+}$  (NB10) and in the DAC are above the detection limit of 500 ppm and a small peak at 33 keV due to the La- $K_\alpha$  fluorescence is obtained. Additional peaks for Ag, Sn, Te and I were detected between 20 and 32 keV. The two-dimensional distribution of these elements in the cells leads to the conclusion that they might be contained as impurities in the detector (Fig. 4.13). Additional information on the origin of the elements in the XRF spectra are given in Appendix C.

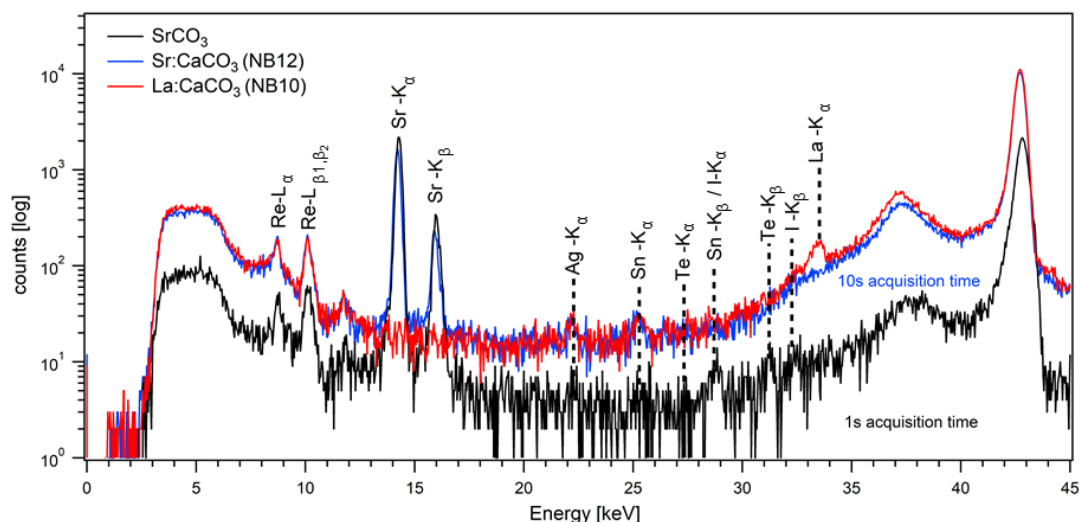


Figure 4.12: XRF spectra with acquisition times of 1 s and 10 s collected from a diamond anvil cell containing pure  $\text{SrCO}_3$  (exp. run DAC04),  $\text{CaCO}_3:\text{Sr}^{2+}$  (exp. run DAC11) and  $\text{CaCO}_3:\text{La}^{3+}$  (exp. run DAC08) with an X-ray excitation energy of 42.7 keV. Re L-lines are produced by the gasket material. Additional peaks for Ag, Sn, Te and I between 20 and 32 keV derive as impurities from the detector and are not correlated to the sample loading (see Fig. 4.13).

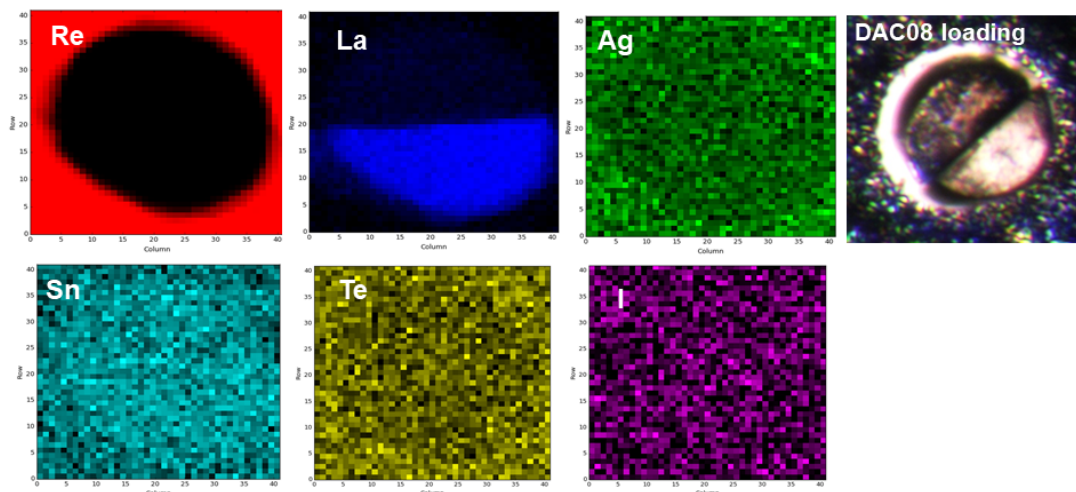


Figure 4.13: Two-dimensional distribution of the fluorescence signal of Re, La, Ag, Sn, Te and I in cell DAC08. The fluorescence of La originates from carbonate sample whereas Re comes from the gasket. A homogeneous distribution of Ag, Sn, Te and I suggests a contamination from the detector itself.

### Redistribution of La during carbonate-silicate reactions

After pre-processing of the XRF data (see section 2.5.2) the integrated intensities of the fluorescence lines of the detected elements are plotted in colour maps where each fluorescence signal corresponds to a certain colour code. For the evaluation of La redistribution during carbonate-silicate reactions, we show two-dimensional distribution of La- $K_{\alpha}$  from run DAC08 in Fig. 4.14. This cell was loaded with two single crystals of enstatite and  $\text{CaCO}_3\text{:La}^{3+}$  in close contact to each other. The cell was heated at a pressure of 42 GPa to a maximum temperature of 2200 K. As shown in Fig. 4.14a, the intensity for La before heating shows the location of the carbonate crystal. During heating, we could detect by using additional XRD the formation of  $\text{CaSiO}_3$ -perovskite at the interface between the two phases.  $\text{CaSiO}_3$ -perovskite might be a suitable candidate for hosting La in its crystal structure. Comparing both XRF maps (normalized to the intensity of the scattered peak) before and after heating allows us to monitor changes in the elemental distribution during reaction. In addition to that, XRF line scans were extracted from the map plot for a better visualization of the elemental reorganization (Fig. 4.14c). Due to the low sensitivity for La fluorescence lines in the used experimental setup at an excitation energy of 42.7 keV, we were not able to detect any changes in the distribution of La after heating. Furthermore, XRF line scans over the heated area present no significant increase of La- $K_{\alpha}$  intensity towards the silicate crystal.



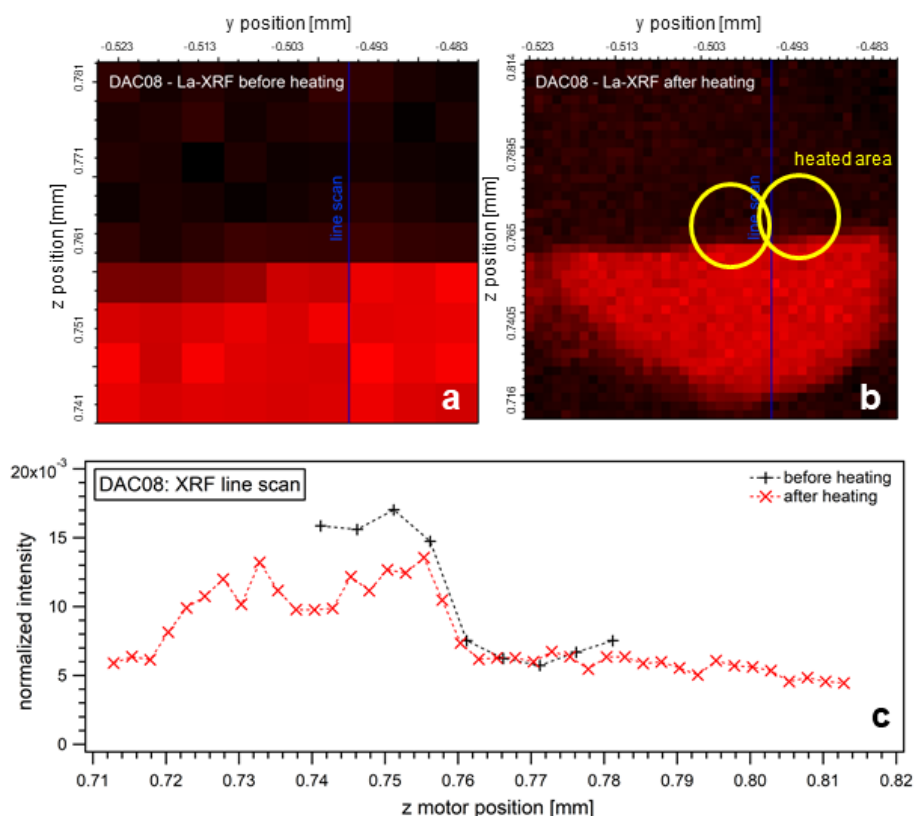


Figure 4.14: a. La- $K_{\alpha}$  intensity maps before (a) and after heating (b) in experiment run DAC08. XRF line scans (c) over the heated area show no major changes in the distribution of La  $K_{\alpha}$  due to the low sensitivity of La in the current experimental setup.

### Redistribution of Sr during carbonate-silicate reactions

In order to study the role of Sr in the carbonate-silicate reactions,  $\text{CaCO}_3\text{:Sr}^{2+}$  (NB12) with doping levels of 24000 ppm of Sr was used as a starting material. Due to the higher concentration levels and the better sensitivity for Sr, the redistribution should be more visible in the chosen experimental setup. Laser-heating was performed to 2100 K (DAC16), 2200 K (DAC11) and 3000 K (DAC12). Heating times varied from 10 to 20 min. After heating, XRF maps were taken on the three laser heated areas. To better visualize and interpret a possible redistribution of the trace element Sr, we extracted XRF line scans across the heated areas of run DAC11, DAC12 and DAC16 as shown in Fig. 4.15. They indicate small changes in the distribution of Sr over an area of a few microns. In some experiments the gasket material has expanded during heating and sample material has moved which made it difficult to correlate Sr intensities before and after heating. Since the Sr distribution does not change significantly for the studied reactions, the results do not allow a clear interpretation with respect to the incorporation of Sr into  $\text{CaSiO}_3$ -perovskite.

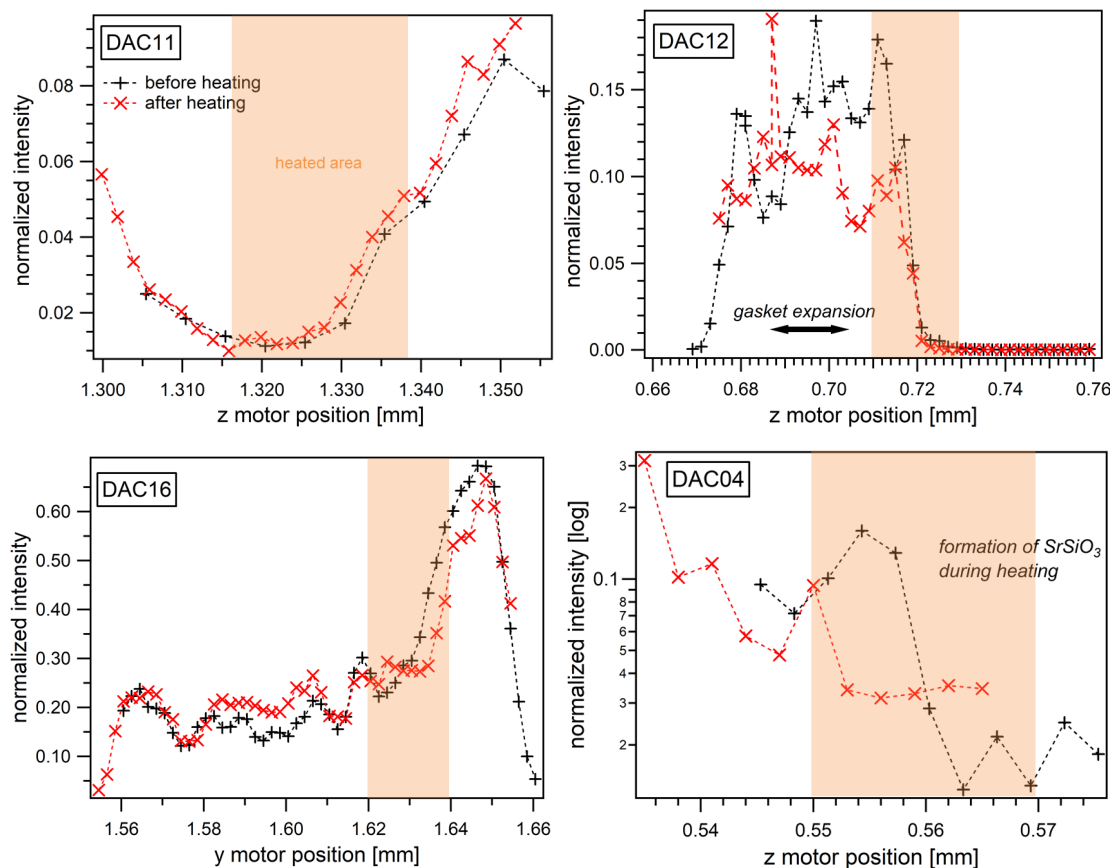


Figure 4.15: XRF line scans of Sr emission lines normalized to the elastic peak across the heated areas from experiments with formation of  $\text{CaSiO}_3$ -perovskite during heating (DAC11, DAC12, DAC16) and from experiments with formation of  $\text{SrSiO}_3$ -perovskite (DAC04). The step size for XRF measurements was  $2\ \mu\text{m}$ . Shaded areas mark the position of heating with a radius for the laser-heated spot of max.  $20\ \mu\text{m}$ . Note that in experiment run DAC12 the Re gasket material expanded during heating and sample material has moved along z direction.

Contrasting observations were made using pure  $\text{SrCO}_3$  as a starting material. As an example, results from measurements on experiment run DAC04 are presented (Fig. 4.15d). The cell was loaded with a single crystal of (hydrous) wadsleyite and pure  $\text{SrCO}_3$  powder. The sample material was heated at 27 GPa for about 15 to 20 min at the interface between silicate and  $\text{SrCO}_3$  powder to a maximum temperature of 2100 K. XRF line scans across the heated area certainly indicate a change in the distribution of Sr around the heated spot. Thanks to the combination of *in-situ* XRD, which were taken at the centered heating spot, and post-heated XRF measurements, we can now directly link the redistribution of Sr to structural changes in the phase assemblage. As mentioned in section 4.1.2 and shown in Fig. 4.8,  $\text{SrSiO}_3$ -perovskite was formed during heating of the sample assemblage  $\text{SrCO}_3 + (\text{Mg,Fe})_2\text{SiO}_4$  and caused a change in the concentrations of Sr locally.

Similar results are obtained in run DAC13 with  $\text{SrCO}_3$  in reaction with olivine. The sample material was heated on two different spots to maximum temperatures of 1850 K (spot 1) and of 2400 K (spot 2). XRF analysis indicates a redistribution of Sr around the heated spots. Consistent with this observation, the formation of perovskite-structured  $\text{SrSiO}_3$  is detected during heating (see appendix B) and a XRD map plot of the (102)-reflection of  $\text{SrSiO}_3$ -perovskite shows highest intensities in the area of the heated spots (Fig. 4.16). We conclude that there is a correlation between the newly formed silicate perovskite phase and an increase in the Sr concentration in this area. In the heated spot 2, reflections corresponding to SrO-B1 phase were observed as well and indicate that the temperature was high enough to partially decompose  $\text{SrCO}_3$  into SrO and  $\text{CO}_2$ .

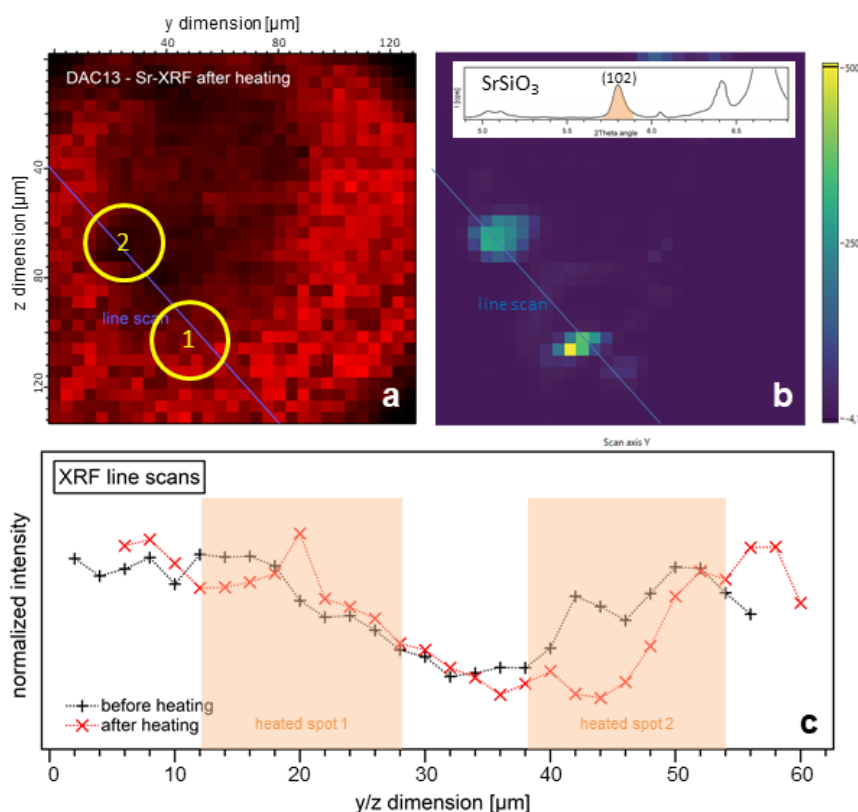


Figure 4.16: a) XRF intensity map of Sr shown in red after heating of run DAC13 with the heated spots drawn as yellow circles. b) XRD map of (102)-reflection of hexagonal  $\text{SrSiO}_3$ -perovskite with highest intensities found in the heated spots. c) XRF line scans over the heated areas show a change in Sr distribution around the heated spots.

### 4.2.3 Optical fluorescence experiments on Eu-doped samples

$\text{CO}_2$  laser-heated diamond anvil cell offline experiments in combination with optical fluorescence measurements were performed in the central laser heating facility of the DFG-funded Research Unit *CarboPaT* at the University of Frankfurt. For that purpose, a single crystal of natural Fe-bearing olivine from San Carlos embedded into a  $\text{CaCO}_3:\text{Eu}^{3+}$  powder layer was loaded into a Böhler-Almax cell equipped with a Re

gasket and a 100  $\mu\text{m}$  hole as a sample chamber. A thin layer of KCl was put on the top of both diamond culets in order to thermally insulate the sample from the diamond anvils. Heating the sample material with a  $\text{CO}_2$ -laser yielded a maximum temperature of 1990(90) K at a pressure of 32(1) GPa. Optical fluorescence measurements on the sample in the cell were carried out in addition to post-heated X-ray diffraction and spectra were obtained at the emission of  $\text{Eu}^{3+}$  at 595.5 nm ( ${}^5\text{D}_0 \rightarrow {}^7\text{F}_1$  transition) before and after heating to follow the chemical distribution of Eu during reaction.

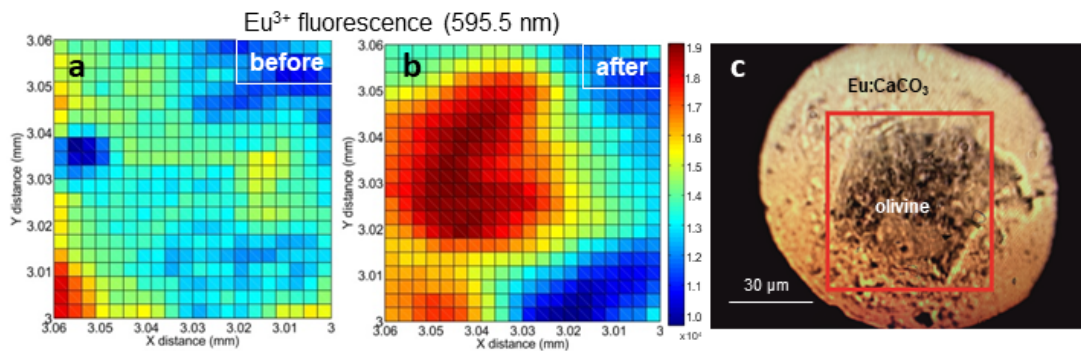


Figure 4.17: Optical fluorescence intensity maps of  $\text{Eu}^{3+}$  at 595.5 nm ( ${}^5\text{D}_0 \rightarrow {}^7\text{F}_1$  transition) before (a) and after heating (b) of experiment run DAC24 showing a redistribution of Eu towards the center of the laser-heated spot. The step size was 3  $\mu\text{m}$ . c) Image taken of the loaded cell DAC24 after heating. The red square marks the laser heated area.

Maps of the size  $60 \times 60 \mu\text{m}$  show a redistribution of Eu after heating towards the center of the laser-heated spot and the silicate phase (Fig. 4.17). With the help of additional XRD measurements after heating, we can detect a transformation of the silicate phase into Fe-bearing bridgmanite and  $(\text{Mg,Fe})\text{O}$  as well as the formation of  $\text{CaSiO}_3$ -perovskite around the heated spot at high pressure. So far, these observations indicate that Eu is being fractionated and may be incorporated into the newly formed silicate perovskite phases during reaction.

### 4.3 Analysis of recovered samples from carbonate-silicate reactions using transmission electron microscopy (TEM)

Analytical transmission electron microscopy (TEM) was carried out to have a three dimensional view on the laser-heated area, to constrain decarbonation reactions in the respective system and detect possible redistribution of the trace elements at the sub-micrometer scale. Figure 4.18 shows a selection of TEM-images of the recovered samples from experiment run DAC04 (hy-wds + SrCO<sub>3</sub>), DAC11 (opx + CaCO<sub>3</sub>:Sr<sup>2+</sup>), DAC24 (ol + Eu:CaCO<sub>3</sub>), DAC27 (oen + SrCO<sub>3</sub>) and DAC29 (ol + CaCO<sub>3</sub>:Sr<sup>2+</sup>). One of our aims was to observe the presence of CaSiO<sub>3</sub> and SrSiO<sub>3</sub> phases in the heated spots of the recovered samples which would document a reaction between the carbonate and the silicate phase. Indeed, we found that a reaction between CaCO<sub>3</sub> and bridgmanite took place along cleavages of the silicate crystals where CaSiO<sub>3</sub>-perovskite was found as shown in recovered sample material from DAC11 (Fig. 4.18a,c) quenched from 32 GPa and 2200 K. This cell was loaded with high-Fe bearing orthopyroxene and CaCO<sub>3</sub>:Sr<sup>2+</sup> powder as starting materials and equilibrium textures of Fe-bearing bridgmanite coexisting with SiO<sub>2</sub> and magnesiowüstite are observed (Fig. 4.18b). This phase assemblage is characteristic for high-Fe bearing silicate phases at mantle conditions of 30-40 GPa and 2000 K (Dorfman, 2016) and has been detected via *in-situ* XRD-measurements as well (Fig. 4.5). In addition to CaSiO<sub>3</sub>, dolomite with a significant amount of Fe was formed during carbonate-silicate reactions and is indicated in the TEM images with a characteristic mosaic-like structure (inset of Fig. 4.18c). Grain sizes are usually ranging from ~100 nm for the newly formed silicate CaSiO<sub>3</sub> down to a few nm for the carbonate phases, suggesting that recrystallization of the carbonates has occurred during temperature quench. Electron diffraction images of the recovered CaCO<sub>3</sub> phases show *d*-spacings and angles corresponding to a rhombohedral, low-P-T calcite structure and indicate that cc-VII is not quenchable.

Investigations on recovered samples from run DAC24 give further insights on olivine reacting with CaCO<sub>3</sub>:Eu<sup>3+</sup> (Fig. 4.18d). We could detect a phase transition from olivine into phase assemblages consisting of Fe-bearing bridgmanite and (Mg,Fe)O by XRD and also by TEM imaging. CaSiO<sub>3</sub> and magnesite were formed at the interface and clearly document a reaction between the newly formed bridgmanite and CaCO<sub>3</sub>. The magnesite usually contains minor amounts of Fe as shown by chemical EDX analyses of the quenched phases (Appendix D). A possible redistribution of Eu towards the silicate phase is absent. Instead, we could observe the formation of isolated accessory phases, mainly in the form of Eu<sub>2</sub>O<sub>3</sub>. In addition, Eu<sub>2</sub>O<sub>3</sub> tends to be enriched towards the pressure transmitting medium KCl and no Eu was found in the silicate phases in detectable amounts. These results contradicting with our observations for DAC24 made by optical fluorescence in combination with XRD. Conclusions have to be revised based on our TEM investigations and will be discussed in the following chapter.

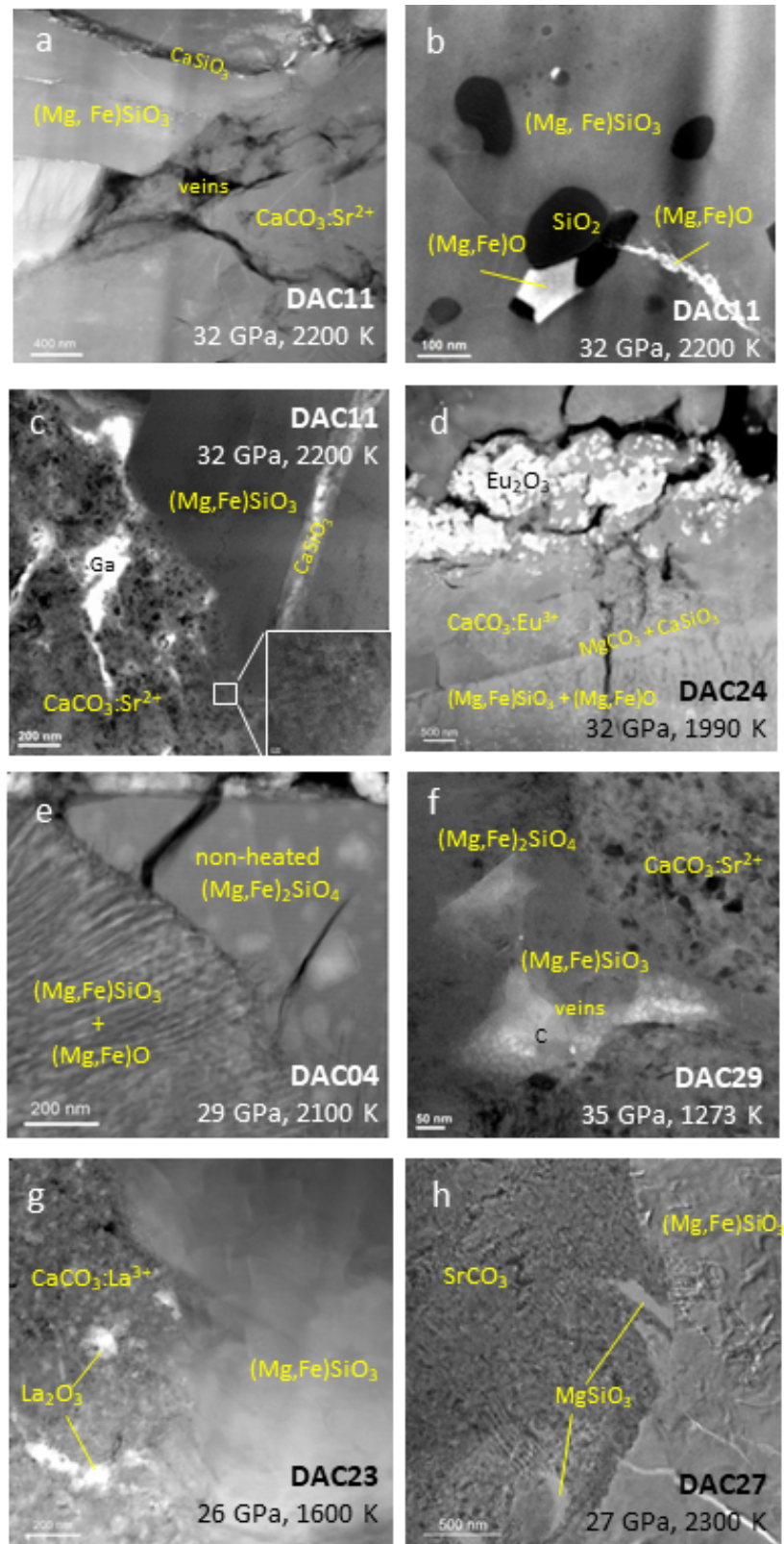


Figure 4.18: TEM on recovered sample material with (doped) carbonates reacted with mantle silicates. HAADF images showing recovered phases of experiment run DAC11 (a,b), DAC24 (d), DAC04 (e), DAC23 (g) and DAC27 (h). Bright field images of present mineral phases of experiment run DAC11 (c) and DAC29 (f) are presented as well.

Electron diffraction images of the quenched (Mg,Fe)SiO<sub>3</sub> phase indicate that bridgmanite has partially transformed into low-pressure (low-P) clinoenstatite with space group  $P2_1/c$  during pressure release and suggests that Fe-bearing bridgmanite is not quenchable. We found that clinoenstatite allows the incorporation of earth alkali elements, such as Ca or Sr originating from the carbonate. Results on this will be discussed in section 5.2.1. The grains of low-P clinoenstatite are crystalline and usually ranging from 100 nm to 500 nm. They have a high number of defects and a slight variation in the Mg,Fe-ratio, indicated by the different brightness of the silicate grains in Fig. 4.18a. The size of the crystals is suitable for crystallographic identification of the mineral phase and unambiguously assigns the structure of  $P2_1/c$ -clinoenstatite to this phase. Bright field imaging further indicates that CaSiO<sub>3</sub>-perovskite and sometimes also bridgmanite turned into an amorphous state during quenching (Fig. 4.18c and f).

In the case of experiment run DAC04, where olivine and pure SrCO<sub>3</sub> are used as starting materials, we could detect (Mg,Fe)<sub>2</sub>SiO<sub>4</sub> in the non-heated area but also Fe-bearing bridgmanite and ferropericlase ((Mg,Fe)O) which were formed during heating (Fig. 4.18e). In addition, areas with SrSiO<sub>3</sub> were observed and are in agreement with our results from *in-situ* XRD measurements of cell DAC04 (Fig. 4.8). Successful recovery of experiment run DAC29 gives insights into resistively heated sample material consisting of (Mg,Fe)<sub>2</sub>SiO<sub>4</sub> + CaCO<sub>3</sub>:Sr<sup>2+</sup> at 1273 K and at 35 GPa (Fig. 4.18f). Voids along the reaction zone are common and very often they are filled with additional non-crystalline materials such as Ga or Cu originating from FIB sample preparation or even with C from the graphite heater, which was close to the hole of the Re gasket, as shown in Fig. 4.18f. Similar to our results from laser-heating, the recovered carbonate phase is polycrystalline and still contains Sr. No observations of CaSiO<sub>3</sub> and magnesite were made in the TEM images and confirm our results from XRD measurements where no reaction was detected and a redistribution of Sr from the carbonate into the silicate phase is absent. In the case La-doped carbonate starting material, one experiment could be recovered successfully and was prepared for TEM analyses. High angle annular dark field (HAADF) image of the recovered sample material is presented in Fig. 4.18g and indicates no redistribution of the trace element La towards the silicate. Similar to our observations with CaCO<sub>3</sub>:Eu<sup>3+</sup>, we observed the formation of isolated accessory phases in form of La<sub>2</sub>O<sub>3</sub>.





# Chapter 5

## Discussion

### 5.1 The fate of $\text{CaCO}_3$ and $\text{SrCO}_3$ in presence of mantle silicates

A number of experiments at various P-T-conditions were conducted in order to better understand the stability of  $\text{CaCO}_3$  and  $\text{SrCO}_3$  in presence of mantle silicates. So far, most of the existing experimental studies on the stability and reactivity of carbonates have been conducted at crustal or shallow mantle conditions (Irving and Wyllie (1973); Newton and Sharp (1975); Wyllie (1987) and references therein). A small number of experimental studies have investigated the stability of carbonates in presence of  $\text{SiO}_2$  at lower mantle conditions (Takafuji et al., 2006; Maeda et al., 2017; Li et al., 2018; Litasov and Shatskiy, 2019) with limited geochemical and geodynamical implications. Our study presents the first experimental data set on  $\text{CaCO}_3$  as well as on  $\text{SrCO}_3$  in reaction with complex mantle silicates, such as  $(\text{Mg,Fe})_2\text{SiO}_4$  and  $(\text{Mg,Fe})\text{SiO}_3$  at high pressure and high temperature. As reported by Seto et al. (2008) and later by Drewitt et al. (2019), calcite-VII or post-aragonite  $\text{CaCO}_3$  (depending on the pressure) indeed react with basaltic compositions to form  $\text{MgCO}_3$  and  $\text{CaSiO}_3$ -perovskite, an important silicate mineral in the lower mantle. Our results based on XRD analyses confirm this reaction, extending it to Mg/Fe-bearing compositions, and we were able to define a reaction boundary for the formation of  $\text{CaSiO}_3$ -perovskite and/or  $\text{SrSiO}_3$ -perovskite, depending on the carbonate starting material. The reaction diagram of  $\text{CaCO}_3$  and  $\text{SrCO}_3$  in contact with silicates of the pseudo-binary system  $(\text{Mg,Fe})_2\text{SiO}_4$ – $(\text{Mg,Fe})\text{SiO}_3$  is shown in Fig. 5.1, and the experimental results can be divided into three groups according to the reactions after R[1.3] - R[1.6] as presented in the introduction: (1) Carbonates reacting with  $(\text{Mg,Fe})_2\text{SiO}_4$ , (2) carbonates reacting with  $(\text{Mg,Fe})\text{SiO}_3$  and (3) decomposition and/or melting of the carbonate phases.

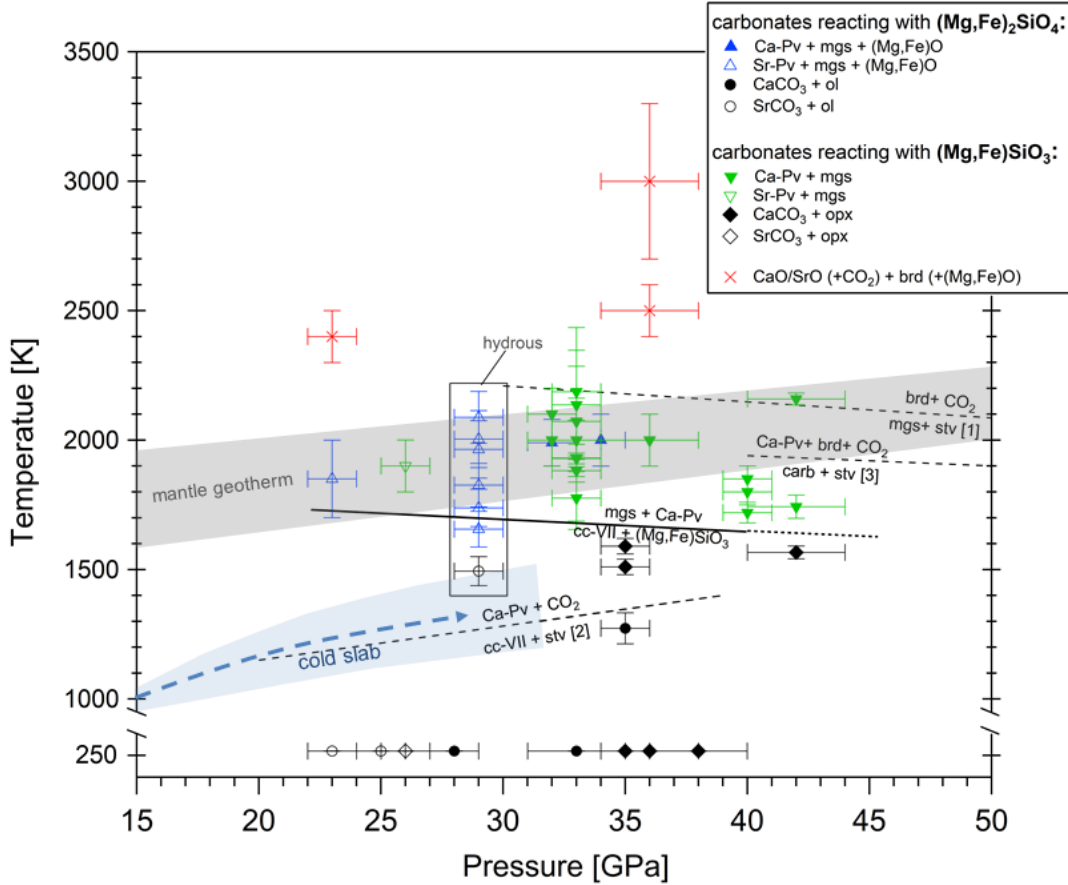


Figure 5.1: Reaction diagram of  $\text{CaCO}_3$  (filled symbols) and  $\text{SrCO}_3$  (open symbols) in presence of mantle silicates determined at high pressure and high temperature. Blue symbols correspond to reactions between carbonates and  $(\text{Mg,Fe})_2\text{SiO}_4$  whereas green symbols are from experiments with carbonates +  $(\text{Mg,Fe})\text{SiO}_3$ . Run DAC04, where hydrous wadsleyite was used as a silicate starting material, is highlighted. Decompositions of the carbonates are marked in red. Boundary for the reaction  $\text{CaCO}_3 + (\text{Mg,Fe})\text{SiO}_3 = \text{CaSiO}_3 + (\text{Mg,Fe})\text{CO}_3$  (R[1.4]) from this study is given as solid line with extension to post-aragonite stability field marked as dashed line. Reaction boundaries from previous studies are given in dashed lines with [1] from Maeda et al. (2017), [2] from Li et al. (2018) and [3] from Drewitt et al. (2019). The mantle geotherm is after Brown and Shankland (1981). Subducting slab geotherms are from Thompson (1992) and Komabayashi (2004). Abbreviations for the run products are as follow: brd = bridgmanite, Ca-Pv =  $\text{CaSiO}_3$ -perovskite, cc = calcite, mgs = magnesite, ol = olivine, opx = orthopyroxene, Sr-Pv =  $\text{SrSiO}_3$ -perovskite, stv = stishovite.

### 5.1.1 Carbonates reacting with $(\text{Mg,Fe})_2\text{SiO}_4$

A reaction between  $(\text{Mg,Fe})_2\text{SiO}_4$  and  $\text{CaCO}_3$  at lower mantle conditions was experimentally documented in three runs before and after heating, whereas the reaction between  $(\text{Mg,Fe})_2\text{SiO}_4$  and  $\text{SrCO}_3$  is studied in two runs but during heating by *in-situ* XRD monitoring. From our experiments, we can constrain that the reaction of the carbonates with mantle silicates is more dependent on temperature rather than

on pressure. This dependence is consistent with findings on the reaction between carbonates and  $\text{SiO}_2$  (Maeda et al., 2017; Li et al., 2018; Litasov and Shatskiy, 2019) as well as between carbonates and basaltic glasses (Seto et al., 2008; Drewitt et al., 2019). The reaction of  $\text{CaCO}_3$  in contact with  $(\text{Mg,Fe})_2\text{SiO}_4$  is characterized by the formation of  $\text{CaSiO}_3$ -perovskite and magnesite with ferropericlase as a byproduct. Temperature conditions for the onset of the present carbonate-silicate reaction is well constrained for  $\text{SrCO}_3$  to about  $\sim 1700$  K based on our results from *in-situ* XRD measurements while it is only broadly constrained for  $\text{CaCO}_3$  between 1500 K and 2000 K. The question that arises is whether the formation of ferropericlase during the transformation from  $(\text{Mg,Fe})_2\text{SiO}_4$  to Fe-bearing bridgmanite and  $(\text{Mg,Fe})\text{O}$  has an effect on the stability of the carbonates and the reaction products.  $(\text{Mg,Fe})\text{O}$  can act as a buffer for  $\text{Fe}^{2+}$ .  $\text{Fe}^{2+}$  is present in the starting silicate material used here and might be redistributed during heating as well.

In general, the distribution of an element depends on pressure, temperature and composition of the phases. In ideal solutions, where the activity coefficient  $\gamma_i$  is equal to 1, the partition coefficient  $K_D$  depends on pressure and temperature, but is independent of composition. If we now consider a partition coefficient for Fe between carbonate (e.g.  $(\text{Mg,Fe})\text{CO}_3$ ) and silicate (e.g.  $(\text{Mg,Fe})\text{SiO}_3$ ) at constant P-T-conditions,  $K_D$  is defined as:

$$K_D = \frac{X_{\text{Fe}^{2+}}^{\text{carb}}}{X_{\text{Fe}^{2+}}^{\text{sil}}} \quad (5.1)$$

with  $X$  as the mole fractions of Fe in the coexisting phases. Mg/Fe-partitioning experiments have shown that Fe is always partitioned preferentially into the silicate phases or oxide phases relative to  $\text{MgCO}_3$  (Martinez et al., 1998) but almost equally between Ca-rich carbonates and olivine (Dalton and Wood, 1993). However, as the solubility of  $\text{FeSiO}_3$  in bridgmanite at high pressure and high temperature is limited (Dorfman, 2016), not all of the Fe is incorporated into the main silicate phase bridgmanite. Besides, Fe is also incorporated into the other reaction products forming Fe-bearing  $\text{MgCO}_3$  and  $(\text{Mg,Fe})\text{O}$ . The formation of  $(\text{Mg,Fe})\text{O}$  thus would stabilize magnesite because of the fact that  $(\text{Mg,Fe})\text{CO}_3$  is much more susceptible to redox breakdown than  $\text{CaCO}_3$  as shown by Dorfman et al. (2018). The role of Fe is also important in the formation of other high-pressure polymorphs and hence for the stability of deep Earth carbonates (Cerantola et al., 2015; Merlini et al., 2015a). The analysis of one experiment where  $\text{CaCO}_3$  reacts with  $(\text{Mg,Fe})_2\text{SiO}_4$  (DAC24) indeed shows the formation of Fe-bearing  $\text{MgCO}_3$  in addition to ferropericlase (see Appendix D for chemical analyses of recovered sample from DAC24). Further experiments are needed to constrain the effect of Fe on the stability of carbonates and to determine the Fe-partitioning coefficient between carbonates and silicates at conditions of the Earth's mantle.

A reaction between  $\text{SrCO}_3$  and  $(\text{Mg,Fe})_2\text{SiO}_4$  at temperatures above 1700 K produces  $\text{SrSiO}_3$ -perovskite, magnesite and  $(\text{Mg,Fe})\text{O}$ . Refinement of the XRD patterns reveals evidence for the presence of a hexagonal, 6H-BaTiO<sub>3</sub>-type structure for the  $\text{SrSiO}_3$ -perovskite phase. This phase has been previously reported by Yusa et al.

(2005) at conditions of 25 GPa and of 1500 K. At higher pressure, SrSiO<sub>3</sub>-perovskite transforms from a octahedral perovskite polytype into a corner-sharing cubic 3C polymorph as most of the hexagonal perovskite polytypes do (Xiao et al., 2013). This high-pressure polymorph is isostructural to CaSiO<sub>3</sub>-perovskite. On pressure release, SrSiO<sub>3</sub>-perovskite changes into an amorphous state as CaSiO<sub>3</sub>-perovskite does, or might even decompose into SrO and SiO<sub>2</sub>. Apart from *in-situ* heating experiments in run DAC04 that document the formation of SrSiO<sub>3</sub>-perovskite very well, additional measurements at 23 GPa and at 1850 K (DAC13) confirm the formation of SrSiO<sub>3</sub>-perovskite in this P-T-region.

### 5.1.2 Carbonates reacting with (Mg,Fe)SiO<sub>3</sub>

The reaction behaviour of CaCO<sub>3</sub> in presence of (Mg,Fe)SiO<sub>3</sub> or pure MgSiO<sub>3</sub> glass was studied as well and is presented in Fig. 5.1. The main difference to the reaction between carbonates and (Mg,Fe)<sub>2</sub>SiO<sub>4</sub> is the absence of (Mg,Fe)O as a byproduct. This consequently simplifies the analyses of the reaction products but does not include the impact of (Mg,Fe)O, an important phase in the deep lower mantle, on the stability of deep Earth carbonates.

Contrary to theoretical DFT calculations made by Oganov et al. (2008) and Pickard and Needs (2015) where the formation of CaSiO<sub>3</sub>-perovskite from carbonate-silicate reactions was postulated only at very high pressures, we can define the onset for a reaction between (Mg,Fe)SiO<sub>3</sub> and CaCO<sub>3</sub> already at shallow lower mantle conditions, e.g. at 33 GPa and 1800 K (see Fig. 4.5, run DAC11). Furthermore, additional *in-situ* XRD measurements during heating at 42 GPa in run DAC08 record the formation of CaSiO<sub>3</sub>-perovskite already at 1600 K suggesting a negative slope for the reaction line CaCO<sub>3</sub> + (Mg,Fe)SiO<sub>3</sub> = CaSiO<sub>3</sub> + (Mg,Fe)CO<sub>3</sub>. However, the simulations by Oganov et al. (2008) and Pickard and Needs (2015) were carried out up to a pressure of 200 GPa and at T = 0 K, and it is unclear whether CaCO<sub>3</sub> is stable also at high temperature. Our results show that a reaction of CaCO<sub>3</sub> with (Mg,Fe)SiO<sub>3</sub> (R[1.4]) above 1700 K will prevent CaCO<sub>3</sub> from being subducted into the deep lower mantle. Instead, magnesite seems to be the most stable carbonate phase. The negative slope for a reaction of CaCO<sub>3</sub> following R[1.4] is in disagreement with experiments on the decarbonation of CaCO<sub>3</sub> in reaction with SiO<sub>2</sub> by Li et al. (2018). The discrepancy between the results from Li et al. (2018) and our results for the onset of the reactions producing CaSiO<sub>3</sub>-perovskite is likely caused by studying different chemical systems. Whereas a reaction between CaCO<sub>3</sub> and SiO<sub>2</sub> produces directly CO<sub>2</sub>, our results rely on the formation of magnesite, suggesting that carbonates are stable at these conditions. Furthermore, different experimental approaches have been applied. Li et al. (2018) have used a powder mixture of natural calcite and SiO<sub>2</sub> embedded in a layer of NaCl or KCl. Carbonates and NaCl/KCl are usually hygroscopic and contamination of H<sub>2</sub>O may affect the reaction temperatures. It is well known that even small amounts of water (e.g. 5 wt% H<sub>2</sub>O) reduces the melting temperature in most silicate systems (Grove et al. (2006); Grove and Till (2019) and references therein). Furthermore, Li et al. (2018) added 5 wt% Pt to the sample material which acted as a pressure calibrant and as a

laser absorber. The mixing with Pt could also have an effect on the differing results of Li et al. (2018) and our current study. Experimental data on the reaction between dolomitic compositions and stishovite are given by Maeda et al. (2017) and Drewitt et al. (2019) as shown in Fig. 5.1 and document the same negative slope for the phase boundaries but at higher temperatures. At conditions above 40 GPa and 2200 K, also magnesite will undergo a decarbonation reaction as proposed (Seto et al., 2008; Maeda et al., 2017; Drewitt et al., 2019) and a subsequent CO<sub>2</sub> dissociation will make diamond as the stable form of carbon transport into the deep lower mantle.

The stability of pure SrCO<sub>3</sub> in contact with (Mg,Fe)SiO<sub>3</sub> was studied at rather low pressures and already moderate temperatures above 1800 K and results from these experiments poorly document the onset conditions for the formation of SrSiO<sub>3</sub>-perovskite plus magnesite. *Ex-situ* TEM analyses on run DAC27 were performed in order to confirm or disprove the formation of SrSiO<sub>3</sub>-perovskite. SEM-Investigations on a FIB foil cut from the recovered sample give information on the chemical composition of the reaction products. Results from element mapping and additional line scans along the interface between heated SrCO<sub>3</sub> and (Mg,Fe)SiO<sub>3</sub> using an EDX detector indicate that Mg and Fe have partitioned into the carbonate phase whereas Sr is incorporated into the silicate along the interface (see Fig. 5.5 and Appendix D). This unambiguously demonstrates that there is elemental redistribution of the cations between carbonates and silicates. As the formation of low-P clinoenstatite during quenching has a significant effect on the stability of Sr-bearing (Mg,Fe)SiO<sub>3</sub>, questions remain whether a redistribution took place during quenching or at high temperature and high pressure.

### 5.1.3 Decomposition and melting of CaCO<sub>3</sub> and SrCO<sub>3</sub>

From our experimental data, we can constrain an upper limit for reaction  $\text{CaCO}_3 + (\text{Mg,Fe})_2\text{SiO}_4 = \text{CaSiO}_3 + (\text{Mg,Fe})\text{CO}_3 + (\text{Mg,Fe})\text{O}$  (R[1.3]) and  $\text{CaCO}_3 + (\text{Mg,Fe})\text{SiO}_3 = \text{CaSiO}_3 + (\text{Mg,Fe})\text{CO}_3$  (R[1.4]) which is defined by the absence of CaSiO<sub>3</sub>-perovskite and the formation of oxide phases (e.g. CaO) at very high temperatures (>2500 K). We observed a formation of CaO in experiment run DAC12 at a maximum temperature of 3000(300) K and in experiment run DAC18 at 2500(100) K and 3000(300) K (see Fig. 4.4). A phase diagram of pure CaCO<sub>3</sub> is presented in Fig. 5.2 and is used for evaluating the possibility of decomposition of CaCO<sub>3</sub> in the presence of mantle silicates. The melting curve in this figure is marked as a blue line and was determined by Li et al. (2017) up to 22 GPa using conductivity measurements in a multi-anvil press. At higher pressure and temperature CaCO<sub>3</sub> starts to decompose into CaO + CO<sub>2</sub> (Bayarjargal et al., 2010; Spivak et al., 2012), where CO<sub>2</sub> itself breaks down to diamond and oxygen under geotherm conditions above 70 GPa. The P-T-conditions of the experiments from this study, where no CaSiO<sub>3</sub>-perovskite was formed, primarily report the absence of a reaction between CaCO<sub>3</sub> and the silicate phase at very high temperatures (<2500 K) and are highlighted in Fig. 5.2. At these temperatures, we can see that melting or even decomposition of the simple system CaCO<sub>3</sub> is possible. Usually, the solidus in multicomponent systems is lower than it is in the simple system. Hence, in a system where CaCO<sub>3</sub> is mixed with

Mg-Fe-silicates, the solidus line of  $\text{CaCO}_3$  can be completely different since the melt also contains Mg and Fe.

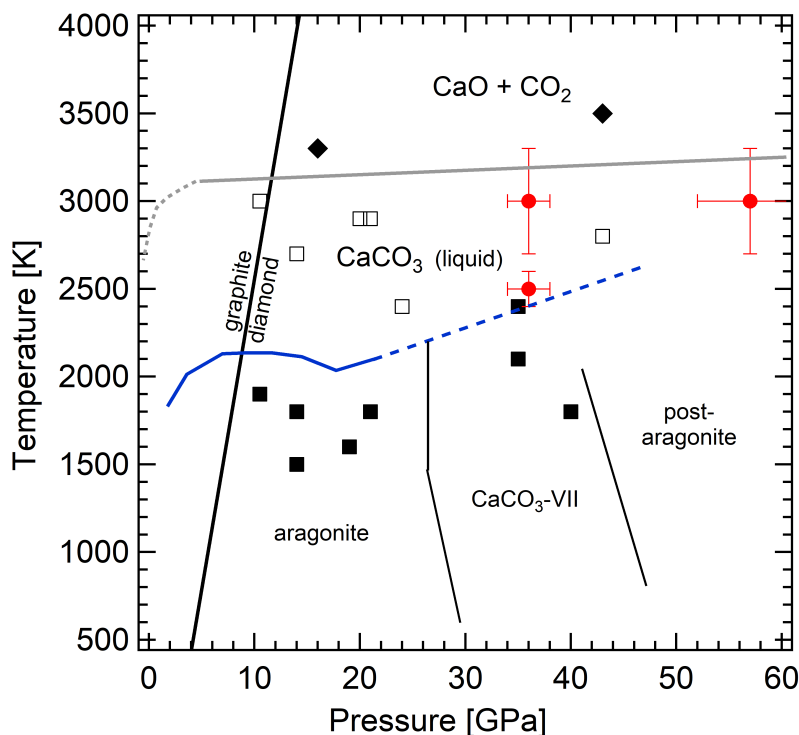


Figure 5.2: P-T-phase diagram of the simple system  $\text{CaCO}_3$ . Black symbols are experimental data from Spivak et al. (2012) without melting (solid squares) and with congruent melting (open squares). Solid diamonds denote the formation of diamond. Experiments of the multicomponent systems  $(\text{Mg,Fe})\text{SiO}_3\text{-CaCO}_3$  and  $(\text{Mg,Fe})_2\text{SiO}_4\text{-CaCO}_3$  from this study with CaO detected in the reaction products are shown as red filled circles. The blue line shows the melting curve determined by Li et al. (2017) with an extrapolation shown as dashed blue line. The grey line denotes the decomposition boundary given by Ivanov and Deutsch (2002). The thick black line marks the phase transformation from graphite to diamond (Bundy et al., 1996). Thin black lines are phase boundaries for the HP polymorphs aragonite,  $\text{CaCO}_3\text{-VII}$  and post-aragonite from Bayarjargal et al. (2018).

In the case of  $\text{SrCO}_3$ , one experiment was conducted at 23(1) GPa and 2400(100) K (DAC13) where evidence is found for the formation of SrO. Up to date, there is no data available for the melting and for the decomposition of  $\text{SrCO}_3$  at high pressure thus making it difficult to constrain the stability of this phase. However, we conclude that the absence of a reaction between  $\text{CaCO}_3$  or  $\text{SrCO}_3$  and the mantle silicates at very high temperatures is caused by a decomposition of the carbonate phase prior to the reaction.

## 5.2 Elemental redistribution of Sr, La and Eu during carbonate-silicate reactions at conditions of the Earth's mantle

A number of studies have investigated the partitioning of trace elements between mantle silicates and melts of peridotitic compositions (Hirose et al., 2004; Corgne et al., 2005) as well as between mantle silicates and carbonatitic melts (Dalou et al., 2009). The analyses on the partitioning of trace elements among mantle phases illustrate that Sr and REE partition preferentially into  $\text{CaSiO}_3$ -perovskite and majoritic garnet rather than into bridgmanite, stishovite or wüstite (Badro et al., 2007; Dalou et al., 2009). Distinct differences exist in the partitioning of trace elements between  $\text{CO}_2$ -bearing silicate systems and  $\text{CO}_2$ -free systems. As shown by Dalou et al. (2009), REE are more compatible with silicates in carbonatitic melts whereas Sr seems to be more incompatible when  $\text{CO}_2$  is present. Investigations on the elemental partitioning *in-situ* at high-pressure and high-temperature were performed in a few studies using  $\mu$ -XRF on fluid-(silicate)-melt interactions (Borchert et al., 2009, 2013) as well as on interactions between silicates and iron melts (Petitgirard et al., 2012). Knowledge is basically missing on the element mobility in solid–solid interactions at conditions of the Earth's mantle.

Our aim was to observe a change in the elemental distribution of selected trace elements during carbonate-silicate reactions by performing spatially resolved  $\mu$ -XRF on the sample material before and after heating. This method has been used previously for the detection of Zr-, Pd- and Ru-partitioning between silicate and iron melts by Petitgirard et al. (2012) and gave reasonable values for the element concentrations on a ppm-level. However, accurate determination of trace element partitioning *in-situ* at high pressure and high temperature remains difficult. Using the experimental setup presented here, some trace elements (La, Eu) could not be reliably quantified with  $\mu$ -XRF because of the fact that their most intense  $K_\alpha$  fluorescence lines are superimposed by the background signal from the inelastic scattering of photons by the diamond. In the case of Eu, emission lines for Eu- $K_\alpha$  are above the maximum excitation energy of 42.7 keV and only Eu-L-lines at an energy between 5.8 keV (Eu- $L_{\alpha 1}$ ) and 7.5 keV (Eu- $L_{\gamma 1}$ ) are excited. A strong absorption of the fluorescence signal in the diamonds and the overlapping Fe- $K_\alpha$  line in that region makes it difficult to measure precisely the Eu-content in the sample material by  $\mu$ -XRF.

Results from optical fluorescence measurements record a dramatic change in the spatial distribution of Eu when comparing fluorescence maps before and after heating (Fig. 4.17). The dominant substitution mechanism for the incorporation of  $\text{Eu}^{3+}$  into Al-free  $\text{CaSiO}_3$ -perovskite takes place by creation of Ca-vacancies such as  $3 \text{Ca}^{2+} \leftrightarrow 2 \text{Eu}^{3+} + \square$  as reported by Corgne et al. (2003). However, this only applies for trace element concentrations below 1000 ppm when Henry's law is complied (Corgne et al., 2003). Usually, the amount of  $\text{Al}^{3+}$  at the Si-site in the  $\text{CaSiO}_3$ -perovskite controls the substitution of  $\text{Ca}^{2+}$  by  $\text{Eu}^{3+}$ . In the absence of Al we would then observe restricted incorporation of  $\text{Eu}^{3+}$  into  $\text{CaSiO}_3$ -perovskite. With the help of additional

TEM analyses on the recovered sample material, we can assign a change in the spatial distribution of Eu mainly to the formation of  $\text{Eu}_2\text{O}_3$  oxide phases as highlighted in Fig. 4.18d and no Eu was detected in the  $(\text{Mg,Fe})\text{SiO}_3$  phase or in the  $\text{CaSiO}_3$  phase. These findings leads us to the conclusion that a redistribution of Eu during heating has occurred but an incorporation of Eu into the silicates cannot be proven. Instead Eu tends to form isolated oxide phases.

In order to evaluate the presence of Sr-incorporation into  $\text{CaSiO}_3$  at a submicrometer scale, TEM imaging was performed with chemical analysis of the recovered sample material. Spectral imaging of amorphous  $\text{CaSiO}_3$  in samples were  $\text{CaCO}_3:\text{Sr}^{2+}$  has reacted with mantle silicates gave no or only very small (below the detection limit) concentrations of Sr in  $\text{CaSiO}_3$ . These measurements are contrary to our expectations and from theoretical calculations (Tab. 5.1). Therefore, further analysis with nanometer-resolution secondary ion mass spectrometry (NanoSIMS) should be considered. This technique allows high analytical precision and sensitivity in terms of element concentrations and with a spatial resolution of the order of 100 nm or even less. In contrast to  $\mu\text{-XRF}$ , the elements are measured in sequences and the detection limit for trace elements is usually better than conventional STEM or EMPA and can reach ppm-levels with proper calibrations.

In the case of pure  $\text{SrCO}_3$  reacting with  $(\text{Mg,Fe})_2\text{SiO}_4$  and/or  $(\text{Mg,Fe})\text{SiO}_3$  we clearly see a distribution of Sr by comparing  $\mu\text{-XRF}$  maps before and after heating (see Fig. 4.15 for DAC04 and Fig. 4.16 for DAC13). A redistribution of Sr is detected within the spatial resolution of the X-ray beam over a section of about 5 to 10  $\mu\text{m}$ . XRD images during heating were recorded and indicate that the change in the concentrations of Sr can be attributed to the formation of  $\text{SrSiO}_3$ -perovskite and/or SrO rather than to an incorporation of Sr into coexisting  $(\text{Mg,Fe})\text{SiO}_3$ -perovskite. At ambient pressure and high temperature,  $\alpha\text{-CaSiO}_3$  (Pseudowollastonite) and  $\text{SrSiO}_3$  build a system that shows binary eutectic behaviour and allows the incorporation of Sr into  $\text{CaSiO}_3$  by about 40 wt% (Moir and Glasser, 1974). At higher pressure, e.g. at  $\sim 38$  GPa, isostructural phases of  $\text{SrSiO}_3$ -perovskite and  $\text{CaSiO}_3$ -perovskite are formed enabling the substitution of  $\text{Ca}^{2+}$  for  $\text{Sr}^{2+}$  with only small local changes in the structure (Xiao et al., 2013). Our results on the stability of  $\text{SrCO}_3$  in presence of mantle silicates clearly demonstrate that an introduction of Sr into the deep Earth is possible by the decarbonation and reaction of  $\text{SrCO}_3$  and the ensuing incorporation of Sr into cubic  $\text{CaSiO}_3$ -perovskite and not into Fe-bearing bridgmanite.

### 5.2.1 Incorporation of $\text{Ca}^{2+}$ and $\text{Sr}^{2+}$ into $(\text{Mg,Fe})\text{SiO}_3$ high pressure polymorphs during carbonate-silicate reactions

Interesting observations were made in experiment run DAC23 with natural enstatite and  $\text{CaCO}_3:\text{La}^{3+}$  as starting materials and at maximum conditions of 26(2) GPa and 1600(100) K. The quenched sample was analysed by TEM and we observed that bridgmanite transformed into low-pressure (low-P) clinoenstatite with structure  $P2_1/c$  during pressure release. More interestingly and thanks to high-resolution TEM analyses, we could observe an incorporation of  $\text{Ca}^{2+}$  into low-P clinoenstatite originating



from the carbonate along the reaction zone. The composition of the quenched silicate phase gradually changes from pure  $(\text{Mg,Fe})\text{SiO}_3$  in the center of the silicate grain to  $(\text{Ca,Mg,Fe})\text{SiO}_3$  at the reaction zone (Fig. 5.3). The change in chemistry has been used to estimate the shift of the reaction front as illustrated in Fig. 5.3. Using the bright field imaging mode additionally shows that all recovered silicate and carbonate phases are crystalline.

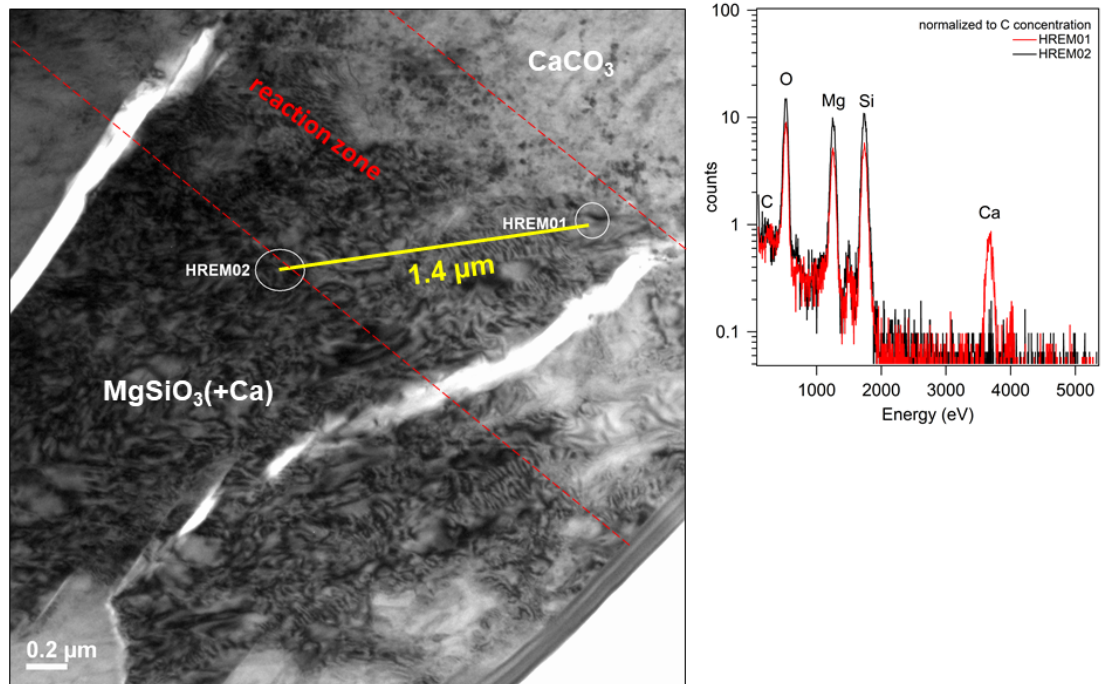


Figure 5.3: Bright field image of recovered sample from run DAC23 heated at 26(2) GPa to a temperature of 1600(100) K. The distance between pigeonite  $((\text{Ca,Mg,Fe})\text{SiO}_3)$  at the reaction front to pure  $(\text{Mg,Fe})\text{SiO}_3$  clinoenstatite in the center of the grain is marked in yellow and gives an estimated path of 1.4  $\mu\text{m}$ .

The incorporation of  $\text{Ca}^{2+}$  widens the crystal structure of  $P2_1/c$ -clinoenstatite to more likely  $P2_1/c$ -pigeonite structure (Fig. 5.4). Lattice parameters for the low-P clinoenstatite are given by Pannhorst (1984) for  $\text{MgSiO}_3$  composition with  $a = 9.620(5) \text{ \AA}$ ,  $b = 8.825(5) \text{ \AA}$ ,  $c = 5.188(5) \text{ \AA}$  and  $\beta = 71.67(17)^\circ$ . The lattice parameters of low-T pigeonite for  $\text{Wo}_9\text{En}_{39}\text{Fs}_{52}$  compositions are  $a = 9.706(2) \text{ \AA}$ ,  $b = 8.950(1) \text{ \AA}$ ,  $c = 5.246(1) \text{ \AA}$  and  $\beta = 108.59(1)^\circ$  (Brown et al., 1972). Pigeonite is known to undergo a reversible non-quenchable  $\text{P} \rightleftharpoons \text{C}$  centered phase transition at high temperature (Brown et al., 1972). The same phase transition occurs also in clinoenstatite during compression (Angel et al., 1992). Estimated lattice parameters from electron diffraction images (Fig. 5.4) of the recovered silicate phases are similar to both the low-P clinoenstatite phase and the low-T pigeonite phase.

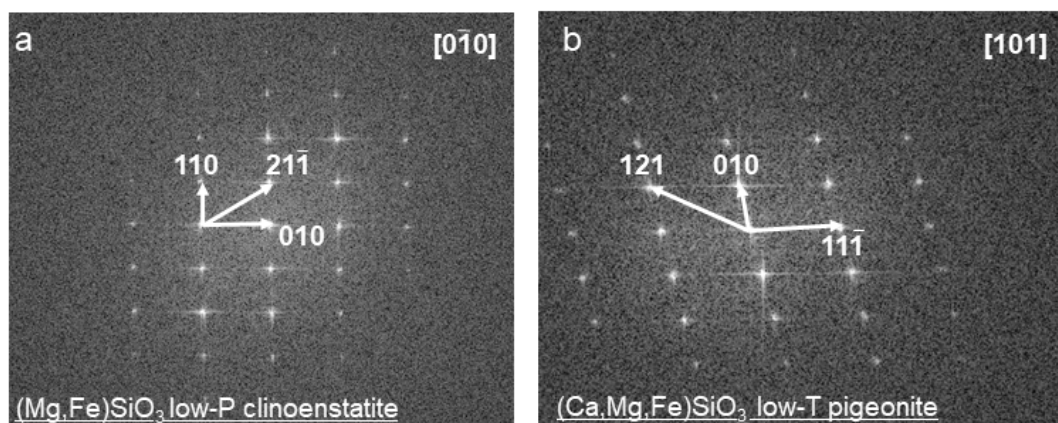


Figure 5.4: a. Electron diffraction image of  $(\text{Mg,Fe})\text{SiO}_3$  low-P clinoenstatite in direction  $[0\bar{1}0]$ . Estimated  $d$ -values for 110,  $2\bar{1}\bar{1}$  and 010 in low-P clinoenstatite are 6.63 Å, 3.53 Å and 4.12 Å, respectively. b. Electron diffraction image of  $(\text{Ca,Mg,Fe})\text{SiO}_3$  low-T pigeonite in direction  $[101]$  with estimated  $d$ -values for 121, 010 and  $1\bar{1}\bar{1}$  of 3.35 Å, 8.13 Å and 4.07 Å, respectively.

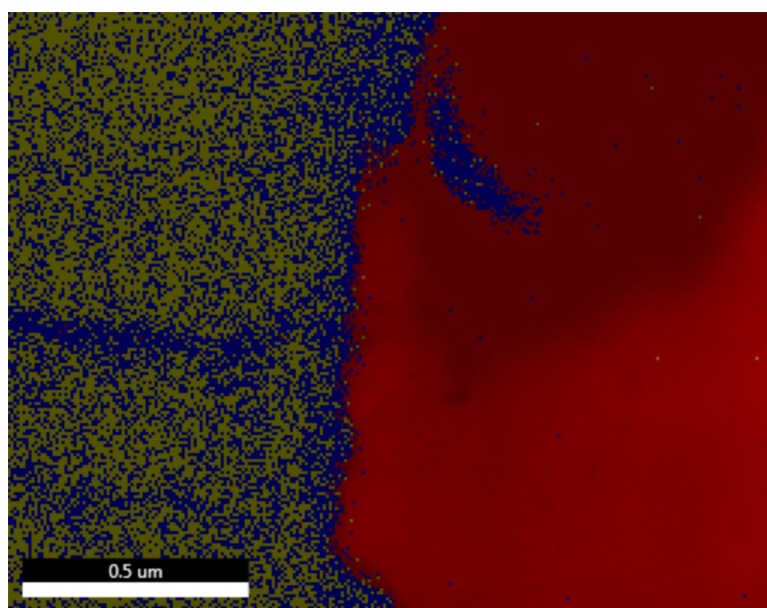


Figure 5.5: (a) Colour map of the recovered sample from run DAC27 ( $\text{SrCO}_3 + (\text{Mg,Fe})\text{SiO}_3$ ) heated at 27(1) GPa to a temperature of 2300(100) K. SEM-EDX element mapping shows three distinct areas with different compositions: Mg- and Fe-bearing  $\text{SrCO}_3$  (red),  $(\text{Mg}_{0.85}\text{Fe}_{0.15})\text{SiO}_3$  low-P clinoenstatite (yellow) and  $(\text{Mg}_{0.65}\text{Fe}_{0.15}\text{Sr}_{0.2})\text{SiO}_3$  clinopyroxene (blue).

A second experiment was conducted on the same natural enstatite starting material in contact with  $\text{SrCO}_3$ . Again, a transformation from bridgmanite into low-P clinoenstatite has occurred during pressure release and the incorporation of Sr into  $(\text{Mg,Fe})\text{SiO}_3$  was observed. Figure 5.5 shows an element map of the recovered sample from experiment DAC27 consisting of  $\text{SrCO}_3$  (red) and  $(\text{Mg,Fe})\text{SiO}_3$  (yellow) and with the formation of Sr-bearing low-P clinoenstatite at the interface (blue). Chemical ana-

lyses and the performance of line scans over the interface further indicate the incorporation of Mg and Fe into  $\text{SrCO}_3$  (see Appendix D). Our observations on carbonate-silicate reactions show that a redistribution of Ca and Sr (originating from the carbonate) into the silicate phase has occurred during quenching and significant changes in the lattice parameters of the  $(\text{Mg,Fe})\text{SiO}_3$  phase have been measured. Further experiments are needed to better understand this phenomenon.

### 5.3 Limitations of the current study

Our research on carbonate stability and the elemental fractionation in carbonate-silicate reactions has two limitations. The first is reaching a thermodynamic equilibrium state in laser-heated diamond anvil cell experiments. The second is a reliable quantification of trace element concentrations in the products. These limitations underline the difficulty of collecting data on solid-solid reactions at Earth mantle conditions.

In general, thermodynamic equilibrium is defined as the minimum of thermodynamic potentials, such as the Gibbs free energy, at constant pressure, temperature and composition. A thermodynamic equilibrium can be reached when the system interacts with the surroundings over a sufficiently long time. In a DAC, there are processes or conditions that may cause the sample material to deviate from thermodynamic equilibrium during heating. The first process is the generation of thermally induced pressure gradients. The volume of the sample chamber is constrained upon heating and hence an increase in pressure is caused that is proportional to the temperature difference (Boehler, 2000). To ideally eliminate this effect, we have chosen the use of hydrostatic pressure media, such as argon or KCl, in dedicated experiments and measured the ruby fluorescence for pressure calibration in only unheated areas. It is clear that a sample which is heated non-uniformly will flow or crack due to thermal expansion and we actually experienced gasket expansion and/or sample movement during heating in some of our experiments where no pressure transmitting medium (PTM) was used (e.g. DAC12).  $\mu$ -XRF-map results from these experiments have to be treated with caution with respect of the trace elemental redistribution since the apparent movement of the trace elements could be caused by gasket expansion and or sample flow. Secondly, compression is applied in the LHDAC along one single axis and hence deviatoric stress exists, especially when no PTM is used. The relaxation of deviatoric stresses during heating leads to a change of the hydrostatic stress in the cell which is not always compensated by the thermal pressure (Kavner and Duffy, 2001). Conditions may not be recovered during thermal quench and therefore *in-situ* pressure monitoring using a PTM with well-known equation of state is essential but was not fulfilled in each of our experiments.

A large thermal gradient within the sample can exist during laser heating. To minimize it, optimized focusing optics were used to produce a large and homogeneous heated area. Usually, a spot size in the order of  $\sim 20\ \mu\text{m}$  was achieved using a Yb-fiber laser in the experiments performed at beamline P02.2, PETRA III, and which is suitable for heating small samples at pressures above 40 GPa that are less thermally insulated. The temperature profile of the laser is Gaussian with a beam quality factor of  $M^2 < 1.1$  implying a very low degree of variation of the laser beam from ideal Gaussian beam (Liermann et al., 2015). However, small temperature gradients occur along the diameter of the sample chamber. As an example, the radial temperature profile on a tungsten foil surrounded by argon at 5 GPa is given by Schultz et al. (2005) with a temperature gradient of approx.  $2.5\ \text{K}/\mu\text{m}$  over a range of  $40\ \mu\text{m}$  and  $3\ \text{K}/\mu\text{m}$  in the region of the laser-heated spot (Fig. 5.6). We can suppose that temperature was more uniformly distributed close to the laser heating spot and in the center. Therefore, elemental redistribution of Sr, La and Eu detected around the laser-heated spot is a result of fractionation processes. Considering a redistribution of the elements at distances of more than  $40\ \mu\text{m}$  away from the laser heated spot, this can be likely caused by larger temperature gradients in the sample chamber also known as Soret effect (Mueller et al. (2010) and references therein) which describes the fractionation of elements by thermally induced diffusion. In the case of using a  $\text{CO}_2$ -laser, only single-sided laser-heating was performed but the temperature was measured on both sides of the sample (see for experimental details section 2.4.2) making it possible to evaluate the thermal gradient along the sample. The difference in temperature between upstream and downstream was usually not larger than 100 K.

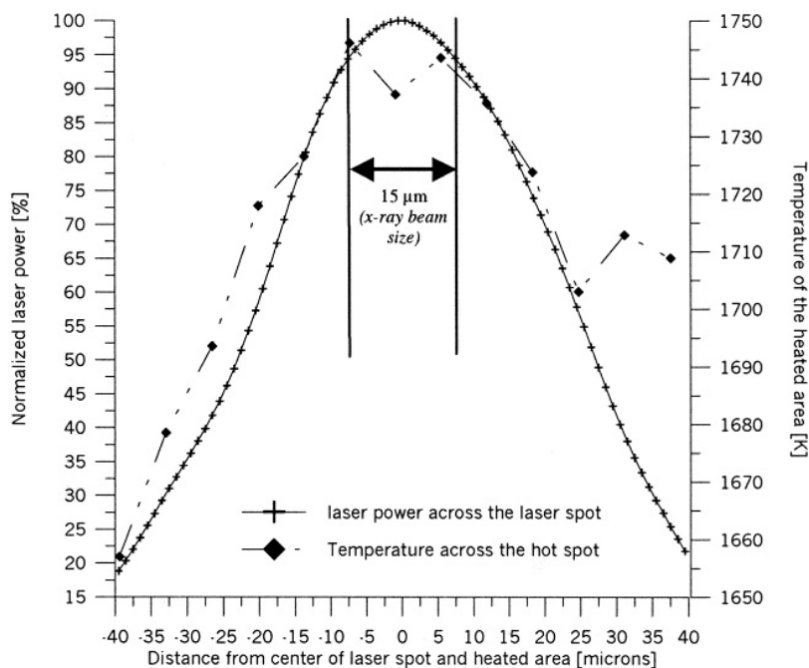


Figure 5.6: Spatial distribution of the laser power and the corresponding temperature variation in a tungsten foil heated at 5 GPa to a maximum temperature of 1750 K after Schultz et al. (2005).

An important key parameter, that we do not consider in our experiments, is the role of oxygen fugacity ( $fO_2$ ). It is controlling the stability of C-bearing phases and the physical and chemical interactions in the deep Earth. In general, the variation in  $fO_2$  changes the oxidation state of multivalent elements. This effect is important for our experiments since Fe, with its multiple valences, is partitioned between the silicates and carbonates. With increasing  $fO_2$  the higher valent species  $Fe^{3+}$  gets stabilized (Zhang, 2010) and this could have an effect on the stability of magnesite, which is formed during carbonate-silicate reaction studied here. Carbon-iron redox interactions have already shown a destabilization of  $MgCO_3$  in presence of metallic Fe (Dorfman et al., 2018) at deep lower mantle conditions. On the other hand, the carbonate phase  $CaCO_3$  is less susceptible to redox break down and will remain stable at redox conditions present at the lower mantle. Controlling the oxygen fugacity in the DAC is difficult as the  $fO_2$  may be buffered by the diamond (CCO buffer) or, in our case, even by the sample material itself (EMOG/D buffer). It is generally accepted that the carbonate-silicate reactions are expected to take place in the average lower mantle with  $fO_2$  conditions below the iron-wüstite buffer (Frost and McCammon, 2008).

Table 5.1: Theoretical mass balance calculation for the content of trace elements in the newly formed  $CaSiO_3$ -perovskite phase. The partition coefficients  $D^{CaPv/melt}$  for Sr and La between  $CaSiO_3$ -perovskite and melt are listed as well (Taura et al., 2001; Corgne and Wood, 2002).

	Sr <sup>2+</sup>	La <sup>3+</sup>	Eu <sup>3+</sup>
$D^{CaPv/melt}$	1.43(5) <sup>1</sup>	1.4 <sup>2</sup>	-
initial content in doped carbonates M:CaCO <sub>3</sub> [ppm]	24000	5000	10000
content in reacted silicate phase M:CaSiO <sub>3</sub> [ppm]	247	9.5	10.2
$C_{mdl}$ for $\mu$ -XRF	7	500	n.a.

<sup>1</sup>Corgne and Wood (2002), <sup>2</sup>Taura et al. (2001).

During heating, rapid reactions should occur at crystal–crystal interfaces. To ensure this, we performed experiments using homogeneous mixed powders. On the other hand, a homogeneous distribution of the phases and the corresponding elements is insufficient for detecting differing concentrations in the ppm-range using the TEM. We therefore choose a compromise: a sample arrangement made of a silicate single crystal embedded into a carbonate powder layer to ensure a close contact between the two phases and a good reactivity. In addition, the silicate single crystals could be easily identified in the XRD-XRF-measurements by the reflections of a single crystal in the XRD maps and, if present, by the fluorescence of Fe. As reported in section 4.2.2, changes in the distribution of the trace elements Sr, La and Eu are small for doped  $CaCO_3$  powder samples reacting with mantle silicates. Usually, grain sizes not larger than 100 - 200 nm were observed in the run products for  $CaSiO_3$ , which is the main host for these trace elements. These grain sizes lie below the spatial resolution of the current experimental

setup with beam diameters of  $2\ \mu\text{m} \times 2\ \mu\text{m}$ . We calculated theoretical trace element concentrations for the reaction products and listed  $\text{CaSiO}_3$  perovskite-melt partitioning coefficients which give a maximum value for the concentration of Sr and La in  $\text{CaSiO}_3$  (Tab. 5.1). Partition coefficients measured by LA-ICP-MS for Sr are 1.43 (Corgne and Wood, 2002) and for La, measured by SIMS, are similar with 1.4 (Taura et al., 2001) suggesting that Sr and La are compatible. Assuming that the starting doped carbonate material  $\text{M:CaCO}_3$  fully reacts into  $\text{M:CaSiO}_3 + (\text{Mg,Fe})\text{CO}_3 (+(\text{Mg,Fe})\text{O})$  after R[1.3] and R[1.4] would give a content for Sr of 247 ppm and for Eu 10.2 ppm in the  $\text{CaSiO}_3$ -perovskite phase and only 9.5 ppm for La. As shown in Tab. 5.1, the concentrations for La in the reaction product  $\text{M:CaSiO}_3$  are below the detection limit of 500 ppm that has been estimated on beamline P02.2 using an excitation energy of 42.7 keV. This could be a possible explanation that we could not detect any changes in the distribution of La detected by  $\mu$ -XRF as shown in Fig. 4.14. Considering the detection limits and a beam diameter of  $2\ \mu\text{m}$  we can conclude that XRF measurements alone do not clearly document the elemental transport of Sr, La or Eu into the newly formed  $\text{CaSiO}_3$ -perovskite phase.

## Chapter 6

# Conclusions and geological implications

Considerable insights have been achieved with regard to the stability of carbonates in contact with mantle silicates and with implications on the redistribution of Sr, La and Eu during carbonate-silicate reactions. In particular, we investigated the reaction between doped  $\text{CaCO}_3$  and silicates in the pseudo-binary system  $(\text{Mg,Fe})_2\text{SiO}_4$ – $(\text{Mg,Fe})\text{SiO}_3$  using laser-heated or resistively heated DACs. We found that  $\text{CaCO}_3$  reacts with Fe-bearing bridgmanite to  $\text{CaSiO}_3$ -perovskite plus Fe-bearing magnesite and/or Ca,Mg,Fe-dolomite at shallow lower mantle conditions. The onset for this reaction boundary is consistent with findings on the reaction between carbonates and  $\text{SiO}_2$ -compounds (Maeda et al., 2017; Drewitt et al., 2019) but at lower temperatures, e.g. at 1500 - 1700 K in a pressure range from 25 - 45 GPa. Our data set allows us to constrain the reaction boundaries of  $\text{CaCO}_3$  much more precisely with an increased number of high-P and high-T measurements as compared to Li et al. (2018) who have studied the decarbonation of  $\text{CaCO}_3$  in reaction with  $\text{SiO}_2$ . Furthermore, we can constrain an upper limit for the reaction  $\text{CaCO}_3 + (\text{Mg,Fe})_2\text{SiO}_4 = \text{CaSiO}_3 + (\text{Mg,Fe})\text{CO}_3 + (\text{Mg,Fe})\text{O}$  (R[1.3]) and for the reaction  $\text{CaCO}_3 + (\text{Mg,Fe})\text{SiO}_3 = \text{CaSiO}_3 + (\text{Mg,Fe})\text{CO}_3$  (R[1.5]) which is defined by the absence of  $\text{CaSiO}_3$ -perovskite and the formation of oxide phases (e.g.  $\text{CaO}$ ) at high temperatures ( $>2500$  K). Our study provides additional first insights on the stability of  $\text{SrCO}_3$  at Earth's mantle conditions and in contact with silicates. We observed a high-pressure phase transition in  $\text{SrCO}_3$  to a  $Pmmn$ -structured post-aragonite phase and were able to calculate the equation of state of this phase with  $V_0 = 229(2) \text{ \AA}^3$ ,  $K_0 = 103(10) \text{ GPa}$  and  $K'_0 = 2.3(6)$ . A reaction between  $\text{SrCO}_3$  and Fe-bearing bridgmanite is characterized by the formation of magnesite and also evidence is given for the formation of a hexagonal structured  $\text{SrSiO}_3$ -perovskite phase although the properties of this phase are based on very limited data. Supposing that carbonates are not melted in the transition zone if transported along cooler geotherms as reported by Thompson (1992) and Komabayashi (2004) then some carbonates may be also subducted into the lower mantle. Recent findings on  $\text{CaCO}_3$  inclusions in diamonds from the lower mantle (Brenker et al., 2007) could be a proof for this statement. In addition and with the results from our study (Fig. 5.1), we

can now specify a maximum temperature of about 1700 K for the environment in which the  $\text{CaCO}_3$ -containing diamond was formed. Our results imply that the environment is rich in Mg and Fe. In the exceptional case that the  $\text{CaCO}_3$ -containing diamond was formed in a Mg-Fe-free system, the temperature might be lower as proposed by Li et al. (2018).

Simultaneous recording of  $\mu$ -XRD and  $\mu$ -XRF over the heated areas provided spatial information about phase reactions and the elemental redistribution within a sample. We could assign a redistribution of Sr during reaction to the newly formed phases. However, a precise detection of the trace element content *in-situ* at high pressure and high temperature remains difficult. The sensitivity for elements with energetically high  $K_\alpha$ -fluorescence lines ( $>33$  keV) is very low due to superimposition by the background signal from Compton scattering of the photons by the diamonds. Thanks to additional TEM measurements on the quenched sample material, we were able to investigate the elemental redistribution at a submicrometer scale. We found that La and Eu were not incorporated into the silicate phases, instead they tend to form isolated oxide phases in the form of  $\text{Eu}_2\text{O}_3$  and  $\text{La}_2\text{O}_3$  or hydroxyl-bastnäsite ( $\text{La}(\text{CO}_3)(\text{OH})$ ) during heating. Our results from TEM further show that Fe-bearing bridgmanite is not always quenchable. Bridgmanite either turns into an amorphous state or into low-pressure clinoenstatite with structure  $P2_1/c$  during pressure release. The low-P clinoenstatite phase can incorporate Ca as shown by EDX analyses on the recovered phases and possibly Sr too. At the same time,  $\text{SrCO}_3$  was found to incorporate Mg and Fe originating from the silicate. This unambiguously demonstrates that elemental redistribution processes between carbonates and silicates take place.

Although  $\text{SrCO}_3$  plays only a minor role in the chemistry of the deep Earth carbonates, our study on the reaction between  $\text{SrCO}_3$  and mantle silicates has shown that carbonates are indeed a source for introducing Sr into  $\text{CaSiO}_3$ -perovskite during carbonate-silicate reactions. The composition of  $\text{CaSiO}_3$ -perovskite is of relevance since it is known that the seismic velocities of  $\text{CaSiO}_3$ -perovskite can explain heterogeneities in the shear wave velocity of the lower mantle. It was found that the incorporation of  $\text{Ti}^{4+}$  at the Si-site in  $\text{CaSiO}_3$ -perovskite stabilizes the tetragonal structure at higher temperatures and thus substantially lowers the materials shear modulus (Thomson et al., 2019). Supposing that  $\text{Sr}^{2+}$  is substituted on the 12-fold coordinated Ca-site of  $\text{CaSiO}_3$ -perovskite, the shear wave velocity would also decrease with increasing Sr-content as it does in the system of  $\text{SrCO}_3$ - $\text{CaCO}_3$ -carbonates (Biedermann et al., 2017a). Moreover,  $\text{SrSiO}_3$ -perovskite at higher pressures, e.g. at 35 GPa, is isostructural to  $\text{CaSiO}_3$ -perovskite (Xiao et al., 2013) and solid solutions between the two phases are likely to occur in the Earth's mantle. Since  $\text{CaSiO}_3$ -perovskite is the third most abundant mineral in the lower mantle, it could be a possible candidate (in addition to accumulated subducted oceanic crust) for understanding the appearance of the so-called larger-low-shear-velocity-provinces (LLSVPs) in the mantle, especially when other elements, such as  $\text{Ti}^{4+}$  or  $\text{Sr}^{2+}$ , are incorporated.



## Chapter 7

# Outlook

The present study is a first step towards enhancing our understanding of trace element fractionation processes between carbonates and silicates at conditions of the Earth's mantle but a wide range of aspects remain subject to future research. An important issue to resolve is the determination of partitioning coefficients not only of the trace elements but also for the main elements Mg and Fe. Most partitioning experiments at high pressure and high temperature have been performed in piston-cylinder (Irving and Wyllie, 1973) or multi-anvil devices (Martinez et al., 1998; Dalou et al., 2009). More recently, LHDAC experiments in combination with microscopic sample extraction techniques (FIB), analytical TEM analyses and NanoSIMS were used for extending the elemental partitioning also to lower mantle conditions (Badro et al., 2007). NanoSIMS has a high sensitivity and can be used to characterize diffusion profiles even on a nanometer-scale. In our study, we experienced that the reaction length scale during LHDAC experiments is shorter than the lateral resolution of the  $\mu$ -XRF-map measurements, which is defined by the diameter of the primary X-ray beam. Furthermore, the content of the trace elements in the run products was below the detection limit of  $\mu$ -XRF. Performing NanoSIMS on promising sample assemblages derived from LHDAC experiments would give quantitative data on the distribution of trace elements between carbonates and silicates, especially for elements that are difficult to detect by  $\mu$ -XRF (high energy of Eu- and La- $K_{\alpha}$ -lines, Fe- $K_{\alpha}$ -lines have overlaps with L-lines of REEs). Concerning the sample specifications, a certain thickness of the sample is needed to have enough material to be analysed by NanoSIMS. As the thickness of TEM foils reaches the transmissivity in the electron beam, they are not suited for such measurements and the correct arrangement of the different analytical measurements, e.g. EMPA, NanoSIMS and TEM, have to be considered.

Ideally, the experimental setup for combined *in-situ* XRD-XRF-measurements needs to be optimized to allow the analysis of trace element concentration changes with a  $\mu$ -XRF spectrometer. To minimize the background radiation caused by Compton and Rayleigh scattering, a "horizontal" geometry should be used (Cherniak et al., 2010). The major limiting factor for the realization of this geometry is the design and opening angle of the DAC as well as the sample configuration inside the DAC. Currently, specially designed BX90 cells from BGI equipped with Boehler-Almax diamonds and seats can

have a maximum opening angle of  $80^\circ$  (Bykova, 2015). The conventional BX90 cells have a symmetrical axial opening that allows acquiring XRF in  $90^\circ$ -geometry when equipped with Be gaskets. By rotating the cell of about  $20^\circ$ , the use of specially prepared Re gaskets is also possible and is referred to as near  $90^\circ$ -geometry (Schmidt and Rickers, 2003; Petitgirard et al., 2012; Spiekermann et al., 2020). Measurements of  $\mu$ -XRF in this configuration would benefit from the fact that the signal is attenuated only by few  $100\ \mu\text{m}$  of diamond as opposed to  $\sim 1.7\ \text{mm}$  in the forward scattering direction (Fig. 7.1). In addition, the proportion of inelastic scattering, e.g. Compton scattering, is reduced to a minimum at  $90^\circ$  and thus would give better background-to-noise ratios for the elements with energetically high  $K_\alpha$ -fluorescence.

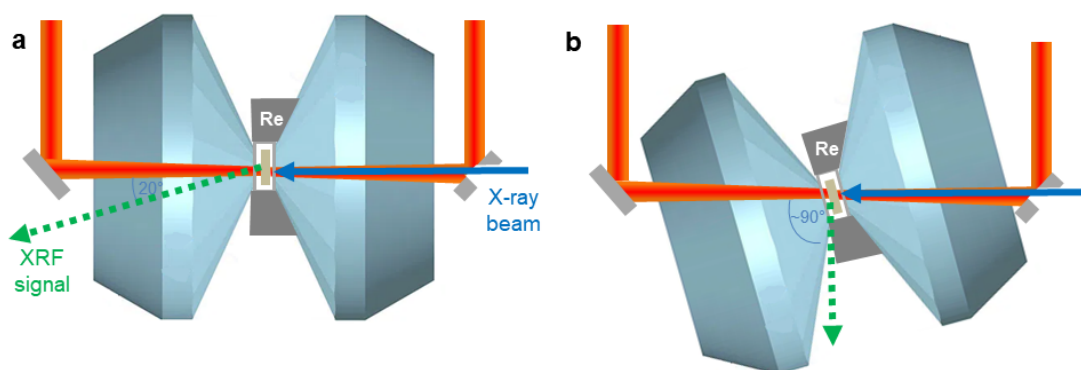


Figure 7.1: Schematic drawing of the experimental LHDAC setups used in this study (a) and an optimized setup (b) with double-sided laser heating (red), incident X-ray beam (blue) and emitted X-ray fluorescence signal (green) at  $\sim 20^\circ$  and  $\sim 90^\circ$  scattering angle, respectively, through the downstream diamond.

Future investigations should also focus on controlling the oxygen fugacity during carbonate-silicate reaction experiments. The form in which carbon is transported down to the lower mantle depends on the redox conditions in the inner Earth. Recent studies show that carbonates are usually reduced to C (graphite or diamond) due to the low oxygen fugacity in the mantle (Frost and McCammon, 2008). But carbon can be oxidized again to produce carbonate melt through the reduction of  $\text{Fe}^{3+}$  in the silicate minerals (Stagno et al., 2013). The depth of this redox melting depends on the  $\text{Fe}^{3+}/\text{Fe}^{total}$ -ratio and has significant implications for the decompressive, upwelling transport of  $\text{CO}_2$  from the upper mantle (Dasgupta and Hirschmann, 2010). It was shown in the study of Martinez et al. (1998) that iron depresses the eutectic melting point of the system  $(\text{Mg,Fe})\text{CO}_3-(\text{Mg,Fe})\text{SiO}_3$  by about 100 K compared to the iron-free system reported by Katsura and Ito (1990). The role of  $\text{Fe}^{3+}$  and  $\text{Fe}^{2+}$  in carbonates is also important in the formation of high-pressure polymorphs. Latest studies reported that Mg-Fe-carbonates transform into several new phases having unknown structures with tetrahedrally coordinated carbon (Boulard et al., 2012; Merlini et al., 2015b). Only a small number of studies have investigated the Mg-Fe-partitioning between silicates and carbonates at high pressure and high temperature (Dalton and Wood, 1993; Martinez et al., 1998). Future studies are needed to elucidate the iron-carbon redox

coupling process in the lower mantle and their impact on the stability of deep Earth carbonates.

Another topic that should be taken into account is the role of water. The presented study only considered one water-bearing experiment in the system  $(\text{Mg,Fe})_2\text{SiO}_4 + \text{SrCO}_3$  and a more detailed investigation on the influence of water on the chemical reactivity is missing. As shown by high-pressure and high-temperature experiments, the nominally anhydrous minerals wadsleyite and ringwoodite ( $(\text{Mg,Fe})_2\text{SiO}_4$ ) can incorporate significant amounts of hydrogen as point defects into their crystal structures (Kohlstedt et al., 1996; Mrosko et al., 2013). This has led to the hypothesis that the transition zone could be a deep water reservoir and which could cause dehydration melting across the 660 km discontinuity (Schmandt et al., 2014). While entering the transition zone during the subduction of carbonate minerals, the stability of the carbonates is further deteriorated due to deep volatile-induced melting (Dasgupta, 2018). Future studies on the  $\text{H}_2\text{O}$ -bearing system of carbonate-silicate reactions could be used to compare it with our results for the onset of a reaction and to evaluate the effect of water more precisely.



# References

- Akahama, Y. and Kawamura, H. (2004). High-pressure Raman spectroscopy of diamond anvils to 250 GPa: Method for pressure determination in the multimegabar pressure range. *Journal of Applied Physics*, 96(7):3748–3751.
- Andrault, D., Petitgirard, S., Nigro, G., Devidal, J.-L., Veronesi, G., Garbarino, G., and Mezouar, M. (2012). Solid-liquid iron partitioning in Earth’s deep mantle. *Nature*, 487:354–357.
- Angel, R. J., Alvaro, M., and Gonzalez-Platas, J. (2014). EosFit7c and a fortran module (library) for Equation of State calculations. *Zeitschrift für Kristallographie - Crystalline Materials*, 229(5).
- Angel, R. J., Chopelas, A., and Ross, N. (1992). Stability of high-density clinoenstatite at upper mantle pressures. *Nature*, 358(6384):322.
- Antao, S. M. and Hassan, I. (2009). The orthorhombic structure of  $\text{CaCO}_3$ ,  $\text{SrCO}_3$ ,  $\text{PbCO}_3$  and  $\text{BaCO}_3$ : Linear structural trends. *The Canadian Mineralogist*, 47(5):1245–1255.
- Arapan, S. and Ahuja, R. (2010). High-pressure phase transformations in carbonates. *Physical Review B*, 82(18).
- Badro, J., Ryerson, F. J., Weber, P. K., Ricolleau, A., Fallon, S. J., and Hutcheon, I. D. (2007). Chemical imaging with NanoSIMS: A window into deep Earth geochemistry. *Earth and Planetary Science Letters*, 262(3-4):543–551.
- Bayarjargal, L., Fruhner, C.-J., Schrodtt, N., and Winkler, B. (2018).  $\text{CaCO}_3$  phase diagram studied with Raman spectroscopy at pressures up to 50 GPa and high temperatures and DFT modeling. *Physics of the Earth and Planetary Interiors*, 281:31–45.
- Bayarjargal, L., Shumilova, T. G., Friedrich, A., and Winkler, B. (2010). Diamond formation from  $\text{CaCO}_3$  at high pressure and temperature. *European Journal of Mineralogy*, 22(1):29–34.
- Berndt, J., Liebske, C., Holtz, F., Freise, M., Nowak, M., Ziegenbein, D., Hurkuck, W., and Koepke, J. (2002). A combined rapid-quench and  $\text{H}_2$ -membrane setup for internally heated pressure vessels: Description and application for water solubility in basaltic melts. *American Mineralogist*, 87(11-12):1717–1726.

- 
- Biedermann, N., Bykova, E., Efthimiopoulos, I., Morgenroth, W., Spiekermann, G., Mueller, J., Glazyrin, K., Pakhomova, A., Appel, K., and Wilke, M. (in review). Equation of state and high-pressure phase behaviour of SrCO<sub>3</sub>. *European Journal of Mineralogy*.
- Biedermann, N., Speziale, S., Winkler, B., Reichmann, H. J., Koch-Müller, M., and Heide, G. (2017a). High-pressure phase behavior of SrCO<sub>3</sub>: an experimental and computational Raman scattering study. *Physics and Chemistry of Minerals*, 44(5):335–343.
- Biedermann, N., Winkler, B., Speziale, S., Reichmann, H. J., and Koch-Müller, M. (2017b). Single-crystal elasticity of SrCO<sub>3</sub> by Brillouin spectroscopy. *High Pressure Research*, 37(2):181–192.
- Birch, F. (1947). Finite elastic strain of cubic crystals. *Physical Review*, 71(11):809–824.
- Blundy, J. and Wood, B. (1994). Prediction of crystal–melt partition coefficients from elastic moduli. *Nature*, 372(6505):452–454.
- Boehler, R. (1992). Melting of the FeFeO and the FeFeS systems at high pressure: Constraints on core temperatures. *Earth and Planetary Science Letters*, 111(2-4):217–227.
- Boehler, R. (2000). High-pressure experiments and the phase diagram of lower mantle and core materials. *Reviews of Geophysics*, 38(2):221–245.
- Boehler, R. (2006). New diamond cell for single-crystal X-ray diffraction. *Review of Scientific Instruments*, 77(11):115103.
- Boehler, R. and Chopelas, A. (1991). A new approach to laser heating in high pressure mineral physics. *Geophysical Research Letters*, 18(6):1147–1150.
- Borchert, M., Wilke, M., Kvashnina, K., Schmidt, C., and Jahn, S. (2013). Complexation of Sr in aqueous solutions equilibrated with silicate melts: Implications for fluid-melt partitioning. *Mineralogical Magazine*, 77(5):739.
- Borchert, M., Wilke, M., Schmidt, C., Cauzid, J., and Tucoulou, R. (2010a). Partitioning of Ba, La, Yb and Y between haplogranitic melts and aqueous solutions: An experimental study. *Chemical Geology*, 276:225–240.
- Borchert, M., Wilke, M., Schmidt, C., and Rickers, K. (2009). Partitioning and equilibration of Rb and Sr between silicate melts and aqueous fluids. *Chemical Geology*, 259:39–47.
- Borchert, M., Wilke, M., Schmidt, C., and Rickers, K. (2010b). Rb and Sr partitioning between haplogranitic melts and aqueous solutions. *Geochimica et Cosmochimica Acta*, 74:1057–1076.
-

- Boulard, E., Menguy, N., Auzende, A. L., Benzerara, K., Bureau, H., Antonangeli, D., Corgne, A., Morard, G., Siebert, J., Perrillat, J. P., Guyot, F., and Fiquet, G. (2012). Experimental investigation of the stability of Fe-rich carbonates in the lower mantle. *Journal of Geophysical Research: Solid Earth*, 117(B2).
- Bragg, W. L. (1924). The structure of aragonite. *Proceedings of the Royal Society of London. Series A, Containing Papers of a Mathematical and Physical Character*, 105(729):16–39.
- Brenker, F., Vollmer, C., Vincze, L., Vekemans, B., Szymanski, A., Janssens, K., Szaloki, I., Nasdala, L., Joswig, W., and Kaminsky, F. (2007). Carbonates from the lower part of transition zone or even the lower mantle. *Earth and Planetary Science Letters*, 260:1–9.
- Brown, G. E., Prewitt, C. T., Papike, J. J., and Sueno, S. (1972). A comparison of the structures of low and high pigeonite. *Journal of Geophysical Research*, 77(29):5778–5789.
- Brown, J. M. and Shankland, T. J. (1981). Thermodynamic parameters in the Earth as determined from seismic profiles. *Geophysical Journal International*, 66(3):579–596.
- Brydson, R., Brown, A., Benning, L. G., and Livi, K. (2014). Analytical transmission electron microscopy. *Reviews in Mineralogy and Geochemistry*, 78(1):219–269.
- Bundy, F. P., Bassett, W. A., Weathers, M. S., R. J. Hemley, H. K. M., and Goncharov, A. F. (1996). The pressure-temperature phase and transformation diagram for carbon. *Carbon*, 34(2):141–153.
- Bykova, E. (2015). *Single-crystal X-ray diffraction at extreme conditions in mineral physics and material sciences*. PhD thesis, University of Bayreuth.
- Canil, D. and Scarfe, C. M. (1990). Phase relations in peridotite + CO<sub>2</sub> systems to 12 GPa: Implications for the origin of kimberlite and carbonate stability in the Earth’s upper mantle. *Journal of Geophysical Research*, 95:15805–15816.
- Carlson, W. (1980). The calcite-aragonite equilibrium: effects of Sr substitution and anion orientational disorder. *American Mineralogist*, 65:1252 – 1262.
- Cerantola, V., Bykova, E., Kuppenko, I., Merlini, M., Ismailova, L., McCammon, C., Bykov, M., Chumakov, A. I., Petitgirard, S., Kantor, I., Svitlyk, V., Jacobs, J., Hanfland, M., Mezouar, M., Prescher, C., Rüffer, R., Prakapenka, V. B., and Dubrovinsky, L. (2017). Stability of iron-bearing carbonates in the deep Earth’s interior. *Nature Communications*, 8(1).
- Cerantola, V., McCammon, C., Kuppenko, I., Kantor, I., Marini, C., Wilke, M., Ismailova, L., Solopova, N., Chumakov, A., Pascarelli, S., and Dubrovinsky, L. (2015). High-pressure spectroscopic study of siderite (FeCO<sub>3</sub>) with a focus on spin crossover. *American Mineralogist*, 100:2670 – 2681.

- 
- Cherniak, D. J., Hervig, R., Koepke, J., Zhang, Y., and Zhao, D. (2010). Analytical methods in diffusion studies. *Reviews in Mineralogy and Geochemistry*, 72(1):107–170.
- Chijioko, A. D., Nellis, W. J., Soldatov, A., and Silvera, I. F. (2005). The ruby pressure standard to 150 GPa. *Journal of Applied Physics*, 98(11):114905.
- Corgne, A., Allan, N. L., and Wood, B. J. (2003). Atomistic simulations of trace element incorporation into the large site of  $\text{MgSiO}_3$  and  $\text{CaSiO}_3$  perovskites. *Physics of the Earth and Planetary Interiors*, 139(1-2):113–127.
- Corgne, A., Liebske, C., Wood, B. J., Rubie, D. C., and Frost, D. J. (2005). Silicate perovskite-melt partitioning of trace elements and geochemical signature of a deep perovskitic reservoir. *Geochimica et Cosmochimica Acta*, 69(2):485–496.
- Corgne, A. and Wood, B. J. (2002).  $\text{CaSiO}_3$  and  $\text{CaTiO}_3$  perovskite-melt partitioning of trace elements: Implications for gross mantle differentiation. *Geophysical Research Letters*, 29(19):39–1–39–4.
- Corgne, A. and Wood, B. J. (2005). Trace element partitioning and substitution mechanisms in calcium perovskites. *Contributions to Mineralogy and Petrology*, 149(1):85–97.
- Dalou, C., Koga, K. T., Hammouda, T., and Poitrasson, F. (2009). Trace element partitioning between carbonatitic melts and mantle transition zone minerals: Implications for the source of carbonatites. *Geochimica et Cosmochimica Acta*, 73(1):239–255.
- Dalton, J. A. and Wood, B. J. (1993). The partitioning of Fe and Mg between olivine and carbonate and the stability of carbonate under mantle conditions. *Contributions to Mineralogy and Petrology*, 114:501 – 509.
- Dasgupta, R. (2018). Volatile-bearing partial melts beneath oceans and continents—where, how much, and of what compositions? *American Journal of Science*, 318(1):141–165.
- Dasgupta, R. and Hirschmann, M. (2010). The deep carbon cycle and melting in Earth’s interior. *Earth and Planetary Science Letters*, 298:1–13.
- Deer, W. A., Howie, R. A., and Zussman, J. (1992). *An introduction to the rock-forming minerals*. Harlow Essex, England, New York, NY:Longman Scientific & Technical.
- Dorfman, S. M. (2016). Phase diagrams and thermodynamics of lower mantle materials. *Deep Earth; Physics and Chemistry of the Lower Mantle and Core*, 217:241–252.
- Dorfman, S. M., Badro, J., Nabiei, F., Prakapenka, V. B., Cantoni, M., and Gillet, P. (2018). Carbonate stability in the reduced lower mantle. *Earth and Planetary Science Letters*, 489:84–91.
-



- Drewitt, J. W., Walter, M. J., Zhang, H., McMahon, S. C., Edwards, D., Heinen, B. J., Lord, O. T., Anzellini, S., and Kleppe, A. K. (2019). The fate of carbonate in oceanic crust subducted into Earth's lower mantle. *Earth and Planetary Science Letters*, 511:213–222.
- Dubrovinskaia, N. and Dubrovinsky, L. (2003). Whole-cell heater for the diamond anvil cell. *Review of Scientific Instruments*, 74(7):3433–3437.
- Efthimiopoulos, I., Jahn, S., Kuras, A., Schade, U., and Koch-Müller, M. (2017). Combined high-pressure and high-temperature vibrational studies of dolomite: phase diagram and evidence of a new distorted modification. *Physics and Chemistry of Minerals*, 44(7):465–476.
- Efthimiopoulos, I., Müller, J., Winkler, B., Otzen, C., Harms, M., Schade, U., and Koch-Müller, M. (2019). Vibrational response of strontianite at high pressures and high temperatures and construction of P-T-phase diagram. *Physics and Chemistry of Minerals*, 46(1):27–35.
- Frost, D. J. and McCammon, C. A. (2008). The redox state of Earth's mantle. *Annual Review of Earth and Planetary Sciences*, 36(1):389–420.
- Fruhner, C.-J. (2019). *Untersuchungen zur Phasenstabilität von Carbonaten mit Fluoreszenz- und Raman-Spektroskopie*. PhD thesis, Goethe-Universität Frankfurt, Frankfurt am Main.
- Gavryushkin, P. N., Martirosyan, N. S., Inerbaev, T. M., Popov, Z. I., Rashchenko, S. V., Likhacheva, A. Y., Lobanov, S. S., Goncharov, A. F., Prakapenka, V. B., and Litasov, K. D. (2017). Aragonite-II and CaCO<sub>3</sub>-VII: New high-pressure, high-temperature polymorphs of CaCO<sub>3</sub>. *Crystal Growth & Design*, 17(12):6291–6296.
- Ghosh, S., Ohtani, E., Litasov, K. D., and Terasaki, H. (2009). Solidus of carbonated peridotite from 10 to 20 GPa and origin of magnesio碳酸ite melt in the Earth's deep mantle. *Chemical Geology*, 262(1-2):17–28.
- Grove, T., Chatterjee, N., Parman, S., and Medard, E. (2006). The influence of H<sub>2</sub>O on mantle wedge melting. *Earth and Planetary Science Letters*, 249(1-2):74–89.
- Grove, T. L. and Till, C. B. (2019). H<sub>2</sub>O-rich mantle melting near the slab-wedge interface. *Contributions to Mineralogy and Petrology*, 174(10).
- Haller, M. and Knoechel, A. (1996). X-ray fluorescence analysis using synchrotron radiation (SYXRF). *Journal of trace and microprobe techniques*.
- Hammersley, A. P. (2016). FIT2D: a multi-purpose data reduction, analysis and visualization program. *Journal of Applied Crystallography*, 49(2):646–652.
- Hazen, R., Jones, A., and (Editors, J. B. (2013). Carbon in Earth. *Reviews in Mineralogy and Geochemistry*, 75:680 p.

- 
- Helfrich, G. R. and Wood, B. J. (2001). The Earth's mantle. *Nature*, 412(6846):501–507.
- Hemley, R. J., Zha, C. S., Jephcoat, A. P., Mao, H. K., Finger, L. W., and Cox, D. E. (1989). X-ray diffraction and equation of state of solid neon to 110 GPa. *Physical Review B*, 39(16):11820–11827.
- Hirose, K., Shimizu, N., van Westrenen, W., and Fei, Y. (2004). Trace element partitioning in Earth's lower mantle and implications for geochemical consequences of partial melting at the core–mantle boundary. *Physics of the Earth and Planetary Interiors*, 146(1-2):249–260.
- Holl, C. M., Smyth, J. R., Laustsen, H. M. S., Jacobsen, S. D., and Downs, R. T. (2000). Compression of witherite to 8 GPa and the crystal structure of BaCO<sub>3</sub>-II. *Physics and Chemistry of Minerals*, 27(7):467–473.
- Hrubiak, R. (2016). *X-ray Diffraction Imaging: XDI - User manual*. HP-CAT, Carnegie Science.
- Ionov, D. A., O'Reilly, S. Y., Genshaft, Y. S., and Kopylova, M. G. (1996). Carbonate-bearing mantle peridotite xenoliths from Spitsbergen: phase relationships, mineral compositions and trace-element residence. *Contributions to Mineralogy and Petrology*, 125(4):375 – 392.
- Iota, V., Yoo, C.-S., Klepeis, J.-H., Jenei, Z., Evans, W., and Cynn, H. (2006). Six-fold coordinated carbon dioxide VI. *Nature Materials*, 6(1):34–38.
- Irifune, T. (1994). Absence of an aluminous phase in the upper part of the Earth's lower mantle. *Nature*, 370:131–133.
- Irving, A. and Wyllie, P. (1973). Melting relationships in CaO-CO<sub>2</sub> and MgO-CO<sub>2</sub> to 36 kbar with comments on CO<sub>2</sub> in the mantle. *Earth and Planetary Science Letters*.
- Isshiki, M., Irifune, T., Hirose, K., Ono, S., Ohishi, Y., Watanuki, T., Nishibori, E., Takata, M., and Sakata, M. (2004). Stability of magnesite and its high-pressure form in the lowermost mantle. *Nature*, 427(6969):60–63.
- Ivanov, B. A. and Deutsch, A. (2002). The phase diagram of CaCO<sub>3</sub> in relation to shock compression and decomposition. *Physics of the Earth and Planetary Interiors*, 129(1-2):131–143.
- Javoy, M. (1997). The major volatile elements of the Earth: Their origin, behavior, and fate. *Geophysical Research Letters*, 24(2):177–180.
- Javoy, M., Kaminski, E., Guyot, F., Andrault, D., Sanloup, C., Moreira, M., Labrosse, S., Jambon, A., Agrinier, P., Davaille, A., and Jaupart, C. (2010). The chemical composition of the Earth: Enstatite chondrite models. *Earth and Planetary Science Letters*, 293(3-4):259–268.
-

- Kakizawa, S., Inoue, T., Siúenami, H., and Kikegawa, T. (2015). Decarbonation and melting in MgCO<sub>3</sub>-SiO<sub>2</sub> system at high temperature and high pressure. *Journal of Mineralogical and Petrological Sciences*, 110(4):179–188.
- Kalliomäki, M. S. and Meisalo, V. P. J. (1979). Structure determination of the high-pressure phases RbNO<sub>3</sub> v, CsNO<sub>3</sub> III, and CsNO<sub>3</sub> IV. *Acta Crystallographica Section B Structural Crystallography and Crystal Chemistry*, 35(12):2829–2835.
- Kaminski, E. and Javoy, M. (2015). The Composition of the Deep Earth. In *The Earth's Heterogeneous Mantle*, pages 303–328. Springer International Publishing.
- Kaminsky, F. (2012). A review of 'super-deep' mineral inclusions in diamond. *Earth-Science Reviews*, 110:127–147.
- Kantor, I., Prakapenka, V., Kantor, A., Dera, P., Kurnosov, A., Sinogeikin, S., Dubrovinskaia, N., and Dubrovinsky, L. (2012). BX90: A new diamond anvil cell design for X-ray diffraction and optical measurements. *Review of Scientific Instruments*, 83(12):125102.
- Kato, T., Ringwood, A., and Irifune, T. (1988). Experimental determination of element partitioning between silicate perovskites, garnets and liquids: constraints on early differentiation of the mantle. *Earth and Planetary Science Letters*, 89(1):123–145.
- Katsura, T. and Ito, E. (1990). Melting and subsolidus phase relations in the MgSiO<sub>3</sub> - MgCO<sub>3</sub> system at high pressures: implications to evolution of the Earth's atmosphere. *Earth and Planetary Science Letters*, 99(1-2):110–117.
- Kavner, A. and Duffy, T. S. (2001). P-V-T-paths in the laser-heated diamond anvil cell. *Journal of Applied Physics*, 89(3):1907.
- Klotz, S., Chervin, J.-C., Munsch, P., and Marchand, G. L. (2009). Hydrostatic limits of 11 pressure transmitting media. *Journal of Physics D: Applied Physics*, 42(7):075413.
- Koch-Müller, M., Jahn, S., Birkholz, N., Ritter, E., and Schade, U. (2016). Phase transitions in the system CaCO<sub>3</sub> at high P and T determined by *in situ* vibrational spectroscopy in diamond anvil cells and first-principles simulations. *Physics and Chemistry of Minerals*, 43(8):545–561.
- Kohlstedt, D. L., Keppler, H., and Rubie, D. C. (1996). Solubility of water in the  $\alpha$ ,  $\beta$  and  $\gamma$  phases of (Mg,Fe)<sub>2</sub>SiO<sub>4</sub>. *Contributions to Mineralogy and Petrology*, 123(4):345–357.
- Komabayashi, T. (2004). Petrogenetic grid in the system MgO-SiO<sub>2</sub>-H<sub>2</sub>O up to 30 GPa, 1600°C: Applications to hydrous peridotite subducting into the Earth's deep interior. *Journal of Geophysical Research*, 109(B3).
- Larson, A. C. and Von Dreele, R. B. (2004). General structure analysis system (GSAS). *Los Alamos, New Mexico: Los Alamos National Laboratory*.

- 
- Lavina, B., Dera, P., and Downs, R. T. (2014). Modern X-ray diffraction methods in mineralogy and geosciences. *Reviews in Mineralogy and Geochemistry*, 78(1):1–31.
- Le Bail, A., Duroy, H., and Fourquet, J. (1988). Ab-initio structure determination of  $\text{LiSbWO}_6$  by X-ray powder diffraction. *Materials Research Bulletin*, 23(3):447–452.
- Li, J., Redfern, S. A., and Giovannelli, D. (2019). Introduction: Deep carbon cycle through five reactions. *American Mineralogist*, 104(4):465–467.
- Li, X., Zhang, Z., Lin, J.-F., Ni, H., Prakapenka, V. B., and Mao, Z. (2018). New high-pressure phase of  $\text{CaCO}_3$  at the topmost lower mantle: Implication for the deep-mantle carbon transportation. *Geophysical Research Letters*, 45(3):1355–1360.
- Li, Z., Li, J., Lange, R., Liu, J., and Militzer, B. (2017). Determination of calcium carbonate and sodium carbonate melting curves up to Earth's transition zone pressures with implications for the deep carbon cycle. *Earth and Planetary Science Letters*, 457:395–402.
- Liermann, H.-P., Konôpková, Z., Morgenroth, W., Glazyrin, K., Bednarčík, J., McBride, E. E., Petitgirard, S., Delitz, J. T., Wendt, M., Bican, Y., Ehnes, A., Schwark, I., Rothkirch, A., Tischer, M., Heuer, J., Schulte-Schrepping, H., Kracht, T., and Franz, H. (2015). The Extreme Conditions Beamline P02.2 and the Extreme Conditions Science Infrastructure at PETRA III. *Journal of Synchrotron Radiation*, 22(4):908–924.
- Liermann, H.-P., Merkel, S., Miyagi, L., Wenk, H.-R., Shen, G., Cynn, H., and Evans, W. J. (2009). Experimental method for *in-situ* determination of material textures at simultaneous high pressure and high temperature by means of radial diffraction in the diamond anvil cell. *Review of Scientific Instruments*, 80(10):104501.
- Lin, C.-C. and Liu, L.-G. (1997). Post-aragonite phase transitions in strontianite and cerussite: A high-pressure Raman spectroscopic study. *Journal of Physics and Chemistry of Solids*, 58(6):977–987.
- Litasov, K. (2011). Physicochemical conditions for melting in the Earth's mantle containing a C-O-H fluid. *Russian Geology and Geophysics*, 52(5):475–492.
- Litasov, K. and Ohtani, E. (2010). The solidus of carbonated eclogite in the system  $\text{CaO-Al}_2\text{O}_3\text{-MgO-SiO}_2\text{-Na}_2\text{O-CO}_2$  to 32 GPa and carbonatite liquid in the deep mantle. *Earth and Planetary Science Letters*, 295(1-2):115–126.
- Litasov, K. D., Shatskiy, A., Ohtani, E., and Yaxley, G. M. (2013). Solidus of alkaline carbonatite in the deep mantle. *Geology*, 41(1):79–82.
- Litasov, K. D. and Shatskiy, A. F. (2019).  $\text{MgCO}_3 + \text{SiO}_2$  reaction at pressures up to 32 GPa studied using *in situ* X-ray diffraction and synchrotron radiation. *Geochemistry International*, 57(9):1024–1033.
-

- Maeda, F., Ohtani, E., Kamada, S., Sakamaki, T., Hirao, N., and Ohishi, Y. (2017). Diamond formation in the deep lower mantle: a high-pressure reaction of  $\text{MgCO}_3$  and  $\text{SiO}_2$ . *Scientific Reports*, 7(1).
- Manning, C. E. (2014). A piece of the deep carbon puzzle. *Nature Geoscience*, 7(5):333–334.
- Mao, H. K., Xu, J., and Bell, P. M. (1986). Calibration of the ruby pressure gauge to 800 kbar under quasi-hydrostatic conditions. *Journal of Geophysical Research*, 91(B5):4673.
- Mao, H K; Hemley, R. J. M. A. L. (1997). Diamond-cell research with synchrotron radiation. *Advances in High Pressure Research*.
- Martinez, I., Chamorro Pérez, E. M., Matas, J., Gillet, P., and Vidal, G. (1998). Experimental investigation of silicate-carbonate system at high pressure and high temperature. *Journal of Geophysical Research, Solid Earth*, 103(B3):5143 – 5163.
- Martinez, I., Zhang, J., and Reeder, R. J. (1996). *In situ* X-ray diffraction of aragonite and dolomite at high pressure and high temperature; evidence for dolomite breakdown to aragonite and magnesite. *American Mineralogist*, 81(5-6):611–624.
- McCammon, C., Bureau, H., Cleaves, J. H., Cottrell, E., Dorfman, S. M., Kellogg, L. H., Li, J., Mikhail, S., Moussallam, Y., Sanloup, C., Thomson, A. R., and Brovarone, A. V. (2020). Deep Earth carbon reactions through time and space. *American Mineralogist*, 105(1):22–27.
- Merlini, M., Crichton, W. A., Hanfland, M., Gemmi, M., Muller, H., Kuppenko, I., and Dubrovinsky, L. (2012). Structures of dolomite at ultrahigh pressure and their influence on the deep carbon cycle. *Proceedings of the National Academy of Sciences*, 109(34):13509–13514.
- Merlini, M., Hanfland, M., and Gemmi, M. (2015a). The  $\text{MnCO}_3$ -II high-pressure polymorph of rhodocrosite. *American Mineralogist*, 100:2625 –2629.
- Merlini, M., Hanfland, M., Salamat, A., Petitgirard, S., and Müller, H. (2015b). The crystal structures of  $\text{Mg}_2\text{Fe}_2\text{C}_4\text{O}_{13}$ , with tetrahedrally coordinated carbon, and  $\text{Fe}_{13}\text{O}_{19}$ , synthesized at deep mantle conditions. *American Mineralogist*, 100(8-9):2001–2004.
- Milliman, J. D., Müller, G., and Förstner, U. (1974). *Recent Sedimentary Carbonates*. Springer Berlin Heidelberg.
- Moir, G. and Glasser, F. (1974). Solid-solutions and phase equilibria in systems  $\text{Na}_2\text{SiO}_3$ - $\text{SrSiO}_3$  and  $\text{Na}_2\text{SiO}_3$ - $\text{CaSiO}_3$ - $\text{SrSiO}_3$ . *Transactions and Journal of the British Ceramic Society*, 73(6):199–206.
- Mrosko, M., Koch-Müller, M., McCammon, C., Rhede, D., Smyth, J., and Wirth, R. (2015). Water, iron, redox environment: effects on the wadsleyite–ringwoodite phase transition. *Contributions to Mineralogy and Petrology*, 170(9):1 – 12.

- 
- Mrosko, M., Lenz, S., McCammon, C. A., Taran, M., Wirth, R., and Koch-Müller, M. (2013). Hydrogen incorporation and the oxidation state of iron in ringwoodite: A spectroscopic study. *American Mineralogist*, 98(4):629–636.
- Mueller, T., Watson, E. B., and Harrison, T. M. (2010). Applications of diffusion data to high-temperature Earth systems. *Reviews in Mineralogy and Geochemistry*, 72(1):997–1038.
- Newton, R. and Sharp, W. (1975). Stability of forsterite + CO<sub>2</sub> and its bearing on the role of CO<sub>2</sub> in the mantle. *Earth and Planetary Science Letters*, 26(2):239–244.
- Newville, M. (2014). Fundamentals of XAFS. *Reviews in Mineralogy and Geochemistry*, 78(1):33–74.
- Nguyen-Thanh, T., Bosak, A., Bauer, J. D., Luchitskaia, R., Refson, K., Milman, V., and Winkler, B. (2016). Lattice dynamics and elasticity of SrCO<sub>3</sub>. *Journal of Applied Crystallography*, 49(6):1982–1990.
- Oganov, A. R., Glass, C., and Ono, S. (2006). High-pressure phases of CaCO<sub>3</sub>: crystal structure prediction and experiment. *Earth and Planetary Science Letters*, 241:95 – 103.
- Oganov, A. R., Ono, S., Ma, Y., Glass, C. W., and Garcia, A. (2008). Novel high-pressure structures of MgCO<sub>3</sub>, CaCO<sub>3</sub> and CO<sub>2</sub> and their role in Earth’s lower mantle. *Earth and Planetary Science Letters*, 273(1):38 – 47.
- Ono, S. (2005). Post-aragonite phase transformation in CaCO<sub>3</sub> at 40 GPa. *American Mineralogist*, 90(4):667–671.
- Ono, S. (2007). New high-pressure phases in BaCO<sub>3</sub>. *Physics and Chemistry of Minerals*, 34(4):215–221.
- Ono, S., Brodholt, J. P., and Price, G. D. (2008). Phase transitions of BaCO<sub>3</sub> at high pressures. *Mineralogical Magazine*, 72(2):659–665.
- Ono, S., Ito, E., and Katsura, T. (2001). Mineralogy of subducted basaltic crust (MORB) from 25 to 37 GPa, and chemical heterogeneity of the lower mantle. *Earth and Planetary Science Letters*, 190(1-2):57–63.
- Ono, S., Shirasaka, M., Kikegawa, T., and Ohishi, Y. (2005). A new high-pressure phase of strontium carbonate. *Physics and Chemistry of Minerals*, 32(1):8–12.
- Pan, Y., Wu, M., and Su, Q. (2003). Synthesis of Eu<sup>3+</sup>-doped calcium and strontium carbonate phosphors at room temperature. *Materials Research Bulletin*, 38(9-10):1537–1544.
- Pannhorst, W. (1984). High temperature crystal structure refinements of low-clinoenstatite up to 700°C. *Neues Jahrbuch für Mineralogie, Abhandlungen*, 150(3):219–228.
-

- Pearce, N. J., Perkins, W. T., Westgate, J. A., Gorton, M. P., Jackson, S. E., Neal, C. R., and Chenery, S. P. (1997). A compilation of new and published major and trace element data for NIST SRM 610 and NIST SRM 612 glass reference materials. *Geostandards and Geoanalytical Research*, 21(1):115–144.
- Petitgirard, S., Borchert, M., Andrault, D., Appel, K., Mezouar, M., and Liermann, H.-P. (2012). An *in situ* approach to study trace element partitioning in the laser heated diamond anvil cell. *Review of Scientific Instruments*, 83(1):013904.
- Petitgirard, S., Malfait, W. J., Sinmyo, R., Kuppenko, I., Hennet, L., Harries, D., Dane, T., Burghammer, M., and Rubie, D. C. (2015). Fate of MgSiO<sub>3</sub> melts at core–mantle boundary conditions. *Proceedings of the National Academy of Sciences*, 112(46):14186–14190.
- Petitgirard, S., Salamat, A., Beck, P., Weck, G., and Bouvier, P. (2014). Strategies for *in-situ* laser heating in the diamond anvil cell at an X-ray diffraction beamline. *Journal of Synchrotron Radiation*, 21(1):89–96.
- Pickard, C. J. and Needs, R. J. (2015). Structures and stability of calcium and magnesium carbonates at mantle pressures. *Physical Review B*, 91(10).
- Prescher, C. and Prakapenka, V. B. (2015). DIOPTAS: a program for reduction of two-dimensional X-ray diffraction data and data exploration. *High Pressure Research*, 35(3):223–230.
- Rigaku Oxford Diffraction (2019). CrysAlis PRO software system, Version 1.171.40.57a. *Rigaku Oxford Diffraction, Oxford, UK*.
- Rodriguez-Carvajal, J. (2008). FULLPROF: Rietveld, Profile Matching and Integrated Intensity Refinement of X-ray and/or Neutron Data (Version 2.0). *Laboratoire Léon Brillouin (CEA-CNRS), France*.
- Santillán, J. and Williams, Q. (2004). A high pressure X-ray diffraction study of aragonite and the post-aragonite phase transition in CaCO<sub>3</sub>. *American Mineralogist*, 89(8-9):1348–1352.
- Santos, S. S., Marcondes, M. L., Justo, J. F., and Assali, L. V. (2019). Stability of calcium and magnesium carbonates at Earth’s lower mantle thermodynamic conditions. *Earth and Planetary Science Letters*, 506:1–7.
- Schmandt, B., Jacobsen, S. D., Becker, T. W., Liu, Z., and Dueker, K. G. (2014). Dehydration melting at the top of the lower mantle. *Science*, 344(6189):1265–1268.
- Schmidt, C. and Rickers, K. (2003). In-situ determination of mineral solubilities in fluids using a hydrothermal diamond-anvil cell and SR-XRF: Solubility of AgCl in water. *American Mineralogist*, 88:288–292.

- Schultz, E., Mezouar, M., Crichton, W., Bauchau, S., Blattmann, G., Andrault, D., Fiquet, G., Boehler, R., Rambert, N., Sitaud, B., and Loubeyre, P. (2005). Double-sided laser heating system for *in situ* high pressure/high temperature monochromatic X-ray diffraction at the ESRF. *High Pressure Research*, 25(1):71–83.
- Seto, Y., Hamane, D., Nagai, T., and Fujino, K. (2008). Fate of carbonates within oceanic plates subducted to the lower mantle, and a possible mechanism of diamond formation. *Physics and Chemistry of Minerals*, 35(4):223 – 229.
- Shannon, R. (1976). Revised effective ionic radii and systematic studies of interatomic distances in halides and chalcogenides. *Acta crystallographica section A: crystal physics, diffraction, theoretical and general crystallography*, 32(5):751–767.
- Shatskiy, A., Litasov, K., and Palyanov, Y. (2015). Phase relations in carbonate systems at pressures and temperatures of lithospheric mantle: Review of experimental data. *Russian Geology and Geophysics*, 56(1-2):113–142.
- Shcheka, S. S., Wiedenbeck, M., Frost, D. J., and Keppler, H. (2006). Carbon solubility in mantle minerals. *Earth and Planetary Science Letters*, 245(3-4):730–742.
- Sheldrick, G. M. (2007). A short history of SHELX. *Acta Crystallographica Section A Foundations of Crystallography*, 64(1):112–122.
- Sheldrick, G. M. (2015). SHELXT– integrated space-group and crystal-structure determination. *Acta Crystallographica Section A Foundations and Advances*, 71(1):3–8.
- Sleep, N. H. and Zahnle, K. (2001). Carbon dioxide cycling and implications for climate on ancient Earth. *Journal of Geophysical Research: Planets*, 106(E1):1373–1399.
- Solé, V., Papillon, E., Cotte, M., Walter, P., and Susini, J. (2007). A multiplatform code for the analysis of energy-dispersive X-ray fluorescence spectra. *Spectrochimica Acta Part B: Atomic Spectroscopy*, 62(1):63–68.
- Solomatova, N. V. and Asimow, P. D. (2017). Ab initio study of the structure and stability of  $\text{CaMg}(\text{CO}_3)_2$  at high pressure. *American Mineralogist*, 102(1):210–215.
- Solopova, N., Dubrovinsky, L., Spivak, A., Litvin, Y., and Dubrovinskaya, N. (2015). Melting and decomposition of  $\text{MgCO}_3$  at pressures up to 84 GPa. *Physics and Chemistry of Minerals*, 42:73 – 81.
- Spiekermann, G., Kuppenko, I., Petitgirard, S., Harder, M., Nyrow, A., Weis, C., Albers, C., Biedermann, N., Libon, L., Sahle, C. J., Cerantola, V., Glazyrin, K., Konôpková, Z., Sinmyo, R., Morgenroth, W., Sergueev, I., Yavaş, H., Dubrovinsky, L., Tolan, M., Sternemann, C., and Wilke, M. (2020). A portable on-axis laser-heating system for near-90° x-ray spectroscopy: application to ferropericlase and iron silicide. *Journal of Synchrotron Radiation*, 27(2):414–424.
- Spivak, A., Litvin, Y., Ovsyannikov, S., Dubrovinskaya, N., and Dubrovinsky, L. (2012). Stability and breakdown of  $\text{Ca}^{13}\text{CO}_3$  melt associated with formation of  $^{13}\text{C}$ -diamond



- in static high pressure experiments up to 43 GPa and 3900 K. *Journal of Solid State Chemistry*, 191:102–106.
- Stachel, T., Harris, J. W., Brey, G. P., and Joswig, W. (2000). Kankan diamonds (guinea) II: lower mantle inclusion parageneses. *Contributions to Mineralogy and Petrology*, 140(1):16–27.
- Stagno, V., Ojwang, D. O., McCammon, C. A., and Frost, D. J. (2013). The oxidation state of the mantle and the extraction of carbon from Earth’s interior. *Nature*, 493(7430):84–88.
- Stixrude, L. and Lithgow-Bertelloni, C. (2007). Influence of phase transformations on lateral heterogeneity and dynamics in Earth’s mantle. *Earth and Planetary Science Letters*, 263(1-2):45–55.
- SYSTAT Software Inc. (2002). *PeakFit™ 4.11 for Windows User’s manual*. Richmond, California.
- Takafuji, N., Fujino, K., Nagai, T., Seto, Y., and Hamane, D. (2006). Decarbonation reaction of magnesite in subducting slabs at the lower mantle. *Physics and Chemistry of Minerals*, 33(10):651–654.
- Taura, H., Yurimoto, H., Kato, T., and Sueno, S. (2001). Trace element partitioning between silicate perovskites and ultracalcic melt. *Physics of the Earth and Planetary Interiors*, 124(1-2):25–32.
- Thompson, A. B. (1992). Water in the Earth’s upper mantle. *Nature*, 358(6384):295.
- Thomson, A., Kohn, S., Bulanova, G., Smith, C., Araujo, D., and Walter, M. (2016). Trace element composition of silicate inclusions in sub-lithospheric diamonds from the juina-5 kimberlite: Evidence for diamond growth from slab melts. *Lithos*, 265:108–124.
- Thomson, A. R., Crichton, W. A., Brodholt, J. P., Wood, I. G., Siersch, N. C., Muir, J. M. R., Dobson, D. P., and Hunt, S. A. (2019). Seismic velocities of CaSiO<sub>3</sub> perovskite can explain LLSVPs in Earth’s lower mantle. *Nature*, 572(7771):643–647.
- Townsend, J. P., Chang, Y.-Y., Lou, X., Merino, M., Kirklin, S. J., Doak, J. W., Issa, A., Wolverton, C., Tkachev, S. N., Dera, P., and Jacobsen, S. D. (2013). Stability and equation of state of post-aragonite BaCO<sub>3</sub>. *Physics and Chemistry of Minerals*, 40(5):447–453.
- Villiers, J. D. (1971). Crystal structures of aragonite, strontianite and witherite. *American Mineralogist*.
- Wang, M., Liu, Q., Nie, S., Li, B., Wu, Y., Gao, J., Wei, X., and Wu, X. (2015). High-pressure phase transitions and compressibilities of aragonite-structure carbonates: SrCO<sub>3</sub> and BaCO<sub>3</sub>. *Physics and Chemistry of Minerals*, 42(6):517–527.

- 
- Wilke, M., Appel, K., Vincze, L., Schmidt, C., Borchert, M., and Pascarelli, S. (2010). A confocal set-up for micro-XRF and XAFS experiments using diamond-anvil cells. *Journal of Synchrotron Radiation*, 17:669–675.
- Wilke, M., Schmidt, C., Dubrail, J., Appel, K., Borchert, M., Kvashnina, K., and Manning, C. (2012). Zircon solubility and zircon complexation in  $\text{H}_2\text{O}+\text{Na}_2\text{O}+\text{SiO}_2\pm\text{Al}_2\text{O}_3$  fluids at high pressure and temperature. *Earth and Planetary Science Letters*, 349-350:15–25.
- Wood, B. and Blundy, J. (2003). Trace element partitioning under crustal and uppermost mantle conditions: The influences of ionic radius, cation charge, pressure, and temperature. In *Treatise on Geochemistry*, pages 395–424. Elsevier.
- Wyllie, P. J. (1987). Discussion of recent papers on carbonated peridotite, bearing on mantle metasomatism and magmatism. *Earth and Planetary Science Letters*, 82(3-4):391–397.
- Xiao, W., Tan, D., Zhou, W., Liu, J., and Xu, J. (2013). Cubic perovskite polymorph of strontium metasilicate at high pressures. *American Mineralogist*, 98(11-12):2096–2104.
- Yusa, H., Akaogi, M., Sata, N., Kojitani, H., Kato, Y., and Ohishi, Y. (2005). Unquenchable hexagonal perovskite in high-pressure polymorphs of strontium silicates. *American Mineralogist*, 90(1117 - 1120).
- Zhang, Y. (2010). Diffusion in minerals and melts: Theoretical background. *Reviews in Mineralogy and Geochemistry*, 72(1):5–59.
- Zhang, Y.-F., Liu, J., Qin, Z.-X., Lin, C.-L., Xiong, L., Li, R., and Bai, L.-G. (2013). A high-pressure study of  $\text{PbCO}_3$  by XRD and raman spectroscopy. *Chinese Physics C*, 37(3):038001.
- Zhang, Z., Mao, Z., Liu, X., Zhang, Y., and Brodholt, J. (2018). Stability and reactions of  $\text{CaCO}_3$  polymorphs in the Earth's deep mantle. *Journal of Geophysical Research: Solid Earth*.
- Zucchini, A., Prencipe, M., Belmonte, D., and Comodi, P. (2017). Ab initio study of the dolomite to dolomite-II high-pressure phase transition. *European Journal of Mineralogy*, 29(2):227–238.

## Appendix A

# Structure refinement of synthesis NB12 ( $\text{CaCO}_3:\text{Sr}^{2+}$ )

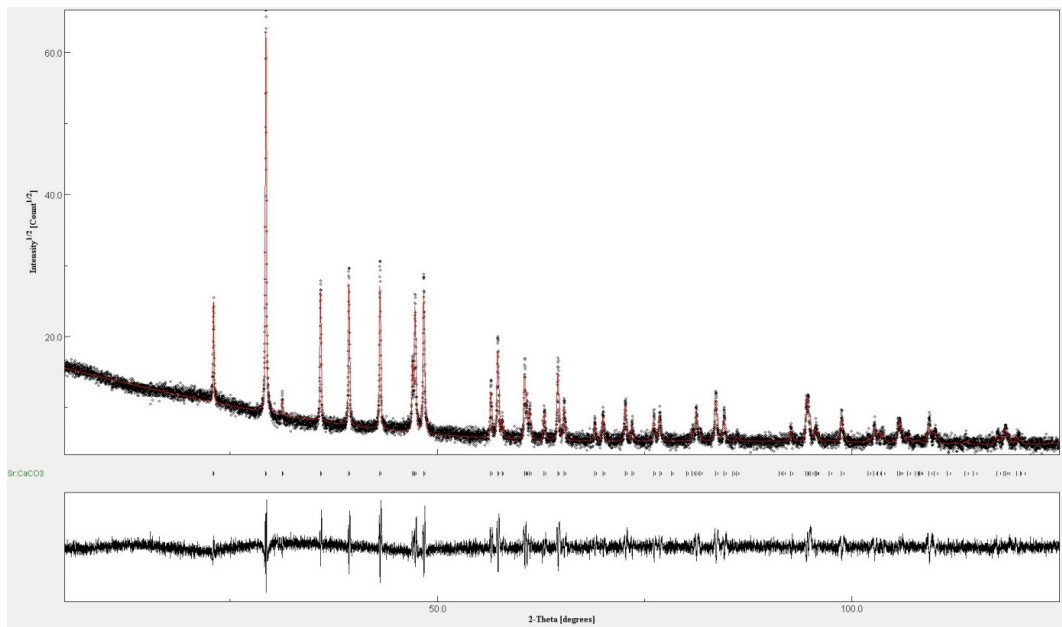


Figure A.1: Refined XRD pattern for the rhombohedral  $\text{CaCO}_3:\text{Sr}^{2+}$  phase from synthesis NB12. Black dots correspond to the measured spectra and the red solid line represents the best refinement. The difference spectra between the measured and the refined patterns are shown on the bottom.

Table A.1: Details of crystal structure refinements of  $\text{CaCO}_3:\text{Sr}^{2+}$  (NB12).

Crystallographic data	$\text{CaCO}_3:\text{Sr}^{2+}$ (NB12)
Crystal system	rhombohedral
Space group	$R\bar{3}cH$
$a$ (Å)	4.998(3)
$c$ (Å)	17.1355(2)
$\alpha$ (°)	90
$\beta$ (°)	90
$\gamma$ (°)	120
$V$ (Å <sup>3</sup> )	370.702(5)
$Z$	6
$2\Theta$ range for data collection (°)	5 to 125
Independent reflections / $R_{int}$	67 / 0.1244
Refinement method	Full matrix least squares on $F^2$
Goodness of fit on $F^2$	1.9614
$R$ indices (all data), $R_1$ / $wR_2$	0.2004 / 0.1635

Table A.2: Atomic coordinates and site occupancy of  $\text{CaCO}_3:\text{Sr}^{2+}$  (NB12).

Site	Wyckoff position	$x$	$y$	$z$	site occupancy
Ca1	$6b$	0	0	0	0.969(4)
Sr1	$6b$	0	0	0	0.022(8)
C1	$6a$	0	0	0.25	1
O1	$18e$	0.25734(6)	0	0.25	1

## Appendix B

# Refinement of XRD patterns from chapter 4

Phases used for Le Bail refinement

Table B.1: Lattice constants and corresponding EoS of the mineral phases that have been used for Le Bail fitting procedures.

Phase	Struct. formula	$a_0$ [Å]	$b_0$ [Å]	$c_0$ [Å]	$\alpha_0$ [°]	$\beta_0$ [°]	$\gamma_0$ [°]	$K_0$ [GPa]	$K'$	Reference
<i>carbonates</i>										
cc-VII	CaCO <sub>3</sub>	4.807	3.354	10.405	90	105.06	90	300	4	Gavryushkin et al. (2017)
post-aragonite	CaCO <sub>3</sub>	4.5785	5.1755	4.495	90	90	90	81.93	4.49	Huang et al. (1997)
magnesite	MgCO <sub>3</sub>	4.6332	4.6332	15.0148	90	90	120	117	2.3	Ross et al. (1997)
strontianite	SrCO <sub>3</sub> -I	5.126	8.472	6.061	90	90	90	67.7	3.2	This study
	SrCO <sub>3</sub> -II	4.528	4.93	12.635	90	90	90	103	2.3	This study
dol-II	Ca(Mg <sub>0.6</sub> Fe <sub>0.4</sub> )(CO <sub>3</sub> ) <sub>2</sub>	4.7407	5.3885	6.743	101.42	89.27	95.72			Merlini et al. (2012)
dol-III	Ca(Mg <sub>0.6</sub> Fe <sub>0.4</sub> )(CO <sub>3</sub> ) <sub>2</sub>	6.2346	9.3025	10.9893	75.89	81.05	89.48			Merlini et al. (2012)
La-bastnäsite	La(CO <sub>3</sub> )F	7.1870	7.1870	9.83	90	90	120	105	5.58	Rowland (2017)
<i>silicates</i>										
enstatite	MgSiO <sub>3</sub>	18.225	8.813	5.18	90	90	90	236	3.9	Ohashi et al. (1984)
orthopyroxene	(Mg <sub>0.54</sub> Fe <sub>0.424</sub> )SiO <sub>3</sub>	18.220	8.765	5.188	90	90	90	120	7.7	Xu et al. (2017)
olivine	(Mg <sub>1.6</sub> Fe <sub>0.4</sub> )SiO <sub>4</sub>	4.765	10.235	5.99727	90	90	90	129.4	4.29	Abramson et al. (1997)
bridgmanite	MgSiO <sub>3</sub>	4.7754	4.929	6.8971	90	90	90	261	4	Mao et al. (1991)
low-Fe bridgmanite	(Mg <sub>0.85</sub> Fe <sub>0.15</sub> )SiO <sub>3</sub>	4.7911	4.9332	6.9062	90	90	90	261	4	Mao et al. (1991)
stishovite	SiO <sub>2</sub>	4.178	4.178	2.668	90	90	90	296	4.2	Nishihara et al. (2005)
Ca-Pv	CaSiO <sub>3</sub>	3.5666	3.5666	3.5666	90	90	90	236	3.9	Shim et al. (1999)
Sr-Pv (hex)	SrSiO <sub>3</sub>	5.0688	5.0688	12.4175	90	90	120			Yusa et al. (2005)
Sr-Pv (c)	SrSiO <sub>3</sub>	3.5034	3.5034	3.5034	90	90	90	211	4	Xiao et al. (2013)
shy B	Mg <sub>10</sub> Si <sub>3</sub> O <sub>14</sub> (OH) <sub>4</sub>	5.031	8.583	13.789	90	90	90	135.3	5.3	Crichton & Ross, (2000)
<i>oxides</i>										
ferropericlase	(Mg,Fe)O (B1)	4.262	4.262	4.262	90	90	90	157	4	Fei et al. (1991)
magnesiowüstite	(Mg <sub>0.4</sub> Fe <sub>0.6</sub> )O (B1)	4.2805	4.2805	4.2805	90	90	90	149	4	Richet et al. (1989)
periclase	MgO	4.213	4.213	4.213	90	90	90	177	4	Duffy et al. (1995)
Calcium oxide	CaO (B2)	2.907	2.907	2.907	90	90	90	130	3.5	Richet et al. (1988)
Strontium oxide	SrO (B1)	5.25	5.25	5.25	90	90	90	106	4	Zupan et al. (1993)
<i>Phases relevant for DAC experiments</i>										
	Re	2.76	2.76	4.4574	90	90	120	433.8	3.46	Zha et al. (2004)
	Ar (fcc)	5.5128	5.5128	5.5128	90	90	90	1.95	7.71	Finger et al. (1981)
	KCl (B2)	3.753	3.753	3.753	90	90	90	28.7	4	Campbell & Heinz, (1991)

## Refined XRD patterns

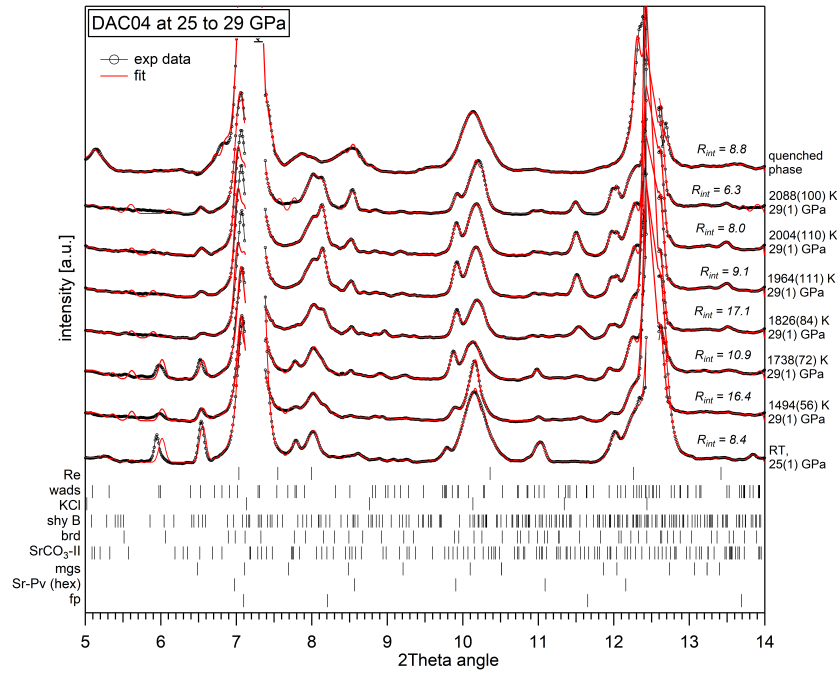


Figure B.1: Refined XRD patterns during heating of run DAC04 at 25 to 29 GPa. Black lines correspond to the measured spectra and the red solid line represents the best refinement. Phases used for fitting the spectra are listed on the left side.

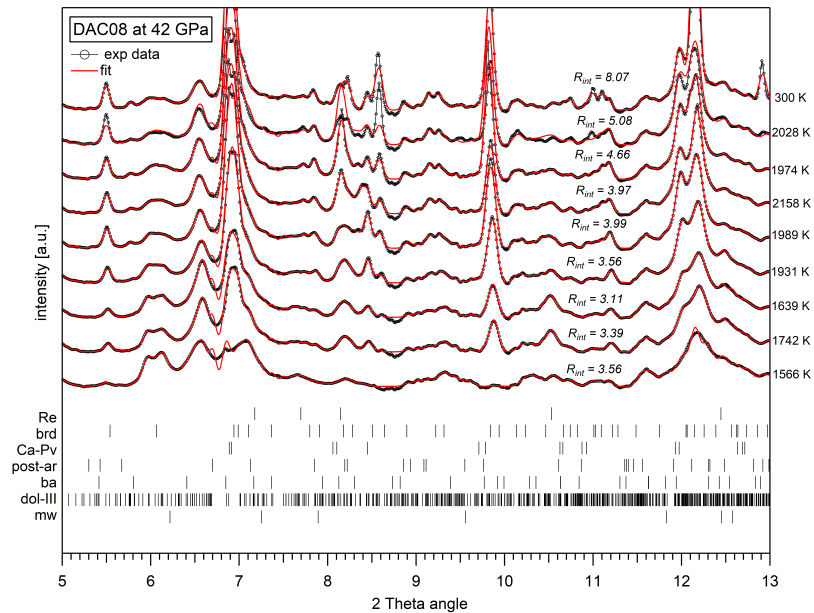


Figure B.2: Refined XRD patterns during heating of run DAC08 at 42 GPa. Black lines correspond to the measured spectra and the red solid line represents the best refinement.

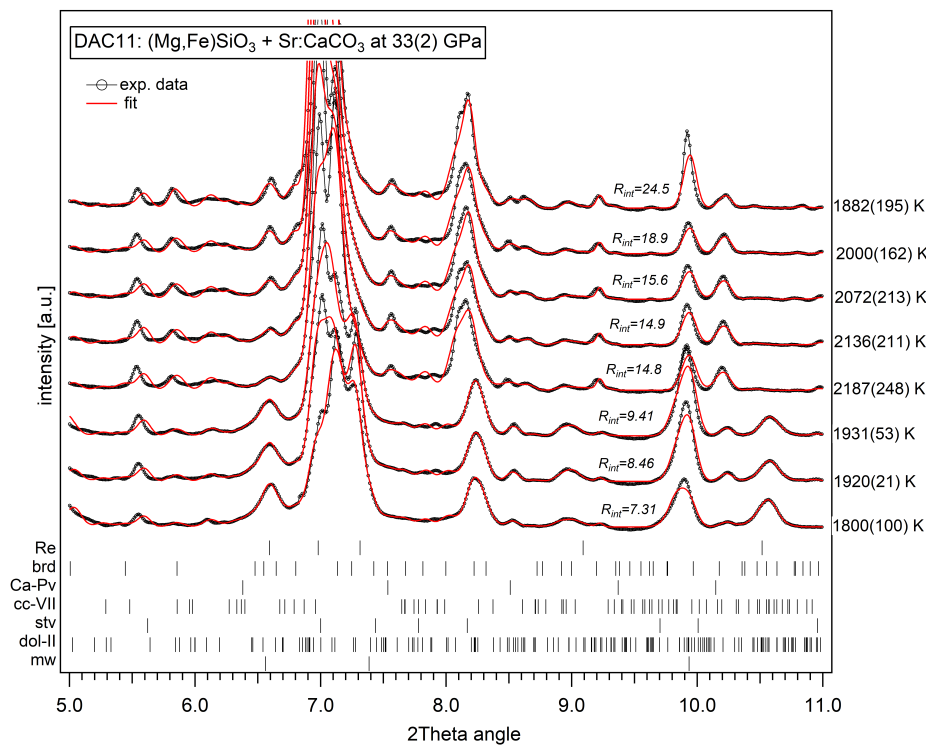


Figure B.3: Refined XRD patterns during heating of run DAC11 at 33 GPa. Black lines correspond to the measured spectra and the red solid lines represent the best refinement.

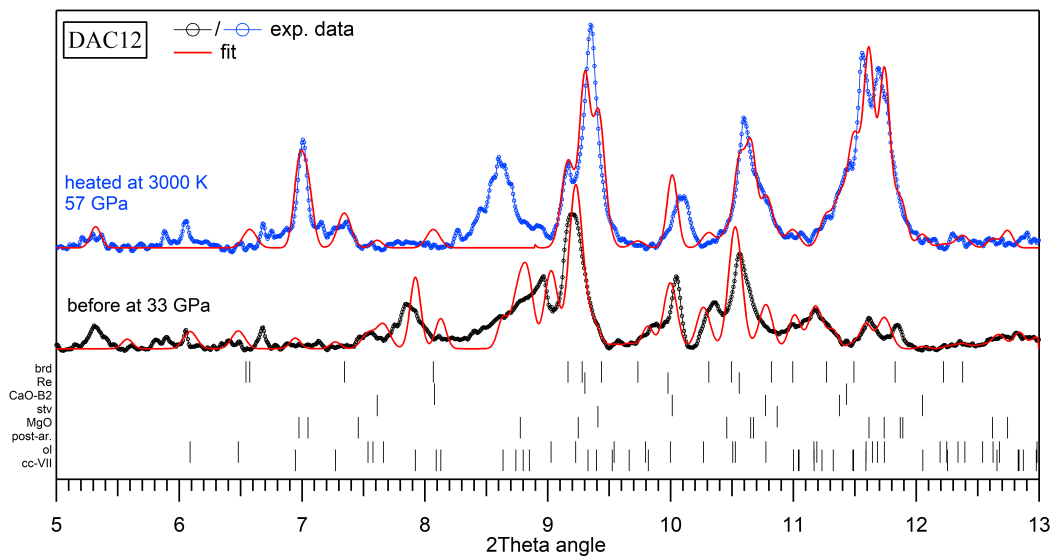


Figure B.4: Refined XRD patterns of run DAC12 before and after heating to a temperature of 3000 K. Black or blue line corresponds to the measured spectrum at 33 GPa and at 57 GPa, respectively. The red solid line represents the best refinement.



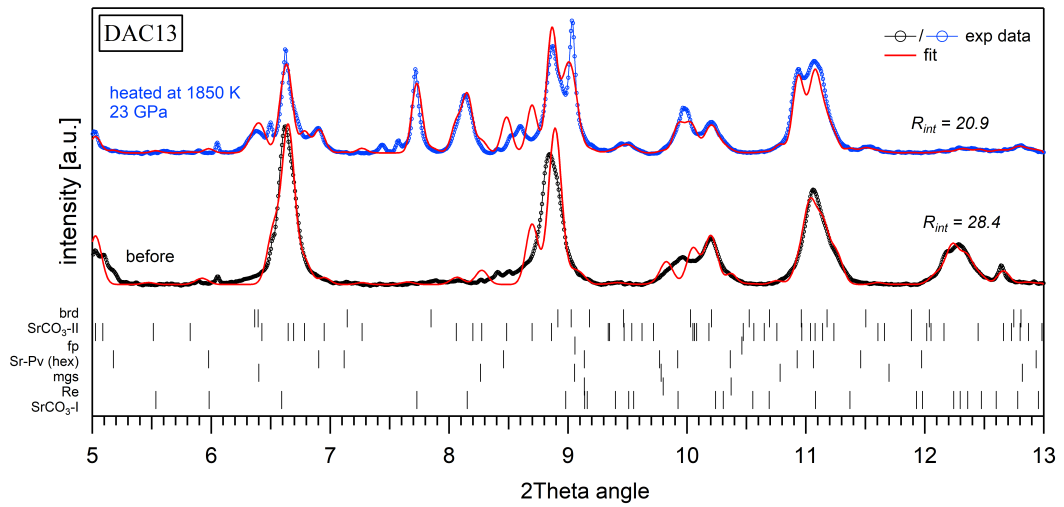


Figure B.5: Refined XRD patterns of run DAC13 heated up to 1850 K. Black or blue line corresponds to the measured spectrum before and after heating, respectively, at 23 GPa. The red solid line represents the best refinement.

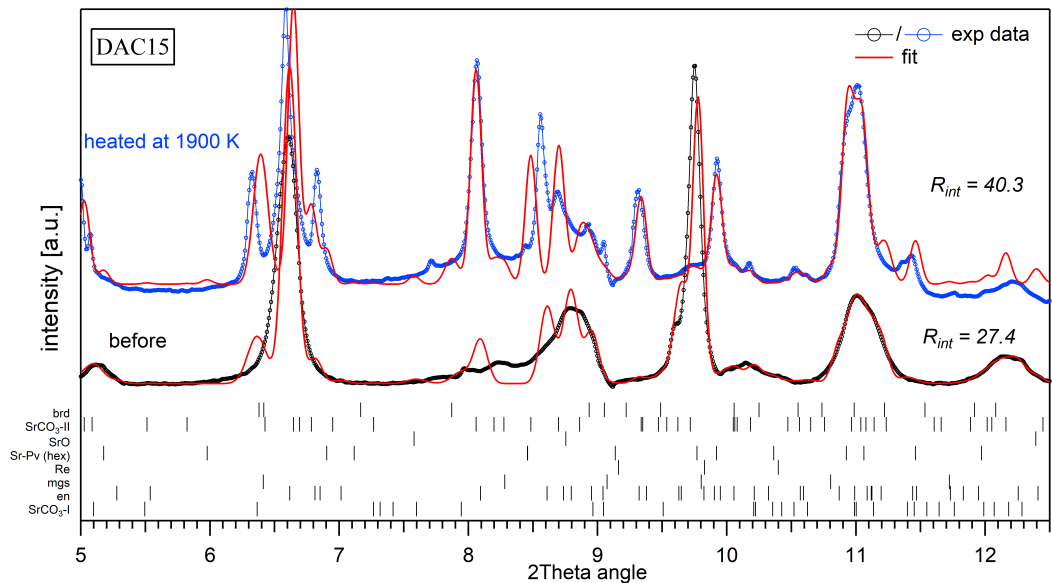


Figure B.6: Refined XRD patterns of run DAC15 heated up to 1900 K. Black or blue line corresponds to the measured spectrum before and after heating, respectively, at 26 GPa. The red solid line represents the best refinement.

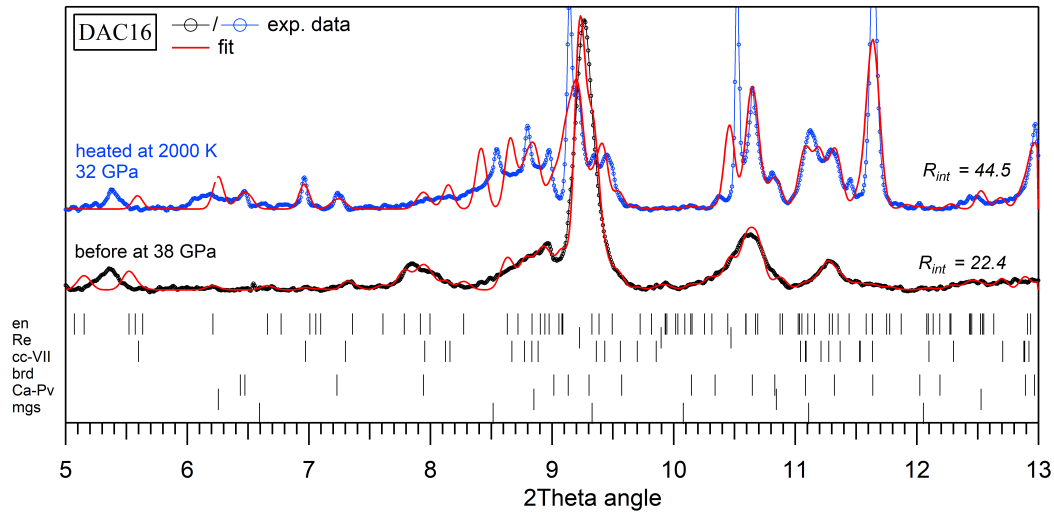


Figure B.7: Refined XRD patterns of run DAC16 before and heated up to 2000 K. Black or blue line corresponds to the measured spectrum before and after heating and at 38 GPa and 32 GPa, respectively. The red solid line represents the best refinement.

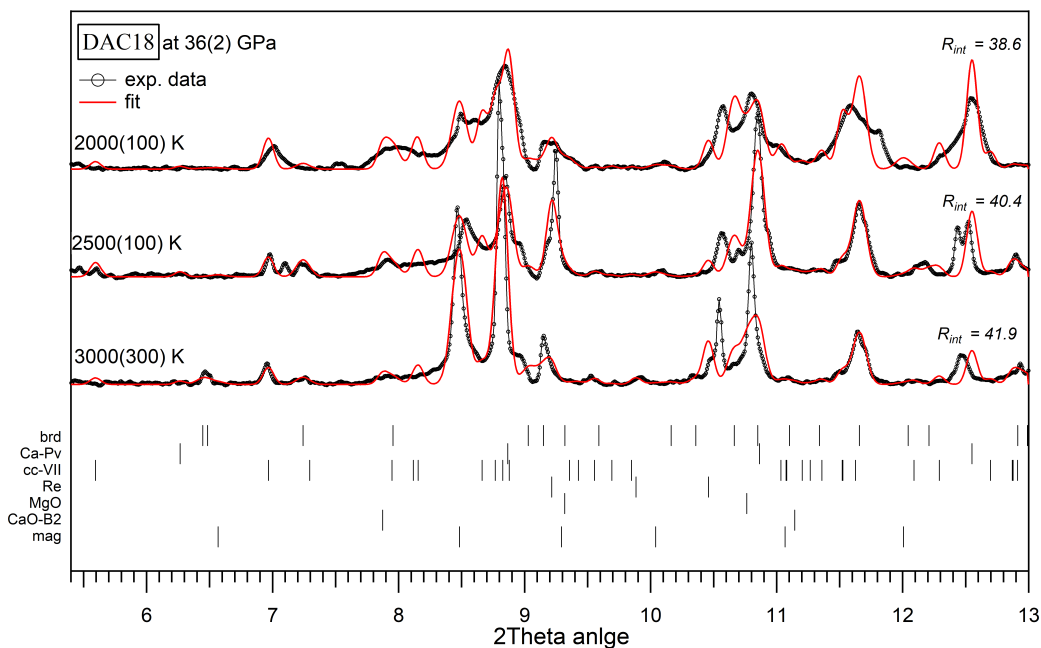


Figure B.8: Refined XRD patterns of run DAC18 at 36 GPa. Black lines correspond to the measured spectra after heating at temperatures of 2000, 2500 and 3000 K. The red solid line represents the best refinement.

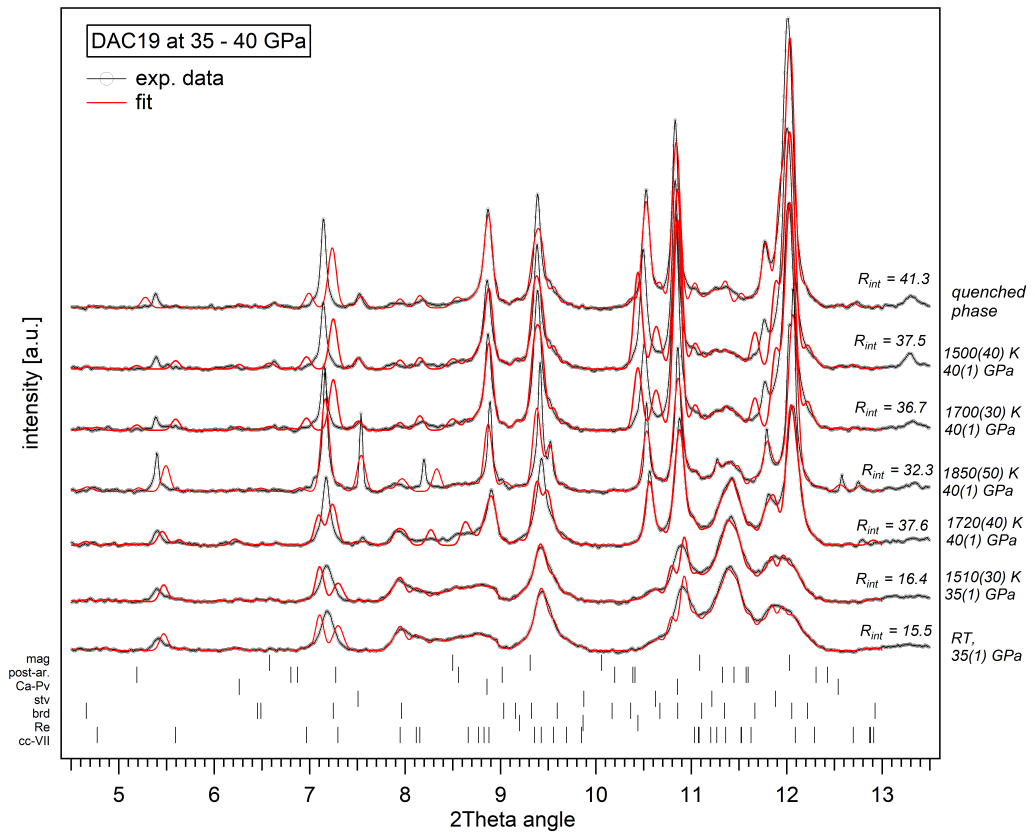


Figure B.9: Refined XRD patterns during heating of run DAC19 at 35 – 40 GPa. Black lines correspond to the measured spectra and the red solid line represents the best refinement.

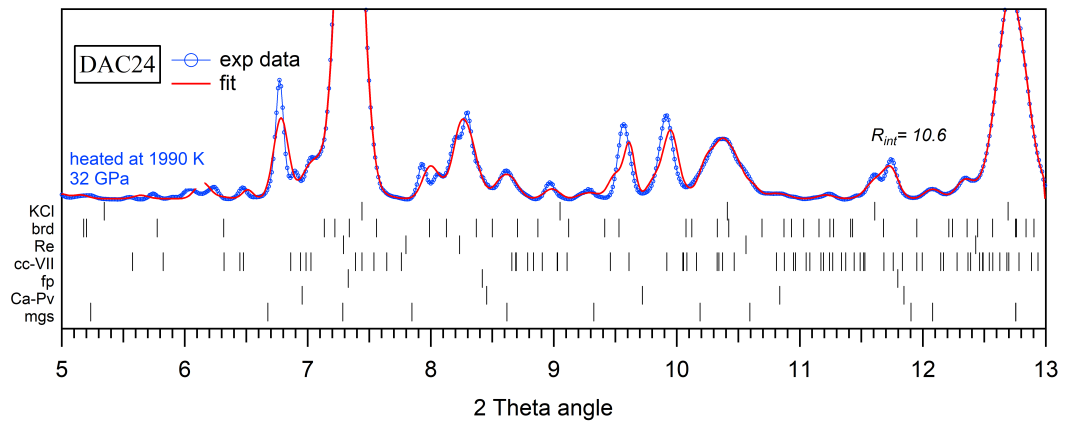


Figure B.10: Refined XRD patterns of run DAC24 heated up to 1990 K. Blue line corresponds to the measured spectrum after heating at 32 GPa and the red solid line represents the best refinement.

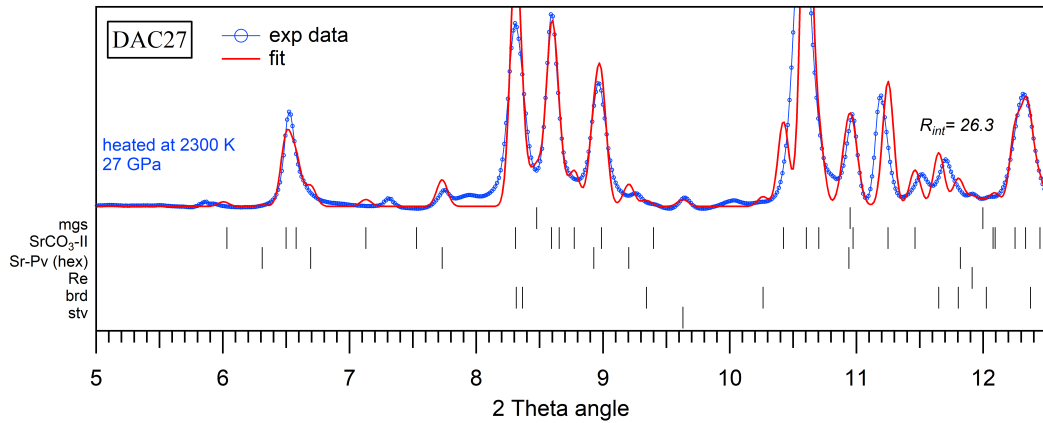


Figure B.11: Refined XRD patterns of run DAC27 heated up to 2300 K. Blue line corresponds to the measured spectrum after heating at 27 GPa and the red solid line represents the best refinement.

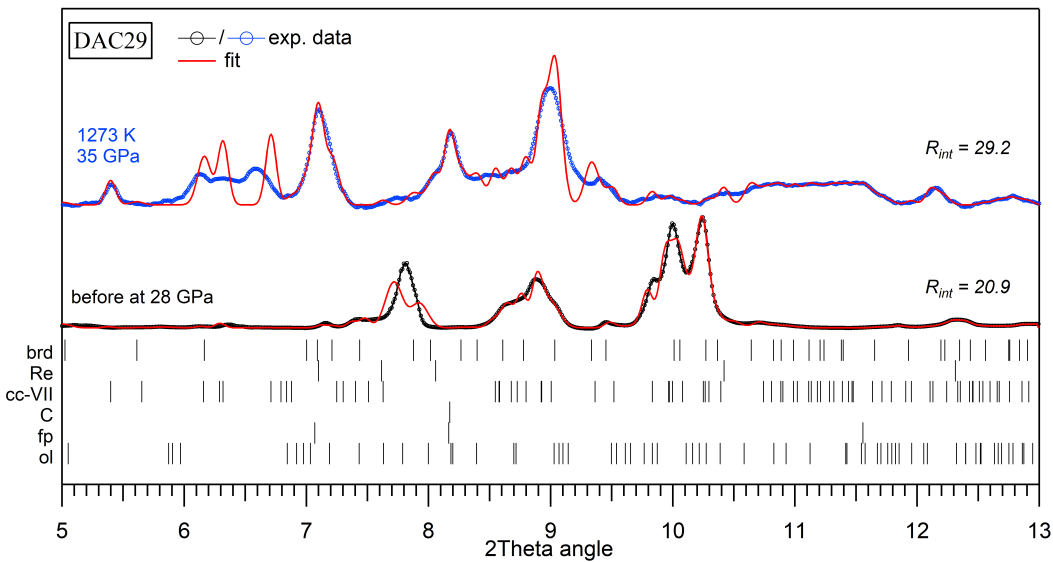


Figure B.12: Refined XRD patterns of run DAC29 heated resistively to a temperature of 1273 K. Black or blue line with grey markers corresponds to the measured spectra at 28 GPa before heating and during heating at 35 GPa, respectively. The red solid line represents the best refinement.

## References cited

- Campbell & Heinz (1991). *J. Phys. Chem. Solids*, 52(3): 495-499.
- Crichton & Ross (2000). AIRAPT-17 Proceeding - Science & Technology of HP, 2: 587-590.
- Duffy et al. (1995). *J. Geophys. Res. B: Solid Earth*, 100(B1): 529-542.
- Fei et al. (1991). *Phys Chem Minerals*, 18(7): 416-422.
- Finger et al. (1981). *Applied Physics Letters*, 39(11): 892-894.
- Gavryushkin et al. (2017). *Crystal Growth & Design*, 17(12): 6291–6296.
- Huang et al. (2017). *Chinese Physics B*, 26(8): 089101.
- Mao et al. (1991). *J. Geophys. Res. B: Solid Earth*, 96(B5): 8069-8079.
- Merlini et al. (2012). *PNAS*, 109(34): 13509–13514.
- Nishihara et al. (2005). *Phys Chem Minerals*, 31(10): 660-670.
- Richet et al. (1988). *J. Geophys. Res. B: Solid Earth*, 93(B12): 15279-15288.
- Ross et al. (1997). *American Mineralogist*, 82(7-8): 682-688.
- Rowland (2017). UNLV Theses, Dissertations. 3164.
- Shim et al. (1999). *Phys. Earth and Planet. Inter.*, 120(4), 327-338.
- Xiao et al. (2013). *American Mineralogist*, 98(11-12): 2096–2104.
- Xu et al. (2017). *High Temperatures – High Pressures*, 46(1).
- Yusa et al. (2005). *American Mineralogist*, 90(1117 - 1120).
- Zha et al. (2004). *Review of Scientific Instruments*, 75(7): 2409-2418.
- Zupan et al. (1993). *Physical Review B*, 48(2): 799.

## Appendix C

# Fitted XRF spectra from chapter 4

### Transitions of the X-ray emission lines

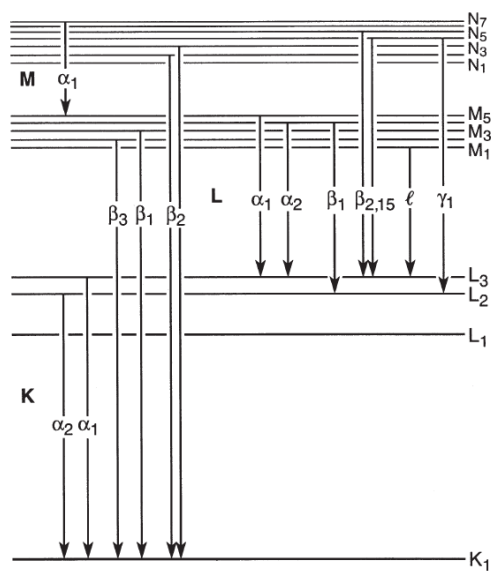


Figure C.1: Definitions for the transitions that give rise to the X-ray emission lines in Fig.C.2 – C.7.

## Fit configuration

### Samples with $\text{SrCO}_3$ at photon energies of 42.7 keV

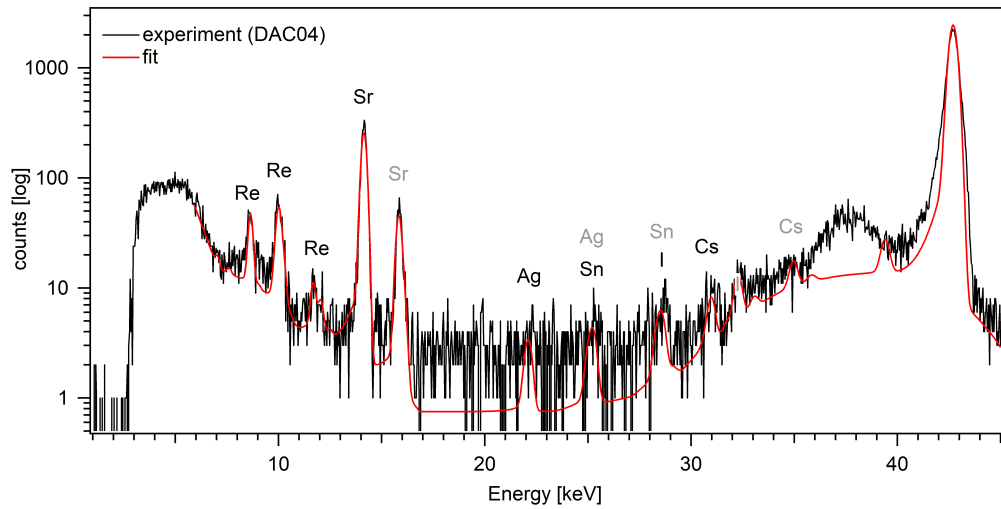


Figure C.2: XRF spectrum (black) of DAC04 (before heating) loaded with  $\text{SrCO}_3$  powder and silicate single crystal (e.g. hydrous wadsleyite). Acquisition time was 5 s. The red line shows the best fit for the measured spectrum. Details of the fit configuration are listed in Tab. C.1.

### Samples with $\text{SrCO}_3$ at photon energies of 33.2 keV

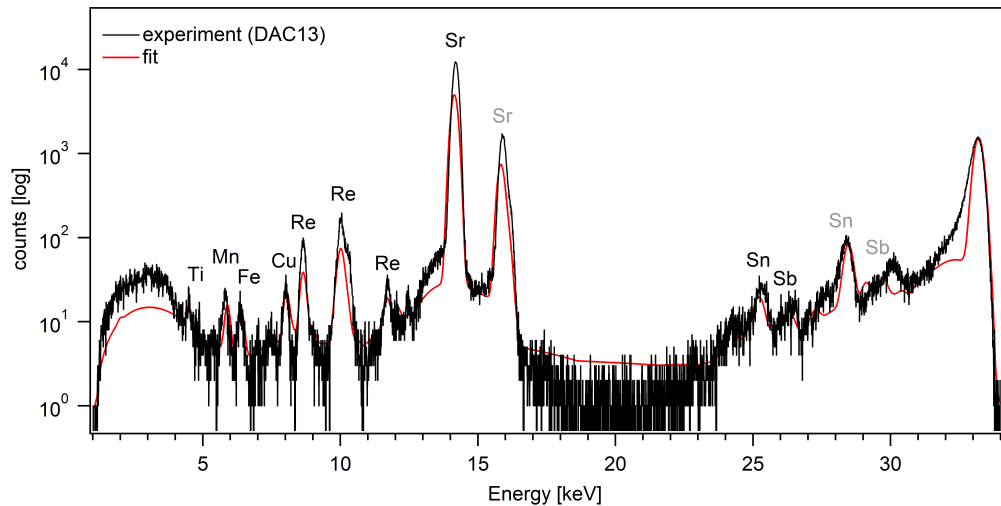


Figure C.3: XRF spectrum (black) of DAC13 (before heating) loaded with  $\text{SrCO}_3$  powder and silicate single crystal (e.g. enstatite). Acquisition time was 10 s. The red line shows the best fit for the measured spectrum. Details of the fit configuration are listed in Tab. C.2.

### Samples with $\text{CaCO}_3:\text{La}^{3+}$ (synthesis NB10) at 42.7 keV

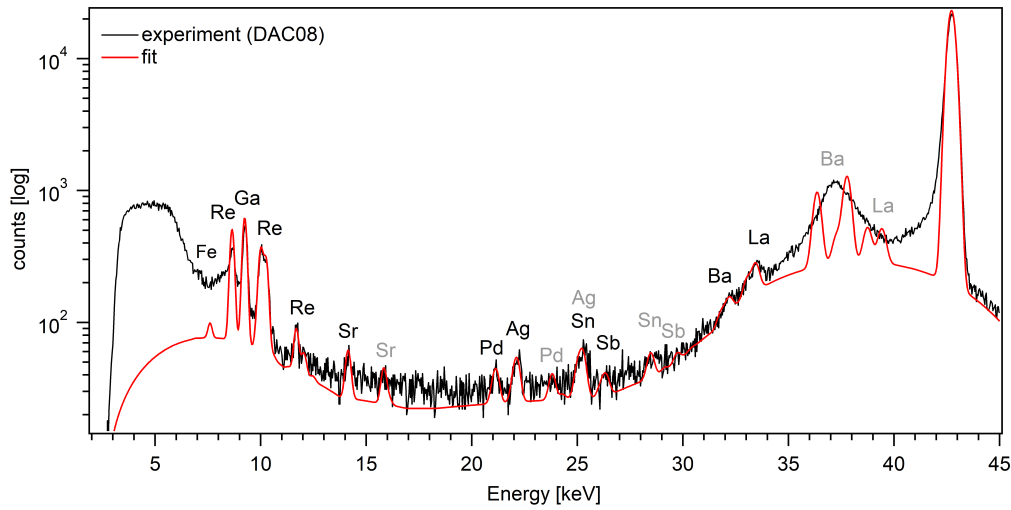


Figure C.4: XRF spectrum (black) of DAC08 (before heating) loaded with  $\text{CaCO}_3:\text{La}^{3+}$  single crystal and orthopyroxene single crystal. The XRF spectrum was extracted from the carbonate crystal. Acquisition time was 10 s. The red line shows the best fit for the measured spectrum. Details of the fit configuration are listed in Tab. C.1.

### Samples with $\text{CaCO}_3:\text{Sr}^{2+}$ (synthesis NB12) at 42.7 keV

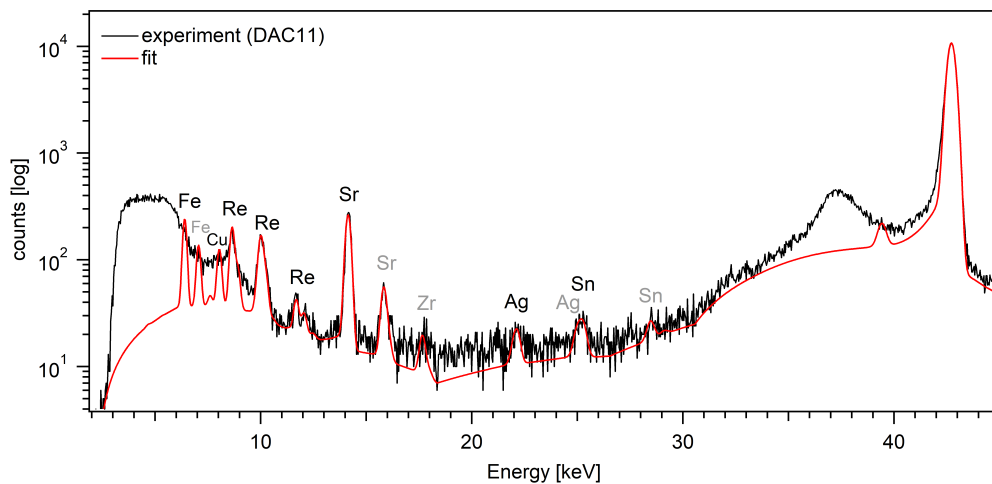


Figure C.5: XRF spectrum (black) of DAC04 (before heating) loaded with  $\text{SrCO}_3$  powder and silicate single crystal (e.g. hydrous wadsleyite). Acquisition time was 5 s. The red line shows the best fit for the measured spectrum. Details of the fit configuration are listed in Tab. C.1.



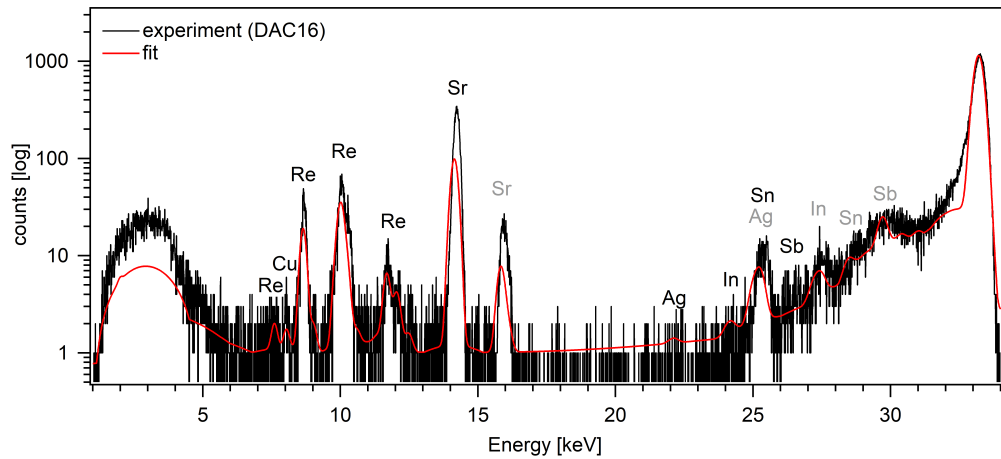
Samples with  $\text{CaCO}_3:\text{Sr}^{2+}$  (synthesis NB12) at 33.2 keV

Figure C.6: XRF spectrum of DAC16 (before heating) loaded with  $\text{CaCO}_3:\text{Sr}^{2+}$  powder and enstatite single crystal shown in black. Acquisition time was 7 s. The red line shows the best fit for the measured spectrum. Details of the fit configuration are listed in Tab. C.2.

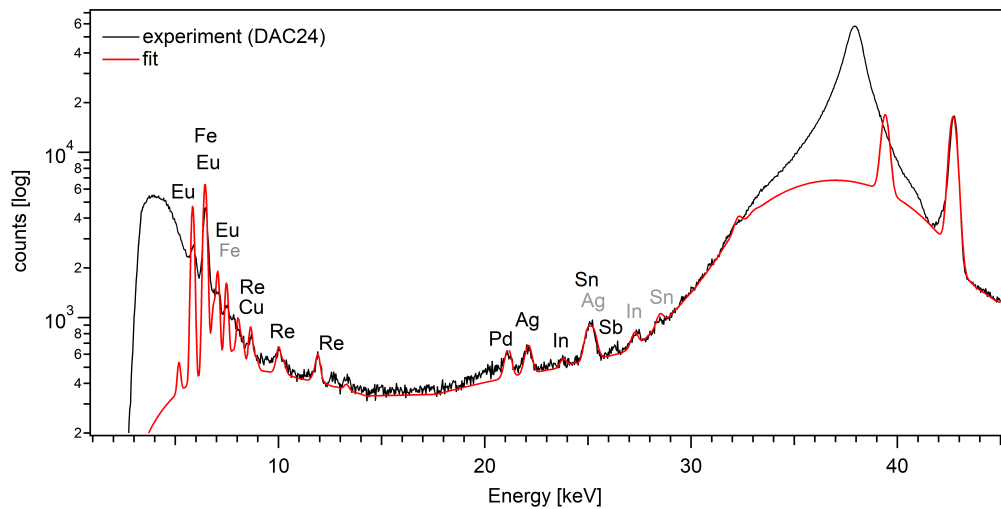
Samples with  $\text{CaCO}_3:\text{Eu}^{3+}$  at 42.7 keV

Figure C.7: XRF spectrum (black) of DAC24 (after heating) loaded with  $\text{CaCO}_3:\text{Eu}^{3+}$  powder and olivine single crystal. Acquisition time was 10 s. The red line shows the best fit for the measured spectrum. Details of the fit configuration are listed in Tab. C.1.

Table C.1: Details of fit configuration using the program PyMca for samples measured at photon energies of 42.7 keV

Fit Function	Mca Hypermet
Continuum type	No continuum
Non-analytical background algorithm	Strip Background
<i>Strip Background Width</i>	1
<i>Strip Background Iterations</i>	20000
<i>Include</i>	Stripping, pile-up peaks
Statistical weighing of data	Poisson (1/Y)
Number of Iterations	10
Matrix	Layer1 = C (density 3.51 g/cm <sup>3</sup> , thickness: 0.2 cm)
<b>Elements</b>	<b>Origin</b>
Fe(Ni)	silicate (e.g. olivine)
Sr, La, Eu	carbonate
Re	gasket material
Ga	FIB preparation
Ag, In, Sn, Sb	impurities from detector
Zr, Ba, Cs	impurities from nat. samples

Table C.2: Details of fit configuration using the program PyMca for samples measured at photon energies of 33.2 keV

Fit Function	Mca Hypermet
Continuum type	Linear Polynomial
<i>Polynomial order</i>	5
Non-analytical background algorithm	Strip Background
<i>Strip Background Width</i>	1
<i>Strip Background Iterations</i>	20000
<i>Include</i>	Stripping, pile-up peaks
Statistical weighing of data	Poisson (1/Y)
Number of Iterations	10
Matrix	Layer1 = C (density 3.51 g/cm <sup>3</sup> , thickness: 0.2 cm)
<b>Elements</b>	<b>Origin</b>
Fe(Ni)	silicate (e.g. olivine)
Sr, La, Eu	carbonate
Re	gasket material
Ga	FIB preparation
Ag, In, Sn, Sb	impurities from detector
Zr, Ba, Cs	impurities from nat. samples

## Distribution and origin of elements

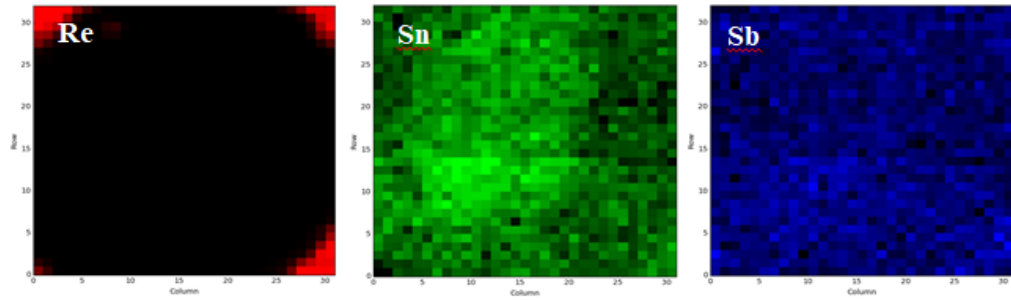


Figure C.8: Comparison between Re-, Sn- and Sb-distribution in DAC13 loaded with  $\text{SrCO}_3$  powder and enstatite single crystal (located in the center of the map). It can be seen that there is no correlation between Re, Sn and Sb.

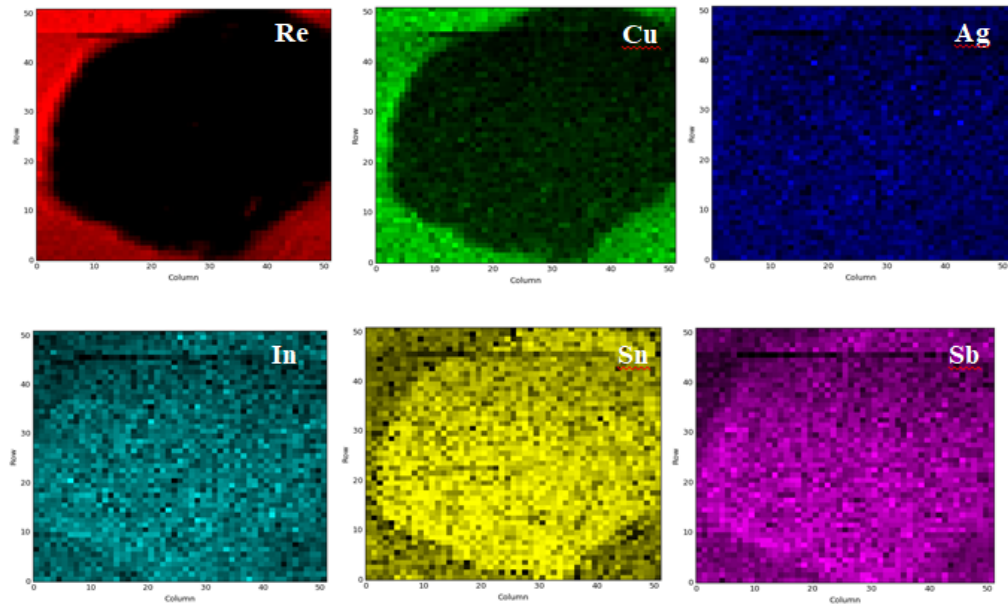


Figure C.9: Comparison between Re-, Cu-, Ag-, In-, Sn- and Sb-distribution in DAC16. Cu signal is mostly overlaid by Re-signal and shows similar distribution. Impurities of Ag, In, Sn and Sb are coming from detector and are not correlated with Re-signal.

## Appendix D

# EDX analyses on recovered sample material using TEM and SEM

Sample DAC24 ( $\text{CaCO}_3:\text{Eu}^{3+} + (\text{Mg,Fe})\text{SiO}_3$ )

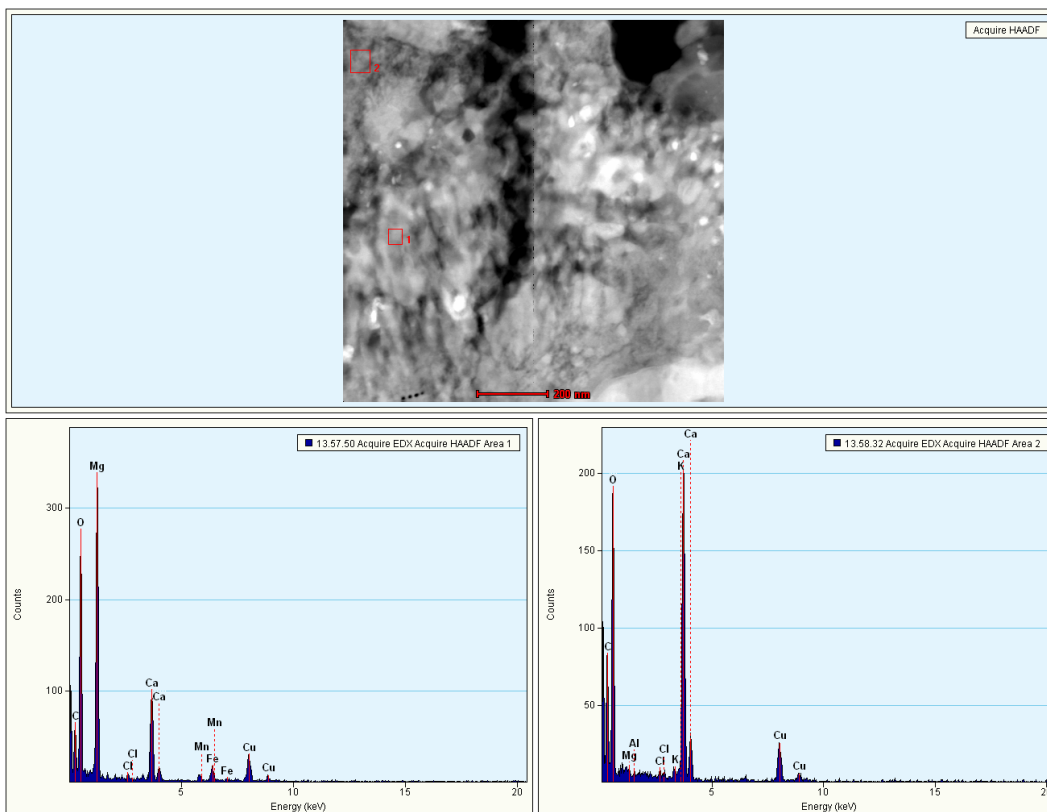


Figure D.1: EDX spectra of two areas in DAC24 showing Fe-bearing magnesite (left, analysis 1) in addition to calcite (right, analysis 2). The magnesite was formed during carbonate-silicate reactions at HP and HT.

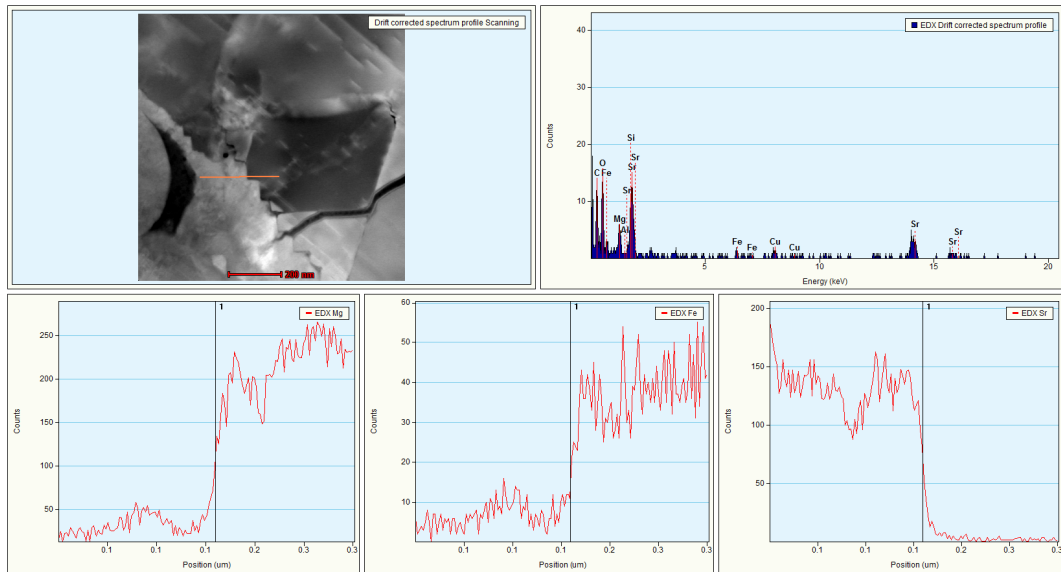
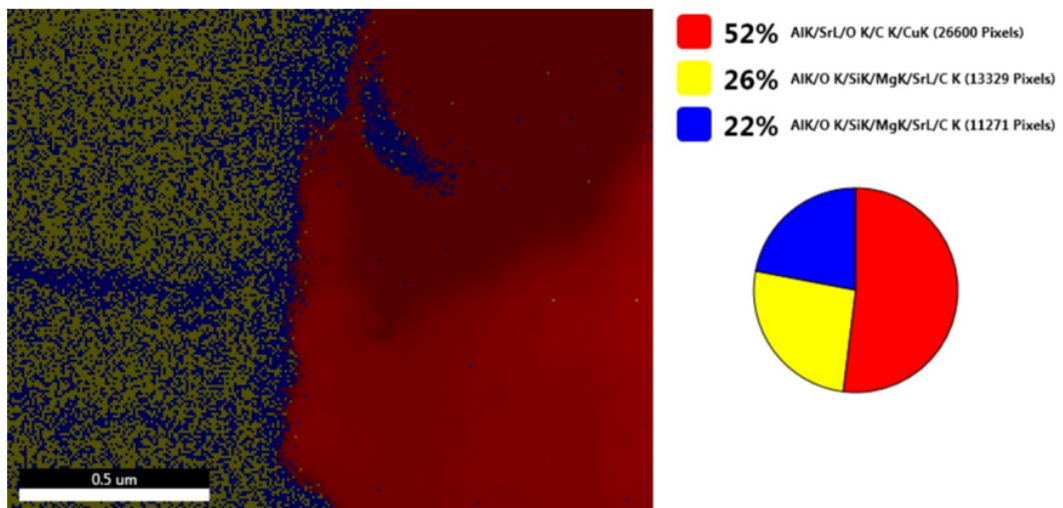
Sample DAC27 ( $\text{SrCO}_3 + (\text{Mg,Fe})\text{SiO}_3$ )

Figure D.2: EDX line scan of DAC27 at the interface between carbonate and silicate.

Figure D.3: Element map of DAC27 at the interface between carbonate and silicate with three distinct areas: Mg,Fe-bearing  $\text{SrCO}_3$  (red),  $(\text{Mg}_{0.85}\text{Fe}_{0.15})\text{SiO}_3$  low-P clinoenstatite (yellow) and  $(\text{Mg}_{0.65}\text{Fe}_{0.15}\text{Sr}_{0.2})\text{SiO}_3$  clinopyroxene (blue). Quantitative analyses are listed in Tab. D.1 – D.3.

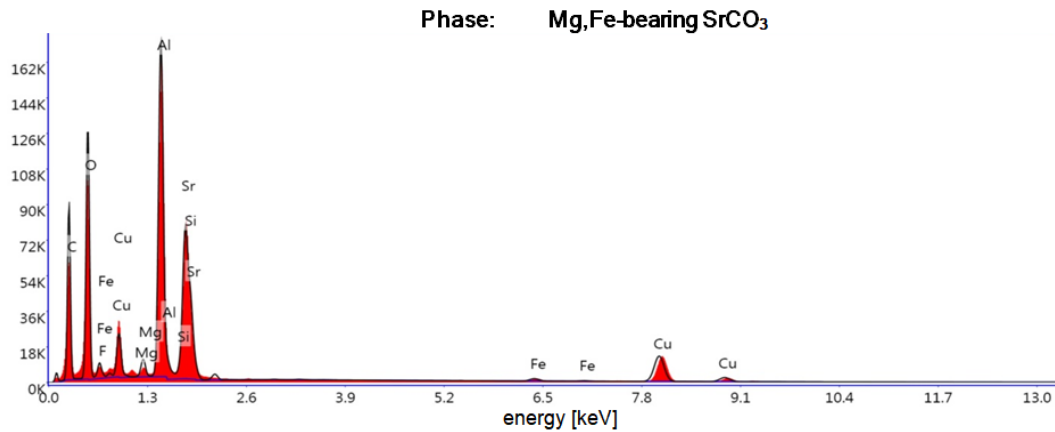


Figure D.4: Spectrum of Mg- and Fe-bearing SrCO<sub>3</sub> in DAC27 (red area in Fig. D.3) acquired at an acceleration voltage of 20 kV in 340 s.

Table D.1: Quantitative analyses of Mg,Fe-bearing SrCO<sub>3</sub> in DAC27 (red area in Fig. D.3).

Element	Weight %	Atomic %	Error %
C	33.0	49.8	9.1
O	28.8	32.6	9.1
F*	2.8	2.6	11.6
Mg	1.1	0.8	6.7
Al*	13.6	9.2	4.8
Si	0.4	0.3	7.1
Sr	11.9	2.5	2.4
Fe	0.5	0.2	4.6
Cu*	8.0	2.3	2.4

\*contamination from SEM sample preparation

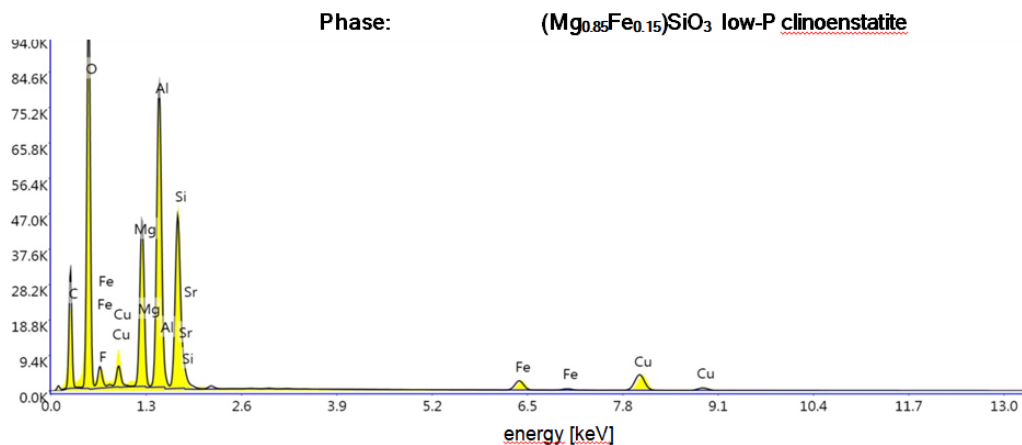
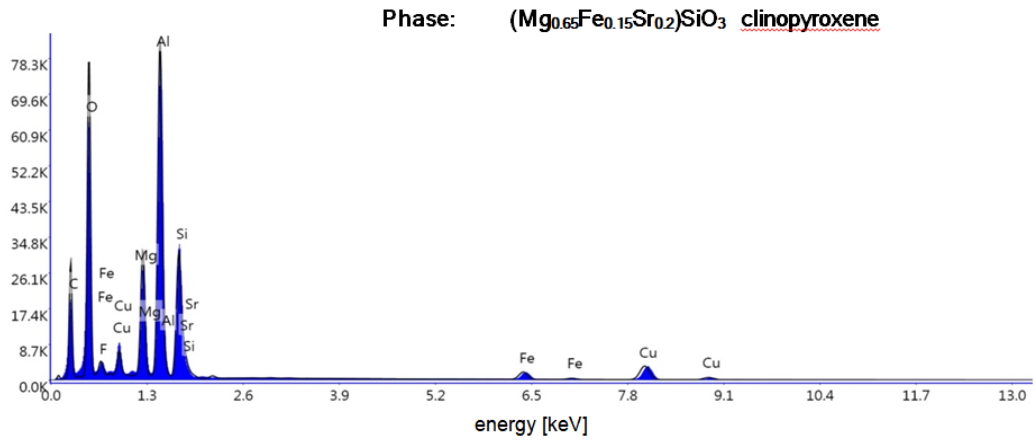


Figure D.5: Spectrum of (Mg<sub>0.85</sub>Fe<sub>0.15</sub>)SiO<sub>3</sub> low-P clinoenstatite in DAC27 (yellow area in Fig. D.3) acquired at an acceleration voltage of 20 kV in 340 s.

Table D.2: Quantitative analyses of  $(\text{Mg}_{0.85}\text{Fe}_{0.15})\text{SiO}_3$  low-P clinoenstatite in DAC27 (yellow area in Fig. D.3).

Element	Weight %	Atomic %	Error %
C	24.2	35.9	9.3
O	35.4	39.4	8.5
F*	3.3	3.1	13.6
Mg	7.8	5.7	6.0
Al*	13.5	8.9	5.2
Si	7.6	4.8	5.1
Sr	1.6	0.3	4.3
Fe	1.6	0.5	3.2
Cu*	5.0	1.4	2.8

\*contamination from SEM sample preparation

Figure D.6: Spectrum of  $(\text{Mg}_{0.65}\text{Fe}_{0.15}\text{Sr}_{0.2})\text{SiO}_3$  clinopyroxene in DAC27 (blue area in Fig. D.3) acquired at an acceleration voltage of 20 kV in 340 s.Table D.3: Quantitative analyses of  $(\text{Mg}_{0.65}\text{Fe}_{0.15}\text{Sr}_{0.2})\text{SiO}_3$  clinopyroxene in DAC27 (blue area in Fig. D.3).

Element	Weight %	Atomic %	Error %
C	26.4	38.9	9.4
O	33.4	36.9	8.6
F*	3.1	2.9	13.2
Mg	6.5	4.8	5.9
Al*	16.0	10.5	5.0
Si	6.2	3.9	5.2
Sr	2.2	0.4	4.0
Fe	1.5	0.5	3.4
Cu*	4.9	1.4	2.9

\*contamination from SEM sample preparation